



**THÈSE DE DOCTORAT**  
**DE L'UNIVERSITÉ PSL**

Préparée à l'Institut Curie

**EXPLORING THE DYNAMICS OF CANCER CELL  
SUBPOPULATIONS AND METASTATIC INVASION  
USING HIGH THROUGHPUT MICROFLUIDIC  
SORTING AND TYPING**

Soutenue par

**Ismail HAJJI**

Le 19 février 2019

Ecole doctorale n° 564

**Physique en Île-de-France**

Spécialité

**Physique**

Composition du jury :

Marie Caroline, JULLIEN  
ESPCI Paris

*Présidente du jury*

Valéry, TALY  
Université Paris Descartes

*Rapporteur*

Catherine, ALIX-PANABIERES  
CHU - Université de Montpellier

*Rapporteur*

Govind, KAIGALA  
IBM Zurich

*Examineur*

Stéphanie, DESCROIX  
Institut Curie

*Co-Directeur de thèse*

Jean-Louis, VIOVY  
Institut Curie

*Directeur de thèse*





# Remerciements

Le temps de la gratitude et des remerciements. Un exercice journalier. Mais, que la coutume a voulu particulièrement célébrer au début de chaque manuscrit de thèse. D'où vient cette coutume ?... Dieu, le Hasard ou l'Entropie nous y ont certainement mené. Gardons l'exercice et respectons la coutume.

Je souhaite sincèrement adresser mes remerciements aux personnes suivantes :

Jean-Louis Viovy et Stéphanie Descroix mes directeurs de thèse. Je souhaite vous remercier pour la confiance que vous m'avez accordée en m'intégrant dans l'équipe, en me donnant les moyens, la liberté et le temps de creuser chacune des questions explorées durant ces trois années. Je vous suis également extrêmement reconnaissant pour l'environnement que vous m'avez offert pour ma thèse. Je m'y suis plu, investi et épanoui. J'espère contribuer du mieux que je puisse à son développement jusqu'à mon départ vers de nouveaux horizons. Et je suis certain de porter avec moi la joie de vivre de cette équipe, peu importe ma destination. Encore MERCI !

Laurent Malaquin qui, par le plus grand des hasards, m'a mis en relation avec Jean-Louis et Stéphanie. Les rapporteurs de ma thèse Valérie Taly et Catherine Alix-Panabières et les examinateurs Marie-Caroline Jullien et Govind Kaigala qui ont accepté de faire partie du Jury et qui ont commenté avec une grande bienveillance ce travail.

Le premier pilier de lancement de cette thèse a été Julien Autebert. Il m'a énormément aidé durant mes premiers mois. J'ai failli être en stage avec lui chez IBM (encore grâce à Laurent). Il est ensuite revenu dans l'équipe quand je débutais ma thèse. L'entropie a fait qu'il avait travaillé sur Ephesia à Curie et sur les gouttes à IBM, ce qui correspondait exactement aux outils que j'allais utiliser durant ma thèse. Il a été incroyablement réceptif à ma motivation et disponible pour répondre à mes 10000 questions journalières. Grosse leçon : "On fait les manips D'ABORD parce que c'est FUN !". Après ça, tout devient plus facile...

Je voudrais ensuite remercier chaleureusement Davide Ferraro qui n'a malheureusement pas pu venir à la soutenance (à cause d'une pratique trop intensive du badminton !). Davide, deuxième pilier de démarrage, est à l'origine du projet de Drop qPCR et a

également travaillé avant son départ pour l'Italie sur le premier chapitre de la thèse. Il m'a beaucoup soutenu au début et à continuer même au-delà des alpes avec des séances de visio-conférences interminables mais tout autant intéressantes. Présent, tant humainement que scientifiquement avec beaucoup de bienveillance.

Rashmi Ramesh et Mathilde Richerd qui ont fait un formidable travail pendant leurs stages et avec qui j'ai beaucoup apprécié travailler. Je leur souhaite beaucoup de réussite dans leurs thèses respectives : Mathilde avec nous dans l'équipe et Rashmi qui s'en est allé deux rues plus loin pour continuer à faire des gouttes à Ulm.

Mon comité de thèse : Leila Perié & Charlotte Proudhon. Tout particulièrement Charlotte qui a été très réceptive à mon enthousiasme sur le projet CRTMA et qui m'a ouvert les portes du BTC lab. Charles Decreane avec qui on a passé quelques soirées sur le CellCelector et Aurore Rampnou. Emile Lakis qui m'a rejoint sur le projet PLA et qui nourrit l'équipe tant de gâteaux que de motivation !

François-Clément Bidard sans qui le projet CRTMA n'aurait jamais commencé. Sa motivation et sa capacité à mobiliser les équipes au bon moment, pour sa confiance en moi également. « Chevaliers de la mat »

Viovyz les anciens : Bastien, Iago, Renaud, Amel, Ayako, Velan, Marco, Jérôme, Cécile... Chacun à son tour et à sa façon m'a accueilli et appris lorsque je commençais dans l'équipe. Ils faisaient régner une belle atmosphère qu'on a essayé de maintenir par la suite.

Mes contemporains : Miza pour toutes les discussions, le feeling des gens, une profonde gentillesse, et une oreille à l'écoute, la découverte de Singapour... j'attends ta prochaine visite au Maroc avec Etienne cette fois-ci. Charles, le survivant de mes co-bureaux, pour une autodérision et un team-spirit exceptionnel à toute heure... Lucile & Lauriane avec qui j'ai eu le sentiment de traverser ses trois années avec beaucoup de rires, de joies et de partage. Une paire exceptionnelle ! Nous avons commencé nos stages côte à côte dans l'équipe avec Lauriane. Et déjà à l'époque, elle voulait ranger tout Curie ! Je suis profondément convaincu que ton acharnement pour l'équipe, l'organisation, et ta volonté de faire « Bien » et « pour les autres » seront un incroyable atout pour l'équipe et où que tu ailles dans le futur.

Lucile co-bureau, co-voyageuse, co-professeuse, j'ai énormément appris à tes côtés. Une très grande passion pour la vulgarisation scientifique dont je suis le premier fan. Merci pour les bouquins que tu m'as fait lire et tous ceux que je n'ai pas encore lu... les joggings

au Luxembourg, les petits-déjeuners, les gouters, les cours de philo, les mille et une discussions sur la science, la vie, les gens, et nos perceptions... de m'avoir soutenu et suivi dans tous mes délires. Merci !

La relève MMBM : la relève est là ! Ils sont vifs, jeunes et dynamiques : Corentin, Caroline, Emile, Manh, Elodie, Mathilde, Théo, Audric, Temple... et tous les autres. L'équipe reprend du volume et c'est avec plaisir que je constate qu'elle garde le même esprit que celui que j'ai connu à mon arrivée. De la bienveillance et une joie de vivre en groupe qui donnent du plaisir et nous font travailler passionnément mais sans aucun labeur. Je remercie tout ce beau monde pour son soutien durant la thèse et vous souhaite le meilleur pour la suite.

Merci également à tous mes amis et la liste serait beaucoup trop longue pour citer tout le monde mais je suis convaincu qu'ils se reconnaîtront. Pour leur présence et leurs encouragements.

Ma famille, mes cousins/cousines (les parisiens et tous les autres), oncles et tantes qui se sont déplacés de Rabat pour voir ma soutenance et tous ceux qui me soutenaient de loin. Ma grand-mère au courage et à l'énergie infaillibles et qui rayonne de vie sur toute la famille. Mes parents, Hicham et Lamia, la base solide derrière ce travail et sans qui rien n'aurait été possible... Merci !



# Abstract

This thesis reports on the development and use of microfluidic tools for the encapsulation and analysis of single cells with applications in biology and cancerology. We describe the development and characterization of a droplet microfluidic platform composed of several modules allowing: the encapsulation and sorting of single cells in aqueous droplets in oil, the injection and merging of the cells with reagents and finally, the analysis of their content by a droplet quantitative PCR device. Thereafter, we present in the context of a clinical research study, the use of a second microfluidic platform ‘Ephesia’ allowing the capture of circulating tumor cells, to study their role in cancer related thrombotic microangiopathies by next generation sequencing.

# Résumé

Cette thèse traite du développement et de l'utilisation d'outils microfluidiques pour l'encapsulation et l'analyse de cellules uniques dans le cadre d'applications en biologie et en cancérologie. Nous y relatons la mise en place et le développement d'une plateforme de microfluidique en gouttes composée de plusieurs modules permettant : l'encapsulation et le tri de cellule unique dans des gouttes aqueuses, l'injection et le mélange des cellules avec des réactifs et enfin l'analyse de leur contenu par un système de PCR quantitative en gouttes. Nous présentons ensuite dans le cadre d'une étude de recherche clinique, l'utilisation d'une seconde plateforme microfluidique ‘Ephesia’ permettant la capture de cellules tumorales circulantes, afin d'étudier leur rôle dans les microangiopathies thrombotiques liées au cancer par séquençage nouvelle-génération.



# *Table of Contents*

1.	Introduction: Microfluidics for cancer research .....	- 14 -
2.	A droplet platform for single-cell analysis.....	- 18 -
2.1	Introduction to single-cell encapsulation.....	- 20 -
2.1.1	Poisson based encapsulation.....	- 20 -
2.1.2	Ordered encapsulation.....	- 22 -
2.1.3	Other improved encapsulations & sorting.....	- 23 -
2.1.4	Encapsulation with hydrodynamic self-sorting.....	- 25 -
2.1.5	Commercial product .....	- 28 -
2.1.6	Aims of the chapter.....	- 29 -
2.2	Single cell encapsulation in fluorinated oil.....	- 30 -
2.2.1	Droplet generation in flow focusing, description by Ca.....	- 31 -
2.2.1.1	Interfacial tension: equilibrium vs. dynamic.....	- 31 -
2.2.1.2	Description by capillary number .....	- 34 -
2.2.1.3	Capillary numbers and IFT in our encapsulation device.....	- 36 -
2.2.2	Material & methods.....	- 44 -
2.2.2.1	Chip design & features:.....	- 44 -
2.2.2.2	Chip fabrication.....	- 46 -
2.2.2.3	Experimental setup.....	- 47 -
2.2.2.4	Dispersed and continuous phases .....	- 49 -
2.2.3	Results & discussion.....	- 52 -
2.2.3.1	Droplet generation in mineral oil with Span 20 and Span 80.....	- 53 -
2.2.3.2	Droplet generation in fluorinated oil with PFD and Krytox.....	- 59 -
2.2.4	Conclusion & perspectives .....	- 65 -
2.2.4.1	Asymmetric configuration.....	- 65 -
2.2.4.2	Encapsulation and sorting of cells using fluorinated oil.....	- 67 -
2.3	Large scale droplet manipulation towards downstream analysis .....	- 70 -

2.3.1	Introduction .....	- 70 -
2.3.2	Device for droplet collection.....	- 71 -
2.3.3	Device for on-demand injection and merging.....	- 73 -
2.3.3.1	Close-pack and spacing .....	- 73 -
2.3.3.2	Pressure pulse for on-demand injection.....	- 77 -
2.3.3.3	Passive merging .....	- 78 -
2.3.4	Conclusion and perspectives .....	- 80 -
2.4	Conclusion on single-cell encapsulation and preparation.....	- 82 -
3.	Drop qPCR .....	- 84 -
3.1	Introduction .....	- 86 -
3.1.1	Polymerase Chain Reaction.....	- 86 -
3.1.1.1	Principle of PCR .....	- 87 -
3.1.1.2	Quantitative PCR .....	- 88 -
3.1.1.3	Real-time PCR principle .....	- 89 -
3.1.1.4	Chemistry for real-time PCR.....	- 90 -
3.1.2	qPCR in microfluidics .....	- 93 -
3.1.2.1	Miniaturized devices.....	- 93 -
3.1.2.2	Static sample PCR .....	- 94 -
3.1.2.3	Continuous-flow PCR.....	- 97 -
3.1.3	Microfluidic PCR commercial devices.....	- 99 -
3.1.5	Aims of the project.....	- 99 -
3.2	Material & methods.....	- 100 -
3.2.1	Genes, cells & Master Mix.....	- 100 -
3.2.2	Fluidic tools.....	- 101 -
3.2.3	RT-qPCR machine.....	- 103 -
3.2.3.1	Heating plates .....	- 103 -
3.2.3.2	Fluorescence measurement .....	- 105 -
3.2.4	Data analysis.....	- 107 -
3.2.4.1	Introduction: from pixels to diagnosis.....	- 107 -



3.2.4.2	ROI & signal processing.....	- 107 -
3.2.4.3	Droplet peaks & normalization.....	- 108 -
3.2.4.4	Kinetic model of PCR: Efficiency & linear regression.....	- 110 -
3.2.4.5	Quantification & Ct value.....	- 111 -
3.2.5	SmartCycler.....	- 113 -
3.3	Results & discussions.....	- 114 -
3.3.1	POC on total RNA.....	- 114 -
3.3.1.1	Description of the POC.....	- 114 -
3.3.1.2	Standard curves of SKBR3.....	- 116 -
3.3.1.3	Standard curves of MCF7.....	- 117 -
3.3.1.4	Discussion & conclusion on total RNA.....	- 119 -
3.3.2	High-throughput and cycling time.....	- 120 -
3.3.2.1	Need for faster qPCR.....	- 120 -
3.3.2.2	Thermalization time.....	- 121 -
3.3.2.3	Hot start DNA polymerase.....	- 123 -
3.3.2.4	Denaturation / annealing-elongation, PCR time.....	- 124 -
3.3.2.5	Reverse transcriptase, RT time.....	- 126 -
3.3.2.6	Discussion & conclusion on Cycling time.....	- 128 -
3.4	Conclusion and perspectives on Droplet qPCR.....	- 129 -
	Appendix: Sequences and primers.....	- 131 -
4.	Role of tumor cells in Cancer related TMA.....	- 132 -
4.1	Introduction.....	- 135 -
4.1.1	Circulating tumor cells.....	- 135 -
4.1.2	Ephesia.....	- 138 -
4.1.2.1	Principle of the Ephesia Platform.....	- 138 -
4.1.2.2	Ephesia from 2010 to 2018.....	- 140 -
4.1.3	Cancer-related TMA.....	- 141 -
4.1.3.1	Introduction: clinical context.....	- 141 -
4.1.3.2	Cancer-related thrombotic microangiopathy.....	- 145 -
4.1.3.3	First experiments and clusters images.....	- 147 -

4.1.3.4	Patients description.....	- 149 -
4.2	Techniques of investigation & results .....	- 151 -
4.2.1	Ephesia experiments.....	- 151 -
4.2.1.1	Controls and protocol biases.....	- 151 -
4.2.1.2	Observations & comments for the four patients.....	- 152 -
4.2.1.3	Bright field injection recording.....	- 152 -
4.2.1.4	Staining observations & discussion.....	- 153 -
4.2.1.5	Conclusion on Ephesia staining.....	- 154 -
4.2.2	Methods of investigation.....	- 155 -
4.2.2.1	Ephesia processing.....	- 156 -
4.2.2.2	Veridex, CellSearch system.....	- 158 -
4.2.2.3	Patient Derived Xenografts.....	- 161 -
4.2.2.4	ISET filters.....	- 162 -
4.2.2.5	CellCelector.....	- 163 -
4.2.2.6	Conclusion on the different methods of investigation.....	- 164 -
4.2.3	Whole Exome Sequencing.....	- 165 -
4.2.3.1	Samples collection & DNA extraction.....	- 165 -
4.2.3.2	Library preparation.....	- 167 -
4.2.3.3	Sequencing and QC.....	- 169 -
4.2.3.4	Sequencing data analysis.....	- 171 -
4.2.3.5	First results & perspectives.....	- 177 -
4.2.4	RNA sequencing.....	- 179 -
4.2.4.1	Sample type & extraction.....	- 179 -
4.2.4.2	Library preparation, sequencing, QC results & mapping.....	- 179 -
4.2.4.3	Bioinformatics data analysis.....	- 182 -
4.2.4.4	Next steps & perspectives.....	- 185 -
4.3	Conclusion CR TMA & perspectives .....	- 186 -
Appendix - 187 -		
	Ephesia video links.....	- 187 -
	Ephesia protocols of chip fabrication processing.....	- 188 -

PDMS chip protocol.....	- 188 -
COC chip protocol.....	- 191 -
Experiments processing.....	- 195 -
Experimental setup.....	- 195 -
Sample pre-treatment.....	- 197 -
Cell fixation & staining.....	- 198 -
5.        General conclusion.....	- 200 -
Résumé en langue française :.....	- 204 -
Bibliography.....	- 214 -



# *1. Introduction:*

*Microfluidics for cancer research*

Genetic mutations are the drivers of species evolution. The diversity created by these mutations makes each individual different from its neighbors and represents a guarantee of specie perpetuity in a certain environment. However, mutations are the consequence of random processes from which humans only begin to discover the underlying mechanism.

Mutations by themselves, as a random process of life, are not intrinsically good or bad for species survival. Indeed, depending on the consequence of the mutation and the specific environment in which it happens, the mutation can be of high advantage or at contrary be a dreadful disadvantage.

In the context of cancer, mutations often happen in genes in charge of cell division and cell proliferation regulation. And the cell in which this specific dysfunction happens, can rapidly spread its own genomic profile compared to its neighboring cells. Therefore, it creates what we call a “tumor” by fast growth, and metastases by dissemination. Furthermore, the process of rapid multiplication, statistically increases the risk of new mutations in the daughter cells and therefore generates, locally in the tumor, subpopulations of high heterogeneity.

Cancer cell heterogeneity “provides the fuel for resistance” to cancer therapies (Dagogo-Jack and Shaw 2018). Indeed, therapies targets in general a genetic profile of tumor based on bulk sequencing. Thus, killing a majority to tumor cells but selectively keeping the most resistant to treatment.

During the last decade, many technological developments have been achieved in order to understand this heterogeneity of cancer cell populations (Lawson et al. 2018) at genetic, epigenetic and proteomic levels toward ‘omics approaches’ (Hasin, Seldin, and Luskis 2017). Within these technics, microfluidics seems to be a major component of the answer.

In this landscape, we report in this manuscript several microfluidic tools developed, adapted or used in biological or medical context, in order to reach, as midterm perspective, single-cell characterization at different omics levels.

The first chapter describes a biphasic microfluidic device allowing single cell encapsulation and sorting in aqueous droplets carried by an oil phase. This device transforms a cell suspension into an emulsion of droplets containing only single cells, thus allowing individual downstream analysis. We describe the initial device developed in my team a few years ago and try to understand some mechanisms driving droplet

---

generation in this particular geometry. Then, based on this better understanding and to fulfill the requirement for further single analysis, we switch from a mineral oil based encapsulation to a fluorinated oil encapsulation and confirm the ability of the device to encapsulate and sort real cells in this configuration. Finally, to move one step further single cells downstream analysis, we develop microfluidic tools for droplets collection and reagents merging.

The second chapter reports the development of a microfluidic continuous-flow droplet qPCR module. The developed system is tested for the quantification of gene expression level down to single cell level. Moreover, the device is later tested for its ability to shorten the PCR cycling time thanks to sample size reduction and faster heat transfer. The qPCR module is complementary to the module of single cell encapsulation and preparation described in the previous chapter and constitutes a first step towards the integration of global platform for single cell analysis.

As my will was not only to develop microfluidic methods but also to take benefit on the unique clinical environment of Institute Curie, I decided during my PhD to dedicate part of my time to clinical applications of microfluidics. In particular, the last chapter is dedicated to clinical applications of the Ephesia technology in Cancer Research. Ephesia is a microfluidic platform for isolation of circulating tumor cells (CTC), we used it in the context of exploratory clinical study, to investigate the roll of CTCs in cancer related thrombotic microangiopathy. The originality of our approach was to combine, in series and in parallel, Ephesia with other systems in order to extract as much information as possible from such rare events. We also used, for the first time, cells enriched thanks to Ephesia for next generation sequencing.

I hope that the reader will appreciate reading this manuscript as much as I appreciated the last three years of work, time and energy invested in each one of these projects and enjoyed learning from my colleagues and collaborators in all topics covered by this thesis.





2. *A droplet platform for*  
*single-cell analysis*

To answer many biological questions especially in Cancer research, we aim to develop a global platform for single-cell analysis. We divide this platform in different modules: an encapsulation and preparation module, and extraction module (magnetic tweezers) and analysis module (Drop qPCR), see Figure 1. These modules can be used altogether or separately. The magnetic tweezers module was developed previously within our team (Ali-Cherif et al. 2012; Ferraro et al. 2016b) and is ready to be used. Consequently, we will describe the two other modules developed during this thesis.

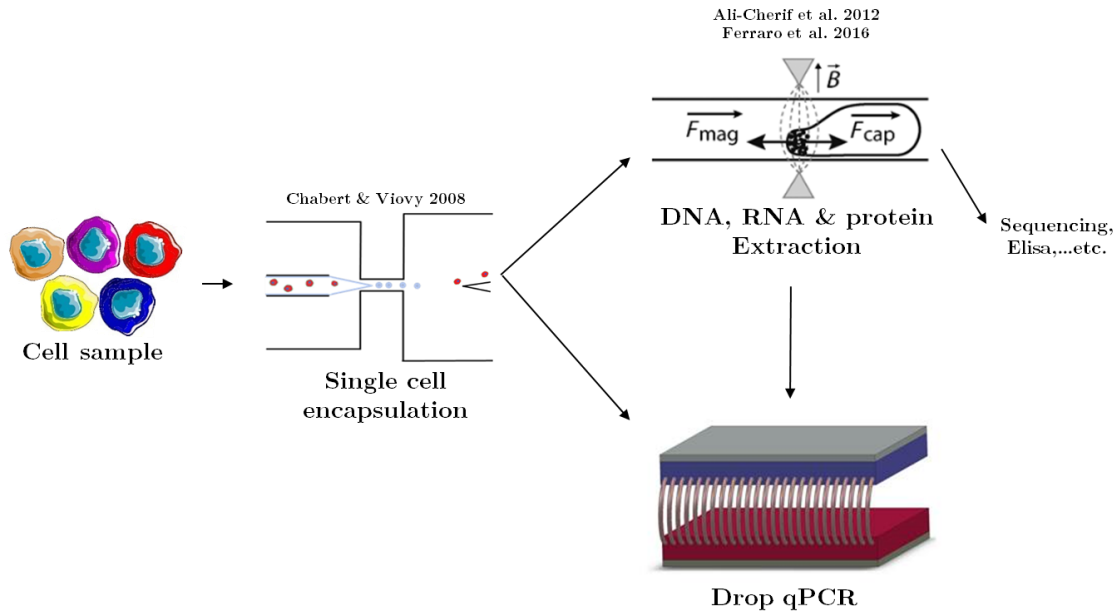


Figure 1: The single cell analysis platform.

The first module of encapsulation and preparation described in this chapter is used for two operations:

- i. To encapsulate the cells in individual compartment (droplets)
- ii. To prepare cells for analysis by mixing them with reagents.

We start this chapter by general introduction about single cell encapsulation methods. Then, we detail the development of each operation with the corresponding chips, from existing materials to the techniques or improvements made during this thesis.

---

## ***2.1 Introduction to single-cell encapsulation***

We will discuss in the introduction of this chapter different types of microfluidic approaches for cell encapsulation & sorting. Starting with the Poisson based encapsulation methods, we describe different other approaches from the literature and we will discuss more in details the one that will be developed in this chapter. Finally, we will give a short overview of the commercial products available on the market and expose the aims of the study and technological development discussed in the following sections of this chapter.

Encapsulation of cells in microfluidic droplet-based compartments has emerged during the last decade as a major technique for manipulation of single-cells, extraction and analysis for their content. It consists in encapsulating the cells of interest individually in droplets of aqueous solution to separate it from its neighboring cells. This encapsulation is in general performed simultaneously with the droplet generation. Thus, a device for droplet generation can be used to encapsulate single-cells, simply by using a cell suspension as the dispersed phase in the droplet emulsion and adjusting the concentration of the suspension to achieve the output of one single-cell per drop. If no improvement mechanism is used, the encapsulation process follows a Poisson distribution. We give in the next sections an example of a Poisson based encapsulation and several types of technical improvement described in the literature.

### ***2.1.1 Poisson based encapsulation***

The groups of Weitz and Griffiths show in 2008 a flow focusing device for single-cell encapsulation (Köster et al. 2008). The described encapsulation process follows a Poisson distribution (see Figure 2.B) as the arrival of individual cells during the droplet generation region can be considered occurring independently from other cells at low cells concentrations (Collins et al. 2015). In a general statistical representation, Poisson distribution is given by:

$$p(\lambda, k) = \frac{\lambda^k e^{-\lambda}}{k!}$$

with the portion of droplets  $p(\lambda, k)$  containing a given number of cells  $k$ .  $p(\lambda, k)$  is plotted in Figure 2.B for different discrete values of  $\lambda$  the average concentration per compartment (droplets). Poisson based encapsulation is also possible in other geometries of droplet production. The Figure 2.A shows three types of geometries used

in microfluidics for droplet generation: T-junction, flow focusing and co-flowing. These geometries can be used for cell encapsulation by replacing the water (dispersed phase) by a cell suspension.

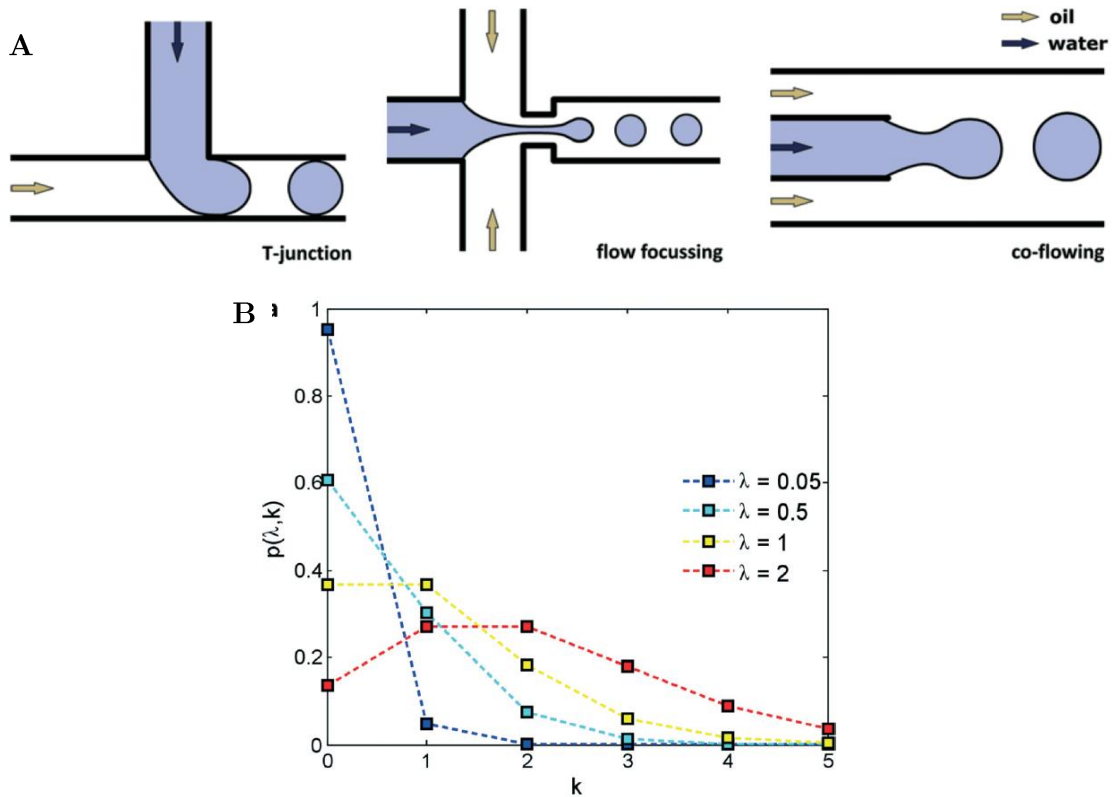


Figure 2: A) Three geometries for droplet generation in microfluidic devices: T-junction, Flow-focusing, Co-flowing. B) Poisson distribution represented with the portion of droplets  $p(\lambda, k)$  containing a given number of cells  $k$  is shown for different discrete values of  $\lambda$  the average concentration per compartment. From (Collins et al. 2015).

From Figure 2.B, we understand that to insure a minimal number of droplets containing multiple cells the Poisson law requires a high dilution of the cell suspension. Consequently, this also increases the number of empty droplets that implies a reduction in the yield of all downstream analysis that will be performed on droplets. Indeed, the ratio of droplets containing a single-cell to empty or droplets containing multiple cells is very low at the outlet of the encapsulation device. This will then similarly impact the following analysis steps with a low yield.

For this reason, several improvements have been developed to enrich the droplet population in droplets containing single-cell by downstream sorting or by directly working on the encapsulation process. We present here a selection of these techniques.

### 2.1.2 Ordered encapsulation

The same group of David Weitz in collaboration with Mehmet Toner shows a few months later a remarkable improvement of the previous approach. They used a method of self-organized inertial ordering, mastered in Toner's lab (Di Carlo et al. 2007) and combined it with a classical flow focusing droplet generation. A precise synchronization of the particles arrival with the frequency of generation allows a significant increase of single-cell encapsulation efficiency with respect to empty or multiple cells Figure 3. Here, the ratio of drops containing single cells on drops containing multiple cells or empty is around 5, meaning that only 20% of drops are not of interest.

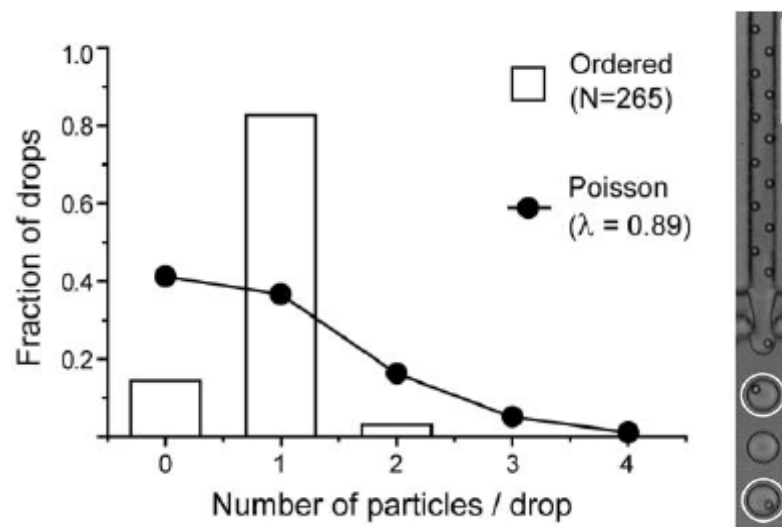
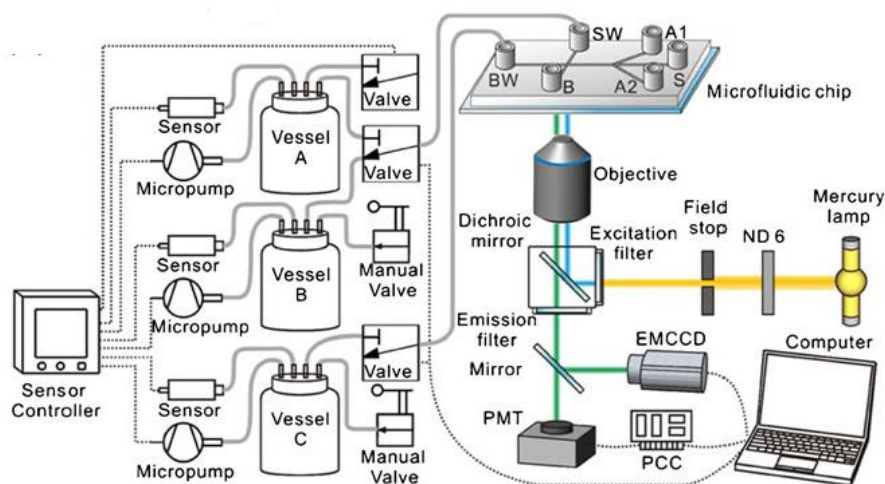


Figure 3: Comparison of single cell encapsulation of Poisson distribution to ordered encapsulation of beads. Picture of the flow focusing with beads ordered before being encapsulated in drops. Scale bar is 100 $\mu$ m. Extracted from (Edd et al. 2008).

### 2.1.3 Other improved encapsulations & sorting

To enrich the encapsulated drops in population of interest, it is also possible to sort them based on a fluorescent readout. Baret et al. (Baret et al., 2009) developed a method called Fluorescence-Activated Droplet Sorting (FADS) making the parallel with the flow cytometry technique (FACS). Their system reads by fluorescent labeling an enzymatic activity and sorts by dielectrophoresis the droplets in different channels based on this enzymatic activity. A sorting rate up to 2000 drop/s was reported. Further improvements in the hydrodynamics of the chip and electrodes positioning allows to reach 30KHz (Sciambi and Abate 2015).

More recently, a pneumatic sorting was developed by Wu et al. (Wu et al. 2013). As with FADS, a fluorescent readout gives a feedback to the pneumatic valves actuation switching the device from one outlet position to the other as shown in Figure 4.



**Figure 4: Schematic of the pressure and optical systems connected to the microfluidic chip. Depending on the fluorescent signal, the droplet is automatically sorted in BW or SW outlet by switching pressure configuration. Extracted from (Wu et al. 2013).**

An original technique was more recently developed by (Kamalakshakurup and Lee 2017). It relies on a modified flow focusing approach, consisting in a fine tuning of the pressures of dispersed and continuous phases to generate micro-vortices in the dispersed phase neck (before droplets detachment) to trap the particles and release them when desired. This leads to a 10 times higher efficiency of single-cell encapsulation than Poisson based encapsulation at equivalent concentration (from 3% to more than 40%). The technique allows also size selection of the particles at low density. The authors describe a selection of blood components i.e. platelets, red and white blood cells using

this device. Nevertheless, the efficiency of single-cell encapsulation does not exceed 50% and must need a retroactive control of the trapping/release mode.

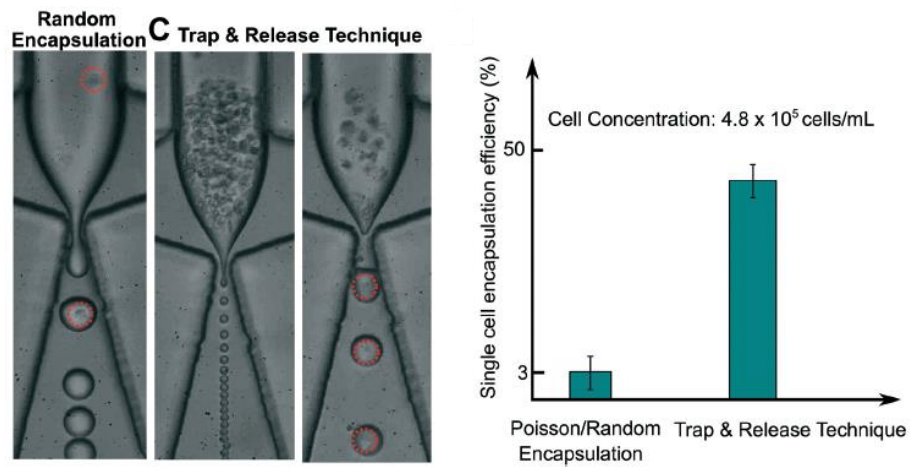
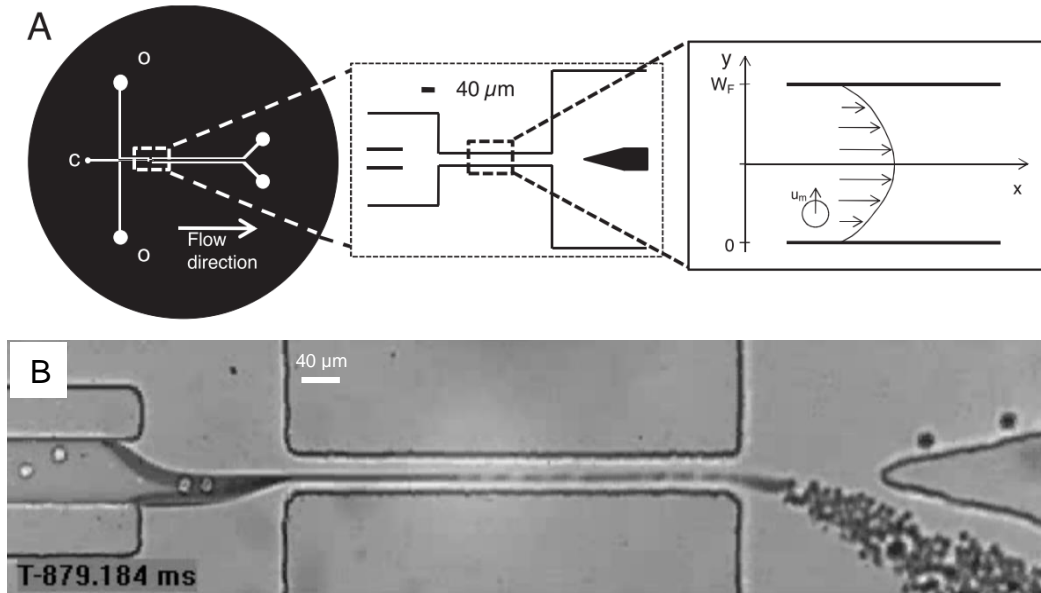


Figure 5: Pictures comparing different single cell encapsulation modes: Left: picture of random encapsulation that follows Poisson distribution. Centre: picture of the trapping mode, cells are concentrated in the neck of the dispersed phase. Right: picture of the release mode. Graph showing single-cell encapsulation efficiency in Poisson encapsulation and comparing it with Trap & release technique at fixed concentration. Extracted from (Kamalakashakurup and Lee 2017).

### 2.1.4 Encapsulation with hydrodynamic self-sorting

In 2008, a flow focusing based encapsulation system was developed within our team (Chabert and Viovy 2008). It is characterized by an innovative way to ensure single-cell encapsulation and on-flight cell-triggered sorting of droplets containing the cells. The device is presented in Figure 6.



**Figure 6: Device for encapsulation and hydrodynamic self-sorting.** Extracted from (Chabert and Viovy 2008). **A)** photolithography mask showing the geometry of the device. ‘c’ and ‘o’ are, respectively, the dispersed and continuous phase inlets. The first zoom itemizes the flow focusing region. The second zoom shows the droplet generation point and the migration in the Poiseuille profile to reach the center of the channel. **B)** picture of the device showing a continuous generation of droplets of  $6\ \mu\text{m}$ . All flows are from left to right. Cells arriving in the elongation generate bigger droplets that migrate faster to the center and will be sorted in the upper outlet.

The device is based on a flow focusing geometry with a  $500\ \mu\text{m}$  constriction/focusing channel before a wide opening divided in two outlets. More details about the geometry can be found on 2.2.2 Material & methods. Droplets of  $\sim 6\ \mu\text{m}$  in diameter are continuously generated in jetting mode. When a cell reaches the jet, it perturbs it and creates a bigger drop of a diameter slightly bigger than cell diameter (around  $20\ \mu\text{m}$ , depending on the cell type and size). At the end of the channel the  $6\ \mu\text{m}$  droplets goes in the bottom outlet, while the ones containing cells are collected in the upper outlet.



---

This hydrodynamic-based cell-triggered sorting relies on two main mechanisms:

**Shear-induced migration of the droplets:** Differently from the use of other flow focusing geometries, the generation in this device is performed with an asymmetry in continuous phase flowrates. Thus, the droplet production takes place close to the wall (at  $15.5\mu\text{m}$  from the wall). The high ratio of viscosity between the continuous and dispersed phases induces a lateral migration of the droplet to reach the center. This migration is proportional to the radius of the droplet. Thereby, a fine tuning of the focusing channel length allows discrimination between droplets of different sizes because, they will arrive in different streamlines at the widening in the collecting channel (see Figure 7).

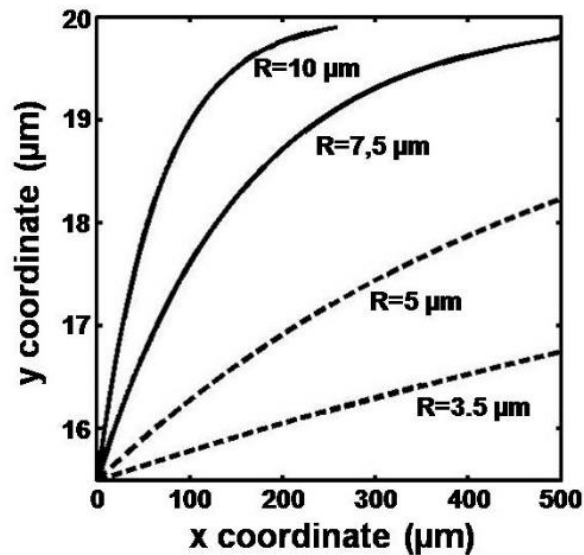


**Figure 7 :** Trajectories of droplets with various radii in the focusing channel as predicted by (Chan and Leal 1979), assuming a 2D parabolic flow, the droplet center of mass starting from  $y= 15.5 \mu\text{m}$ . We observe from this figure that a fine tuning of channel length, x coordinate, can allow good discrimination between droplets of different sizes at the opening region after the focusing. Extracted from (Chabert and Viovy 2008).

**Drop-drop interaction:** a steric effect of droplet repulsion will increase further the separation between the droplets that contain or not a single cell. As they reach the end of the focusing channel, droplets are slowed down and touch each other in a zig-zag thread. As small droplets are of the same size, they compact easily and reject the bigger ones that are in different streamlines even farther.

### Advantages for the approach:

This approach has the advantages of **time and efficiency** compared to random Poisson based encapsulations. In fact, to guarantee around 5% of droplets containing a single-cell with almost no double cells in a drop, the Poisson law required to have ~95% of empty droplets (Figure 2). This involved that, in absence of sorting, all the downstream analyses that are processed on the droplets, would also be on 95% of empty ones. Meaning that time, reagent and processing cost would also be of same percentage loss for these droplets.

On the other hand, the approach developed by Chabert & Viovy guarantees for optimal flowrates, that <1% of collected droplets are empty and less than 1.5% of the droplets contain more than one cell. However, we should also mention that to reach this selectivity, around 20% of the cells can be lost during the sorting step in the trash channel (see SI Movies 3 and 4 in Chabert and Viovy 2008). This may be of significant importance or could have no impact on the results, depending on the type of analysis and the sample quantity and rarity.

A last remarkable benefit of this device is given by the **independency between sorting and cell concentration**. Indeed, the two mechanisms involved in the sorting do not rely on concentration and, successful encapsulation and sorting of cell suspensions up to  $10^8$  per mL was reported with a throughput of  $160 \pm 10$  cells per second. As we will see later in this chapter, this throughput can also be improved by increasing the flowrates of the dispersed phase and keeping the same size of produced the droplets to allow efficient sorting. However, at this stage, a better understanding of the mechanisms underlying droplet formation in this geometry is still missing.

---

### 2.1.5 Commercial product

During the last five years, few commercial products for single cell encapsulation have been introduced on the microfluidic market. Almost all the companies are spinoff companies from academic laboratories involved in Microfluidics and cited previously in this chapter. All of the commercial products rely on a flow focusing geometry and are Poisson based since it is the simplest and cheapest techniques so far. Table 1 summarizes the different products and their associated fluidic control (pressure vs flow rate).

**Table 1: Classification of existing commercial products for single cell encapsulation in pressure vs. flowrate controlled.**

	Pressure-based control	Flowrate-based control
Products	<ul style="list-style-type: none"><li>• <math>\mu</math>encapsulator system (Dolomite bio)</li><li>• Droplet pack (Elveflow)</li><li>• Droplet starter kit (Fluigent)</li></ul>	<ul style="list-style-type: none"><li>• In Drop System (1 Cell Bio)</li><li>• Picodroplet single cell assay &amp; isolation system (Spherefluidics)</li></ul>

### *2.1.6 Aims of the chapter*

From this overview of the literature on droplet encapsulation & sorting devices, it is worth noting that the device described by Chabert & Viovy in 2008 presents several competitive advantages. Indeed, to our knowledge no other approach has reached so far similar selectivity of encapsulation (98% of droplets containing single-cells) with only a hydrodynamic passive self-sorting and no complex fabrication for active enrichment. For this purpose, we decided to push further the potentialities of this device and try to make it compatible with other droplet-based bioanalytical tools. In particular, the study of single-cells content at all levels (DNA, RNA or proteins) or single-cells secretion (Eyer et al. 2017) can be performed downstream the encapsulation step in a highly enriched population of droplets. Among the different droplet based assays, our team developed a magnetic tweezers device for solid support extraction in droplet microfluidic format (Ali-Cherif et al. 2012). This device allows the implementation of complex multi-steps bioassays involving, extraction, dispersion and elution in nanoliter droplets (Ferraro et al. 2016a). A second example of downstream analysis device concerns a microfluidic RT-qPCR device that has been developed during my PhD. This system integrates a conventional protocol of RT-qPCR in 200nL droplets, as it will be described in the next chapter. To achieve the goal of combining the advantageous single cell encapsulation with these droplet-based bioanalytical tools, we faced two main challenges:

- Making the single cells encapsulation device compatible with fluorinated oil
- Developing a device to manipulate the encapsulated cells and merge them on-demand with specific reagents

During this thesis, each challenge was studied as a project on its own, converging to build a global platform for single-cell encapsulation, manipulation and on-demand merging. These two projects are developed in the sections 2.2 and 2.3.

---

## *2.2 Single cell encapsulation in fluorinated oil*

The following work was started during my first year of PhD by several discussions with Davide Ferraro and Marco Serra. It was continued by Rashmi Ramesh during her Master 2 internship that I supervised.

### Need for fluorinated oil?

Within the last ten years of development of droplet microfluidics, few requirements regarding oil properties were identified being crucial for oils in emulsions (of water-in-oil) used in bioanalytical applications:

- Inert: chemical stability to avoid reaction with any droplet compound (proteins, RNA, DNA) or reagents used in the bioassays.
- Thermostable: depending on the application it may be needed to keep the other properties over a large range of temperature (e.g. from 0°C to 100°C for PCR)
- Permeable to oxygen: allowing transport oxygen to encapsulated cells (e.g. cell culture)

For these reasons and as they fulfilled all these requirements, Fluorocarbon based oils are considered as the best choice (Gruner et al. 2015) for cell-based droplet microfluidic applications. One should also keep in mind that the three features above, need also to be satisfied by the surfactant used to generate and stabilize the emulsion (Roach, Song, and Ismagilov 2005).

In our case, the encapsulation system initially developed by (Chabert and Viovy 2008) was using heavy mineral oil (Rectapur, Prolabo) of a viscosity  $\mu=120\text{mPa}\cdot\text{s}$  (120 cP), containing 5%(m/m) of Span 80 surfactant. Thus, to flow our path of constructing a platform dedicated to droplet-based cell analysis, the first step was to change the composition of the continuous phase using FC 40 fluorinated oil and consequently to optimize the experimental conditions to achieve cells encapsulation and sorting. Thereby, the objectives of this project are:

- Better understanding of the mechanism of encapsulation and sorting depending on continuous phase properties.
- Determining the operating conditions to get performance of encapsulation with fluorinated oil at least as good as the ones achieved with mineral oil.

### 2.2.1 Droplet generation in flow focusing, description by $Ca$

In the next sections below, we will give a brief overview of the concepts of interfacial tension (IFT) and capillary number ( $Ca$ ). We will then describe concisely the literature related to our work using these two concepts.

#### 2.2.1.1 Interfacial tension: equilibrium vs. dynamic

The **InterFacial Tension (IFT)** between two immiscible fluids quantifies the energy needed to create new interface. The work required to generate an extra-interface of surface  $dA$  is given by  $W = \gamma \cdot dA$  with  $\gamma$  being the IFT of the system.

**Surfactants** are molecules that lower the interfacial tension. They are added in one of the phases or in both. Thanks to their composition, they adsorb at the interface between the two phases. These molecules are amphiphilic with two parts, each one having an affinity for one of the phases. In the case of water-in-oil emulsion, the molecule has a hydrophilic head and a lipophilic tail as shown in Figure 8.

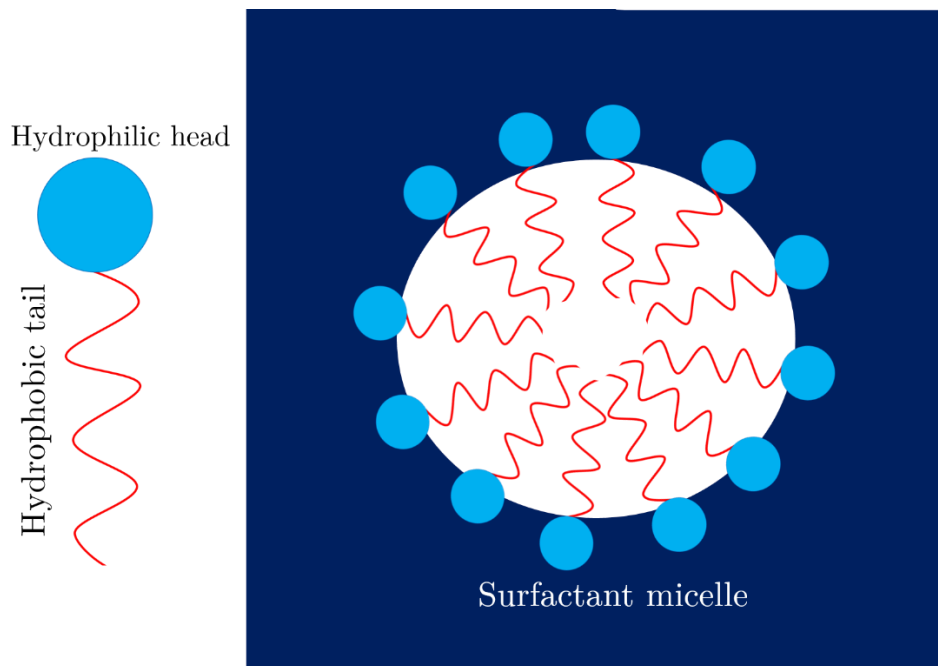


**Figure 8:** Left: schematic representation of a surfactant monomer. Right: Micelle of surfactant molecules in an aqueous phase.

---

**In droplets microfluidics**, surfactants are commonly used for:

1) Lowering the IFT:

Measurement of IFT as function of surfactant concentration shows a decrease in IFT with the increase of surfactant concentration. This is due to the fact that each side of the surfactant that covers the interface has a good affinity with the phase. Thus the creation of new interface is less demanding energetically, means a lower IFT. This decrease reaches a plateau that corresponds to the saturation of the interface with surfactants and the limit of surfactant solubility in bulk that involves formation of micelles (above Krafft temperature). The point at which the plateau is reached is called **Critical Micelle Concentration** or **CMC**.

2) Stabilizing the emulsion:

The second role for which surfactants are used, is to stabilize the emulsion by avoiding droplet merging. This can be ensured thanks to repulsive forces between surfactants tails.

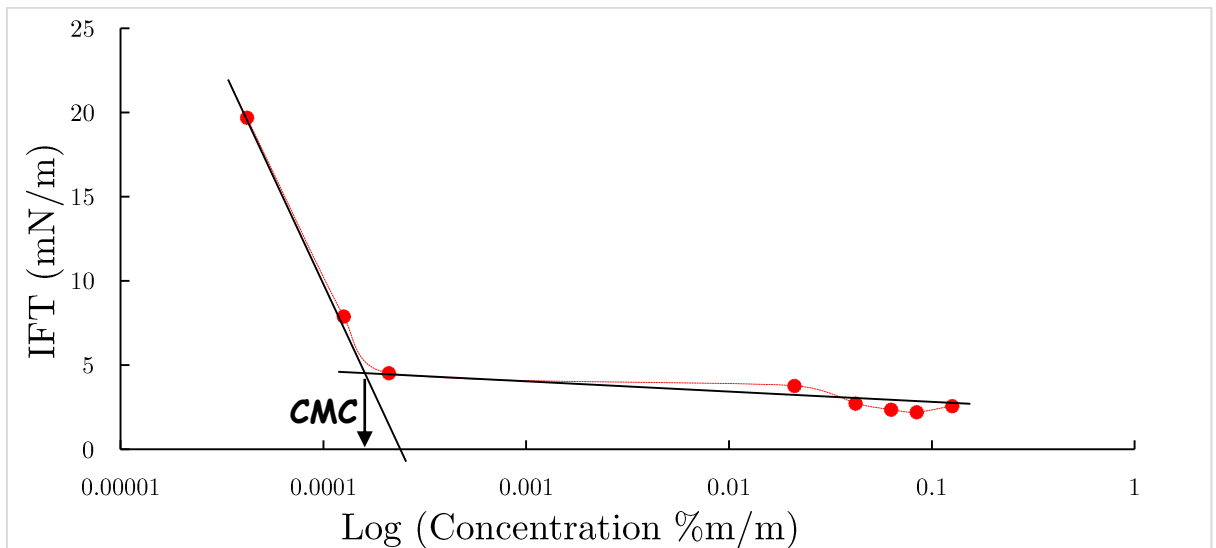


**Figure 9: IFT measurement as function of span 80 concentration. IFT is measured by pendant drop technique between phosphate buffer saline and light mineral oil with Span 80 at 22°C**

When considering the curve Figure 9, each point of the curve is the final (equilibrium) value of the surface tension measured at a given surfactant concentration. Figure 10 shows an example of IFT measurements with a given concentration (0.005%) of Span

20 (lower than CMC) as a function of time (over few minutes). The decrease of the surface tension as a function of time represents the time needed by the surfactant molecules to get adsorbed at the interface and to reach an equilibrium value.

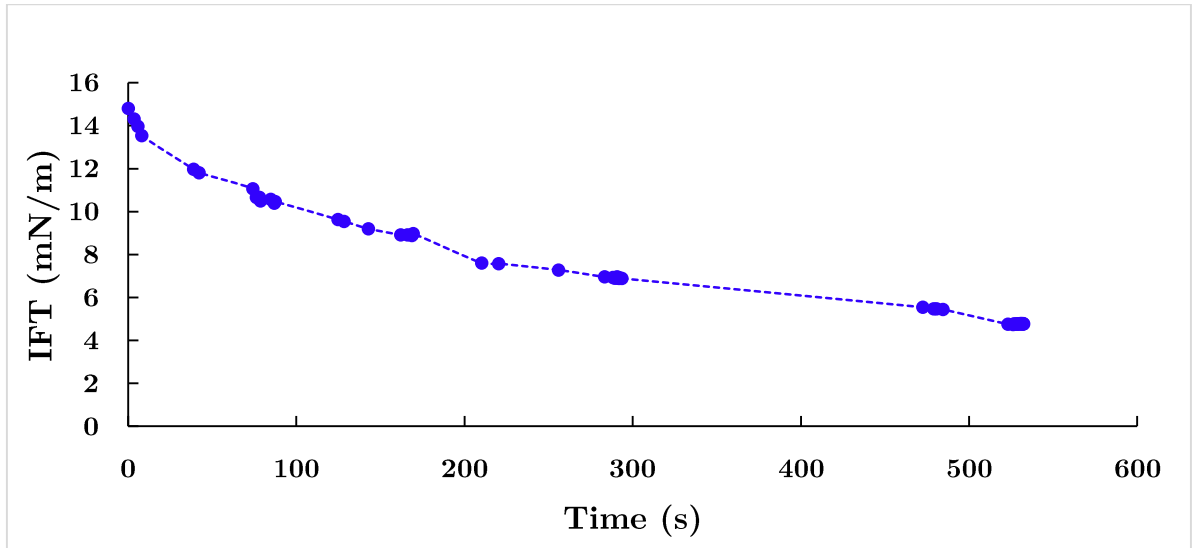


Figure 10: Pendant drop IFT measurement over time of phosphate buffer saline PBS solution with light mineral oil containing 0.005%(m/m) of Span20.  $T=0$  is the time at which the droplet (1 $\mu$ L) is generated in the mineral oil.

In droplets microfluidics, this time scale needs to be much lower than the time for all the operations performed in droplets to insure a complete surfactant coverage of droplet interface, thus their stability, reproducibility and avoiding cross-contamination between samples.



### 2.2.1.2 Description by capillary number

**Capillary number** is a dimensionless number in fluid mechanics that compares viscous force vs capillary force (interfacial tension acting across an interface).

$$Ca = \frac{\mu V}{\gamma}$$

$\mu$  Dynamic viscosity,  $V$  Norm of the tangential speed and  $\gamma$  Interfacial tension.

In droplets microfluidic, the capillary number can be used to describe the different modes of droplets generation in all 2D-geometries: T-junction, co-flow and flow focusing (Nunes et al. 2013). This description of the droplet generation regime was recently supplemented by the review of (P. Zhu and Wang 2017a). Figure 11 represents the effect of continuous phase capillary number components on the interface behavior in a flow focusing geometry. The viscous drag of the dispersed phase is not represented as it has much less impact on the phenomenon (see difference in axis scales Figure 12).

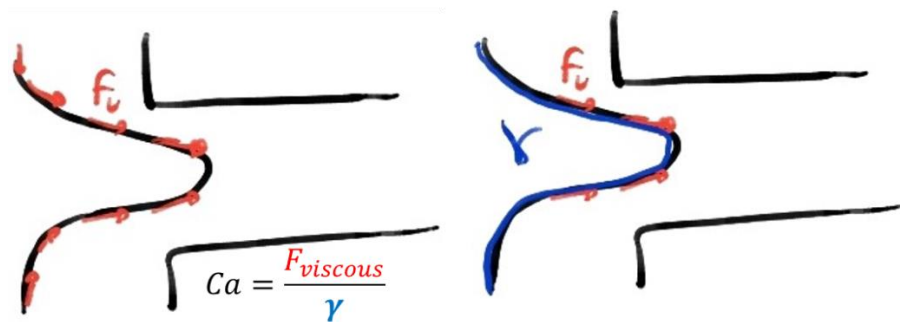


Figure 11: Representation of the effects of the two sides of the continuous phase capillary number in a flow focusing geometry. The **viscous drag** tends to stretch the interface to push it through the focusing channel and could perhaps breaks it in droplets. While the **surface tension** tends to maintain the interface as unified (of minimum area) as possible, against applied forces.

As shown in Figure 12, they represent, for flow focusing geometry, the capillary number of the dispersed phase as function of the capillary number of the continuous phase and the associated droplet generation regimes. Since regimes of droplet production are described by mechanisms of interface breakup. These interface behaviors result from a balance between IFT and viscous forces and thus included in the capillary numbers. And thereby, each area of this graph corresponds to a mode of droplet production: squeezing, dripping, jetting, tip-streaming, and tip-multi-breaking. Most of encapsulation devices are used in dripping or jetting regimes, as they are very stable;

large area in the graph Figure 12; and specifically the dripping mode allows very reproducible droplet size easily controllable by design dimensions and flowrates.

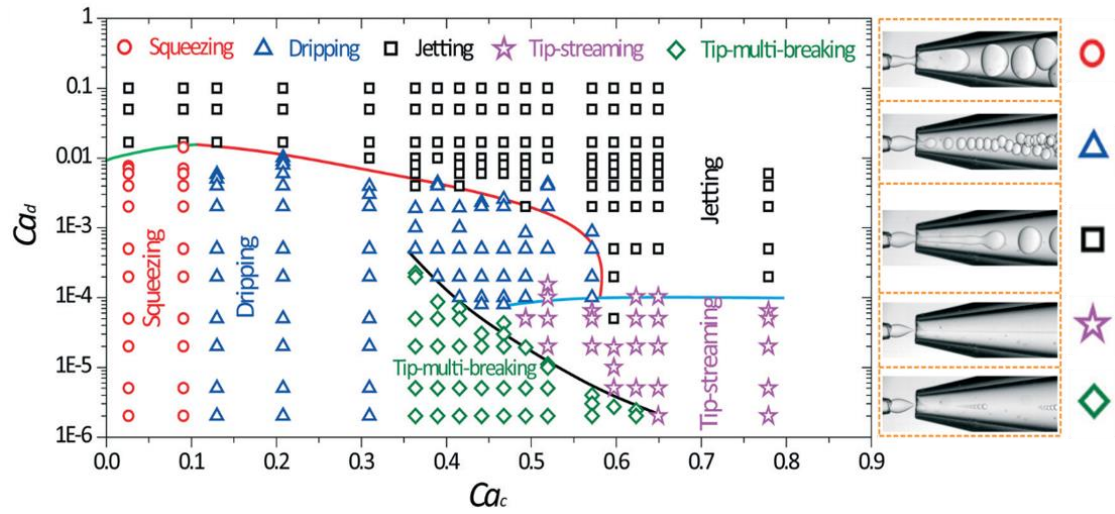


Figure 12: Representation of droplet generation regimes in a flow focusing geometry as a phase diagram with the capillary number of the dispersed phase in the y-axis as function of capillary number of the continuous phase in the x-axis. This figure is extracted from (P. Zhu and Wang 2017a).

---

### 2.2.1.3 *Capillary numbers and IFT in our encapsulation device*

Before modifying the continuous phase used in our device, we needed to understand the experimental conditions in which the system was optimized previously by Chabert for cell encapsulation and sorting.

By plotting the variation of the IFT (between PBS and Mineral) oil as function of the concentration of Span 80; we obtain a CMC value of the Span 80 around 0.025% $m/m$  (Figure 22). This value is in agreement with data found in the literature (Opawale and Burgess 1998). Thus, for a fixed shear force and above this concentration, the IFT and the capillary number must be constant. And in our case, the encapsulation was performed with a mineral oil at 5% of Span 80, meaning that we are 200 higher than this CMC value. Referring to (Nunes et al. 2013; P. Zhu and Wang 2017b) the behavior of the jet and droplet generation must also be similar above CMC as the capillary number is constant.

However, when using Span concentration ranging from 0.5 to 5% (w/w), we can observe that the regimes of droplet generation and the size of the droplets produced are very different and depend on the surfactant concentration as showed in Figure 13. The flowrates in the three pictures are fixed to 150 $\mu L/h$  top channel and 75 $\mu L/h$  bottom channel for mineral oil and 8 $\mu L/h$  center for PBS. One should keep in mind that differently from other devices referred at in the review for Figure 12, the flowrates are kept here in Figure 13 asymmetric in purpose to be able to compare them with real conditions of encapsulation and sorting using the device. Nevertheless, all the following observations (except about asymmetry) stay valid in symmetric flowrates; tested but not shown here; between 70 $\mu L/h$  and 200 $\mu L/h$ .

#### Observations:

1. We can notice that the shape of the neck (i.e. elongation of the interface between continuous and dispersed phase) is more curved/pinched, forming a smaller tip, at 5% than for lower Span 80 concentration. The higher the concentration, the more the interface seems to be deformable and sensitive to asymmetry of the continuous phase flows.
2. The increase in concentration is correlated with the decrease in droplet diameter between 1% and 5 % of Span 80.

3. The increase in concentration is also correlated with the loss of droplet coalescence after the focusing channel that happens at 0.5% but not at 1% or above.

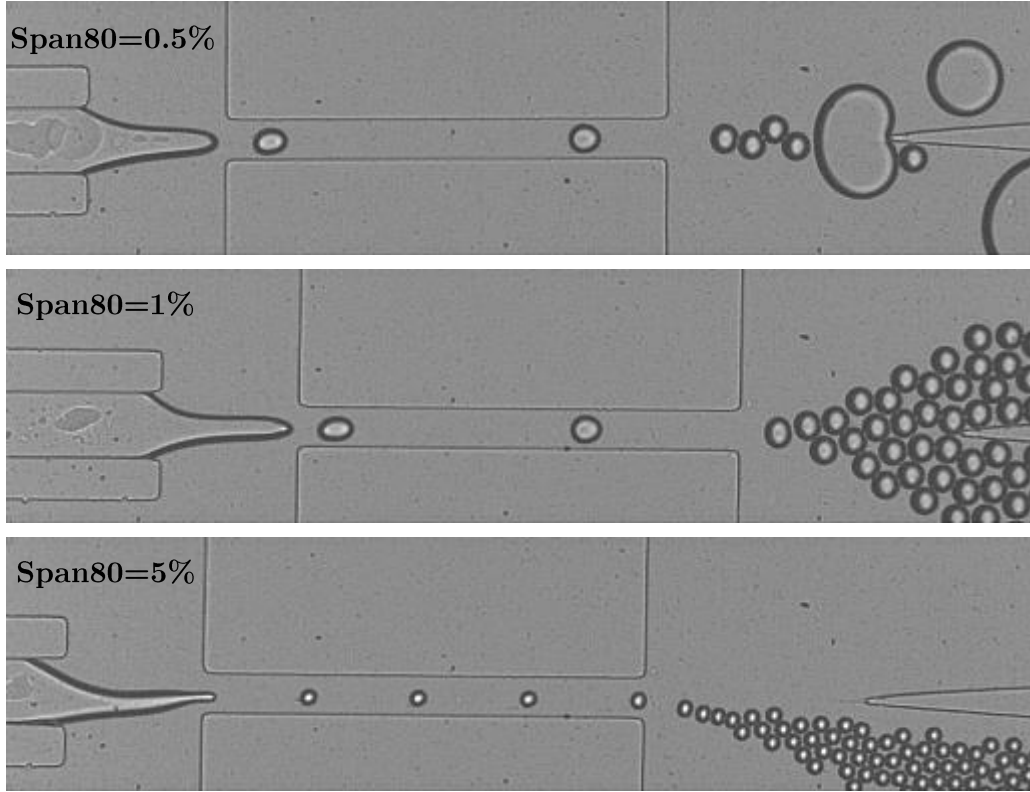


Figure 13: Droplets of PBS generated in light mineral oil. The same flowrates are used (150 $\mu$ L/h top, 75 $\mu$ L/h bottom, 8 $\mu$ L/h center) in the three pictures and different concentrations (%m/m) of surfactant Span 80 in the oil above CMC. 40 $\mu$ m is the width of the focusing channel where droplets are generated.

These observations indicate that the **change in surfactant concentration**; even **above the CMC**; affects at least one the components of the **capillary number**  $C_a = \frac{\mu V}{\gamma}$ , namely the viscous drag forces  $\mu V$  and interfacial tension  $\gamma$ . In the viscous drag, the speed  $V$  is fixed as the flowrates are controlled by the syringe pumps. So the change could possibly be coming from a variation in viscosity  $\mu$  due to the variation in surfactant concentration (**assumption 1**). However, the third observation would poorly be explained by the viscosity change. On the other hand, IFT is supposedly having very poor variation above CMC; about few mN/m; (**assumption 2**) but would more likely explain all the three observations. Nevertheless, we investigated both assumptions in following section as the phenomenon could be the consequence of a combination of both.

---

**2.2.1.3.1. Assumption 1: viscosity is affected by the concentration of surfactant**

A first explanation could be an increase in the viscosity caused by the increase of surfactant concentration in the continuous phase that could affect the shear at the interface. Higher shear would stretch more the interface and lead to smaller droplets as observed in Figure 13. To investigate this assumption, we performed viscosity measurements with Anton Paar rheometer MCR 302 at three different concentrations in Span (0 to 10% (w/w)) and at three temperatures ranging from 15 to 25°C.

The goal here is to compare the supposed variation in oil viscosity  $\mu$  at fixed concentration of surfactant (5%) for a room temperature change, with  $\mu$  variation at fixed temperature (25°C) for different surfactant concentrations.

As shown in Table 2, the variation in viscosity over these concentrations is lower than the variation over temperatures between 20°C and 25°C (Room temperature variations). Therefore, the argument of viscosity change by surfactant addition is not valid and we eliminated this hypothesis from further conclusions.

**Table 2** Viscosity (mPa.s) of light mineral oil with Span 80 at different concentrations (%w/w) and different temperature (°C). The variation of the viscosity between 0% and 10% is lower than its variation between 20°C and 25°C at 5%.

Span 80 concentration (%m/m)	0%	5%	10%
15°C	-	44.5	-
20°C	-	34.8	-
25°C	27.45	27.6	28.7

### ***2.2.1.3.2. Assumption 2: IFT is affected by the increase in surfactant concentration above CMC***

From the literature detailed below, the only possibility a second explanation could be given by the variation of surface tension also called **dynamic IFT**. Indeed, the droplet generation occurs at very high rate (tens of kHz) and consequently a new interface is generated within the same time scale. We could be in a configuration in which the droplet generation time (generation of new interface) is too low considering the diffusion time and the adsorption time needed by the surfactant molecules to reach the new interface, and completely covers it. Thereby, the increase in concentration shown Figure 13 would be reducing the equilibrium time and thus lead to lower value of IFT closer to equilibrium value at CMC.

Similar phenomenon has already been described qualitatively by Anna & Mayer (Anna and Mayer 2006), to explain surfactant-dependent tipstreaming regime in flow focusing geometry. This publication is detailed later in this section. A related work was published by Guangsheng Luo team (K. Wang et al. 2009) and developed later over several aspects from semi-empirical models to a numerical model of surfactant kinetics. We will highlight the following publications of this group:

A first semi-empirical model was proposed (K. Wang et al. 2009) to determine the effect of dynamic IFT on droplet formation, in particular regarding the droplet size in T-junction. Thanks to the measurements of drop diameter made at equilibrium value of IFT for quickly diffusive surfactant, it was possible to estimate the dynamic IFT for a surfactant having a lower kinetics. A second semi-empirical model was proposed to describe the effects of surfactants type and concentration during droplet formation in a co-axial geometry (Xu et al. 2012). Thereby, a comparison between SDS (sodium dodecyl sulfate) and CTAB (cetyl trimethylammonium bromide) complemented by data for Triton X-100 in T-junction shows (Kai Wang et al. 2016) that the surfactant transport time from the bulk to the subsurface and the time for micelles breakup compared to droplet generation time are critical parameters that control the droplet production process (see Figure 14).



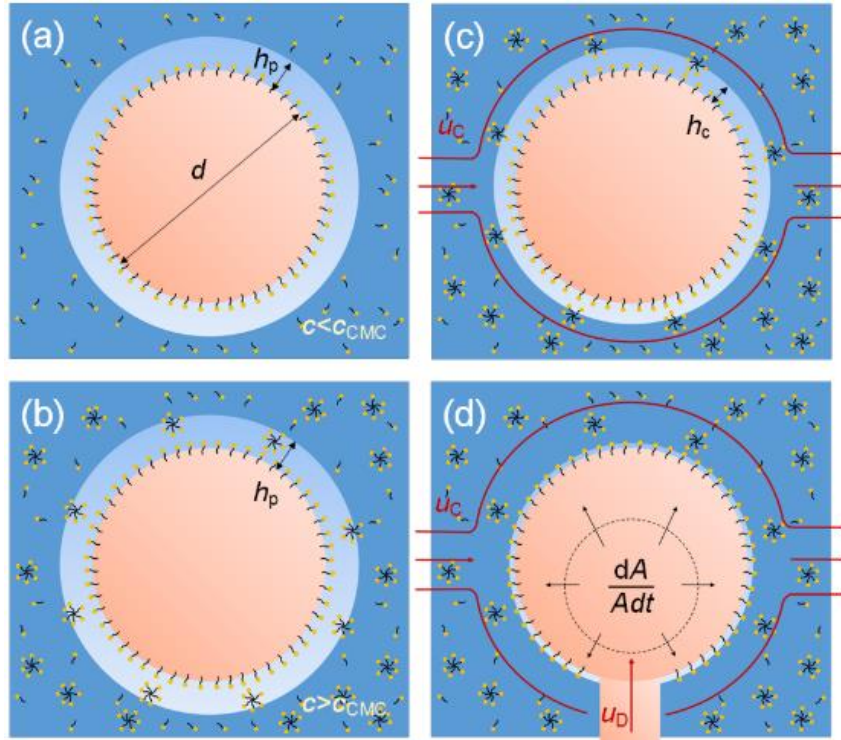


Figure 14: Representation of the mechanisms of mass transfer and adsorption of a surfactant extracted from (Kai Wang et al. 2016). Dark blue is the bulk solution, light blue is the diffusion subsurface layer, salmon-pink color is the droplet. (a) A droplet in surfactant solution with a monomer (yellow dot in black line) concentration lower than the CMC. (b) A droplet in surfactant solution with a concentration higher than the CMC. (c) A droplet in a flowing surfactant solution with a concentration higher than the CMC. Depth of the subsurface layer is reduced thanks to convection. (d) A growing droplet in a flowing surfactant solution without mass transfer resistance.

In 2014, the same group of Luo developed a numerical model in Lattice Boltzmann Method for modeling dilute species in multiphase flows (Riaud et al. 2014). Following this work in 2018 by a numerical study of surfactant distribution on growing droplets in T-junction geometry (Riaud et al. 2018) as described by Figure 15 .

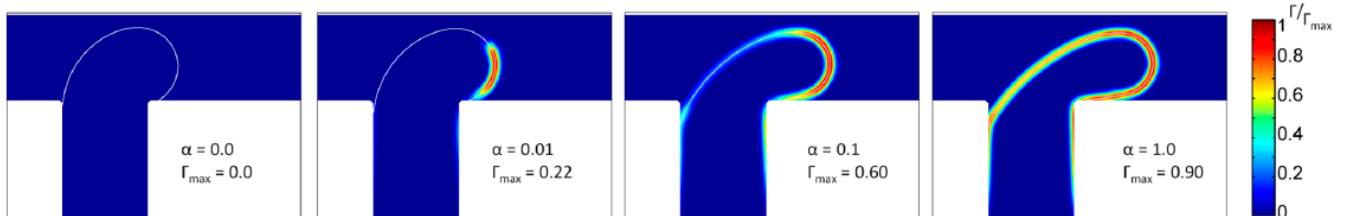


Figure 15: Extracted from (Riaud et al. 2018). Simulation snapshots with different surfactant kinetics and identical capillary number. From left to right, the pictures correspond to the progressive increase in surfactant kinetics ( $\alpha$  varies from 0 to 1).  $\alpha$  is a parameter to compare

surfactant adsorption rate and the droplet formation time.  $\Gamma$  is the surfactant coverage and the white line is the droplet boundary.

The main contribution of this work is the introduction of the Damköhler number in the predictive approach. In fact, this dimensionless number represents the flow time scale to the chemical time scale ratio and it gives an interesting tool to combine with the capillary number in order to describe any surfactant-laden biphasic experiments.

Another relevant approach for understanding these surfactant dynamic effects on droplet formation was proposed by Kovalchuk et al., 2018. They used  $C_{12}TAB$  and  $C_{16}TAB$  as these surfactants have similar structures, with a longer chain for the  $C_{16}TAB$ , which has lower diffusion coefficient, while having close value of IFT above CMC as shown in the Figure 16. They measured the dynamics of IFT depending on surfactant concentration below and above CMC for the two surfactants, but since direct measurement of IFT dynamics using the maximum bubble pressure tensiometer BPA-1S (Sinterface, Germany) with two liquid phases is not feasible, the authors measured IFT between air and aqueous solution containing the surfactant. Indeed, even if the adsorption isotherms should be quite different, the plots in Figure 16 provide a great guideline for diffusion kinetics in the bulk, as it is independent of the second phase. This graph shows in particular a remarkable decrease (almost 20mN/m) in IFT for the  $C_{16}TAB$  at 5mM (2.5 times its CMC) in few tens of milliseconds. While,  $C_{12}TAB$  is almost already at equilibrium at 50mM (also 2.5 times of its CMC). These measurements were then compared with microfluidic experiments for droplets generation, in which silicone oil was used as a continuous phase, whereas water/glycerol mixture was used as the dispersed phase and surfactants were dissolved in the dispersed phase as previously with bubble pressure experiments. The assumption made to calculate the IFT, is that the capillary number at transition from jetting to dripping is independent of surfactant presence. Thus, a comparison between surfactant-free and surfactant-laden systems, at transition point, allows the calculation of the dynamic IFT. Indeed, by matching the capillary numbers in surfactant-free and surfactant-laden situations at transition, we can obtain the equation:  $\gamma_{SL} = \gamma_{SF} \frac{\mu_{SL} Q_{SL}}{\mu_{SF} Q_{SF}}$  where  $\gamma_{SL}$ ,  $\mu_{SL}$  and  $Q_{SL}$  are correspondingly the interfacial tension, viscosity and flowrate for surfactant-laden system,  $\gamma_{SF}$ ,  $\mu_{SF}$  and  $Q_{SF}$  are their equivalents for surfactant-free system.



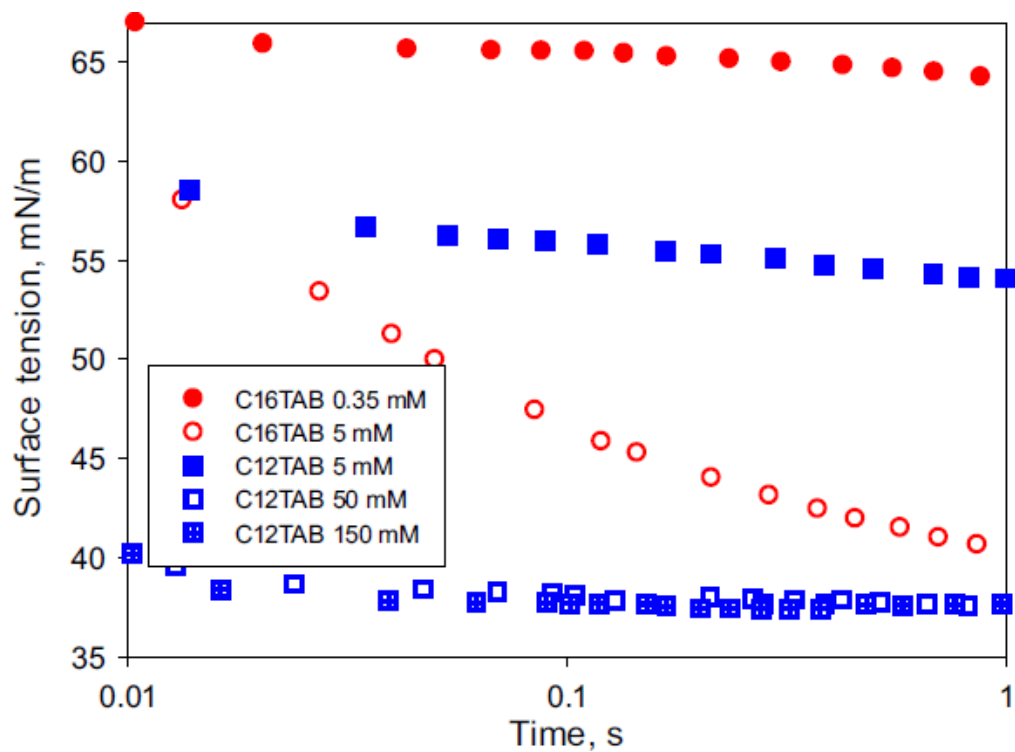


**Figure 16:** Measure of dynamic IFT extracted from (Kovalchuk et al. 2018). IFT is measured between air and aqueous solution containing the surfactant. Empty or crossed signs are above CMC, filled ones are below.

One should keep in mind that this assumption is true only if we consider a homogeneous repartition of surfactant molecules at the interface. This condition may not necessarily be satisfied, depending on the kinetics of surfactant and the distribution of velocity field at the interface. For example, (Anna and Mayer 2006) discuss the tipstreaming mechanism in which a gradient of IFT is formed along the interface (Figure 17). They describe that thanks to the elongational flow during droplet formation, surfactants are not homogeneously covering the interface. Thus, a gradient of IFT is settled which makes the interface easier to stretch, and a tip highly packed with surfactant appears. In this location the IFT is so low that a thread, from which tiny droplets will break, is formed under shear forces imposed in the direction of the elongational flow.

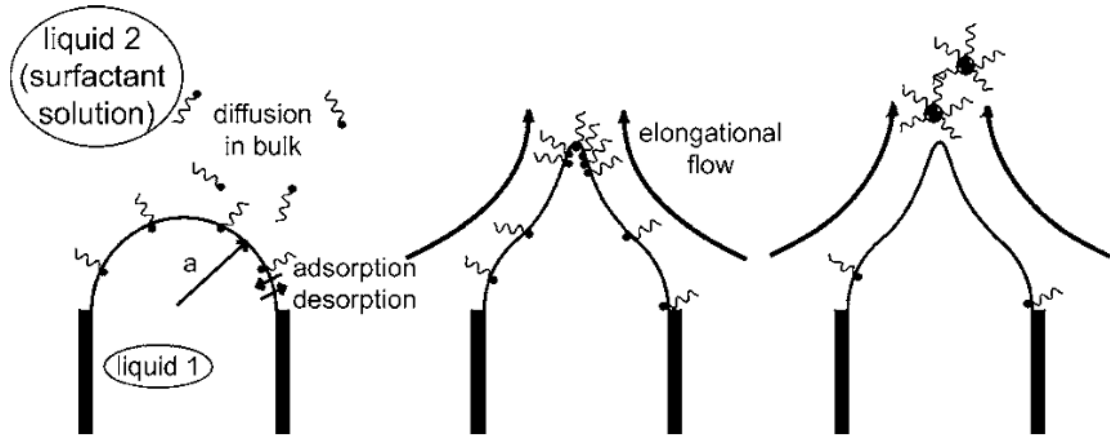


Figure 17: Schematic representation of surfactant behaviour in tipstreaming regime. Left: two phenomenon had to be considered, diffusion and adsorption/desorption to the interface. Center: Thanks to the elongational flow of the continuous phase, surfactant molecules are packed at the tip creating an IFT gradient. Right: The IFT gradient helps forming tiny droplets at the tip of the dispersed phase. Extracted from (Anna & Mayer, 2006).

However, in these studies no general rule can be extrapolated to our geometry using different phases and surfactants. In particular, as far as we know, there is no instrument allowing the measurement of surfactant kinetics at hundreds of microseconds, which is the range of the droplet generation time in our device.

Thereby, to verify our second assumption, we present in the following sections a series of experiments performed with our flow focusing geometry with different oils and surfactants. **The objectives** behind these experiments are:

- To improve our knowledge on the mechanisms underlying the control of droplet formation by surfactant concentration.
- To find the critical parameters allowing precise control of the droplet production for diameters lower than 10 $\mu$ m in fluorinated oil.

---

## 2.2.2 Material & methods

### 2.2.2.1 Chip design & features:

The chip design is composed of three inlets, two for the continuous phase and one for the dispersed phase; a long focusing channel and two outlets, one for the droplets containing cells and one for empty droplets. This design is very similar to commonly used flow focusing in literature (P. Zhu and Wang 2017a) but with two main differences: a longer focusing channel (500 $\mu\text{m}$ ) and two outlets instead of one to sort droplet.

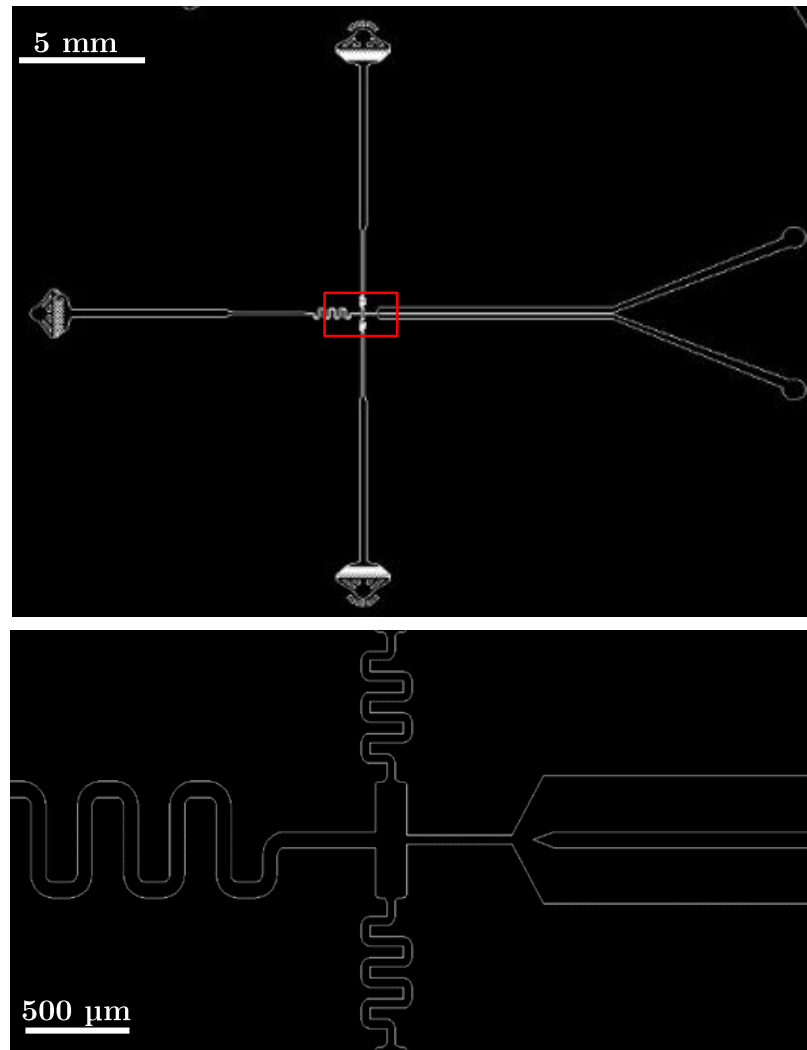


Figure 18: Design of the device on Solidworks. Top picture: General view showing two inlets for the continuous phase with filters (5 $\mu\text{m}$ ) and one inlet for dispersed phase (25 $\mu\text{m}$ ). Bottom picture zooms on the focusing region. Resistances before the flow focusing region helps avoiding backflow to inlets. Focusing channel where droplets are produced and sorted is 500  $\mu\text{m}$ . One of the outlets collects empty droplets and the second, the ones loaded with cells.

The long focusing channel is a central feature of this device (compared to the conventional systems). Indeed, it is involved in two main functions: encapsulation and sorting. Thanks to the length of this channel, a high shear force is maintained on the interface over few tens of microns and thus allows the production of small droplets in a jetting regime. As described by Chabert (Chabert and Viovy 2008), it is inside the focusing channel that the sorting between negative (empty) droplets and positive ones (containing cells) takes place. Depending on the starting point of generation and the difference in size between negative and positive droplets, the length of channel is the critical parameter to achieve an efficient sorting Figure 7.

Compared to the device of Chabert Figure 6, we improved the following features as shown in Figure 18:

- We add hydraulic resistances just before the flow focusing region, to avoid backflows to the inlets when stopping the syringe pumps and thus contamination between phases. This was observed previously, due to the high resistance of the focusing channel (500 $\mu\text{m}$  with a cross section of 30 $\mu\text{m}$ x40 $\mu\text{m}$ ) compared to resistance of inlet channels.
- Filters inspired from the geometries of (Mazutis et al. 2013), protect the device from clogging with small dust that can be transported by oil or PBS to the focusing region.

---

### 2.2.2.2 *Chip fabrication*

#### Top part: channels

The chip pattern is designed on Solidworks software and developed on a transparent flexible mask by Selba S.A. The photolithography is made using this mask and SU8 resin from Microchem. The chip height is  $30\pm 2\mu\text{m}$ , controlled with either optical or mechanical profilometer. A polydimethylsiloxane (PDMS) with a ratio of curing agent 1:10 is then poured on the Silicium wafer and cured for 2h at  $65^\circ\text{C}$ . The reticulated solid PDMS is then cut and peeled off. The inlets and outlets are punched with a biopsy puncher of 0.75mm diameter.

#### Bottom part:

For a better visualization of droplets under 40x objective, we choose to use a  $160\mu\text{m}$  thick glass slide. To ensure homogenous wettability on all channel walls, we spin-coat a thin layer of PDMS ( $17\mu\text{m}$  height) on top of the glass slide. The reticulated layer of PDMS on the glass slide is the bottom part of the chip.

Plasma treatment is applied to bottom and top parts for PDMS-PDMS bonding. They are then put in contact and pressed to close the microchannels.

#### Channels wettability:

A main advantage of the co-flow geometry is that the channels bringing the two phases in contact are physically different objects and can also be made in different materials. In the case of planar flow focusing (also named 2D flow focusing), these channels are made in the same material in the same plan. Thus, a dewetting of the dispersed phase from the channel and a wetting of the continuous phase is happening in the focusing region. Consequently, the wetting properties of the channel surface with regards to both fluids is of great importance for shaping the interface in addition to hydrodynamic flow features (namely velocity and viscosity) and IFT between the two phases. Furthermore, wetting properties have been used as an active method for fine tuning droplet generation by electrowetting (Gu et al. 2008) or photosensitive surfactant (Diguët et al. 2011). Therefore, we used the following strategies depending on continuous phases:

- For mineral oil experiment, the chips were let (after plasma bonding) at  $65^\circ\text{C}$  for at least 15 hours to insure perfect recovery of PDMS hydrophobicity.
- For fluorinated oil experiment, a liquid silanization is applied to the chip. A solution of (Tridecafluoro-1, 1, 2, 2-tetrahydrooctyl) trichlorosilane in FC-40

(5% v/v) is injected in all the channels for 20min to ensure good wetting of the oil on the PDMS. We rinse thoroughly the chip with 500 $\mu$ L of pure FC-40.

### 2.2.2.3 *Experimental setup*

The experimental setup is composed of the following parts:

- Nemesys syringe pump equipped with SGE syringes (one of 250 $\mu$ L and two of 1mL)
- Flexible silicone tubing connects the three syringes to polytetrafluoroethylene (PTFE) tubing OD=0.76mm ID=0.3mm L=85cm which are directly plugged in the PDMS inlets and held only by clamping thanks to the PDMS elasticity and the 8mm thickness of the top part (No glue is used).
- The chip is mounted on an Eclipse Ti-E Nikon microscope with 10x, 20x and 40x objectives.
- A High speed camera, Phantom 4.2 from Vision Research is used for visualization of droplets generation at tens of kHz frequencies.
- Two PTFE tubing OD=0.76mm ID=0.3mm L=20cm are connected to a reservoir disposed at a constant height to insure the same hydrostatic pressure over experiments.

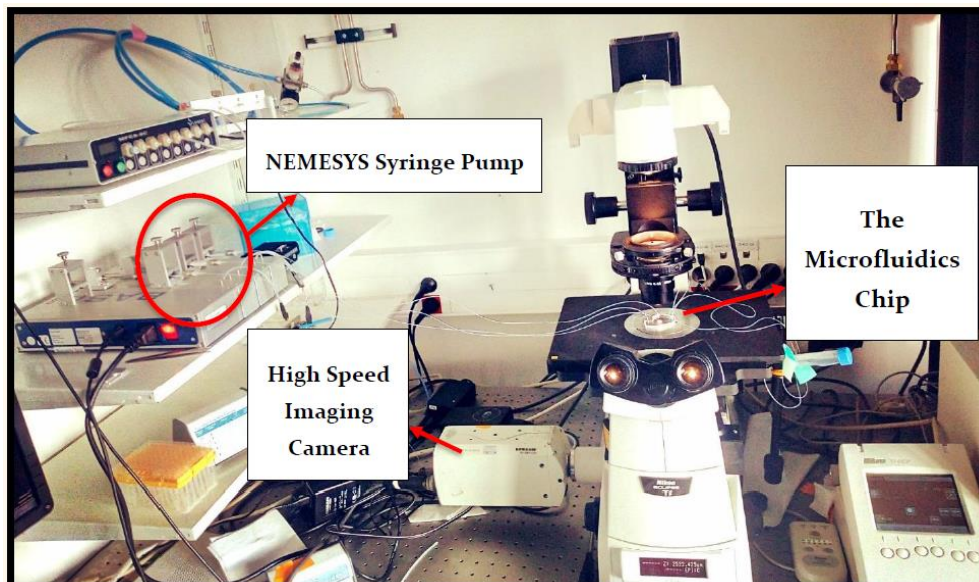


Figure 19: Picture of the experimental setup for droplet generation and observation. The chip inlets are connected to the syringe pump for injection of the continuous and dispersed phases. The outlets are connected to a reservoir kept at a constant height. The chip is

---

mounted on a microscope and a fast camera is used for observation of droplet generation at few tens of kHz frequency.

Image analysis:

The images are acquired using Phantom Camera Control software (PCC software from Vision Research). They are saved in specific format “.cine” of the PCC software that saves the acquisition parameters and then converted to “.avi” format.

A dedicated ImageJ Macro was developed by Rashmi Ramesh to analysis the acquired image and extract the droplet size of each condition of flowrate and surfactant concentration.

### 2.2.2.4 *Dispersed and continuous phases*

To investigate the versatility of our flow focusing approach for small droplets generation (compatible with single cell encapsulation), different continuous and dispersed phases and surfactants have been studied:

#### Dispersed phase:

Dulbecco's phosphate-buffered saline (14190094, Thermofischer), referred to it in this manuscript as PBS, is perfectly suitable for cell washing and handling thanks to his isotonicity and non-toxicity. We chose to use it as our default **dispersed phase** because we can suspend most of the biological targets for encapsulation: cells, proteins or other biomolecules of interest attached to solid support (magnetic or polystyrene beads).

#### Continuous phase: oils

Two mineral oils were tested: "heavy mineral oil" (Rectapur, Prolabo) and Mineral oil (light oil (neat) -M8410 from Sigma-Aldrich) with, respectively, viscosities of  $\mu=120$  mPa.s and  $\mu=27.5$  mPa.s at 25°C. The high viscosity oil is the one used by Chabert in his study. It induces four times higher hydraulic resistance than the light oil. For this reason, we decided to perform our study with light oil.

Fluorinated oil (Fluorinert™ FC-40FC40, F9755, sigma) with a viscosity of  $\mu = 4.1$  mPa.s at 25°C. FC-40 is used in a wide variety of applications: cooling electronic devices, cleaning medical device... It is also currently used as a reference oil in droplet microfluidic because of the advantages of fluorinated oils described at the beginning of this chapter.

#### Surfactants:

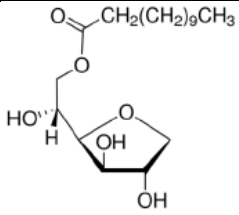
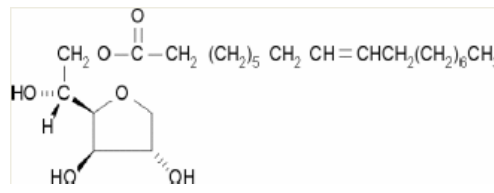
For droplet production with light mineral oil, we used two surfactants from the Span family of Sorbitan esters, Span 80 (S6760 Sigma-Aldrich) and Span 20 (85544 Sigma-Aldrich).

For droplet production with fluorinated oil, we used the Krytox 157FSH (Miller-Stephenson) and 1H,1H,2H,2H-perfluoro-1-decanol (532789 Sigma-Aldrich).

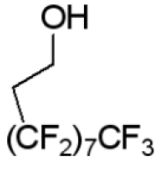
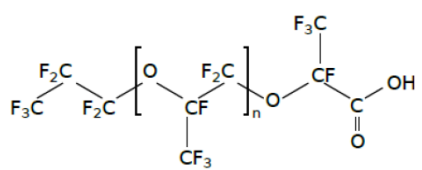
The chemical structure, density and molecular mass of each the surfactant are given in Table 3 and Table 4.



**Table 3: Properties of the surfactants Span 20 and Span 80 used with mineral oil**

Properties	Span 20	Span80
Density (g/mL at 25°C)	1.032	0.986
Molecular mass (g/mol)	346.46	428.60
Chemical structure		

**Table 4: Properties of the surfactants PFD and Krytox 157FSH used with mineral oil**

Properties	PFD	Krytox 157FSH
Density (g/mL)	1.678 at 25°C	1.032 at -9°C
Molecular mass (g/mol)	464.12	7000-7500
Chemical structure		

We performed IFT measurement by pendant drop method using the Drop Shape Analyser (DSA2, Kruss). The IFT are measured between PBS and mineral oil or fluorinated oil for different concentrations of the surfactants used. Results are presented in Figure 20.

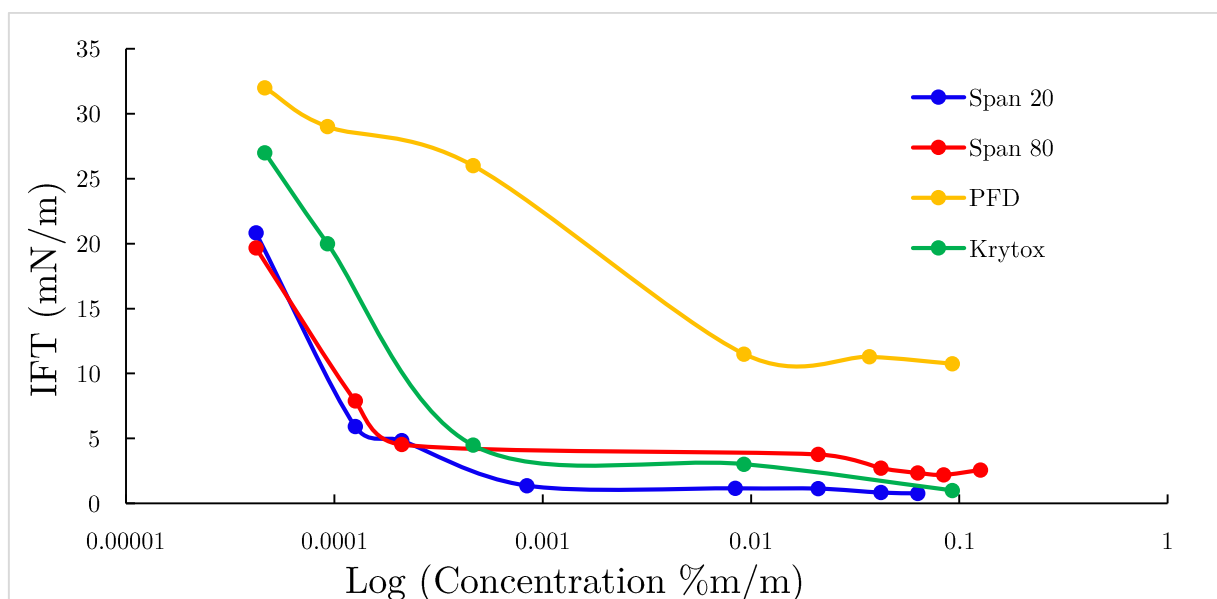


**Figure 20: IFT of Span 20 and Span 80 in light mineral oil, and PFD and Krytox 157FSH in FC-40 with PBS at 22°C.**



---

### ***2.2.3 Results & discussion***

We decided to investigate the behavior of our system by first keeping mineral oil as continuous phase as described by the seminal paper of Chabert et al. However, to better understand the mechanism of this droplet generation approach, three parameters have been varied:

1. First, surfactants with **different molecular masses**. In particular, we used Span 20 which has the lowest molecular mass (346.46g/mol) of the Span family to compare it with our reference Span 80 (428.60g/mol) used by (Chabert and Viovy 2008).
2. Secondly, the concentration of the surfactant was also modified in a range of **concentrations equal or higher than the CMC**. Indeed, this is the central parameter of this study for which we want to investigate the behavior of our device above CMC. Additionally, the effect of the concentration on the kinetics of the surfactant (diffusion and adsorption on interface) was interpreted from droplet diameter and interface curvature.
3. Finally, the effect of **flowrate of the dispersed** phase was also studied. As it could potentially destabilize droplet production regimes by changing the capillary number of the dispersed phase. Or, on the contrary, helps us in adjusting droplet diameter in a stable regime. The flowrate of the continuous phase was kept constant since, from our experimental observation, it is a very sensitive parameter that switches rapidly regimes of droplet production (see Figure 12). Particularly, in our configuration the surfactant is dissolved in the continuous phase, and thus, variations of the flowrate of this phase will interfere with the surfactant kinetics.

Keeping in mind that through better understanding of the effect of these parameters, we will also characterize the device for droplets production, in mineral and fluorinated oils. Targeting at the end droplets slightly smaller than the size of the objects that we want to encapsulate and sort. Typically, we aim at encapsulating objects with a diameter between 5  $\mu\text{m}$  and 50  $\mu\text{m}$  for cells or beads that can be used for solid support extraction.

### ***2.2.3.1 Droplet generation in mineral oil with Span 20 and Span 80***

Figure 21 and Figure 22 present the variation of the diameter of the droplets generated in our device as function of the concentration of Span 20 and Span 80 respectively and for five different flowrates of PBS. The lowest surfactant concentration is of 0.025%, CMC value of Span 80. Each point of these figures is the average over 3 chips. Error bars are the corresponding standard deviations. The droplet size for one chip with a fixed concentration and flowrate is an average value over 200 droplets. Flowrates of dispersed phase, PBS, were varied between 7 $\mu$ L/h and 50 $\mu$ L/h for obtaining droplets in the range of 5 $\mu$ m to 50 $\mu$ m in diameter in Span 80, and kept similar in Span 20 for comparison. Flowrates in each channel of continuous phase, providing light mineral oil, are kept constant at 150 $\mu$ L/h and symmetric in these experiments as to be compared with other studies. Asymmetric flowrates for droplet sorting will be discussed later in this chapter.

#### ***Molar mass effect:***

The comparison between the behaviors of Span 20 and Span 80 from Figure 21 and Figure 22, as having different molar mass, shows no significant difference between these surfactants. Indeed, Span 20 seems to produce slightly smaller droplets (1 $\mu$ m to 1.5 $\mu$ m, within error bars) than Span 80 for concentrations between 0.025% to 7.5% but it is the opposite situation from concentrations equal or higher than 10%. This can be the consequence of other factors involved in surfactant diffusion and adsorption to interface, which could compensate the effect of molar mass, such as the micelle aggregation number. Indeed, the disintegration of micelles to monomers can also affect dynamic surface tension as previously described by (Kai Wang et al. 2016). Nevertheless, we can notice that the first screened parameter, surfactant molar mass (and consequently the diffusion coefficient), does not have a significant impact on droplet diameter in the range (346 g/mol to 428 g/mol) with the studied surfactants and our operating conditions.

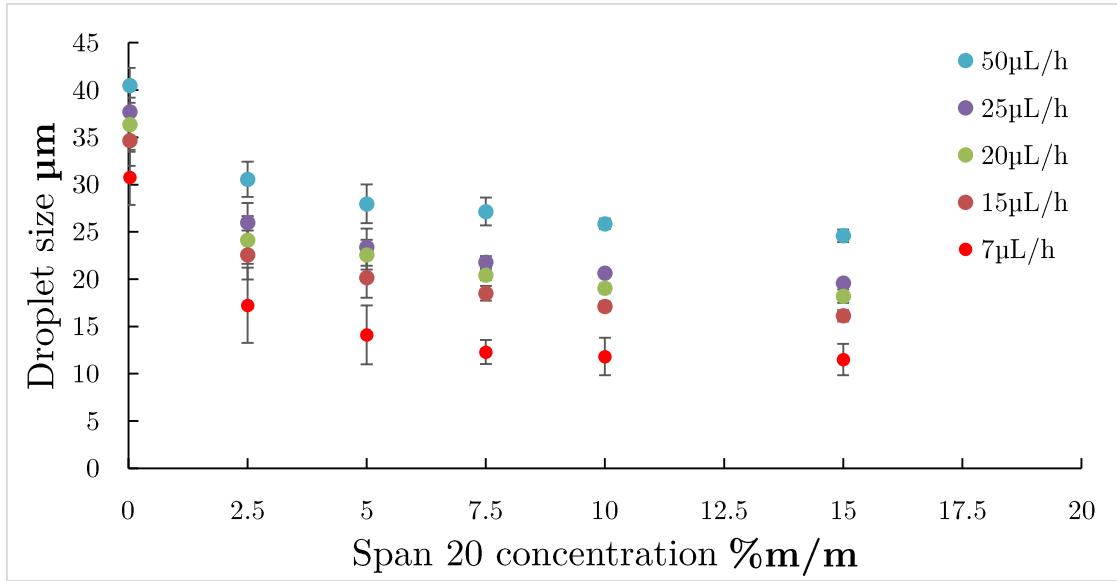


Figure 21: Droplet diameter as function of Span 20 concentration in light mineral oil

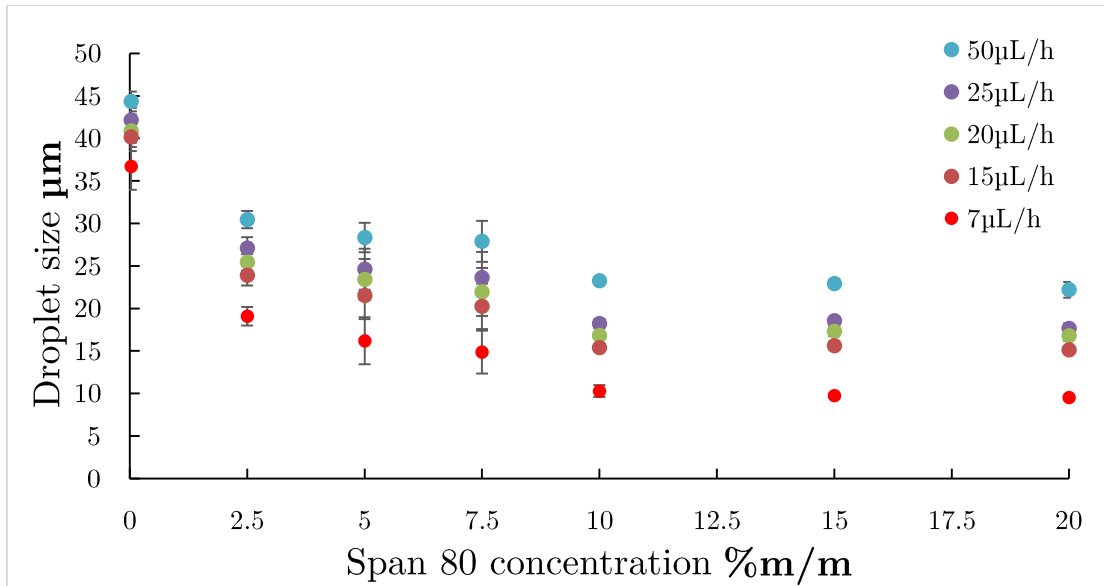


Figure 22: Droplet diameter as function of Span 80 concentration in light mineral oil

**Flowrate effect:**

Figure 23 represents the same data of Span 80 as Figure 22 but taking the **flowrate of dispersed phase  $Q_d$**  as x-axis. As expected, the droplet diameter increases with the increase of  $Q_d$ .

Looking more in detail to the recorded videos, we noticed that the increase in flowrate  $Q_d$  does not change the shape of the interface at a fixed surfactant concentration. Indeed, as shown in Figure 24 for a Span 20 concentration of 2.5% and 10%, the increase of  $Q_d$  seems only to push more PBS to fill the droplet at its formation point, without

changing the shape nor the position of the interface in the device at fixed concentration. This observation seems to show that the distribution of IFT along the interface and so, the distribution of surfactant molecules is kept similar for different flowrates  $Q_d$  at a given surfactant concentration.

Moreover, the curves in Figure 23 can be approximated by a cube root function (dotted line), which is the expected relation between the volume of a spherical droplet  $V_s$ ; included in  $Q_d = \frac{V_s}{time}$ ; and the diameter of the sphere. Consequently,  $Q_d$  is not affecting the frequency of droplet production as we will see in the next section with another surfactant (PFD).

The graph Figure 23 can be very useful in practical terms as a reference for droplets diameter. Since the regimes of droplet formation are very stable, we can precisely control droplet size by keeping  $Q_c$  fixed and varying  $Q_d$  to reach the desired diameter for encapsulation and sorting. Pictures of droplet generation, illustrating all these observations, are reported in Figure 24 using Span 20, for which the results present similar trends with Span 80 in Figure 23.

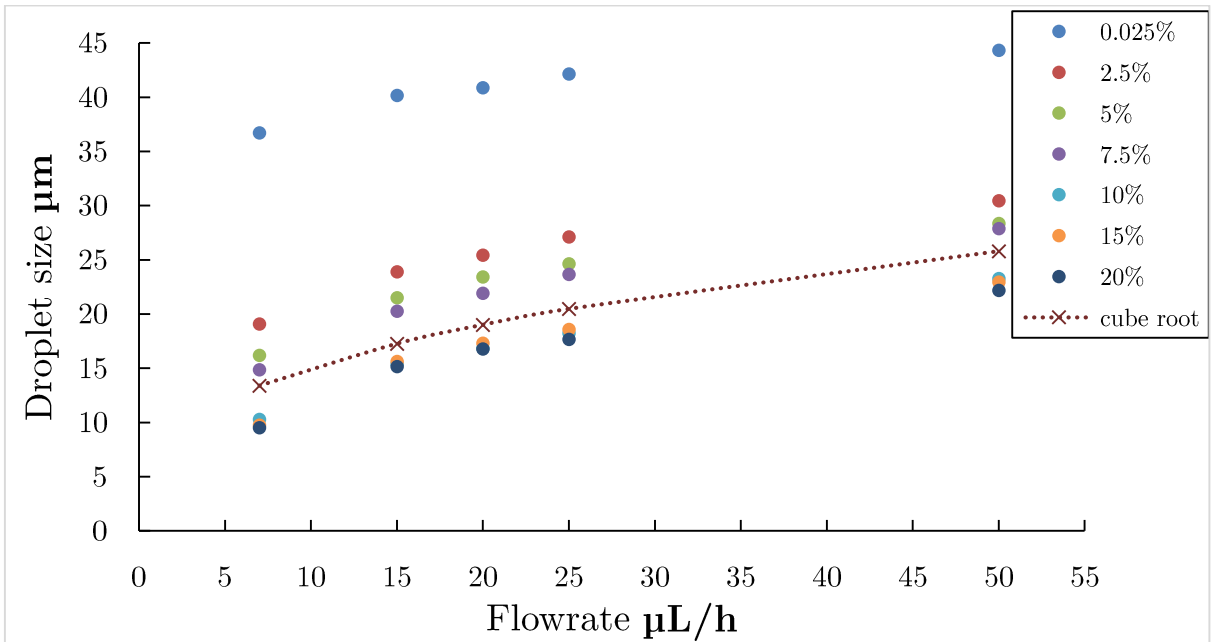


Figure 23: Droplet diameter as function of dispersed phase flowrate for different concentrations of Span 80.

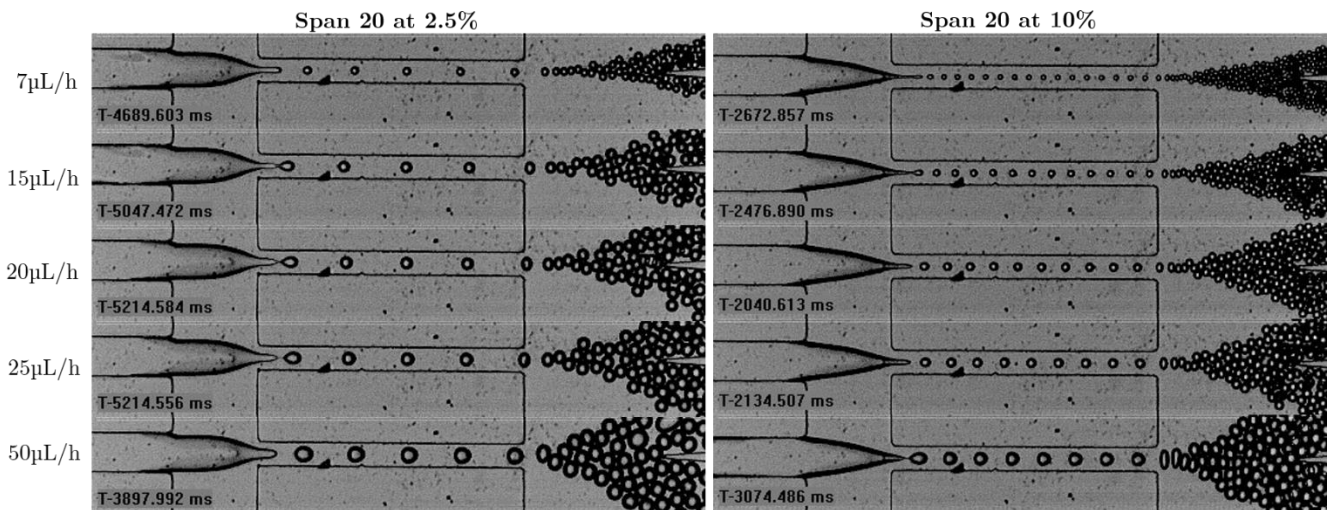


Figure 24: Bright field images with a 10x magnification showing droplet formation in mineral oil with two concentrations of Span 20 and five flowrates of the dispersed phase. The focusing region in which droplets are formed is 40μm width.

***Concentration of surfactant:***

As previously observed in Figure 13, we can notice in Figure 21 and Figure 22 that the droplet diameter decreases with the increase in, respectively, Span 20 and Span 80 concentration even above their CMC whatever the flowrate of the dispersed phase. This seems to confirm the assumption 2 on a larger range of concentrations, stating that droplet generation time is shorter than the time needed by surfactant to diffuse and adsorb on the interface for these experimental conditions. For this reason, the IFT is not at equilibrium state and this is why droplet size is decreasing even above CMC.

### ***Discussions & perspectives:***

Moreover, we can notice in Figure 21 and Figure 24 that in the range of droplet diameter  $17\mu\text{m}$  to  $26\mu\text{m}$  the two conditions of concentrations 2.5% and 10% overlap (for different flowrates). However, when looking in detail to the shape of the interface before droplet detachment point, we can observe that at fixed diameter the shape is very different between 2.5% and 10% but does not change for different flowrates at one of these concentrations. This is suggesting that models based on droplet diameter for estimating the value of dynamic IFT as developed by Luo group (K. Wang et al. 2009; Kai Wang et al. 2016; Xu et al. 2012) is not necessarily relevant in our case. Also, calculation of the dynamic IFT based on equating capillary number at regime transition in surfactant-free and surfactant-laden systems is not possible in the studied device because the wetting conditions are not favorable in surfactant-free system with mineral oil and PBS (or water). Indeed, the dispersed phase tends to wet the PDMS at the focusing region or farther in the channels for any combination of flowrates (images not shown). Therefore, no stable droplet formation regime can be reached with a surfactant-free configuration.

Furthermore, measurements by pendant drop method as presented in Figure 10 confirm that Spans surfactant needs several minutes before reaching equilibrium even for concentration above CMC. Unfortunately, this technique allows measurements neither at time scale, nor at drop volumes comparable with those involved in our experiments. However, (Brosseau, Vrignon, and Baret 2014) exposed an original approach for tensiometry measurements in a microfluidic system and showed that the adsorption kinetics in their device is much faster than the kinetics of the corresponding pendant drop experiment. Nevertheless, downscaling of the measurement volume to picoliter and measurement time to tens of microseconds is still needed to be relevant for our device.

As perspectives of the analysis of these data, we are planning to characterize quantitatively the shapes of the interface at the focusing region (called “neck”). Indeed, as said above, this shape can provide relevant information about IFT. As viscosities and velocity field can be calculated, the characterization of the interface shape could lead to a local estimation of the IFT. We identified for that purpose the following parameters: length and curvature of the whole interface, length and width of the elongated tip in the focusing channel (see Figure 25). Also, comparably to (Brosseau,



Vrignon, and Baret 2014) the deformation of the droplet at the end of the focusing channel is also a complementary information about the kinetics of surfactants in picoliter droplets that can be supplemented by information about droplet merging or not merging when brought in contact to each other in the same area (see Figure 13).

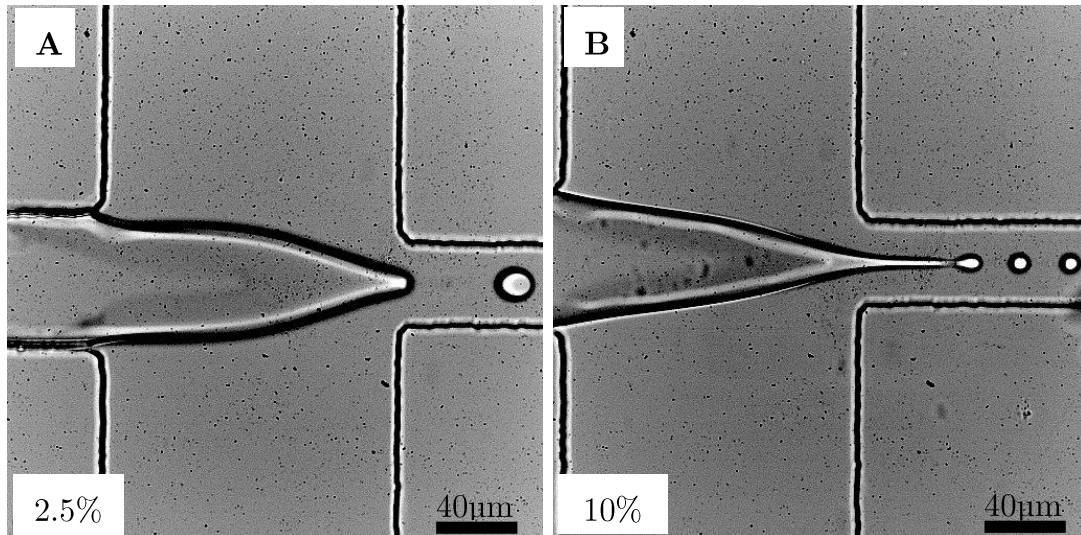


**Figure 25: Droplet generation at 7 $\mu$ L/h dispersed phase flowrate, concentration of span 20 are 2.5% (A), 10% (B). Images taken in bright field, with a 40x magnification. These pictures illustrate the shape deformation of the interface. In A, the neck is concave and not elongated in the focusing channel. In the right panel, the neck is more linear and sometimes locally convex with a tip elongated in the focusing channel. This change in shape can be related to IFT.**

### ***Size distribution***

Calculation of the polydispersity index PDI for the same chip, as the standard deviation of the droplet diameter divided by its average over 200 values, show a **highly monodisperse distribution** in both cases. Indeed, for all the concentrations and flow rates the value of **PDI is  $\leq 0.05$** . On the other hand, variations between different chips are given by error bars in Figure 21 and Figure 22. They show 0 to 5 $\mu$ m differences, only for average value higher than 15 $\mu$ m with both surfactants. These variations can be explained by pressure fluctuations between experiments due to inlets and outlets length and PDMS elasticity. They can be improved in further experiments by using a stronger material and adjusting design proportions if needed.

### 2.2.3.2 *Droplet generation in fluorinated oil with PFD and Krytox*

Taking into account the previous results using mineral oil and Spans, we decided to investigate the behavior of our device with fluorinated oil FC-40 and PFD and Krytox 157FSH as fluorinated surfactants. We choose these surfactants, because they have a difference in molecular mass about 80 times higher than between Span 80 and Span 20. Thus, increasing our chance to observe a difference in droplet formation behavior caused by this parameter.

Figure 26 and Figure 27 present the variation of droplets diameter with the concentration of PFD and Krytox 157FSH, respectively, and for five different flowrates. The lowest concentration is 0.5% $m/m$ , higher than their CMC values. Each point is the average over 3 chips. Error bars are the corresponding standard deviations. The droplet size for one chip with a fixed concentration and flowrate is also an average value over 20 droplets, as polydispersity index shows a very low value, we reduced, compared to Spans experiments, the number of counted drops to 20.

Flowrates of the dispersed phase, PBS, were varied for five different values between 15 $\mu\text{L}/\text{h}$  and 70 $\mu\text{L}/\text{h}$  in Krytox to obtain droplets in the range 5 $\mu\text{m}$  to 40 $\mu\text{m}$ , and kept similar in PFD for comparison. 15 $\mu\text{L}/\text{h}$  and 25 $\mu\text{L}/\text{h}$  are not shown in the PFD graph because they correspond to an unstable droplet generation regime, thus no droplet diameter could be measured at any surfactant concentrations used. Flowrates in each channel of continuous phase, FC-40 fluorinated oil, are kept constant at 1100 $\mu\text{L}/\text{h}$  and symmetric in these experiments for the same reasons as explained in section 2.2.3.1.

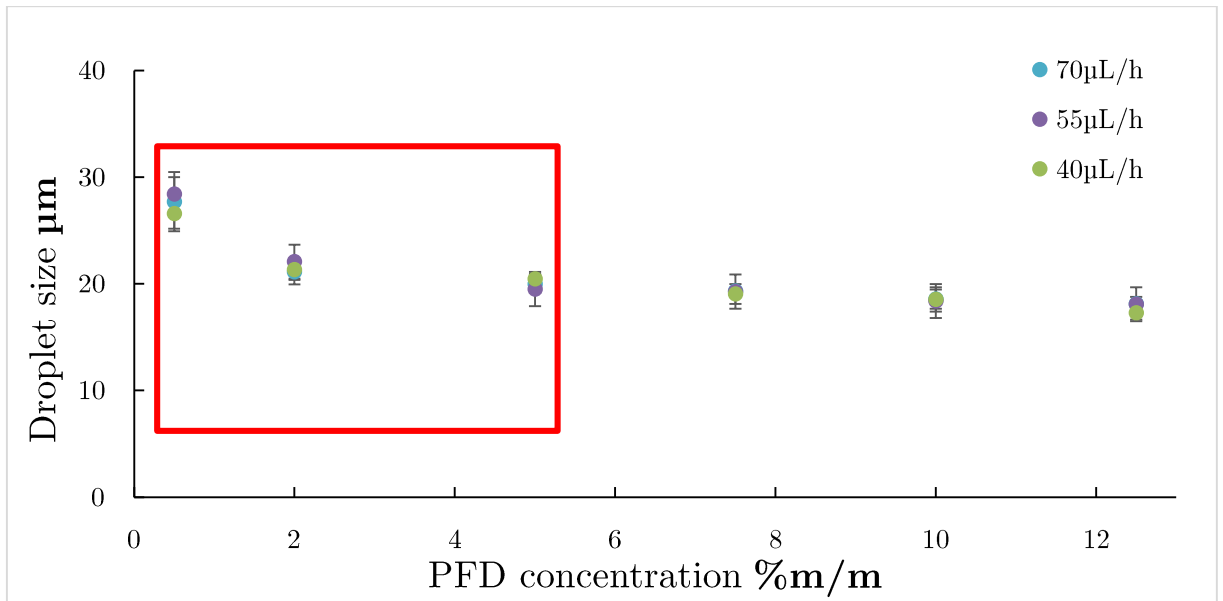


Figure 26: Droplet diameter as function of PFD concentration in FC-40. Red rectangles highlights regions of multiple droplets size generation. Red rectangles highlight regimes of multiple droplets size. In these cases, data points represent only the highest value.

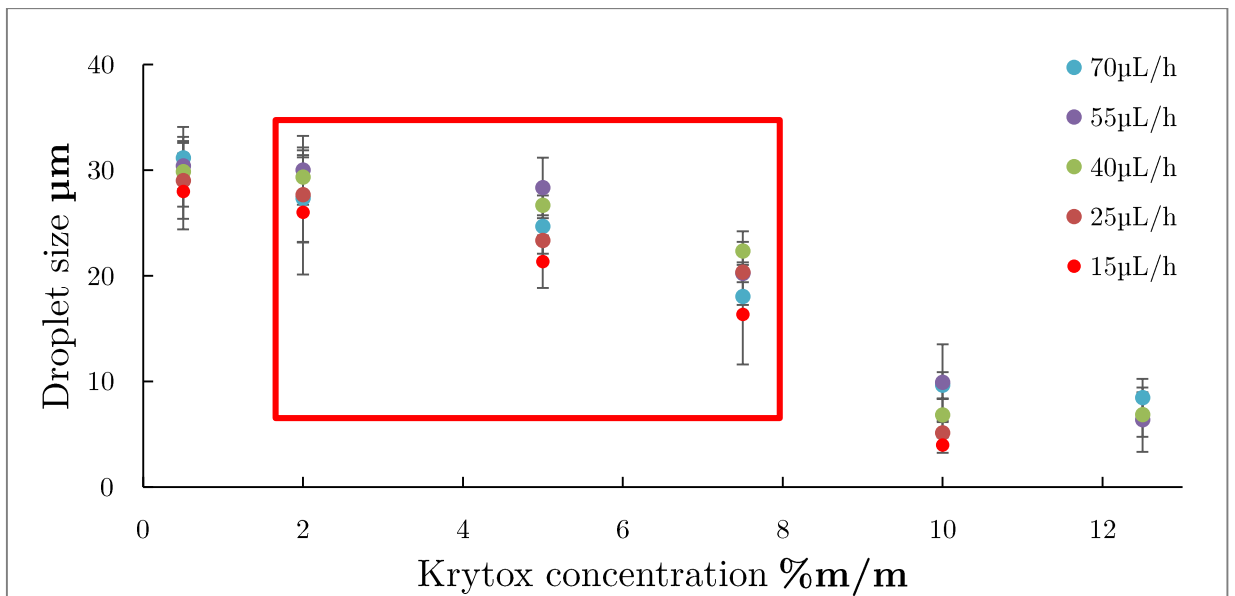


Figure 27: Droplet diameter as function of Krytox 157FSH concentration in FC-40. Red rectangles highlights regions of multiple droplets size generation. Red rectangles highlight regimes of multiple droplets size. In these cases, data points represent only the highest value.

### **Regimes of multiple droplet size generation:**

Red rectangles in Figure 26 and Figure 27 highlight regimes of multiple droplets size generation. We choose to represent in the graph, the size of the biggest droplet as it is the most useful information in the case of sorting. In these regimes, droplets of different sizes are produced one after the other. Moreover, the shape and the position of the interface in the focusing region are not stable in time. Indeed, as showed in Figure 28, the interface balances between states that we describe and discuss as following :

- A highly convex state, indicated by ● , in which the IFT seems to be dominant. This keeps the interface far from the focusing channel for **few milliseconds** until the meniscus grows by the flowrate of PBS and the interface becomes more charged by the surfactant molecules that reduces the IFT allowing the apparition of the second state.
- A conical state for **few hundreds of microseconds**, indicated by ▲ . Thanks to the surfactant molecules, the interface can easily be stretched by the viscous drag of the surrounding oil leading to the conical shape. Consequently, the interface at the tip is subject to higher shear due to the physical constriction and its IFT continues to decrease by the adsorption of surfactant until it breaks, ejecting several droplets of different sizes before going back to the first state.

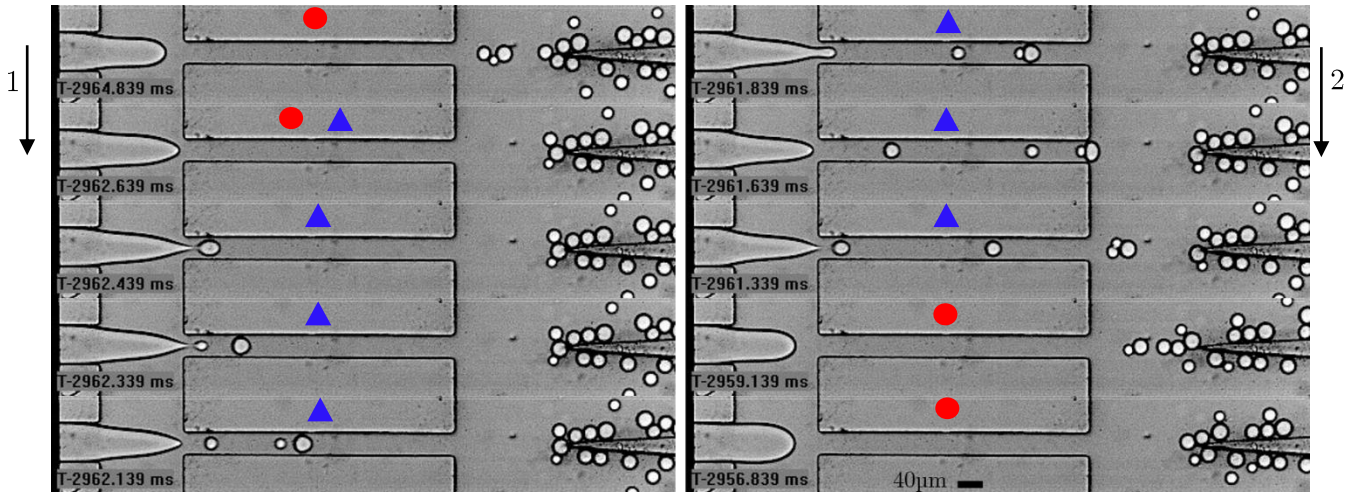


Figure 28: Sequence of images showing a “multiple droplet regime” extracted from the same movie of droplet formation. We used PBS as dispersed phase ( $Q_d=40\mu\text{L/h}$ ) and FC40 containing Krytox at 5% $\text{m/m}$  ( $Q_c=1100\mu\text{L/h}$ ). Red dots indicate the convex state and blue triangles the conical state. The second image shows a transition between the two states. Time is increasing from top to bottom, then left to right.

---

This possible mechanism is similar to the one described by (Anna and Mayer 2006) for tipstreaming (Figure 17).

***Comparison of PFD vs Krytox for three parameters:***

As compared to Krytox, we observe for PFD a slow decrease (around  $6.5\mu\text{m}/2.5\%$  vs.  $1.2\mu\text{m}/2.5\%$ , respectively) and lower total value of decrease ( $25\mu\text{m}$  vs.  $9\mu\text{m}$ , respectively) in droplet diameter with the increase in concentration. Also, PFD shows a much lower decrease of droplet diameter with the decrease in PBS flowrate, such that most of the points overlap at a fixed concentration (see Figure 25). However, the concentration 0.5% seems to be an exception, in which data points are still distinguishable and has droplet diameter around  $5\mu\text{m}$  higher than the other concentrations.

We explain the invariance for different flowrates by the fact that PFD can diffuse faster than Krytox and thus can reach equilibrium IFT faster. Moreover, PFD has a higher equilibrium IFT value at CMC ( $11\text{mN/m}$ ) than Krytox. Thus, even by changing the **dispersed phase flowrate** when reaching this equilibrium ( $>0.5\%$ ), the droplet size is not reduced anymore and instead, the device continues generating droplets of similar size but with a higher frequency directly proportional to the PBS flowrate.

Identically to Spans, the droplet size decreases with the increase in **surfactant concentration**. However, for low concentrations ( $\leq 5\%$ ), the PFD has a faster kinetics to reach the interface and thus, reduces the IFT and produces, in average over flowrates, smaller droplet than the Krytox. But as explained before for flowrate variation, the high IFT equilibrium value limits the decrease in droplet diameter, which became lower than  $1\mu\text{m}$  between two successive concentrations  $>5\%$ .

We understand here that the high difference in molecular mass between PFD and Krytox is a key parameter impacting the kinetics of IFT and thus droplet formation. Indeed, contrary to the Spans situation where no significant difference was observed, we can notice that molecular mass limits here the effect of both concentration and dispersed phase flowrate as they are both observable for Krytox (high molecular mass) and negligible for PFD (low molecular mass).

Furthermore, the instable regime in PFD for  $15\mu\text{L/h}$  and  $25\mu\text{L/h}$  can be explained by its high equilibrium IFT. Indeed, to obtain the same capillary number i.e. same stable regime of droplet production as for flowrates  $\geq 40\mu\text{L/h}$ , the high IFT of PFD necessitate a high shear force and thus a high flowrate at fixed viscosity. If the flowrate is not

compensating the high in IFT, we may transit to a different regime. Therefore, at 15 $\mu$ L/h and 25 $\mu$ L/h we might be below this threshold of compensation and for this reason we transit to an unstable regime.





### ***2.2.4 Conclusion & perspectives***

Experiments run with the PFD show that we had possibly reached equilibrium value of IFT when using this surfactant (PFD) at 7.5% or 10% in fluorinated oil (FC40). If confirmed, this would allow us to use this surfactant as a reference for stable calibration of the device by calculating the corresponding capillary numbers and screening a whole range of droplet diameter through the increase of continuous phase flowrate  $Q_c$ .

For Krytox, we succeeded in producing droplets smaller than 10 $\mu$ m with a good reproducibility with Krytox concentration higher than 10% (w/w). This size range is of high interest for the development of our platform because it can allow the sorting of mammalian cells. Further improvements are currently engaged to switch for a non-ionic surfactant, the Pico-Surf (Sphere Fluidics), which is similar to the Krytox 157FSH but with a PEG end. Pico-Surf is more suitable for biological reaction, since in contrast to Krytox, it will not interact with the content of the droplet. Based on the experiments developed here, we will use the same type of characterization to find the appropriate concentration and flowrates for production of droplets of size suitable for sorting in an asymmetric configuration.

#### ***2.2.4.1 Asymmetric configuration***

We then run experiments using Krytox 157FSH in an asymmetric continuous flowrate configuration to compare it to the symmetric configuration used in the experiments above. Figure 29 shows a configuration with flowrates for oil 1250 $\mu$ L/h top, 1000 $\mu$ L/h bottom and 30 $\mu$ L/h for PBS.

We can notice that almost no significant difference in the droplet diameter is observed compared to the closest situation in Figure 27, which is 1100 $\mu$ L/h for both oil flowrates and 25 $\mu$ L/h for PBS. Drop size was 5.1 $\mu$ m and is 6.5 $\mu$ m, a difference <1.5 $\mu$ m (within error bars). However, in accordance with the described mechanisms underlying this phenomenon of droplet production, we can also notice that the interface in the side of the higher flowrate is slightly more deflected than the other one (see Figure 30). Indeed, higher  $Q_c$  implies higher viscous drag because it increases the linear speed at the interface, but also since we are not at equilibrium IFT, it should bring more surfactant to the interface, and makes it more flexible by lowering the IFT.



---

This last point is more obviously observed in the case of light mineral oil (Figure 13), and even more exacerbated in the case of heavy mineral oil (Figure 6), as the viscosities of these oil are respectively 27.5 mPa.s and 120 mPa.s at 25°C, as compared to 4.1 mPa.s at 25°C for FC-40 the fluorinated oil used. Thus, the effect of the viscous drag on the interface is increased proportionally to the viscosity.

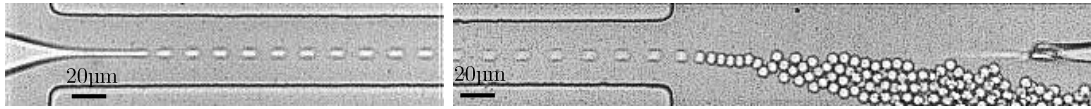


**Figure 29: Asymmetric droplet generation with fluorinated oil at 10% of Krytox. Flowrates are for oil 1250µL/h top, 1000µL/h bottom and 30µL/h for PBS. These pictures were taken with 20x magnification for better visualization of the tiny droplet 6.5µm. During their travel through the focusing channel, droplets are fuzzy because we reached the lower limit of exposure time of the fast camera, 10µs, for which droplet movement at these flowrates, is not negligible anymore. Their speed is about 0.5µm/µs.**

Therefore, we had successfully achieved the two goals of this first project. Indeed, we investigated and understood, at least qualitatively, the main mechanisms underlying droplet formation and the effect of surfactant concentration above CMC. The hypotheses of these mechanisms were confirmed by the experimental data on two sets of experiments using mineral and fluorinated oils with the corresponding surfactants. Furthermore, in the case of fluorinated oil, we found experimental conditions of flowrates, surfactant type and concentration for which we can successfully generate droplet of diameter lower than 10µm and thus suitable for cell encapsulation and sorting with the studied device.

### 2.2.4.2 Encapsulation and sorting of cells using fluorinated oil

Finally, to confirm the latest statement, we tried to encapsulate and sort real cells from SKBR3 cell line ([SKBR3] (ATCC® HTB-30™)), which have an average size of  $15\mu\text{m}$  (cell concentration and size distribution performed with Scepter™ 2.0 Cell Counter by Merck). As shown in Figure 30, successful encapsulation and sorting can be achieved with the krytox 157FSH at 10% and flowrates of oil at  $1430\mu\text{L/h}$  Top,  $890\mu\text{L/h}$  bottom, and  $45\mu\text{L/h}$  for the cell suspension. The empty droplets continuously generated are about  $4.5\mu\text{m}$ , the cell  $15\mu\text{m}$  and the encapsulating droplet  $21\mu\text{m}$ .

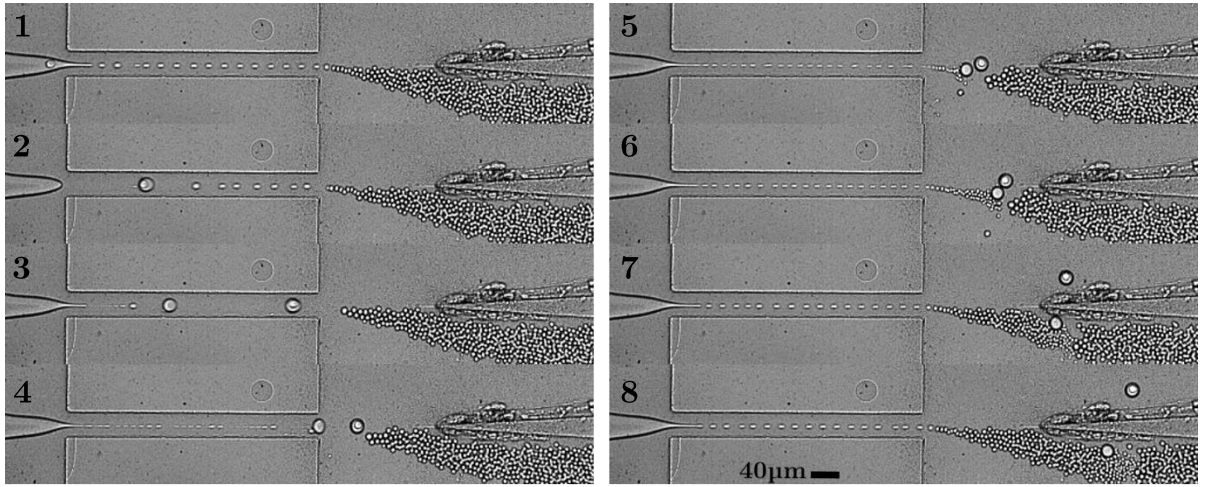


**Figure 30: Encapsulation and sorting of a single cell in fluorinated oil with 10% Krytox. Flowrates are: oil  $1430\mu\text{L/h}$  Top,  $890\mu\text{L/h}$  bottom, and cell suspensions  $45\mu\text{L/h}$ . The second big droplet generated after the cell encapsulation is empty and sorted in the trash. It is formed because the initial elongation of the dispersed phase in the focusing channel is too small ( $5\mu\text{m}$ ), as compared to the size of the cell ( $15\mu\text{m}$ ), so the cell cut this jet for its encapsulation and the second droplet is ejected before stabilization of the new elongation. Pressure of the bottom channel  $60\text{mbar}$  higher than top channel, to increase its hydraulic resistance and shift the streamline upward.**

Furthermore, we improved the sorting step by adding a pressure controller at the outlets of the device to shift the streamlines after the focusing channel. Indeed, as shown by Chabert & Viovy (movie 4 of the Supporting information) some cells may be lost in the trash outlet due to drop-drop interactions (containing cells) in the focusing channel, which push some cells in a streamline slightly lower than the central streamline but still distinguishable from empty droplets. By adjusting the pressure in the two outlets it was possible for us to shift this streamline to the collecting channel and put the empty droplet streamline to the limit of the wall separating the outlet channels, as

---

shown in Figure 30. Therefore, we are able to collect the cells that were lost in the previous configuration but without contamination by the empty droplets.

A first perspective of this work is to produce quantitative data for droplet sorting efficiency with different sizes of cells and beads and to adapt the outlets design to the corresponding optimized flowrates in fluorinated oil. Secondly, it will be necessary to confirm the biocompatibility of the surfactants and the viability of cells after encapsulation, if live-cells investigations are sought after sorting. For direct analysis of the cells content, a toxicity of surfactants in the carrier oil is not a problem, as long as it does not inhibit the biochemical reactions and/or enzymes at play (e.g. polymerases, etc).

Finally, the next section and the next chapter of this manuscript are presenting the perspectives that we choose to develop during this thesis: How can we recover the droplets, manipulate them and merge their content with reagents? How can we analyze the content of the encapsulated cells? And what type of assay can be suitable in this case?



---

## 2.3 Large scale droplet manipulation towards downstream analysis

### 2.3.1 Introduction

The following work was started during my second year of PhD in collaboration with Davide Ferraro. And part of this work was performed by Mathilde Richerd during her Master 2 internship that I supervised.

### 2.3.1 Introduction

Once having encapsulated single cells in droplets, the final goal of the developed platform would be to analyze the content of each cell. To do so, we have to merge the droplet with reagents brought by a second droplet of higher volume to perform our assays. We identified a series of bottleneck operations to be developed and optimized:

- The collection of the single cell encapsulated droplets: to collect and concentrate them at the outlet of the encapsulation/sorting device.
- The controlled storage of the droplets.
- The development of an approach to control the injection of reagent to each droplet (on-demand injection and coalescence)

We present in Figure 31, the workflow that we propose to implement in our platform. This workflow is divided in two parts performed sequentially. The first step consists in encapsulating the cells and collecting them in a chip. The second step is then to inject the droplets from this chip to a third one in order to space and merge them on-demand. Each step is detailed in the next sections with the corresponding chips fabrication and use.

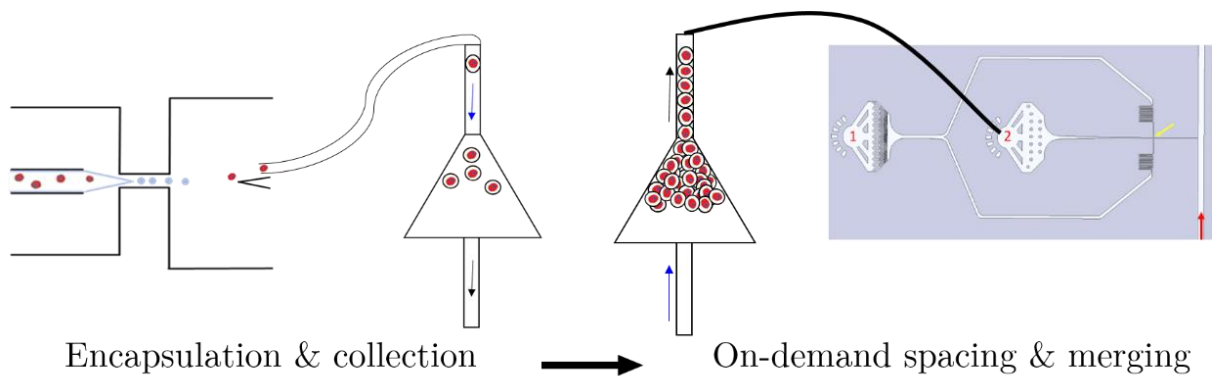


Figure 31: Workflow of the encapsulation and merging module.

### *2.3.2 Device for droplet collection*

Starting from the outlet of the encapsulation chip, we have first to develop a simple and efficient approach to collect the sorted droplets containing cells in order to further address them, one by one, by fluidic manipulation. Two main difficulties have to be considered in this operation:

- The sorting has no specific frequency, due to the random arrival of the cells in the focusing channel: the droplets come out randomly from the positive outlet.
- The volume fraction of the sorted droplets in the positive outlet is very low,  $V_{frac} = \text{volume of droplets} / \text{volume of oil}$ , is around 1%.

To collect and concentrate the droplets, we choose a physical method based on the density difference between PBS and fluorinated oil. The device fabrication is rather simple. It consists in i: molding a conically shaped 0.5 mL PDMS piece using an Eppendorf tubes as mold, puncturing the inlet at the tip of the cone; ii: puncturing the outlet on a flat PDMS that will be used to close the cone with liquid PDMS. The liquid PDMS is here used as a glue between the two parts and cured at 70°C to avoid plasma treatment and silanization.

The droplets enter from the top in the conical chamber and are slowed down thanks to the enlargement of the cone (drag force decrease) and the buoyancy that pushes them in the opposite direction. The oil is evacuated by the bottom tubing because it is denser than the aqueous droplets. Depending on the initial concentration of cells, after few minutes, the cone is filled by the droplets and we can stop the encapsulation. Finally, the next step consists in reversing the flow (see Figure 32) and injecting the droplets close-packed in a new chip, to be merged with reagents droplets.

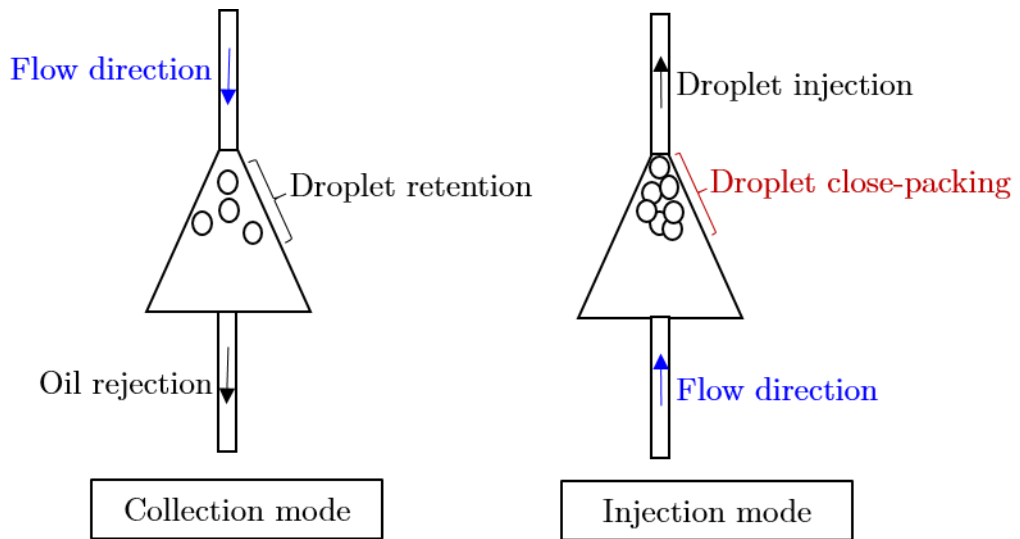


Figure 32: Chip for droplet collection used with a continuous phase denser than dispersed phase. During collection, the chip is connected to the outlet of encapsulation device from its upper tube. Enlargement of the channel in the cone reduces the speed of the droplets and retain them by buoyancy in the direction opposite to the flow, while oil is rejected from the bottom outlet. After collection, the flow is stopped and droplets are close-packed and ready for injection into the merging chip in the opposite direction.

### ***2.3.3 Device for on-demand injection and merging***

#### ***2.3.3.1 Close-pack and spacing***

Once the droplet collected, we aim at controlling the sequential injection of encapsulating droplets in the device to further merge them with nanoliter reagents droplets. To do so, we made a design based on (Mazutis et al. 2013) and adapt it to our needs. At this stage, two cell analysis platform were considered: a droplet qPCR system (that will be described in the next chapter) and a magnetic tweezers based approach. Indeed in the team, we have proposed an approach combining droplets and magnetic tweezers (Ali-Cherif et al. 2012; Ferraro et al. 2016a) to perform multi-omics analysis by performing solid support extraction in droplets.

Taking these systems into account, we designed an injection chip that could fit directly with these two types of devices. This means that altogether our devices should provide droplets in the range of hundred nanoliters to fit the inlets of these analysis systems. This implies that we have to merge in a controlled manner the droplet containing a single cell (volume about 4pL) with nanoliter reagents droplet for downstream analysis. The main examples in the literature report either the injection of picoliter volume from a monophasic to a nanoliter droplet (Abate et al. 2010) or merging of droplets having a maximum diameter ratio of about 4 (Chung et al. 2017; Gu, Duits, and Mugele 2011; Niu et al. 2011). In our case, the diameter ratio is about 25.

So inspired from some of these approach, we developed the chip showed in Figure 33. It is divided in the following areas:

- A first area which is 20 $\mu$ m height, where the picoliters droplets (surrounded by FC40 with 10% of Krytox 157FSH) are injected, stored and spaced in a controlled manner.
- A channel of 200 $\mu$ m height with flowing 50nL droplets produced upstream and moving them to the merging zone and then to the outlet. These droplets are surrounded by FC40 with 1% of 1H,1H,2H,2H-perfluoro-1-décanol (called PFD) as this surfactant allows droplet merging by drop-drop contact.
- A merging area (dashed square in Figure 33), which will finally deliver the mixed droplets to the outlet.



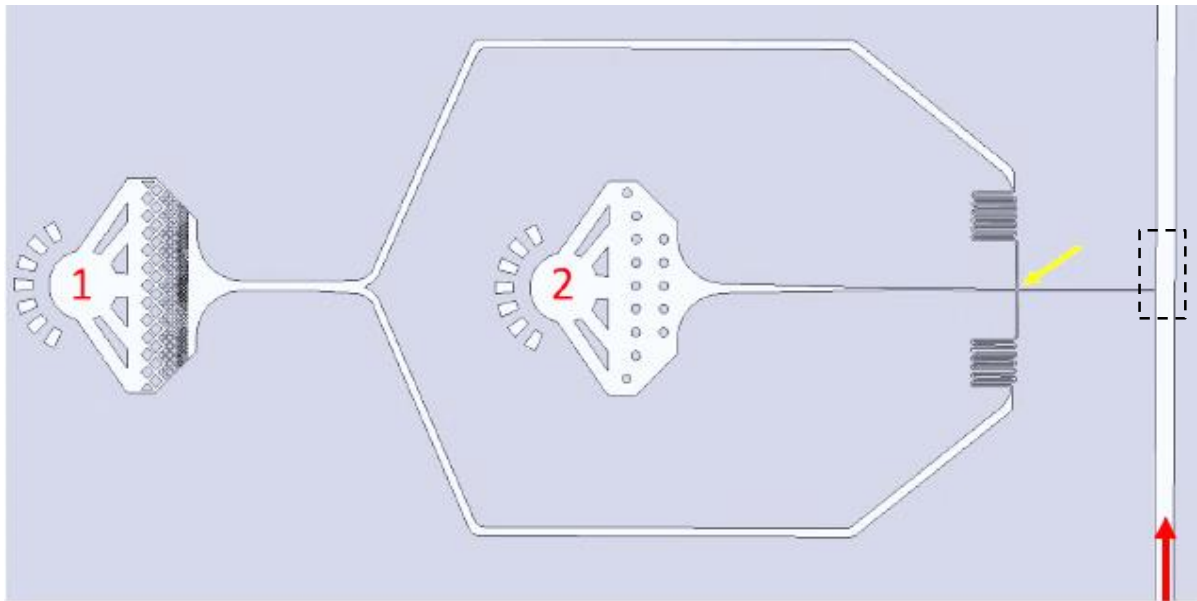


**Figure 33: Design of the merging device inspired from (Mazutis et al. 2013). 1. Inlet for oil 2. Inlet for close-packed droplets. Yellow arrow indicates the droplet spacing zone. Red arrow indicates the direction of 50nL droplet flowing in the 200 $\mu$ m main channel. Except for the main channel, which is at 200 $\mu$ m height, the rest of the chip is 20 $\mu$ m height. Dashed rectangle indicates the merging area.**

The inlet 2 is controlled with a pressure controller whereas the spacing oil inlet 1 and the main channel are controlled in flowrate (with a syringe-pump). The choice of this configuration is driven by preliminary tests:

- Inlet 2 was controlled by flow rate (syringe-pump): the minimum flow rate reachable by this method is around 1nL/s which represents for droplets of 20 $\mu$ m in diameter at a packing factor of 0.5 a flow of 125 droplets/s. Moreover, the On/off switch needed to deliver picoliter droplet only when the 50nL plug is in the merging zone, which is not possible in these conditions. In fact, the relaxation time of all the PDMS parts (cone and merging chip) observed experimentally is about 10min
- A large number of the picoliteric droplets coalesce spontaneously when reaching the inlet or before in the tubing (see Figure 33). We explain that by the fact the PTFE capillaries can be charged when touched during the connection to the chip and the use of Krytox 157FSH which is an ionic surfactant. Thus, electrostatic interaction between the PTFE and the surfactant may lead to droplets random merging. To avoid this unwanted effect, we manage on latest experiments to substitute, in the collection device, the Krytox 157FSH by the

Picosurf (non-ionic surfactant, by Sphere Fluidics) through oil replacement (2mL of FC-40 at 2%) before injection in the last chip.

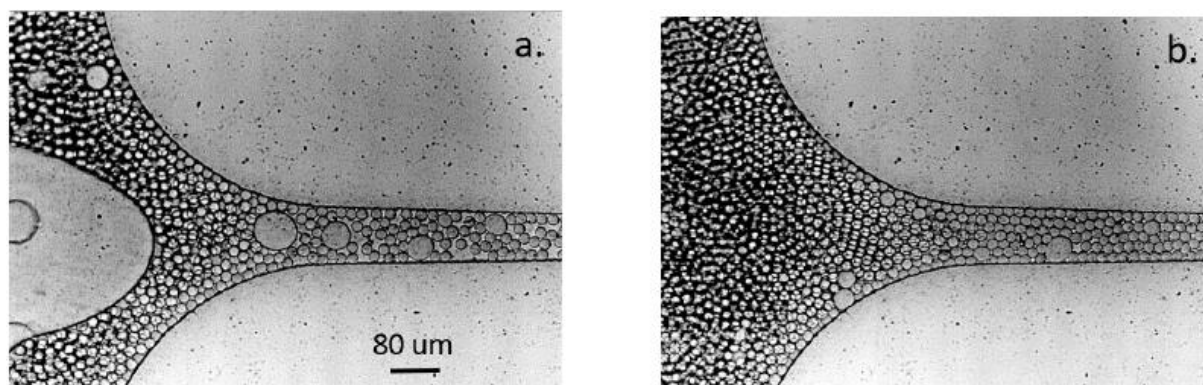
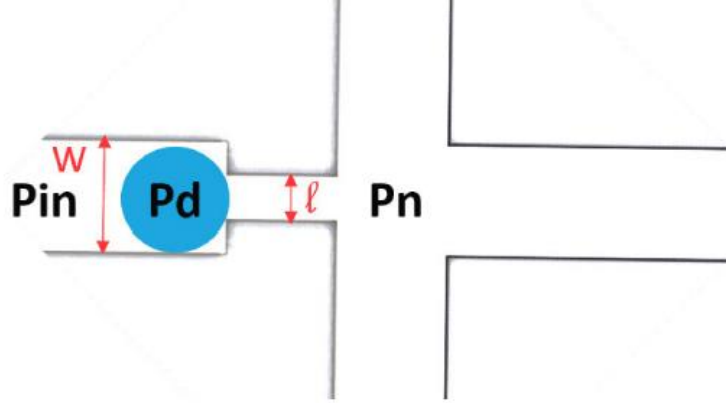


Figure 34: Pictures of close-packed droplets in the inlet 2. In the image a. some of the droplets have coalesced due to electrostatic interaction between charged PTFE and the ionic surfactant. In the image b. Good close-packing of the droplets with almost no coalescence.



**2.3.3.2 Pressure pulse for on-demand injection**

To stabilize the droplet at the intersection (Figure 34,) and controlled their injection in the merging zone, we designed a constriction in the storage channel inspired by droplet on demand device developed by (Zhou and Yao 2014). A substantial difference with their work, is that in our case the droplets are not produced on-demand at the junction but, instead, we want to deliver them on-demand by applying a pressure pulse.



**Figure 35:** Schematic view of the spacing zone. The droplet in blue is stopped by the constriction. It will need a pressure pulse to pass in the next channel. The value of the pulse is depending on the widths W and l, and on the steady-state pressures Pin and Pn.

To adjust the pressure pulse for on-demand injection of droplets, we have to consider the Laplace pressure and the different pressures resulting at this channel's intersection. The equation of Young-Laplace gives:

$$P_d - P_{in} = 2\gamma\left(\frac{1}{H} + \frac{1}{W}\right)$$

$P_d$  Pressure inside the droplet

$P_{in}$  Pressure before the constriction

$\gamma$  Interfacial tension between inner and outer phases of the droplet

H, W Respectively the height and width of the channel before the constriction

To jump the constriction, the pressure inside the droplet (confined in the constriction) must be higher than Laplace pressure:

$$P_d - P_n \geq 2\gamma\left(\frac{1}{H} + \frac{1}{l}\right)$$

This means that we need to increase the pressure  $P_{in}$  at least by:

$$\Delta P = P_{in} - P_n = 2\gamma\left(\frac{1}{l} - \frac{1}{W}\right)$$

If we consider a constriction of  $l=6\mu\text{m}$  and  $\gamma\approx 2\text{mN}\cdot\text{m}^{-1}$  then  $\Delta P\approx 500\text{Pa}\approx 5\text{mbar}$ . This pressure difference is in the range of the pressure controller that we are using (MFCS, Fluigent).

The first experiments ran using the constriction are very promising. The droplets are efficiently stopped by the constriction and get through it after the pulse (see Figure 36).

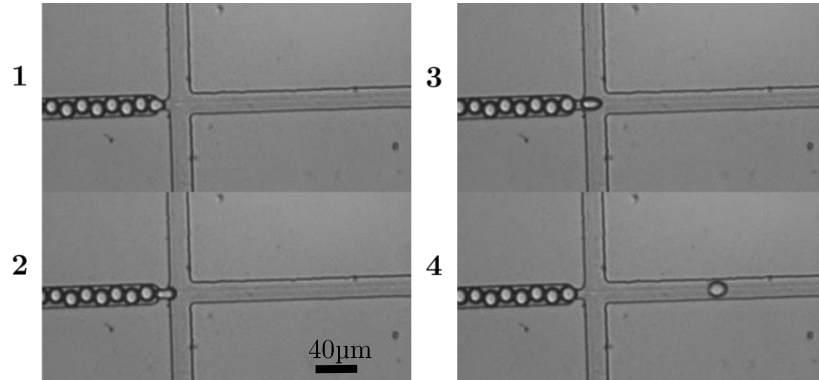


**Figure 36: Visualization of on-demand single droplet injection.**

However, the triggering of droplet transit in the constriction often pushes more than one droplet and there is still a short relaxation time between the ON and the OFF state.

We correlate that with observations made at the inlet number 2: Inlet has a large surface (Figure 33) compared to their height ( $H=20\mu\text{m}$ ), the inlet acts like a reservoir (or a hydraulic condenser) that swells when we increase the pressure and elastically returns to its initial state after some time. This induces the observed relaxation time after the pressure pulse.

To overcome this problem, we recently designed new inlets and reduced the size of the tubing to minimize the area of the “hydraulic condenser”. We are currently optimizing the on-demand single injection by adjusting the hydraulic resistance and the pressure pulse intensity and duration.

### **2.3.3.3 *Passive merging***

For the coalescence of the droplets, we made the choice of a passive chemical method. In this technique, the chip fabrication is much cheaper and simple than

electrocoalescence, as described for e.g. in (Chabert, Dorfman, and Viovy 2005). It is also specifically suitable in our case because we need to change the surfactant used to generate the picoliter droplets (Krytox 157 FSH) to the one used in with the nanoliter droplets (1H,1H,2H,2H-perfluoro-1-decanol, PFD). The PFD gives to PBS/FC40 interface an IFT at 11mN.m, and allows the generation of long, stable pancake/cylindrical shaped droplets of volumes between 50nL to 1 $\mu$ L. As another advantage in our specific application, it does not prevent coalescence of two droplets brought in contact as strongly as, e.g. Krytox or Picosurf.

Thereby, we inject a droplet containing the cell (4pL) and stabilized by the Krytox in the main channel containing 50nL droplets stabilized by PFD. When the two droplets enter in contact, they coalesce without external activation (see Figure 37). Indeed, the oil at 10% Krytox is diluted by a factor 50 in the oil of the main channel with 1% PFD. Thus, the stabilization given by the Krytox and needed for the close-packing is relieved by dilution to allow the droplets merging.

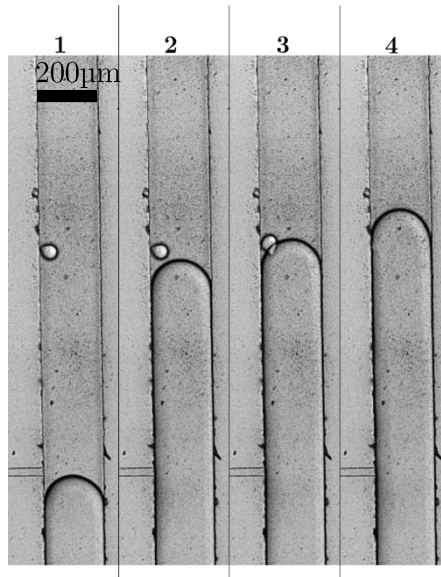


**Figure 37: Merging of 4pL droplet to 50nL droplet by a passive method using a destabilizing surfactant**

Once the merging achieved, the confined droplet passing in front of the spacing channel (from position 1 to position 2 in Figure 38) increases the hydraulic resistance and so the pressure  $P_c$  (Baroud, Gallaire, and Dangla 2010). This affects the droplets arrangement (close-packed in the direction of the blue arrow) and can even push them in the opposite direction because of the spacing oil (red arrows) if the pressure  $P_c$  became too high. Figure 39 shows a deformation of the confined droplet after few

hundreds of milliseconds due to these pressures issues. To overcome this limitation, we are planning in a future design to by-pass the front and back of the confined droplets by a tiny lateral channel along the main one or by de-confining the droplets after their merging.

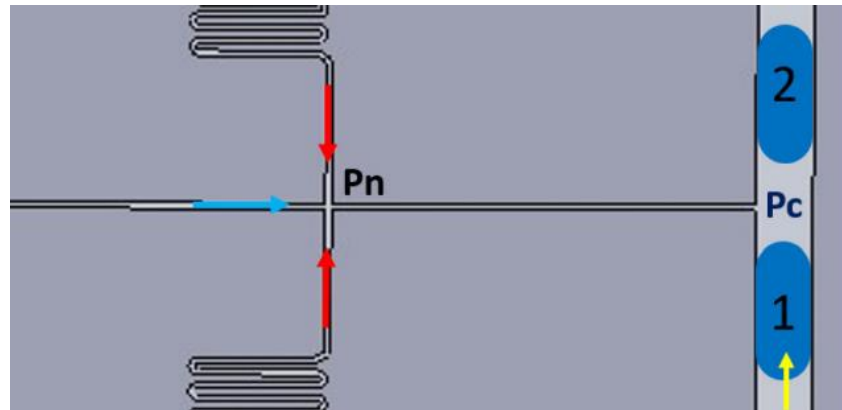


Figure 38: Schematic view of pressures during confined droplets flowing and merging.

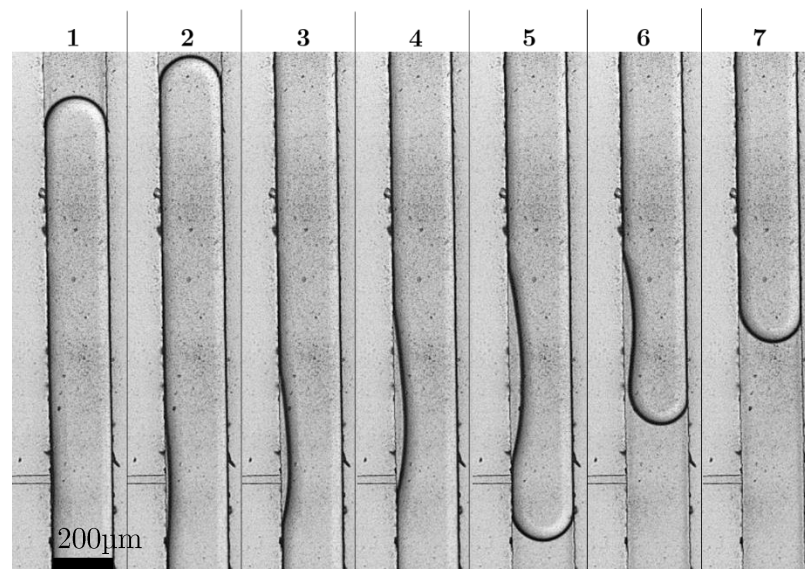


Figure 39: Visualization of confined droplet closing the injection channel. These pictures are the following of Figure 38.

### 2.3.4 Conclusion and perspectives

This second project consists in integrating several operations to control the collection, the storage of droplets encapsulating single cells and their merging with

reagents droplets. We decompose these operations and developed a dedicated chip or area of a chip to each operation.

We manage to successfully collect the droplets of 4pL, store the close-pack, inject and merge them with droplets of 50nL. We are currently optimizing the “on-demand” approach and the pressure feedback after merging, to reach a continuous merging of droplets containing single-cells with droplets containing reagents for downstream analysis.



---

## *2.4 Conclusion on single-cell encapsulation and preparation*

We demonstrated in this chapter the potential of our single cell encapsulation device and highlighted some of the mechanisms underlying the control of droplet formation in this type of microfluidic approach. A better understanding of the approach has allowed us to exchange the continuous phase and to work with fluorinated oil. Furthermore, we developed new tools for the collection of droplets containing the cells and their individual injection and merging with reagents as an essential step of preparation for analysis of their content.

This work fits in a more general frame drawn during this thesis, consisting in the development of a microfluidic droplet platform for single cell analysis. In particular, we will see in the next chapter how can we use droplets such the ones prepared in the devices discussed previously, to analysis the expression level of some genes of interest down to single cell level.



### ***3. Drop qPCR***

This chapter reports on the development of a droplet microfluidic device allowing the quantification of nucleic acids of cells by quantitative Polymerase Chain Reaction qPCR. This system represents one possible analysis module of our platform for single cell analysis.

By the nature of the assay used (qPCR) and its applications, the project described here consists in topic closer to everyday life applications of microfluidic technologies. It involves physics (optics, thermic), soft matter physics and engineering for the fabrication of the device, and molecular biology for data analysis, experimental design and results discussion.

Thus, this project requires multidisciplinary skills and brings many people to work together: The project was initiated by Davide Ferraro. He designed the machine, developed the setup, performed several experiments and supervised the project. Lauriane Geremie worked during her 6 months' master 2 internship on this topic. Macro Serra developed a first Labview version of the data analysis program and helped for the experiments and discussions. Renaud Renault helped on the development of the optical setup, and Ivan Ferrante helped on the micro-milling. I developed the Matlab script for data analysis, performed all the experiments presented in the two results sections below, and improved mechanical and optical aspects of the setup.

We will start this chapter by an introduction about PCR and qPCR technologies. Then, we will describe the device components, the reagents used and the data analysis program. Later, we will show and discuss the results validating the proof of concept and optimization of the device performances before concluding and given the perspectives of use for this analysis module.

### 3.1 Introduction

#### 3.1.1 Polymerase Chain Reaction

Polymerase Chain Reaction, or PCR, is a major technique in molecular biology, used for nucleic acid amplification, identification and quantification. Since its invention in 1986 by Kary Mullis (Mullis et al. 1986), Nobel Prize 1993 in chemistry, it has become over the years the most used technique in molecular diagnosis as well as in research laboratories (see **Figure 40**). It allows direct detection of infectious pathogenic agent by enzymatic amplification of a subpart of this agent's genome. Human Immunodeficiency Virus (HIV), E-coli infections and other viral or bacterial pathogens and genetic mutations are routinely diagnosed by quantitative PCR for example. It has the advantage of working with very low quantities of material extracted from very different biological source (tissue, blood, urine...), generating thousands to millions of copies of a particular section of DNA from a very small initial amount and with a high specificity on the target. A strong main disadvantage of PCR is that the samples are prone to DNA contamination, demanding strict conditions of sample preparation to avoid this contamination. Furthermore, PCR remains expensive due to reagents and consumables price, which limits the number of markers that can be targeted for a reasonable price.

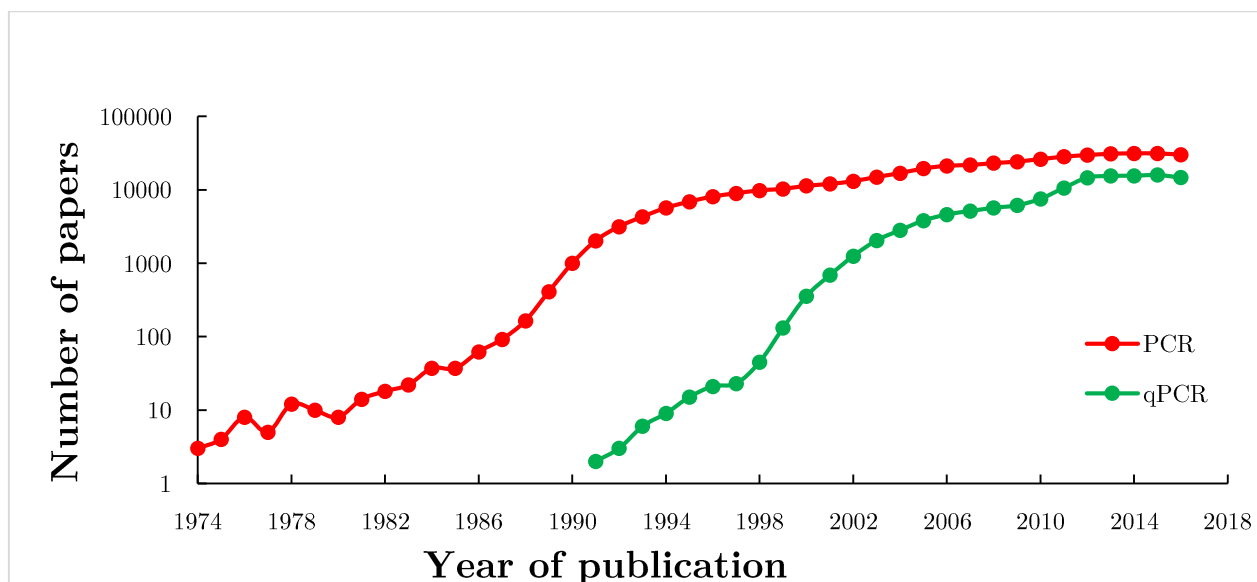


**Figure 40:** Number of articles in PubMed with date of publication between 1974 and 2016 discussing PCR technics in general (red) and specifically qPCR (green). This graph was generated using Medline trend: automated yearly statistics of PubMed results for any query, 2004 developed by Alexandru Dan Corlan.

### 3.1.1.1 Principle of PCR

PCR consists in a series of thermal cycles, each cycle composed of 3 steps described below and also detailed in **Figure 41** with a complementary schema:

1. Denaturation at 95°C: the increase in temperature breaks the hydrogen bonds of the double-stranded (ds) DNA at 95°C.
2. Annealing at 58°C: primers enabling the specific recognition of a targeted region bind to this region at 5' and 3' ends
3. Elongation at 62°C: the polymerase starts from the primers and synthetize the complementary strand on each single strand using dNTPs present in the solution.

Depending on the initial amount of DNA and on the target of the experiment, several cycles, 10 to 50 cycles, can be run for amplification and/or quantification.

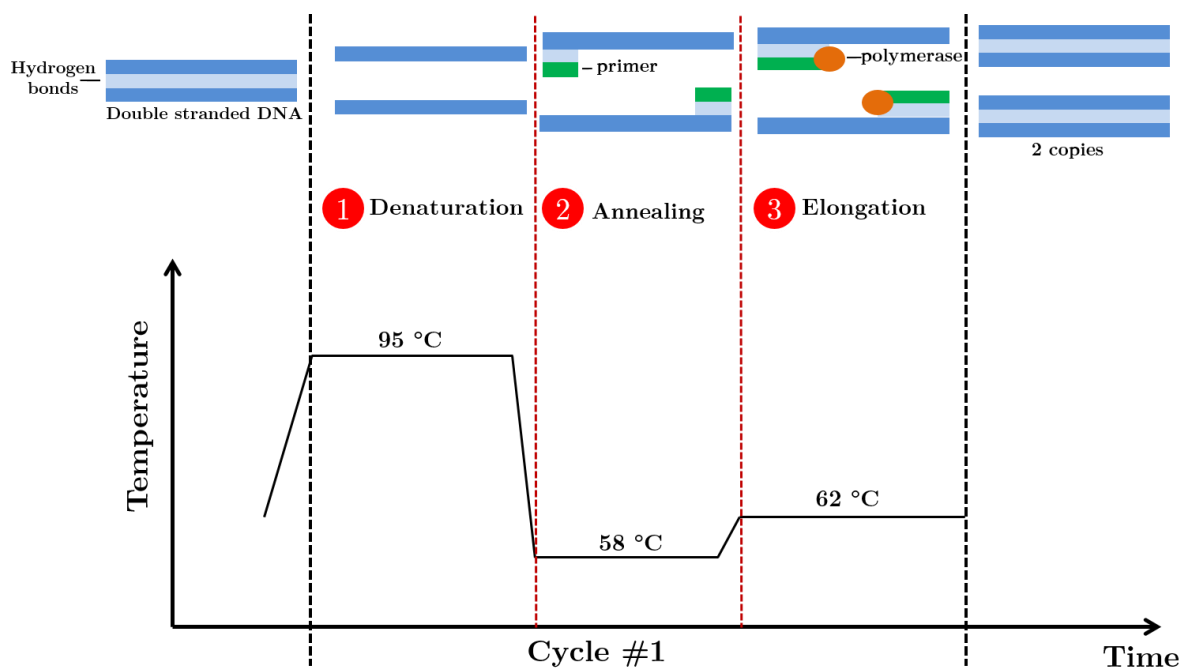


**Figure 41: Steps for one cycle of Polymerase Chain Reaction (PCR).**

The described reaction can be used directly as a quantification protocol, as discussed in the next section, allowing the detection of mutations or measurement of expression levels. It can also be used simply as method to amplify the amount of DNA needed for the next steps of a more complex protocol, for instance in the preparation of samples for Next Generation Sequencing.

---

### 3.1.1.2 *Quantitative PCR*

To quantify the amount of DNA amplified during the PCR, it is possible to measure the fluorescence intensity of a reporter binding to DNA and to correlate this value with the DNA quantity. Historically, there has been different ways to quantify DNA. **Endpoint PCR** consists in quantifying the PCR product after cycling by staining with Ethidium Bromide (EtBr), an intercalating agent of DNA, on agarose gel electrophoresis. This technique, however, does not allow quantitation of DNA, but only the presence of a target sequence above a threshold (often considered as a simple presence/absence answer). **Semi-quantitative PCR** consists in doing the same process but interrupting the thermal cycling at different time points to quantify the amplified DNA.

Nowadays, the appellation “**quantitative PCR**” or **qPCR** is most used for real-time follow-up of the reaction kinetics, also named **real-time PCR** or **rtPCR**. Practically, a fluorescent reporter is directly mixed with the PCR reagents from the beginning of the reaction, and a real-time imaging (in continuous or at each cycle) is performed during thermal cycling. Finally, **digital PCR** or **dPCR** consists in segmenting the sample in very small compartment (usually a few nanoliters) such as every compartment contains at most one molecule. **Digital droplet PCR** or **ddPCR** is a type of dPCR in which the compartmentalization is made in droplets. dPCR has emerged during the last decade as a promising technology for two reasons: First, it allows absolute quantification without the need for prior calibration; Second, it allows to reduce interference between targeted and other DNA molecules, notably other mutants, and increasing the specificity for distinguishing e.g. point mutations by typically two orders of magnitudes, e.g. from 1/100 to 1/ 10 000. This technique however, remains rather expensive and requires specific equipment.

### 3.1.1.3 Real-time PCR principle

We will use the term ‘qPCR’ for the rest of this manuscript, in the same meaning as ‘rtPCR’. We develop in this section the principle of real time monitoring of PCR kinetics by the example of the first setup used for this purpose. Higuchi et al. were the firsts to relate, in 1993, a system to perform real-time PCR. **Figure 42**, shows their experimental setup. A UV lamp at 302nm, is used to excite the samples stained with Ethidium Bromide and positioned on a thermal cycler. CCD camera mounted with an adapted filter and lens record on real-time the fluorescence of the samples.

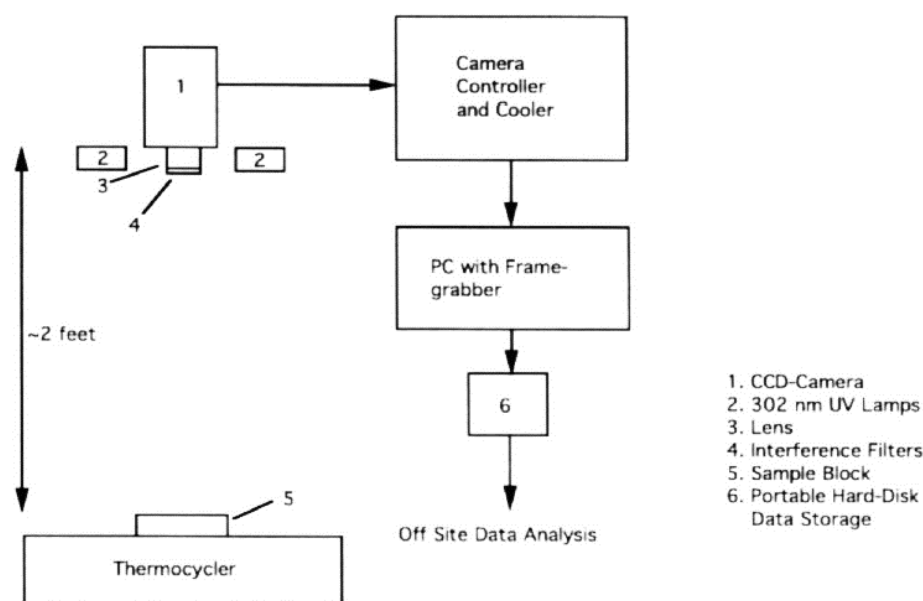


**Figure 42:** First experimental setup of real-time PCR (qPCR) from (Higuchi et al. 1993). UV lamps (2) illuminate the samples placed in the thermal cycler (5). Reflected light is collected by the CCD camera (1) through the filters (4) and lens (3). A computer controls the image acquisition and storage on a hard-disk. Data analysis are performed off site.

A typical qPCR curve is presented on **Figure 43**. During the first cycles (1) the signal is only given by the auto-fluorescence of the solution and the amplified amplicons are not yet detectable by the camera. After few cycles, (2) the signal starts to exponentially increase and we can directly link the fluorescence measurement to the amount of DNA. (3) Linear phase: the polymerase becomes the limiting factor of the reaction, its quantity becomes insufficient as compared to the DNA that has to be amplified to keep the initial rate of DNA replication (4) Plateau phase: other limiting factors, such as dNTP, fluorophores, degradation of the polymerase, etc. can dampen the reaction and stop the increase in fluorescence intensity.



## qPCR amplification curve

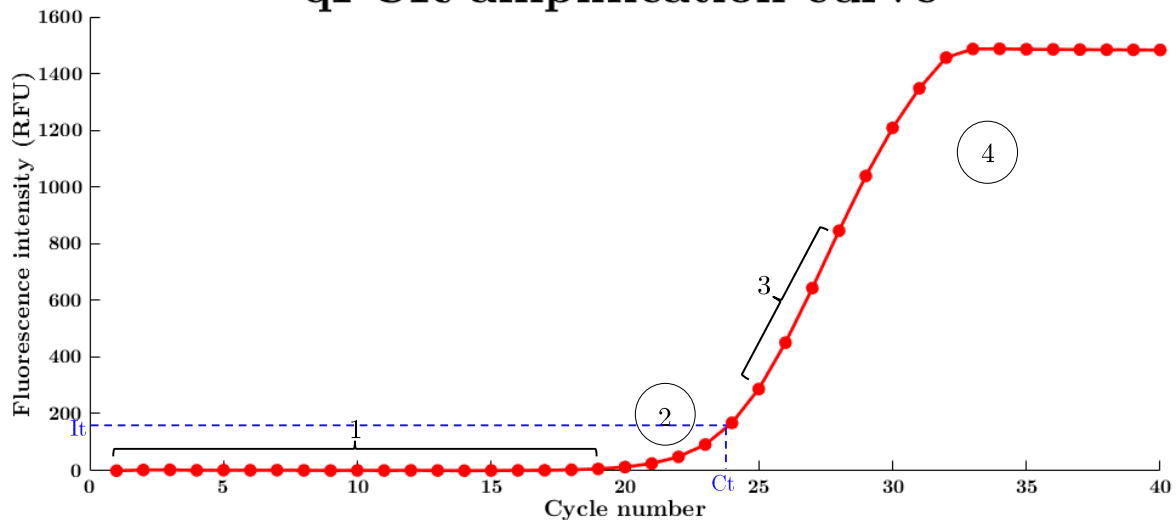


**Figure 43: Example of qPCR amplification curve: Fluorescence intensity as function of cycle number.**

By setting a threshold of intensity in the range of the exponential phase (2), it is possible to compare different amplification curves by comparing the number of cycles corresponding to the threshold (named Cycle Threshold or Ct). Indeed, the intensity is proportional to a DNA mass or copy number, when using respectively, nucleic acids stains or Taqman probes, described below. A serial dilution of a known quantity allows the calibration of a linear relation between DNA quantity and Ct values. Then, the quantification of any known sample is possible by relating to the calibration curve. Furthermore, preceding a qPCR by a **reverse transcriptase** (called **RT-qPCR**) to convert single strands of RNA into complementary DNA, allows the quantification of the initial RNA. This provides access to the expression level of a certain gene.

### **3.1.1.4 Chemistry for real-time PCR**

Two types of chemistry can be used to report amplified DNA during qPCR, nucleic acid stains or fluorescent probes (Navarro et al. 2015). We detail in the following their principle and focus on the probes in the Taqman probes technology, since this is the most used nowadays.

Nucleic acid stains: Ethidium Bromide was initially used as the first reporter, but it was quickly replaced by SYBR Green I, more sensitive and less toxic. SG binds to dsDNA and absorbs blue light 497nm and emits green light at 520nm. It can also bind to ssDNA or RNA with less performance. The main advantage of this type of staining is its cost, as it is much cheaper than probes. Nevertheless, it is not specific to the

targeted sequence and can thus bind to any nonspecific PCR product (e.g. primers dimer).

Fluorescent probes: Taqman probes were developed by the Cetus corporation, first using radioactive probes (Holland et al. 1991) before moving to fluorescent labeling. The technology made a revolution in the field and was later on bought and widely commercialized by Roche Molecular diagnosis. The probe consists in a fluorescently labelled oligonucleotide sequence, complementary to a sequence of the target downstream of one of the primers. A fluorescent reporter molecule is attached to the 5' end of the sequence and a quencher is attached at the 3' end. Therefore, in the absence of target the fluorescence of the reporter is quenched. During PCR, the probe binds to its complementary sequence in the annealing phase, and is cleaved by the polymerase (chosen to have an exonuclease activity) during the elongation phase. The reporter fluorophore is released and there is no quenching effect anymore. Therefore, in contrast to nucleic acid stains, the probes introduce an additional specificity to that of the primers. Second, probes fluorescing at different wavelengths can be used in the same run, allowing for multiplexed amplification and detection in a single run. Their disadvantages are for sure the cost and the time of engineering to design the adequate sequences.

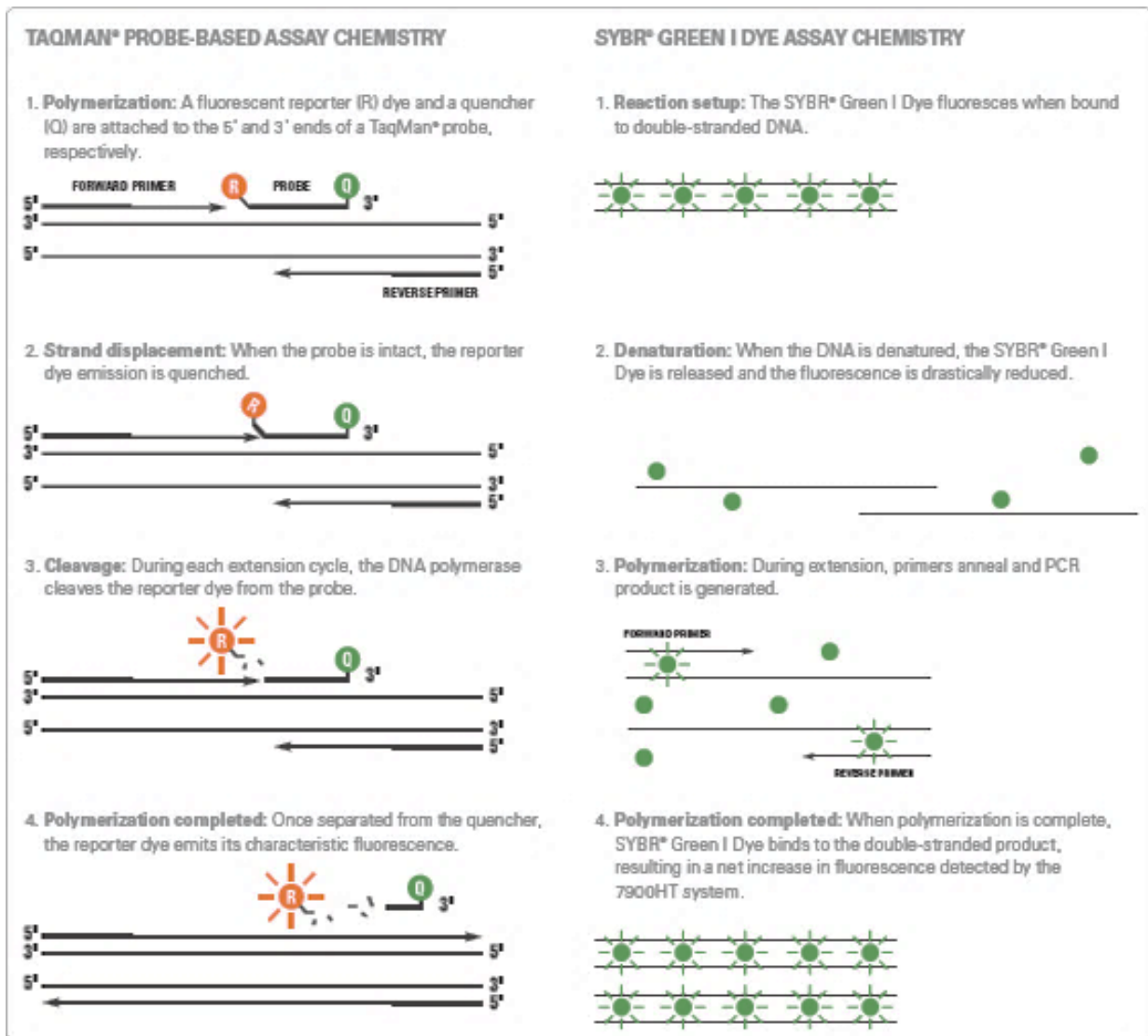


Figure 44: The two types of chemistry for qPCR. Extracted from: <https://www.thermofisher.com/us/en/home/life-science/pcr/real-time-pcr/real-time-pcr-learning-center/real-time-pcr-basics/taqman-vs-sybr-chemistry-real-time-pcr.html>

### *3.1.2 qPCR in microfluidics*

#### *3.1.2.1 Miniaturized devices*

There is an obviously need for miniaturization of PCR assays. Indeed, both cost and sensitivity can tremendously be improved by reducing the reaction volume. For these reasons, a lot of efforts have been invested from the beginning of microfluidics to miniaturize PCR and qPCR assays by manipulation tiny volumes of reagents and cell contents. These two assays are naturally linked for their development and standardization, as qPCR is the extension of PCR to the quantitative/kinetic area of chemistry, mostly thanks to the advances in fluorescents reporters' chemistry and optical detection tools made in the last decades. We will describe in the next sections the combined story of miniaturization of PCR and qPCR, jumping from one to the other depending on the context of scientific production and technological advancements of the topic. We discriminate between:

- Conventional PCR, with a reaction volume equal or higher than 10 $\mu$ L. This is in general performed in polypropylene microtubes or well-plates.
- Microfluidic PCR, with a reaction volume lower than 10 $\mu$ L. It can be performed either in monophasic systems in e.g. microchambers, or in biphasic systems where reactions are performed in droplets.

To miniaturize PCR/qPCR assays, different engineering questions are raised:

- Contamination: How to separate samples and manipulate them? How to avoid contaminations between samples? What surface treatment can be used?
- Heating: How do we heat the samples? What materials should we use for heating? How to avoid evaporation of small volumes?
- Fluorescent detection: What type of light source to use? How to identify a fluorescent signal coming from tiny volumes? How to follow this signal over cycles? What sensors to use for reading emitted signal?

We made the choice, for the next sections, to classify the described devices following the criterion used in (Ahrberg, Manz, and Chung 2016) who introduce, respectively **Space domain PCR** vs **Time domain PCR**, for static samples vs samples moving in continuous-flow. Moreover, within the discussion we include the originality of some optical detection methods (qPCR), and we focus on the heating aspect relatively to a static or a moving sample. Indeed, this aspect can significantly affect the engineering of the others.

---

### 3.1.2.2 *Static sample PCR*

We group in this section several types of technologies that may seem different but have the common point of performing thermal cycling with a sample held on a fixed substrate that changes temperature periodically.

Miniaturization of PCR or qPCR assays can present several advantages. Indeed, smaller volume can provide better thermal control, better signal/noise ratio and lower reagents consumption. Thereby, the firsts examples showing microfluidic PCR devices appeared around 1998 (Daniel et al. 1998). These authors described a silicon device made of a reaction chamber of about 1 $\mu$ L. Platinum heaters and sensors are placed underside the chamber and control the temperature through Labview software. Fast heating and cooling properties were shown but no PCR was demonstrated.

The group of Quake reported in 2006 a PDMS micro-device with a capacity of 8 parallel samples each one divided in nine 450-pL chambers for RT-PCR reaction (Marcus, Anderson, and Quake 2006). The fluidic control was insured by an upper channels layer of “Quake valves”. For heating, the chip was simply placed on a flat plate thermal cycler and probed for fluorescence with a commercial microarray reader at the end of the experiment. This technology led to the creation of Fluidigm company, that commercialize also other aspects of Quakes’ group work. (Bontoux et al. 2008) used a similar approach and (Mary et al. 2011) integrated it in droplets and continuously recorded fluorescence at each cycle to generate qPCR amplification curves. In 2011 (White et al. 2011) reported the development of a PDMS device based on the same ideas as the Quake group. They used a prototype from Fluidigm for heating and detection with further improvements on single-cell manipulation. Figure 45 shows the different steps in chambers for cell capture, washing and lysis (either by heating at 85°C or chemically). An RT mix is loaded or the RT can be performed on one step with the qPCR. The main disadvantage of this device is the waiting time for mixing by diffusion that takes 40 min before starting the RT-qPCR. Later, PCR is performed in a conventional machine cycling time. This device represents a big advancement in the field of single-cell RT-qPCR. To our knowledge, it was the first time that all these steps were integrated in one single device. The same group of Hansen presented recently (VanInsberghe et al. 2018) a new version of the device more robust and with a higher parallelization. Nevertheless, this type of approach is more dedicated to fundamental studies such as single-cell heterogeneity and still lacks sensitivity as shown in Figure

46. Furthermore, it is indicated for parallel processing of samples and it is expensive because of complicated soft-lithography fabrication plus single use of the devices.

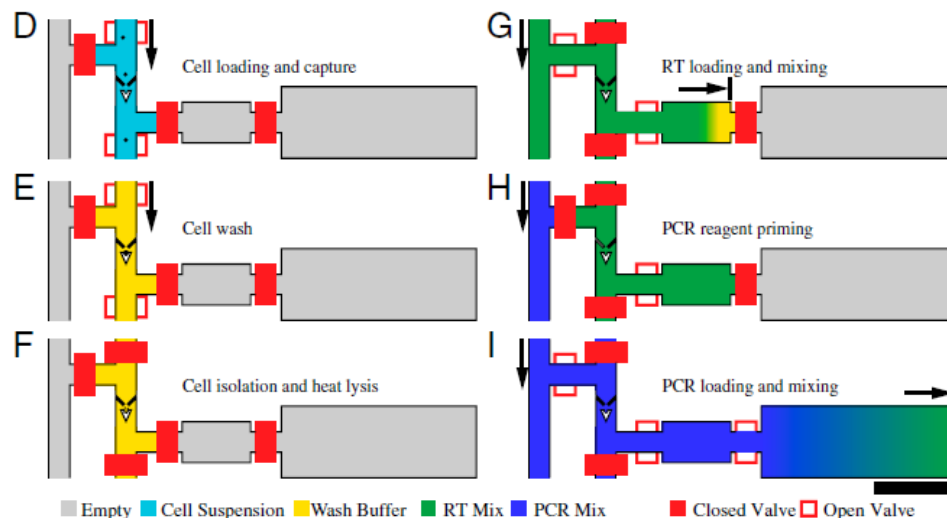


**Figure 45:** Representation of the device during injections steps extracted from (White et al. 2011). D. the valves are opened for cell loading. E. the captured cell is washed. F. the chamber is close and heated at 85°C for 7min to lyse the cell. G. The valves are opened to load the RT reagents. RT is performed by thermal cycling for 2.5h. H. The PCR reagents are loaded in the main channel. I. The valves are opened for PCR loading and mixing. The mixing time by diffusion 40min before starting PCR thermal cycling. The scale bar in the bottom right is 400µm.

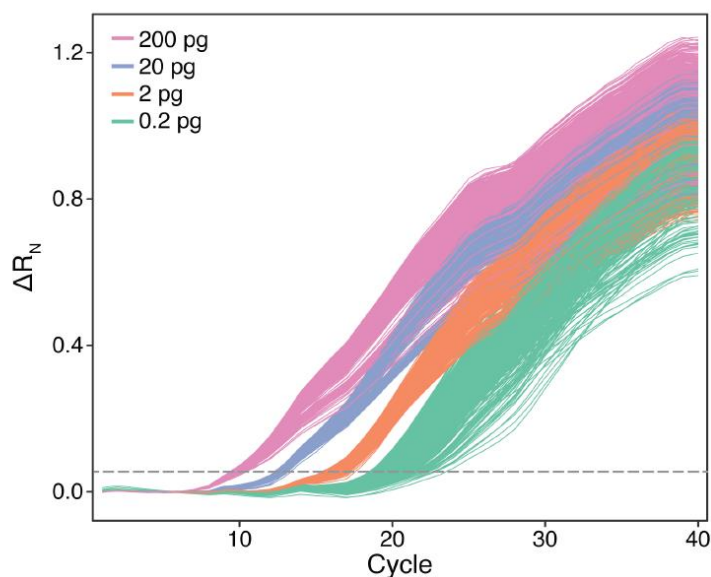


**Figure 46:** Extracted from (VanInsberghe et al. 2018). The figure shows amplification curves for 10× dilution series of purified total K562 RNA. The dashed line is the threshold intensity for Ct values. We can notice a significant increase of Ct values variability with the decrease in concentration.

---

Another very original approach was described by (Y. Zhu et al. 2015). They developed a device for printing nanoliter to picoliter droplet on a silicon microchip containing hydrophilic spots to position the drops and covered with mineral oil. This technic allows a significant reduction in volume consumption, as the final reaction volume is 50nL. The sample processing is similar to previous ones, as the whole chip is placed on a flat thermal cycler performing a parallel run for all the samples.

### 3.1.2.3 Continuous-flow PCR

Continuous-flow PCR started with the pioneering work of (Nakano et al. 1994). To our knowledge, it is the first time that a continuous flow PCR was performed. Figure 47 shows the experimental setup. The device is composed of a Teflon capillary (ID 0.5mm) rolled in spiral for 30 cycles. During each cycle, the capillary passes through three oil baths regulated at 94°C, 55°C and 72°C for PCR thermal cycling. A 50µL sample is flown between two 5µL air bubbles inside this tubing thanks to a syringe pump, and collected at the outlet for quantification on agarose gel.

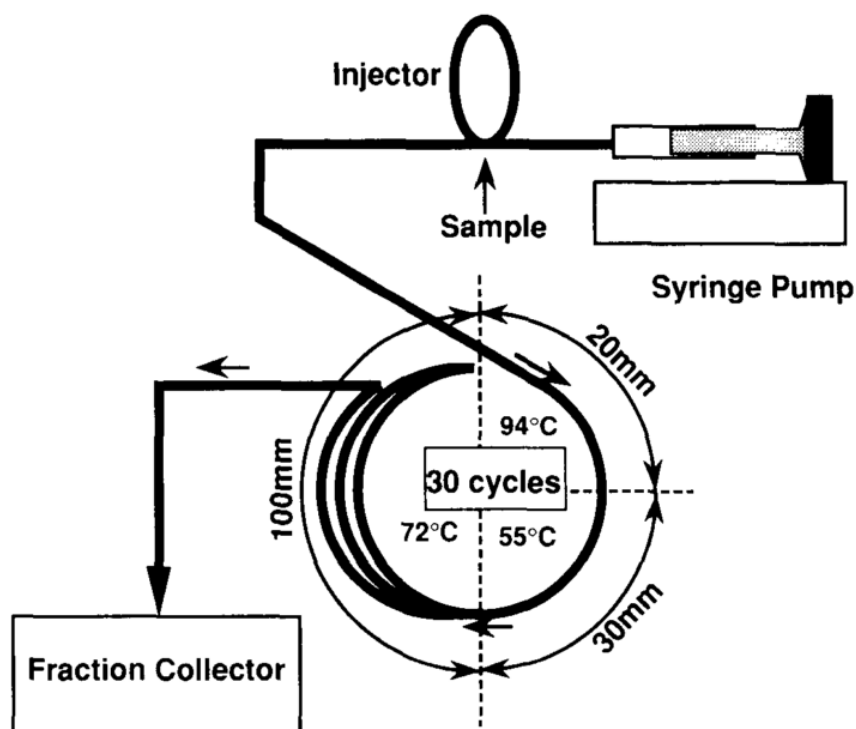


**Figure 47: Schema of the first continuous flow PCR device extracted from** (Nakano et al. 1994). The same principle was later used by (Kopp, De Mello, and Manz 1998), with 10µL sample volumes separated by a washing buffer 8µL passing through silanized glass capillary on copper heating blocks. It was then followed by (Curcio and Roeraade 2003), who were to our knowledge the first to implement PCR in water-in-oil droplet microfluidics format. They used 300nL droplet sample carried in fluorocarbon or hydrocarbon oils with water baths for thermal cycling. Within our group, (Dorfman et al. 2005) and (Chabert et al. 2006) optimized this principle and integrated it within a contamination-free droplet platform with automated pipetting and end-point detection of the PCR product. More recently, (Hayes and Dalton 2015) reported a qPCR version of this concept coupled with liquid-bridge technic for reagents and sample mixing. The most interesting parts are the excitation and detection. They are achieved thanks to a



matrix of 280 fibers aligned with LED source for illumination and three high resolution CCD camera for fluorescence reading (see Figure 48), thus reaching a very good signal-to-noise ratio. However, this type of optics is quiet complex to integrate and very expensive, due to the cost of using few hundreds of fibers and three CCD cameras.

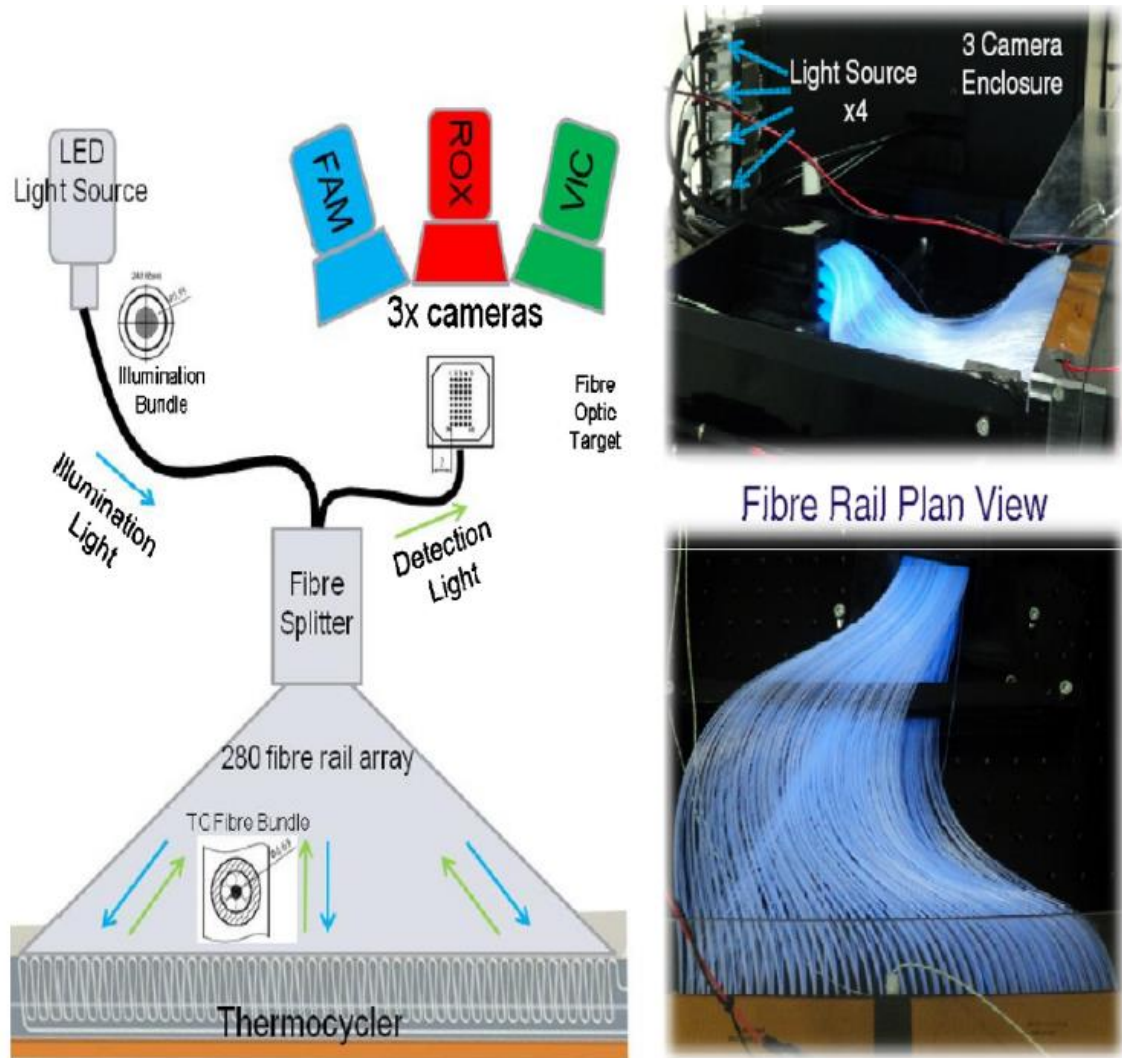


Figure 48: Representation of a qPCR device developed by Hayes & Dalton, 2015. On the left side, a schematic representation of the optics of the device. LED light source provides excitation to the samples through the fiber splitter and the 280 fibers. The emitted light from the sample is also passing by these fibers to reach the 3 detection CCD camera for each color channel. On the right top picture of the setup showing light sources. On the bottom right, a picture of the fiber rail.

### ***3.1.3 Microfluidic PCR commercial devices***

Several PCR systems based on microfluidics have been developed during the last decade, but most of them use microfluidics only for sample preparation or cell isolation. To our knowledge none of these systems propose a qPCR in microfluidic format. For example, the Fluidigm C1 is dedicated to single-cell isolation and preparation for sequencing, qPCR or other types of analysis but the qPCR is performed off chip. Roche also developed the cobas® Liat PCR system which propose integrated PCR with preloaded reagents on a cartridge for 3 different assays DNA or RNA based in 20 minutes but no qPCR. In commercial ddPCR devices, microfluidics is in general used for encapsulation, and detection is done in a separate instrument. More details about microfluidic-based PCR commercial systems can be found in the review of Ahrberg, Manz, and Chung 2016. We hope that the approach reported in this chapter will help to improve the current offers available in this market.

### ***3.1.5 Aims of the project***

From this overview of literature on microfluidic PCR devices, we aimed in this project to develop an RT-qPCR platform in continuous-flow with the following characteristics:

- Easy and low-cost fabrication of both thermic and optical parts: to afford an accessible and potentially portable device that can significantly reduce the mean cost of a qPCR analysis.
- Automated and on-demand processing of samples: to be easily integrated in analytical platforms such as in hospitals where samples can arrive at any time and need to be treated rapidly.
- Lower processing time: benefit from the advantages of microfluidics to decrease the processing time (typically 30 cycles in less than 10 minutes).
- Strongly reduce operation cost: thanks to a drastic reduction of reagents per assay.

We will see in the next section how we implement our device and how we tried to tackle each one of these criteria, first by a comparison with a conventional qPCR system and second improving the performances of the developed device.

---

## 3.2 *Material & methods*

### 3.2.1 *Genes, cells & Master Mix*

To show a first proof of concept for our device, we compared RNA expression level of two genes:

- Actin beta (ACTB) gene encoding one of the isoforms of actin. This protein is highly expressed in human cells and involved in cell integrity, motility and structure. The ACTB gene is a housekeeping gene, widely used as reference for RNA expression level as it is highly expressed in most of human tissues.
- HER2 or ERB2 gene encoding a member of the Epithelial Growth Factor (EGF) receptor family of receptor tyrosine kinases. HER2 is overexpressed in ~30% of invasive breast cancer carcinomas. HER2+ breast cancers are known to be the more aggressive and metastatic ones. They are nowadays treated with a HE2-targeted therapy using a monoclonal antibody.

We choose for this purpose two human cell lines:

- SK-BR-3 [SKBR3] (ATCC® HTB-30™) is a human breast adenocarcinoma cell line. It is commonly used as a reference for its high expression level of HER2 gene.
- MCF7 (ATCC® HTB-22™) is a human breast adenocarcinoma cell line. It is particularly studied as it presents progesterone receptor positive and HER2 negative characteristics.

ACTB is our gene of reference (housekeeping gene) and HER2 the gene of interest. SKBR3 is chosen as the cell line of high HER2 expression, and MCF7 the reference.

We used silica-membrane spin columns method (RNeasy Mini Kit by Qiagen) for RNA extraction from the two cell lines. We quantified the extracted RNA using fluorescent labeling and fluorometer (Qubit® RNA HS Assay Kits and Qubit3.0 from Life technologies).

As RT-qPCR master mix, we used CellsDirect™ One-Step qRT-PCR Kit (11753100 – Thermofischer Scientific). This kit contains a one-step enzyme mix including both SuperScript® III Reverse Transcriptase and Platinum® Taq DNA Polymerase. It allows to perform both RT and PCR reactions one after the other without manipulations in between. We also add Anchored Oligo(dT)20 Primer (12577011–Thermofischer Scientific) for more efficient cDNA synthesis. We used Taqman probes technology as report for DNA amplification during PCR. Design of the primers and the probe are

given the Appendix with the corresponding targeted sequences. The volumes and concentrations of each reagent were adapted depending on the experiment (tube versus droplet). Details are given in Table 5. We can highlight that the only change in concentration concern buffer and water (they were changed only for the ease of pipetting), and the probe, whose concentration was increased to be able to detect the droplets before the exponential phase.

**Table 5: Comparison between compositions of the PCR Master Mix+sample in tube for SmartCycler and droplet in our device. Left side are volumes. Right side are volume concentrations  $V_i/V_t$ , where  $V_i$  is the volume of the reagent and  $V_t$  the total volume.**

	In tube $\mu L$	In drop $nL$	In tube $V_i/V_t$	In drop $V_i/V_t$
2x mix buffer	12.5	60	0.5	0.3
Anchored Oligo (dT)	1	8	0.04	0.04
Primers F 10 $\mu M$	1	8	0.04	0.04
Primers R 10 $\mu M$	1	8	0.04	0.04
FAM probe 10 $\mu M$	0.5	8	0.02	0.04
Enzymes	1	8	0.04	0.04
RNA + Water	8	100	0.32	0.5
<i>Total volume (<math>V_t</math>)</i>	<i>25</i>	<i>200</i>		

### 3.2.2 Fluidic tools

We choose to generate droplet through a pipetting robot (Compact Positioning System rotAXYS) combined with a low-pressure syringe-pump from Cetoni mounted with a glass syringe of 250 $\mu L$  from SGE (509477 from Sigma-Aldrich). The syringe is connected to a PTFE tubing (I.D.  $\times$  O.D. 0.3 mm  $\times$  0.6 mm Bohlender<sup>TM</sup>) through a Luer lock (A7427 Sigma-Aldrich) and a flexible Silicone tubing (Fisherbrand Translucent Platinum-Cured Silicone Tubing by Fischer scientific). The user writes a script to control the movement of the pipetting robot and of the syringe-pump. It specifies flowrates of aspiration and positions of oil, samples, RT-qPCR mix, DEPC water, and calibration solution in a well-plate (Abgene 384-well PCR plate from Thermofischer AB1384Y). The syringe and the tube are full of fluorinated oil (Fluorinert<sup>TM</sup> FC-40, F9755, from Sigma-Aldrich), with a thermal conductivity of 65mW/mK, and aspirate a specified volume of aqueous solutions to generate water-in-oil droplets.

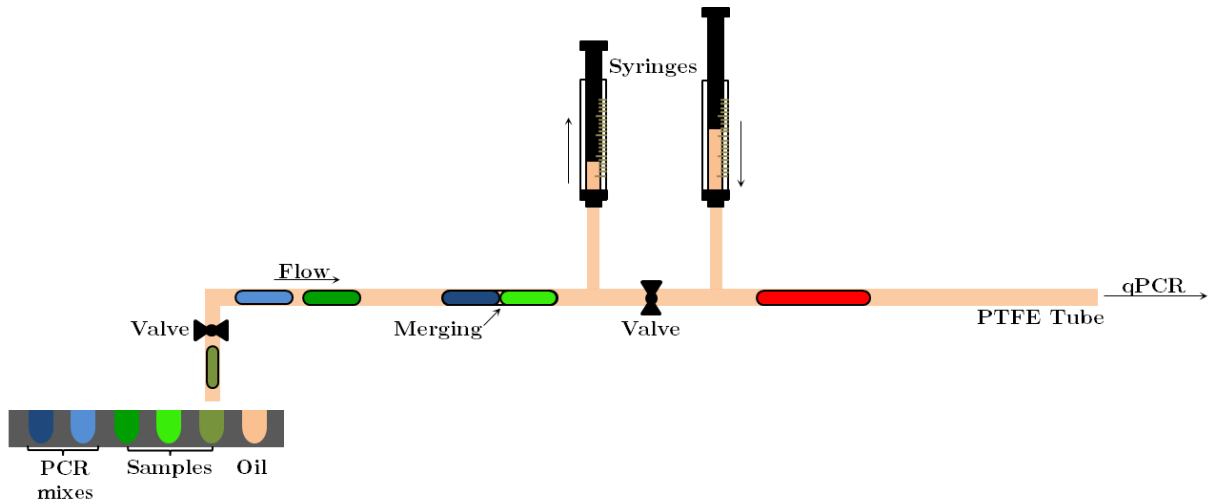


Figure 49: Fluidic setup for droplet generation and merging.

The protocol starts by pipetting successively a droplet of RNA (100nL), 50nL of oil to avoid contamination of RNA in the mix well, and a droplet of RT-qPCR mix (100nL). The two droplets are confined in the tube and they merge passively during their displacement. The difference between interfacial tensions of each solution and the oil, induces a difference in their linear speed inside the tube. By placing the fastest one (mix droplet) after the slowest (RNA droplet), they end-up merging after few millimeters. This effect was recently described by our team and is more detailed in (Ferraro et al. 2018). Following the pipetting program, the robot generates a train of droplets in a defined sequence. e.g. for the RNA experiments described in the next section: 2 Negative Controls (NC)+ 7\*[triplicate of [concentration i] + NC] + 5 calibration droplets. Calibration droplets are placed at the end of the train of droplets generated as described above, to avoid coalescence with the samples. They contain fewer enzymes, have a higher surface tension and are thus slower than the sample droplets. When the droplet train is loaded, the tube is transferred to a second syringe of 2.5mL (509493 from Sigma-Aldrich) for injection of the train in the qPCR system or can be transfer thanks to valves as shown in Figure 49.

### 3.2.3 RT-qPCR machine

#### 3.2.3.1 Heating plates

As heating source, we choose a ceramic Peltier ThermoElectric Module (TEM) (CP2-127-06L, by Laird Technologies) instead of an electric resistance. TEM insures a better homogeneity over a large surface (62.00 x 62.00 mm<sup>2</sup> here). It is put in contact with a heat sink thanks to thermal paste (503-357, by RS Pro) to improve thermal conductivity. Fans ventilate the sink for faster thermal conduction. On the other side of the TEM, we placed a micro-milled brass piece, 40mm x 60mm, (CuZn39Pb2 from Grem, milled with Mini-Mill, by Minitech) to hold the capillary containing the droplets and to transfer the heat (thermal conductivity of brass 121W/m.K). A thermal sensor (PT100, 362-9799, by RS Pro) is placed at the center of the brass part and gives a feedback to the Proportional Integrative Derivative (PID) board controlling the TEM. Thermal paste insures also the contact between TEM, the brass and the PT100.

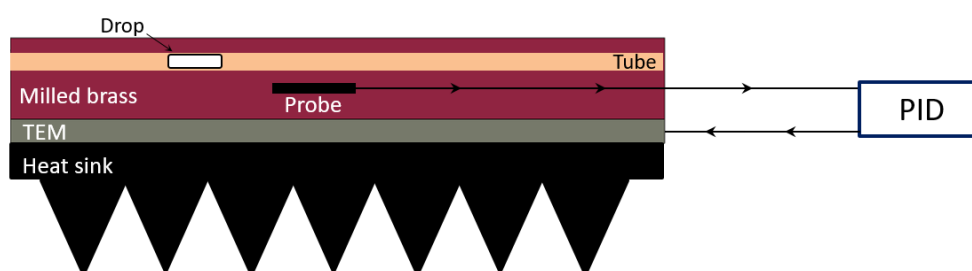


**Figure 50:** Schematic sectional representation of a heating plate. The milled brass holding the tube is heated by a Peltier ThermoElectric Module (TEM). Temperature of the brass is adjusted thanks to a PT100 probe giving the feedback loop to a PID controlling the TEM. A ventilated heat sink is placed on the other side of the TEM to improve heat convection and avoid TEM breaking by thermal stress. This easy engineered heating plate ensures homogeneous and reproducible thermalization of the drop traveling in the fluorinated oil filling the PTFE tube.

Contrary to static approaches, and as in other continuous-flow systems, the droplet containing the sample travels across heating areas maintained at different steady-state temperatures. In our system, one single PTFE tube is rolled in spiral inside two heating plates (Figure 50) facing each other and kept at constant temperatures (96°C for denaturation and 60°C for annealing-elongation). Polyimide adhesive tape with high thermal resistance (Kapton SCOTCH 92 33X19 by 3M) fix the tube in



1x1mm<sup>2</sup> micro-milled rail along the brass piece 40mm. A polyethylene foam (ref 61653480 by Leroy Merlin) is used to ensure thermal insulation between the two heating plates. It also guarantees a continuous tension on the tube spiral and avoids movements due to thermal stress. Finally, an ABS 3D printed structure is placed all around the device to minimize heat leaking. Thus, the droplet flowing inside the tube is alternatively subjected to thermal cycling (95°C -> 60°C) and fluorescent detection for 44 Cycles (**Figure 51**).

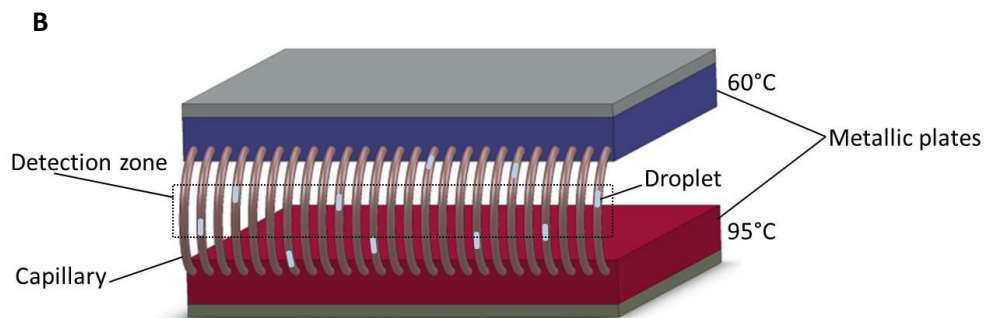
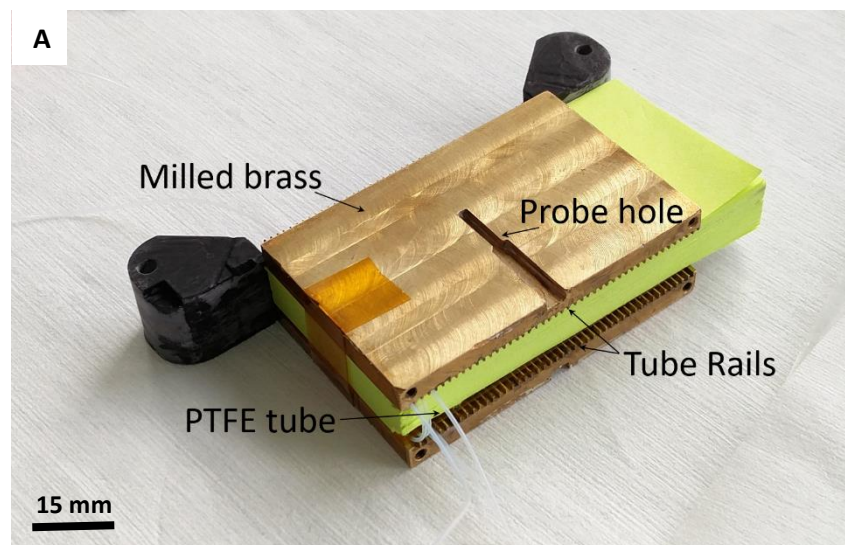
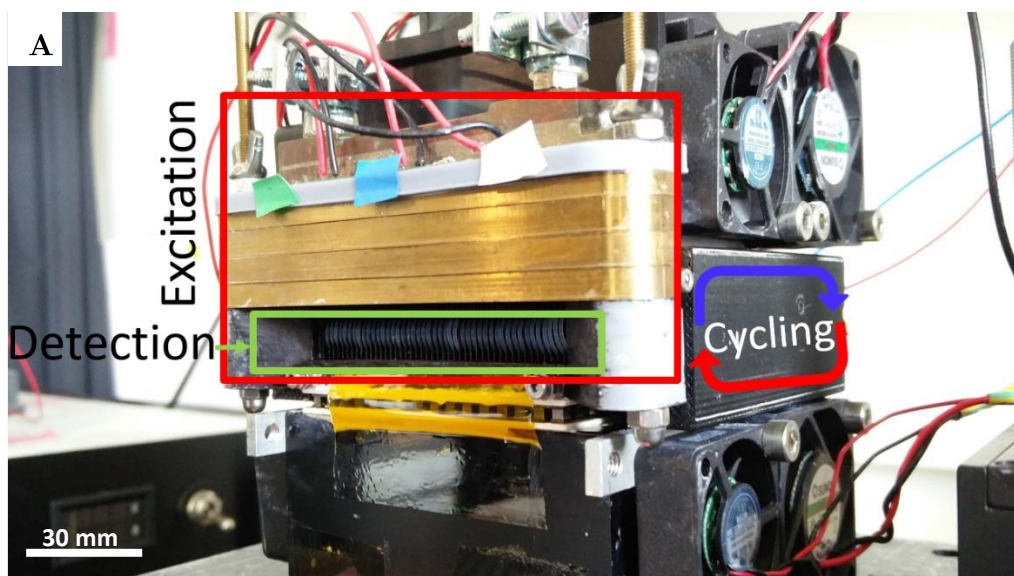


**Figure 51:** A. Picture of the qPCR module under construction. The two milled brass piece and the 3D printed optical holder (in black) are compacted together and adjusted in height with a pile of post-it papers. The PTFE tube is then inserted manually in each rail and through the windows of the optical holder for 44 cycles. B. Schematic 3D view of the assembled heating plates in the qPCR module. The droplets flowing inside the tube will be subjected to thermal cycling (95°C -> 60°C) in the thermalization zone and fluorescent reading in the detection zone.

### 3.2.3.2 Fluorescence measurement

As light source, we choose Light Emitting Diodes (LEDs). As compared to Argon-Laser or halogen lamp, it has a much lower cost and a longer lifetime. One disadvantage for LEDs in qPCR, is the need for several LEDs with different colors to perform multiplex screening in the same reaction tube. This can be compensated in our device by the high sensitivity of the fluorescence detection (lower Ct value) and lower sample consumption, allowing the splitting of the sample in several droplets to multiplex quantification.

Thereby, an array of 13 LEDs (465 nm, CP7P-GZHX-1, by OSRAM) disposed in a Printed Circuit Board (PCB) is used to excite the droplets. The high power needed by the LEDs creates heat dissipation by Joule effect. Thus, we overlaid the PCB by a water cooling system (18201 Bioblock Fischer Scientific). The light beams emitted by the LEDs are collimated by aspheric lenses (354140-A, by Thorlabs), followed by an excitation filter (485nm bandwidth=20nm, FF02-485/77-14 from Semrock). At last, the beams are converged by cylindrical lenses (LJ1598L1-A, by Thorlabs) (see Figure 52) before reaching the PTFE tube. A 3D printed piece is holding the tube in a narrow window at the exit of each “turn” in the heating device. The windows contain two perpendicular bars used to align the tube facing the excitation beam. They are also designed deep enough to protect the tube/droplets from cross-illumination between two neighboring turns (cycles).





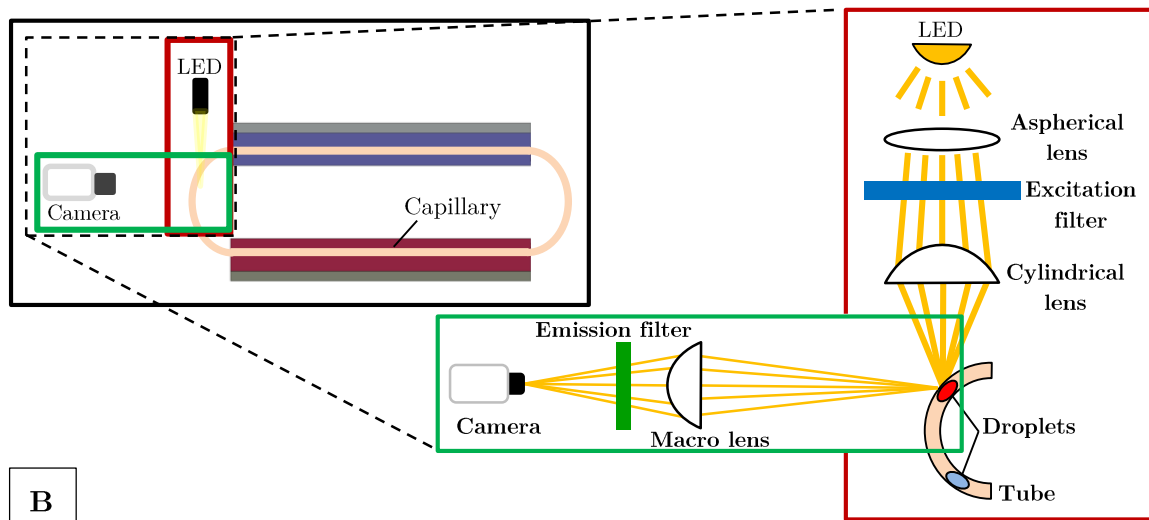


**Figure 52:** A. Picture of the assembled qPCR platform: thermic and optical part and their cooling systems. Highlighted, the cycling region detailed on Figure 51 and the excitation zone containing: LEDs, PCB, filter, and lenses. At the end the optical path, the light beam reaches the tube at each end of cycle rail in the rectangular detection region. B. Schematic side view of the device. Droplet samples travels in the PTFE tube filled with fluorinated oil and inserted inside milled brass heated by Peltier modules at cycling temperatures. After each cycle, the droplet is excited by a light beam at 485nm thanks to the lenses system and the excitation filter, then the emitted signal is collected by a CMOS camera placed in front of the device after going through a macro lens and an emission filter at 530nm. Collected images are further analyzed by a dedicated Matlab script.

After excitation, droplets emit a signal that is collected by a macro lens (Zoom 7000, Navitar) from all capillaries and passing through an emission filter (530nm bandwidth=43nm, MF530-43 Thorlabs) before reaching a CMOS camera (Basler ace ac2500-60um from Basler). Images are collected continuously (Figure 53), during the 44 cycles run, in TIFF format with a depth of 10-bit per pixel. Framerate and exposure time are tuned depending on flowrate and dyes concentrations.

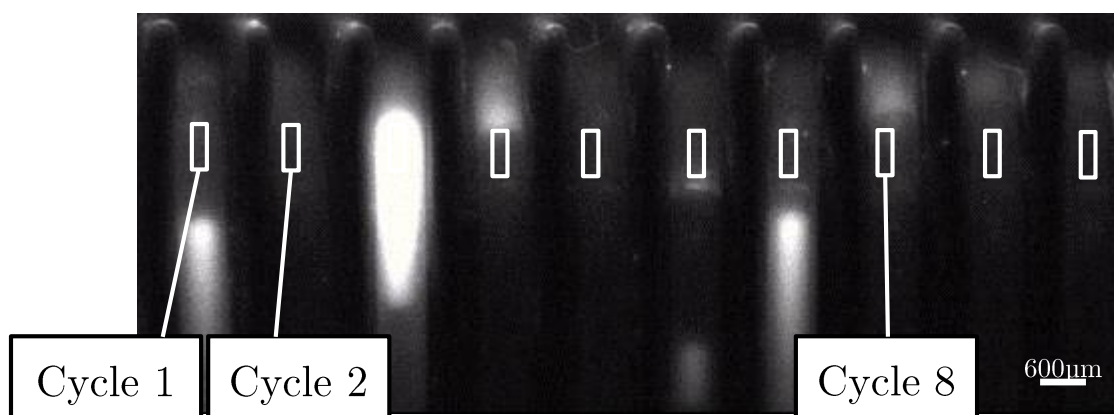


**Figure 53:** Grayscale image collected by the CMOS camera, cropped on the ten first cycles. White rectangles represent the regions of interest (ROI) in which fluorescence is measured after each cycle. The high intensity (white) in the third cycle is a droplet flowing in the PTFE tube through the third ROI position.

### 3.2.4 Data analysis

#### 3.2.4.1 Introduction: from pixels to diagnosis

We will describe in the next sections how we translate the series of frames of droplets flowing inside a PTFE tube, to a clinically relevant information. To do so, a first step is to extract the information of fluorescence intensity of each droplet at each cycle. Secondly, we calibrate the extracted signals and fit them to existing mathematical models of kinetics of polymerase chain reaction (Rutledge and Côté 2003). Finally, based on literature (Bustin 2009; Svec et al. 2015) we use methods of quantification to compare our results and extract the biological information.

#### 3.2.4.2 ROI & signal processing

We define 44 Regions Of Interest (ROI) in the collected images, centered on the tube to measure samples fluorescence at each cycle, as shown in Figure 53. A dedicated Matlab script, calculate the average value of each ROI ( $8 \times 8$  pixel<sup>2</sup>) on each image and stores these values in one single matrix. The matrix lines are time points and depend on framerate. The matrix columns correspond to ROIs, thus to cycle numbers.

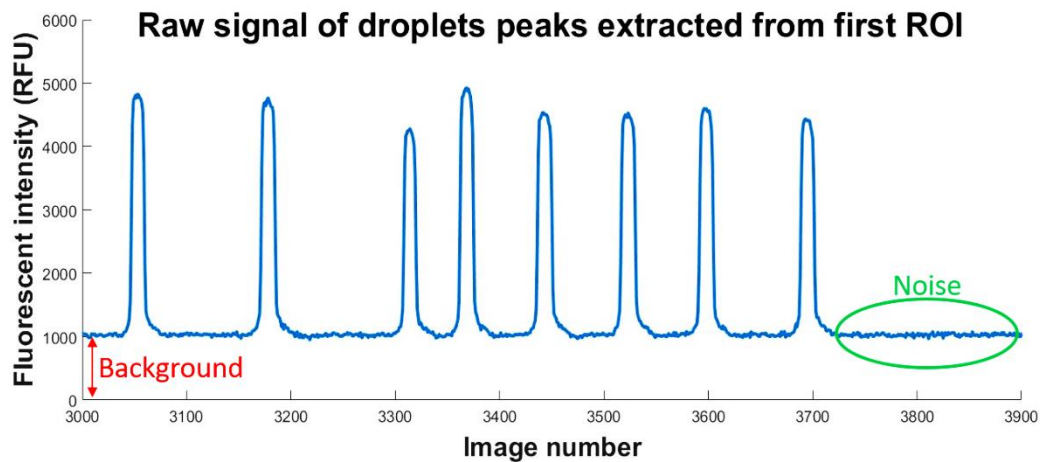


Figure 54: Raw signal extracted from ROI of the first cycle. Each peak is the transit of a droplet in the ROI. Different spacing of the droplets is used to differentiate between samples (two firsts peaks) and calibration droplets (six right peaks). We highlighted the background signal coming from the PTFE tube, and the electronic noise of the CMOS camera.

One ROI/column signal is presented in Figure 54, peaks correspond to droplets transit. A second script measures and subtracts the average background due to auto fluorescence of the PTFE tube. This value is different for each ROI because the excitation beam is not perfectly homogenous along the 60mm containing all cycles.

---

As shown in Figure 54, the fluorescence measurement is also perturbed by a small electronic noise due to the CMOS camera. We use a second script that smooths the signal by a moving average function. The window size  $W$  of this function is critical. It needs to be carefully adapted depending on the width of the peak, thus to the flowrate and the framerate of the camera. Overestimating  $W$  would flatten too much the peak, while underestimation leads to inefficient smoothing, thus noise persistence in the peak signal.

### ***3.2.4.3 Droplet peaks & normalization***

The script applies a function to find local maxima in each column. This corresponds to the maximum values of the peaks in Figure 54, and is considered as the measurement of droplet fluorescence in a given cycle. Thanks to the deterministic positioning of the confined droplets, we are able to correlate each measure with the corresponding droplet. All the measurements are collected in a single matrix where columns are successive droplets, lines successive cycles.

As said earlier in this section, the excitation beam is not homogenous on the tube over cycles. This results in a variation of fluorescence intensity even for a constant dye concentration. To compensate for this effect, we perform a calibration for each turn of the tube, using the variations of signal from a droplet containing a standard concentration of FAM probe diluted in the buffer. Thus, we obtain a curve relating the basic level of samples auto-fluorescence without any amplification and use it as a calibration reference. The following script normalizes the signal on this calibration and plots the qPCR amplification curve as in Figure 55.

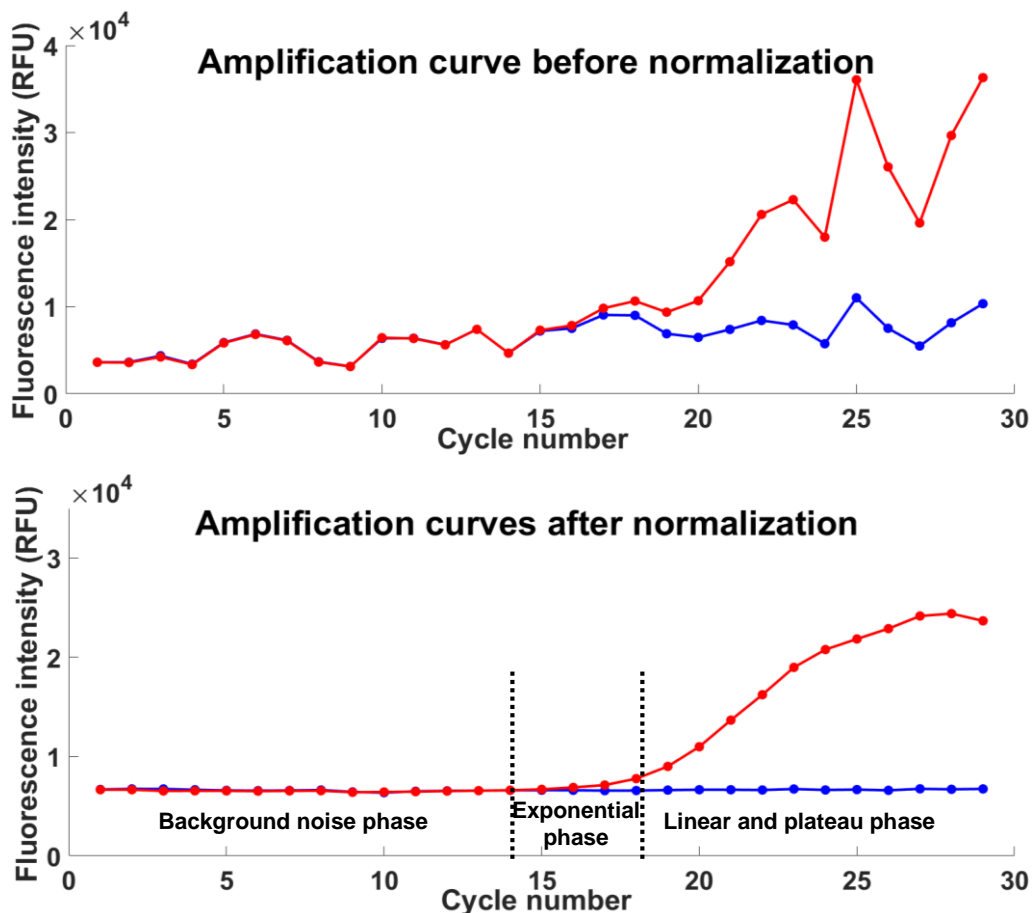


Figure 55: Amplification curves, Fluorescence intensity as function of cycle number, of a sample droplet in red containing 1ng total RNA from MCF7 suspended in DEPC-treated water with master mix, primers and probe for ACTB quantification and a negative control in blue containing only DEPC-treated water with same master mix, primers and probe. First curve, before calibration. Second curve after calibration. Dashed line separate the phases of the red curve: Background noise phase where the signal is given by the auto fluorescence of the probe and no amplification can be observed. Exponential phase where the exponential amplification can be measured, efficiency and Ct value calculated. Linear and plateau phase during which primers and probe start to be lacking for completing PCR and its observation.

After all these processing steps, we finally obtain an amplification curve comparable to what can be achieved with a standard commercial machine. Furthermore, thanks to the deterministic arrangement of the confined droplets, we manage to reconstitute independently the path of each sample flowing in the device and thus its corresponding amplification curve. Now, we will describe how we fit the resulting curves to the kinetic model of PCR and what type of quantification method we used to compare our results.

---

#### 3.2.4.4 Kinetic model of PCR: Efficiency & linear regression

Ideally the PCR amplification follows the equation:

$$I = I_0 2^{Cx}$$

Where  $I$  is the fluorescence intensity at cycle number  $Cx$

$I_0$  the fluorescence intensity before cycle number 1

This equation assumes that the DNA quantity is doubled at each cycle. However, because of imperfect conditions for the biochemical reaction, we introduce the PCR efficiency (noted  $E$ ) which is in general smaller than 2. The previous equation can thus be written as:

$$I = I_0 E^{Cx}$$

In addition to this signal due to DNA amplification, the taqman probe gives rise to a fluorescent response even before thermal cycling. We call this fluorescent background “auto-fluorescence of the solution” and note it  $I_{AF}$ . (In **Figure 55**, for instance, this auto-fluorescence is around 5000 RFU). This will add a second term to the equation:

$$I = I_{AF} + I_0 E^{Cx}$$

During the first cycles, the PCR amplification is not detectable because  $I_{AF} \gg I_0 E^{Cx}$ .  $I_{AF}$  screens the increase of fluorescent signal from amplified DNA at each cycle. Thus, for the same PCR amplification with the same efficiency, the sensitivity of the assay depends on:

- $I_{AF}$  related to the probe concentration
- The sensitivity of the camera and pixel depth (dynamic range) and its background noise

After this first phase,  $I_0 E^{Cx}$  is no more negligible as compared to  $I_{AF}$ , and we can observe the exponential increase of DNA (exponential phase). All the quantifications are made during this phase. We choose three criteria to characterize our device:

- Ct value: Cycle threshold is a theoretical fractional cycle corresponding to the arbitrary fluorescent threshold defined by the user within the exponential phase to quantify and compare between samples.
- E: PCR efficiency varies between 1 and 2. It equals 2 when all the DNA strands are doubled, and 1 when no duplication happens. For a better significance of the represented numbers, we choose the notation in percentage as 100% is equivalent to 2 and 0% is equivalent to 1.

- $R^2$ : Sum of the squares of the residuals of the best linear regression in “least squares” sense when estimation PCR efficiency. This criterion gives an idea of how accurate is the calculation of the efficiency  $E$ , and provides an evaluation of the quality of the fit. The closer  $R^2$  is to 1, the more accurate the fit is.

Therefore, to calculate the efficiency of the PCR reaction for each droplet, we subtract the background  $I_{AF}$  from  $I$  and convert the second curve in **Figure 55** to Logarithm (chosen arbitrarily of base 2). We thus obtain a linear part on the exponential phase of the curve:

$$\text{Log}(I) = \text{Log}(E)C_x + \text{Log}(I_0)$$

Assimilated to  $F(x) = Ax + B$ . Where  $A = \text{Log}(E)$  is the slope of the line and  $B = \text{Log}(I_0)$  is the intercept. Then, the PCR efficiency is calculated as 2 to the power of the slope  $E = 2^A$ . This is one way of calculating the efficiency of a PCR on every single sample. We will also see in the next section a different way of calculation on standard curve, as an average value over different sample dilutions.

We noticed experimentally that the exponential phase lasts in general 5 cycles. To automatize the analysis, we wrote a script that applies on the Log converted curve a moving fit for 5 points (best linear regression in “least squares” sense). For each fit, identified by their starting cycle, it saves the efficiency and the  $R^2$  of the linear regression. It compares between all the fits, chooses the one with the best efficiency (closest to 2) and save it (as the exponential phase) with its corresponding  $R^2$ .

#### 3.2.4.5 Quantification & Ct value

To quantify the amount of target DNA in a sample, we use a comparative method based on a fluorescent threshold. Indeed, depending on the chemistry used, fluorescence intensity can be correlated to a fixed amount of DNA or copy number. This assumption, however, is valid only in a phase where no reagents are lacking and the amplification is detectable i.e. during the exponential phase.

Thus, we choose a threshold of intensity  $I_t$  inside the interval of the linear regression  $[I(C_{fit\ min}), I(C_{fit\ max})]$ , where  $C_{fit\ min}$  corresponds to the first cycle included in the best linear regression and  $C_{fit\ max}$  to the last cycle included. The Ct is thus the solution of the equation:

$$I(Ct) = I_t$$

It corresponds to a theoretical fractional value at which the amplification curve (its linear fit) crosses the defined fluorescent intensity threshold.

---

To compare between different initial DNA amounts of sample using their Ct values,  $I_t$  must be fixed for a given gene and probe, primers and other reagents composition of the Master Mix. It is also specific to each qPCR machine and its optical excitation/detection system.

Based on Ct values of series dilutions of the same DNA solution, it is possible to build a “Standard curve”. Standard curve is a representation of the Ct values as function of the logarithm of the quantity of DNA (Example in Figure 58). If we consider the previous equation, we obtain:

$$I_t = I_{0i} E^{C_{ti}}$$

Where  $i$  is one point of the serial dilution.

Reversing this equation to plot  $C_{ti}$  as function of  $I_{0i}$  (proportional to the DNA mass), we can write it as follow:

$$C_{ti} = -\frac{1}{\text{Log}(E)} \text{Log} \frac{I_{0i}}{I_t}$$

When plotted in semi-logarithmic representation, this equation gives a linear fit with a slope equal to  $-\frac{1}{\text{Log}(E)}$ , allowing to evaluate the efficiency and providing an absolute quantification of any unknown sample. Indeed, after proceeding to qPCR and finding Ct, the projection of its Ct value on the linear fit of the standard curve gives the corresponding mass of targeted DNA.

A second type of quantification is the  $\Delta\Delta\text{Ct}$  method, that allows a relative quantification of genes expression level. It uses a housekeeping gene in addition to the targeted gene, plus a calibrator sample to which samples are compared.

The first  $\Delta$  is  $\Delta\text{Ct}_{\text{sample}} = C_{t(\text{target})} - C_{t(\text{housekeeping})}$  that compare on the same sample the expression level of the target relatively to the housekeeping gene. The second  $\Delta$  is a  $\Delta\Delta\text{Ct} = \Delta\text{Ct}_{\text{sample}} - \Delta\text{Ct}_{\text{calibrator}}$ , which normalizes the expression level of the sample with regards to that of the calibrator. We will show, in the results of this chapter, a comparison between our device and a commercial qPCR system using the  $\Delta\Delta\text{Ct}$ .

### 3.2.5 SmartCycler

In order to validate the potential of our droplet based approach, we compared it with a real-time PCR system developed by Cepheid and commercialized under the name “SmartCycler”. This system is composed of 16 I-core modules (details in **Figure 56**) that host one reaction tube per module. The I-core module and the reaction tubes fitting within are a proprietary technology developed specifically for this application. The tubes are made in polypropylene and composed of two parts. the first one is a conical shape where the sample is loaded by the user. Then, the tubes are centrifuged for few seconds to push the sample in the second compartment which is a square parallelepiped of 25 $\mu$ L volume. The squared walls are very thin (tens of microns) and bend under pressure when closing the lid, thus maximizing the contact with the heating plates. The optical block excites and detects the sample fluorescence thanks to LEDs and silicon photodetectors from dedicated spots on the edges of the heating window (see **Figure 56**).

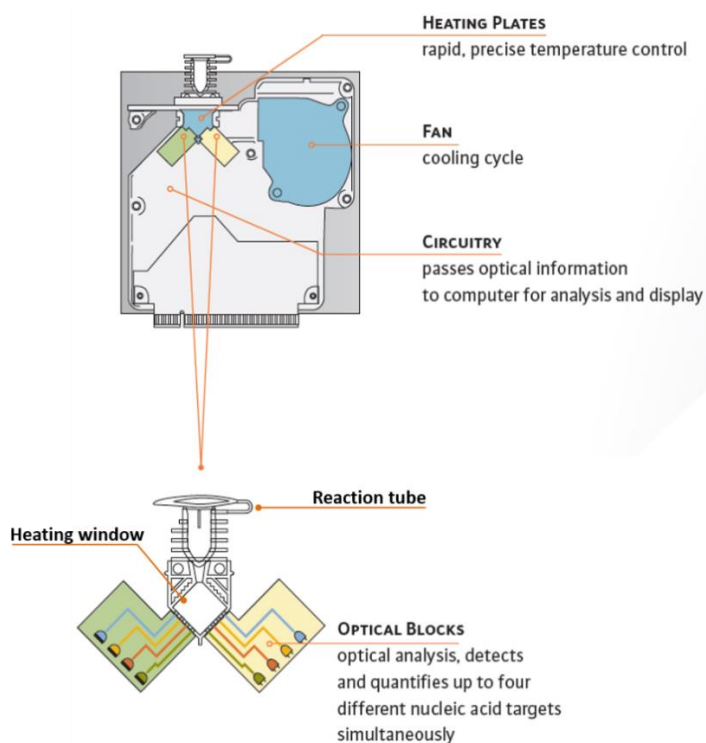


**Figure 56:** I-core module of the SmartCycler real-time PCR system. This module is composed of a thermic part (heating plates, cooling fans controlled by its integrated circuitry) and an optical part (LEDs and silicon photodetectors also controlled by the integrated circuitry). The I-core module and the tubes used with it are a patented technology specifically developed for qPCR application. Thereby, the cost of the consumables (tubes) has a high impact on the total cost of daily qPCR diagnosis.



---

### ***3.3 Results & discussions***

#### ***3.3.1 POC on total RNA***

##### ***3.3.1.1 Description of the POC***

To assess the performance of our qPCR device, we did a first proof of concept (POC) by comparing it with a commercial device available: The SmartCycler. To do so, we used a RT-qPCR assay on total RNA extracted from two cells lines MCF7 and SKBR3, and compared the expression level of the HER2 gene by  $\Delta\Delta C_t$  method in reference to the ACTB gene in these two cell lines. We made the choice of HER2 gene as it is a relevant target in breast cancer. HER2 is overexpressed in ~15-20% of primary breast cancer carcinomas, which are known to be more aggressive. A targeted therapy against HER2 using a monoclonal antibody (Trastuzumab, Herceptin) that binds to the extracellular receptor of HER2 was developed and gives an increase in the overall survival these patients. The diagnosis of HER2 status for breast cancer patient can be done with IHC ImmunoHistoChemistry or FISH techniques. These methods, however, are prone to user judgment in the reading of the fluorescence labelling. RT-qPCR can also be used for HER2 diagnosis, but it is rather expensive.

We hope that our approach can improve this aspect. Therewith, on a more general perspective, RT-qPCR is one of the most difficult assays to run with a qPCR device, due to RNA fragility, and also one of the most used in routine at biology laboratories or hospitals. Thus, performing a RT-qPCR assay with our device is a good assay to prove its robustness, and to demonstrate its clinical utility for daily diagnosis.

We describe in the following sections, the samples preparation for comparing our droplet-based approach with a commercial tube-based device:

- To get the same amount of starting RNA per sample in tube and in droplet, as the volumes are different, the initial concentrations of RNA are different, contrary to almost all other reagents for which concentrations are kept similar (see **Table 5**). Smartcycler experiments were performed by preparing seven 2-fold dilutions of total RNA in DEPC-treated water ranging from 1ng/ $\mu$ L to 15.6pg/ $\mu$ L. Each tube contains 24 $\mu$ L of master mix and 1 $\mu$ L of sample. This dilution corresponds to amounts of RNA ranging from 1ng to 15.6pg. (worth notice for the following discussion regarding potential applications of the

technique, the latter value corresponds to the average amount of total RNA contained in a single-cell). Each data point was triplicated.

- Droplet experiments were performed by preparing seven 2-fold dilutions of total RNA in DEPC-treated water ranging from 10ng/ $\mu$ L to 156pg/ $\mu$ L. Each droplet (equivalent to a tube) was a merge of a first 100nL sample droplet and a second 100nL master mix droplet.
- For each gene, the standard curve on each cell line is a run of droplet train composed of a train car of negative controls, 7 train cars of samples and a train car of calibration. The negative controls train car contains 3 to 5 negative controls. The train car of samples contains a triplicate of the same concentration plus a negative control. The calibration train car contains 5 droplets of calibration solution.
- The negative controls are made of the same master mix as used with the samples, and pure DEPC-treated water without RNA. In all the presented experiments, they remain mainly at the background fluorescence level as shown in Figure 55, or may arise at late cycles (>35, due to primers dimers) but with a low efficiency thus allowing their discrimination.

After loading, the droplet trains were flown through the droplet RT-qPCR device at a flowrate of 120nL/s. This corresponds to less than half of the annealing-extension time performed in tube i.e. around 25s in droplet vs 60s in tube (denaturation time: 25s vs 15s, respectively) and for RT 11min in droplets vs 20min in tube.

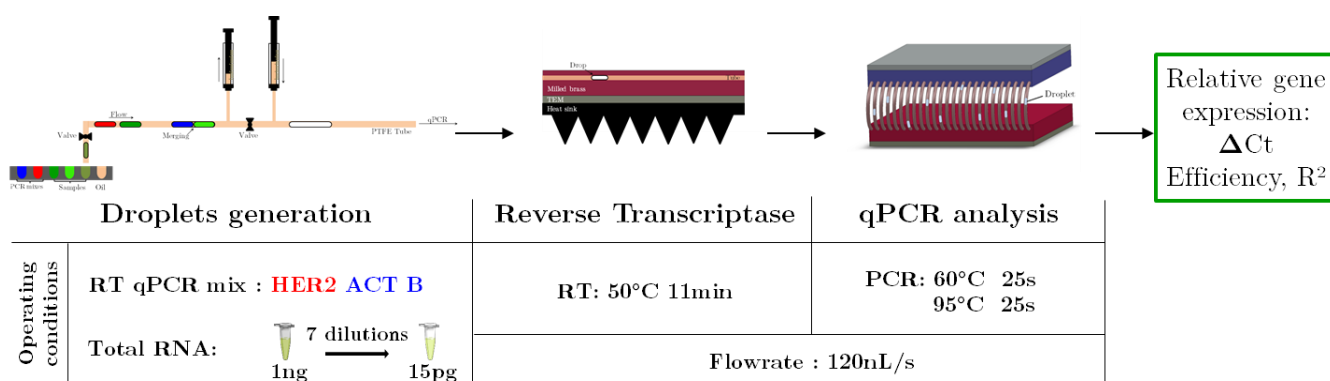


**Figure 57: Workflow of RT qPCR experiments using three modules in series. The first module produces the droplets containing the samples, the second module is a simple heating plate for reverse transcriptase and the last one is the qPCR module.**

### 3.3.1.2 Standard curves of SKBR3

The Figure 58 and Figure 59 show the standard curves for both genes in SKBR3 using respectively the SmartCycler and the Droplet qPCR system. The efficiencies of all the standard curves are higher than 90% with a  $R^2$  higher than 0.99. The  $\Delta Ct$  are almost the same, 3.464 and 3.567 respectively. The error bars are lower than 0.4 in both SmartCycler and Drop qPCR experiments. We can notice a decrease of 6 cycles in Ct values for both genes from SmartCycler to the droplet device.

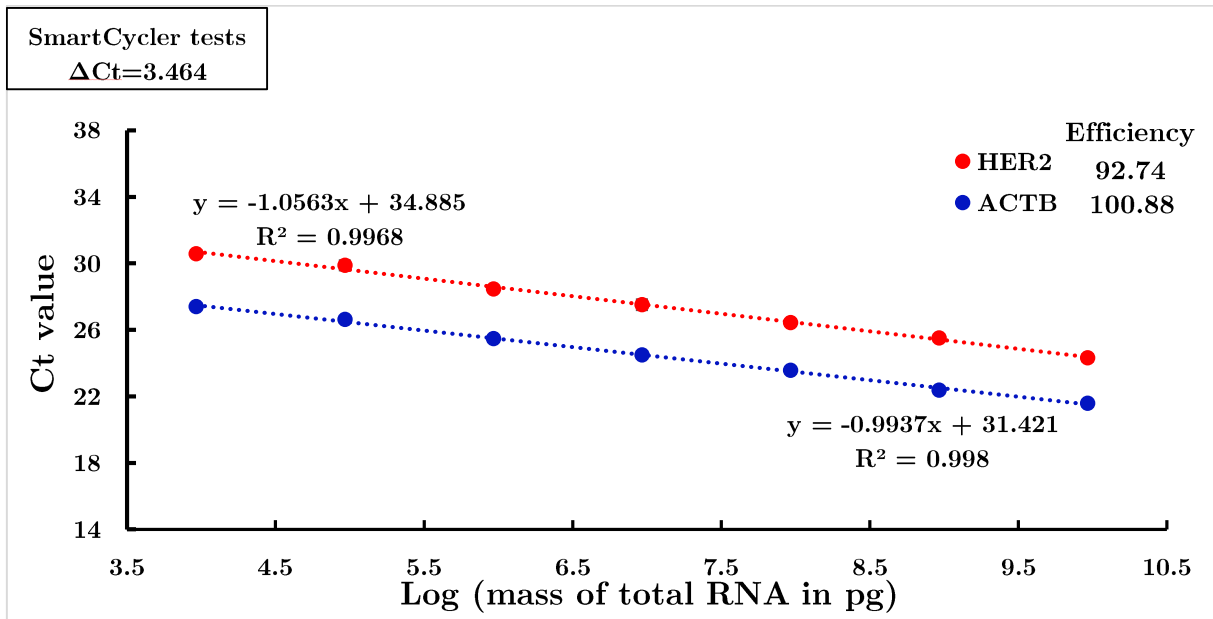


Figure 58: Standard curve for ACTB and HER2 in SKBR3 using the SmartCycler. N=3 on each point. If error bars are not visible, they are smaller than the data point.

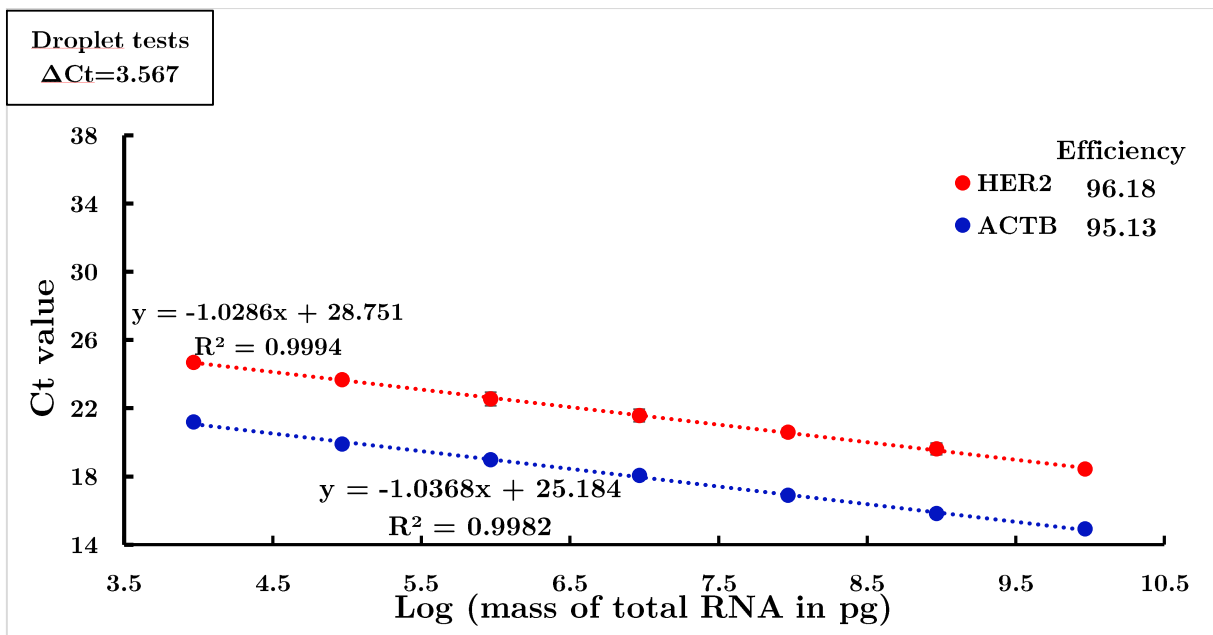


Figure 59: Standard curve for ACTB and HER2 in SKBR3 using the Droplet qPCR. N=3 on each point. If error bars are not visible, they are smaller than the data point.

### 3.3.1.3 Standard curves of MCF7

The Figure 60 and Figure 61 show the standard curves for both genes in MCF7 using respectively the SmartCycler and the Droplet qPCR system. The efficiencies of the standard curves are approximately 80% with a  $R^2$  higher than 0.98 except one value at 92.6% with a corresponding  $R^2$  at 0.92. These values, slightly lower than SKBR3 cell line, can be explained by an abrupt deterioration in RNA, even if they were manipulated in the same conditions. Indeed, contrary to DNA, RNA has the inconvenient to degrade quickly as RNase is in high abundance in the environment. Moreover, RNA quality is largely described in the literature as a potential source affecting RT-qPCR performance (Fleige and Pfaffl 2006)(Vermeulen et al. 2011). However, in our case this effect is the same on the SmartCycler and Droplet qPCR and do not alter our results as the  $\Delta Ct$  value are very similar in the two devices, 9.455 and 9.268 respectively. Similarly, to SKBR3 standard curves, we notice a decrease of almost 6 cycles in Ct value for from SmartCycler to the droplet device.

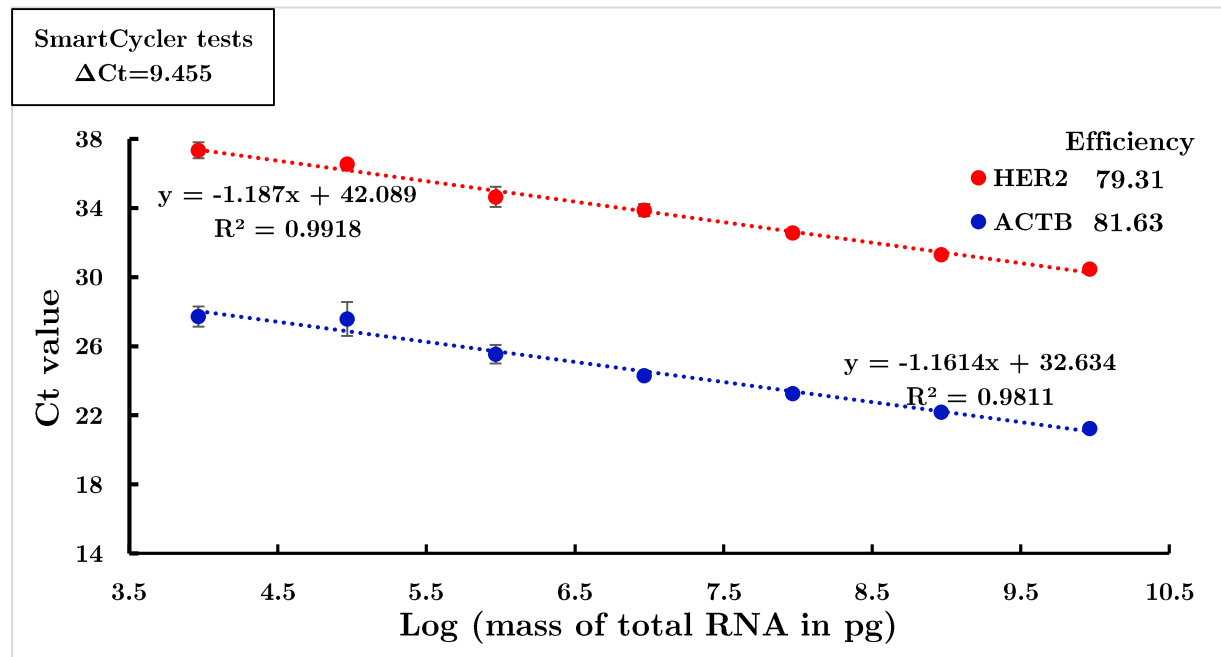


Figure 60: Standard curve for ACTB and HER2 in MCF7 using the SmartCycler. N=3 on each point. If error bars are not visible, they are confused with the point.

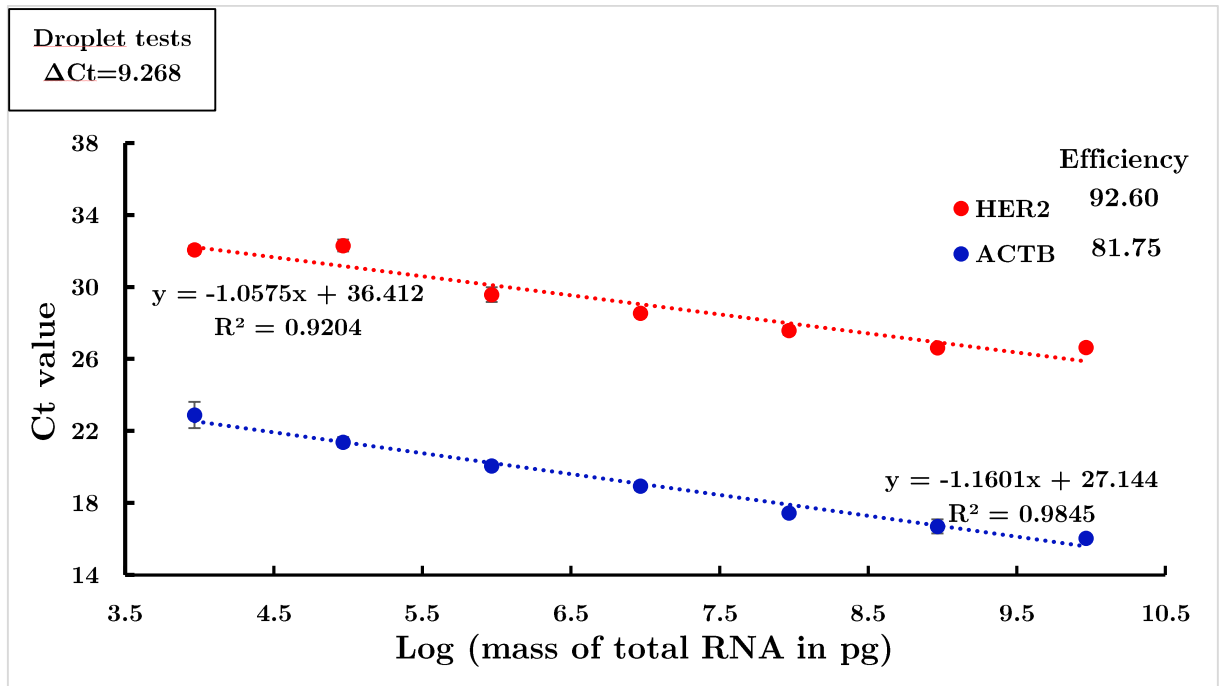


Figure 61: Standard curve for ACTB and HER2 in MCF7 using the Droplet qPCR. N=3 on each point. If error bars are not visible, they are confused with the point.

### 3.3.1.4 Discussion & conclusion on total RNA

The global  $\Delta\Delta Ct$  value relating the expression level of HER2 in SKBR3 relatively to MCF7 with ACTB as reference gene, shows good agreement between Droplet qPCR  $\Delta\Delta Ct_{Droplet\ qPCR}=5.991$  its equivalent in SmartCycler  $\Delta\Delta Ct_{SmartCycler}=5.701$ .

A decrease of around 6 cycles in Ct value is observed in all cases (for the same gene and the same cell line), from SmartCycler to the droplet device. This shows a considerable gain in sensitivity in the Drop qPCR system compared to SmartCycler.

We explain this effect for equivalently sensitive optics, by the increase in microfluidics of initial sample concentration (before the first cycle) for quantification of the same DNA or RNA mass. Indeed, qPCR compare quantities of DNA, so to have the same quantity in droplet and in tube, the initial concentration of sample is increased by the ratio of volumes between tube and droplet ( $25\mu\text{L}/0.2\mu\text{L}=125$ ). Therefore, we can expect for similar optics performance, to detect the signal approximately 7 cycles earlier ( $2^7=128$ , 2 as the maximum possible efficiency). Fluctuations around this value can be explained by optics differences, an increased probe concentration in droplets and the subjective way of setting the fluorescent threshold to determine the Ct value.

This higher sensitivity is a major advantage in our device as it can be exploited in two manners. The first one is obviously the detection of genes of very low expression level without the need for prior pre-amplification and at earlier cycles than in tube. The second one is the possibility of multiplexing without the need for different color channels. Indeed, if we compare standard curves obtained for the same gene and the same cell line (e.g. HER2 in SKBR3) with SmartCycler and with our device: for a given Ct value, the quantity used in droplet is between  $2^5=32$  and  $2^6=64$  lower than the quantity used in tube. This allows us to divide our sample in 32 different droplets, screening for at least a panel of 32 genes whereas consuming the same quantity used for one single gene in tube and reaching similar sensitivities.

Consequently, this POC performed on total RNA proves the possibility to use our droplet RT-qPCR platform for quantification of gene expression levels as it allows in the presented case the discrimination between two cell lines a HER2+ and a HER2-one. Moreover, the comparison with the SmartCycler validates that our device is as reliable as a commercial machine with a volume reduction higher than 200-fold, a higher sensitivity and possibility of multiplexing. We will add to these in the next section, a last feature: high-throughput.

---

### 3.3.2 High-throughput and cycling time

#### 3.3.2.1 Need for faster qPCR

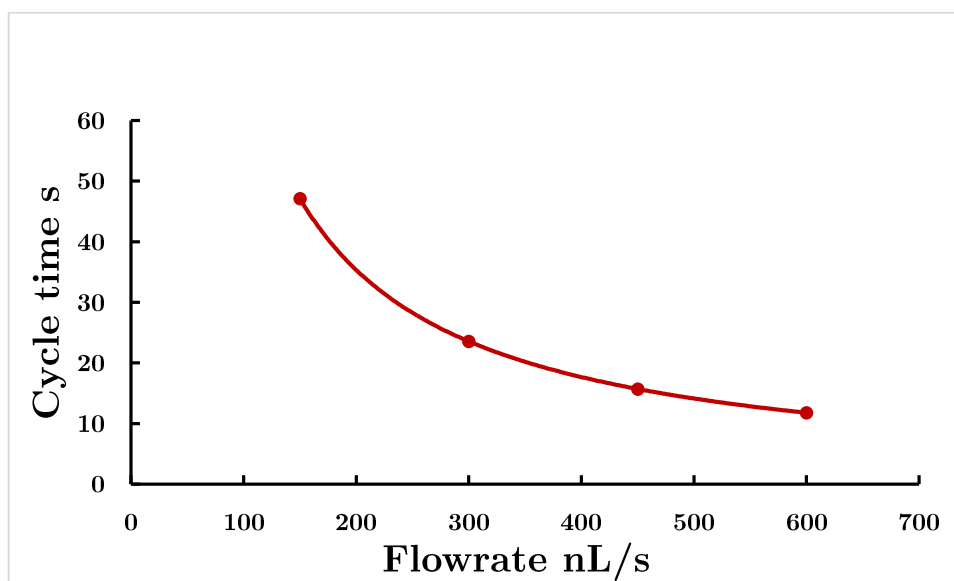


**Figure 62:** Duration of one PCR cycle as function of flowrate. The line is a fit with a reciprocal function.

Taking advantage of the microfluidics aspects of our device; smaller volumes and faster thermal inertia; we investigate how fast samples can be processed in it without any loss in efficiency or error in sample quantification. To answer this question, we increased the flowrate by steps from 150nL/s to 600nL/s. Figure 62 gives the corresponding cycle durations. It is taken here as the time needed to travel 4cm in each heating plate and 1cm in each junction between the plates (a total of 10cm in a 300 $\mu$ m-inner diameter tube) and follows obviously a reciprocal function of the flowrate.

A limit to the increase in flowrate could come from an incomplete reaction during the process. This can be the consequence of an unsuitable temperature or/and an insufficient time to complete the reaction. In our device, these two parameters are related in the sense that even if the temperature of the heating plate is optimal, the droplet can be flowing too fast to reach the temperature of the plate before coming out of it. Furthermore, temperatures are given in the instructions of the RT-qPCR kit and where already validated by the SmartCycler tests, with good reproducibility and efficiency. We will, consequently, limit our discussion to reaction times.

We shall first investigate the thermalization time, and then discuss the reaction kinetics during the three phases of a PCR cycle.

### 3.3.2.2 Thermalization time

Before testing different flowrate/cycling time, we estimated the thermalization time based on the model of Chabert (Chabert 2007). To use this model, we consider our device fitting within the following hypotheses:

- Droplets lubrication film thickness is negligible. Thus, we consider the droplet receiving directly heat from the PTFE tube.
- Curvature of the interface due to surface tension is negligible as compared to the length of the drop. An approximation can then be given by the Graetz problem, i.e. heat transfer from a wall in a Poiseuille profile.
- The external walls of the tubing are at the heating plate temperature.
- Internal recirculation inside the droplet makes instantaneous homogenization of temperature.

The thermalization time given by this model is given by the following equation:

$$t = \sqrt{\frac{Q}{V \cdot 2\pi \cdot \Delta T_m \left[ \frac{x}{k_w R_m} + \frac{1}{1,83k_o} \right]}}$$

$Q = \rho \cdot v \cdot C \cdot \Delta T$ , is the heat to extract from the drop ( $\rho$  water density,  $v$  drop volume,  $C$  mass heat capacity of water and  $\Delta T$  temperature difference).

$V$  Norm of linear speed of the drop

$\Delta T_m$  Logarithmic average temperature difference

$x$  Thickness of PTFE tube

$R_m$  Mean radius of inner and outer radius of the tube

$k_w$  Thermal conductivity of PTFE

$k_o$  Thermal conductivity of oil

In our case, for a droplet volume of 200nL and a capillary of 0.3 mm inner diameter and 0.6 mm outer diameter, moving from 95°C to 60°C, the corresponding thermalization times for the flowrates used are given in Figure 63. The transition from 95°C to 60°C correspond to the largest temperature jump undergone by the droplets in our device. It thus provides an upper bound to the temperature stabilization time.

However, one should have in mind that we neglect here the 10mm between the two plates. This travelling distance should, nevertheless, be favorable as a temperature gradient might be present, smoothing the transition from 95°C to 60°C and thus lowering the values calculated in Figure 63.



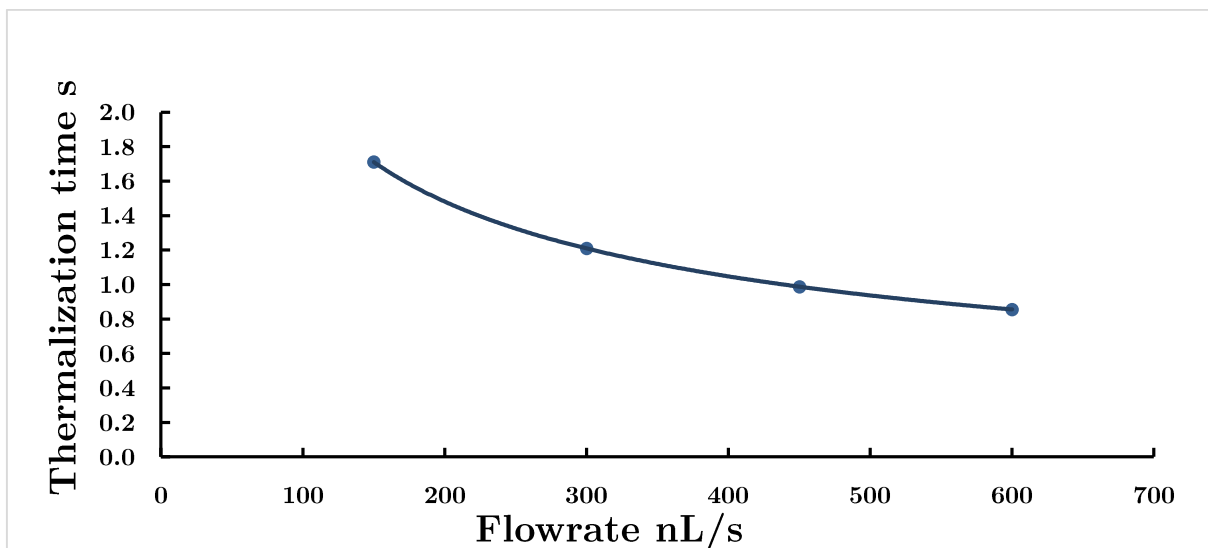


Figure 63: Thermalization time of a 200nL droplet in the qPCR device moving from 95°C to 60°C. The line is a fit with a reciprocal function.

These results imply that at each cycle for a given flowrate, the real time spent by the droplet at the temperature of the heating plate is equal to the traveling time in the plate minus the thermalization time given in Figure 64.

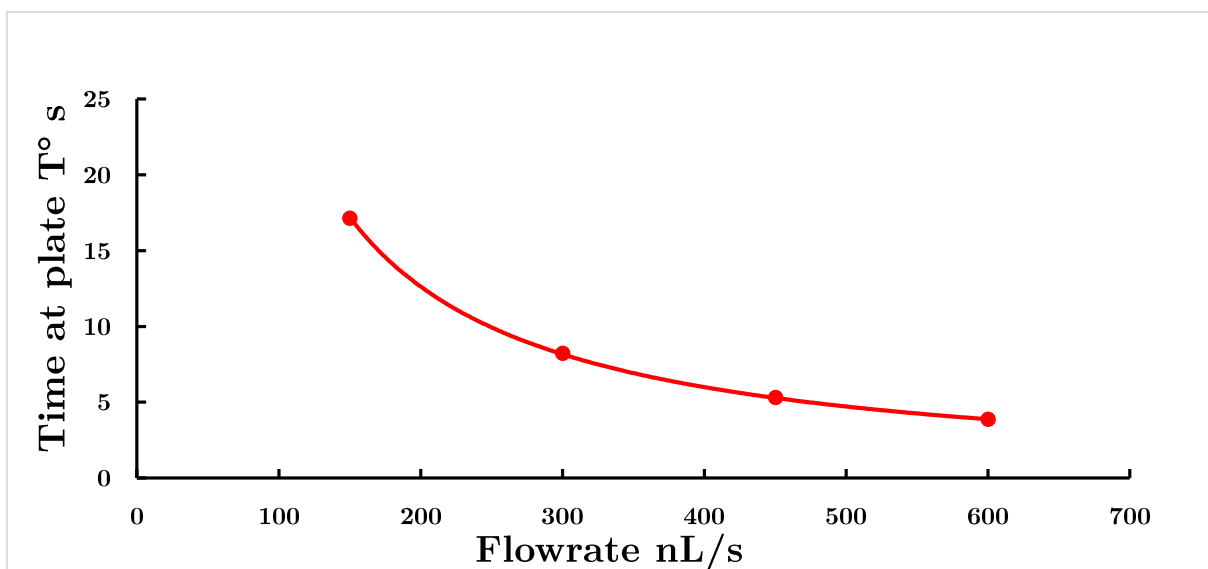


Figure 64: Time at plate temperature for a droplet moving from 95°C heating plate to the 60°C plate. The line is a fit with a reciprocal function.

We now consider chemical kinetics during the steps of the RT qPCR protocol, associated with three critical reaction times.

### ***3.3.2.3 Hot start DNA polymerase***

Hot start DNA polymerase: The CellsDirect™ One-Step qRT-PCR Kits include a chemically modified polymerase. The modifications block its activity during reaction setup and require an initial activation of the polymerase recommended for 2min at 95°C after RT and before starting PCR cycling. In the SmartCycler experiments described later in this chapter, the Hot start time is set at 90s. Using the same machine and kit, we performed RT-qPCR comparing protocols with versus without this activation time. For 4 different concentrations of RNA, the Ct variation was less than (+/-)0.7Ct (Results not shown here). However, if the Hot start time (for about 120s) was limiting, one could expect to obtain a strict increase of the Ct value for the samples performed without. This observation can be explained by the fact that the activation can happen during the first seconds of the first cycle (15s at 95°C). Consequently, we did not include any supplementary heating plate in the workflow as described Figure 57, and performed all the experiments described in our device considering the activation time as included in the first cycle of PCR.

### 3.3.2.4 Denaturation / annealing-elongation, PCR time

Denaturation / annealing-elongation, PCR time: In conventional PCR systems, the denaturation (95°C) is set for much shorter times than annealing and elongation (60°C). For example, the experiments shown in this chapter were performed in the SmartCycler with 15s as denaturation time and 60s as annealing-elongation time (based on the recommendation of CellsDirect™ One-Step qRTPCR Kits). In our device, for the ease of fabrication, we made the choice to use the same size of heating plates, thus, equal times for these two steps. In these conditions, the limiting time will be the annealing-elongation, and the denaturation time will be in excess.

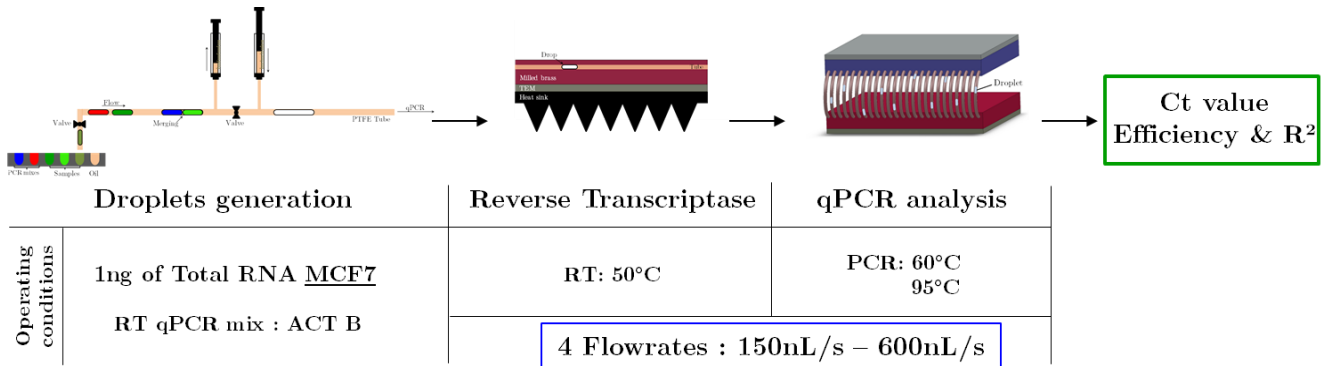


**Figure 65:** Workflow used for RT qPCR experiments to compare different operating flowrates in the heating plate for reverse transcriptase and the Drop qPCR module.

Thus, to find the limit of the annealing-elongation time in our device for droplets of 200nL, we compared the PCR efficiency, its corresponding  $R^2$  and the Ct value for different flowrates (150, 300, 450 and 600 nL/s). In the same way as previous experiments, we performed an RT qPCR assay for the gene ACTB on droplets containing 1ng of total RNA extracted from the cell line MCF7. Figure 65 summarizes the workflow used for these experiments.

Figure 66 and Figure 67 shows the PCR efficiency and its  $R^2$  calculated on each droplet sample as described in Materials & methods, as a function of flowrate. We observe that the efficiency is around 86% for 150, 300 and 450nL/s with a standard deviation lower than 4.7%. The corresponding  $R^2$  are around 0.9962 with a maximum standard deviation at 0.0030. For 600nL/s the efficiency drops down to 74.85% with a standard deviation higher than 10% and a corresponding  $R^2$  of 0.9819 (standard deviation 0.0166).

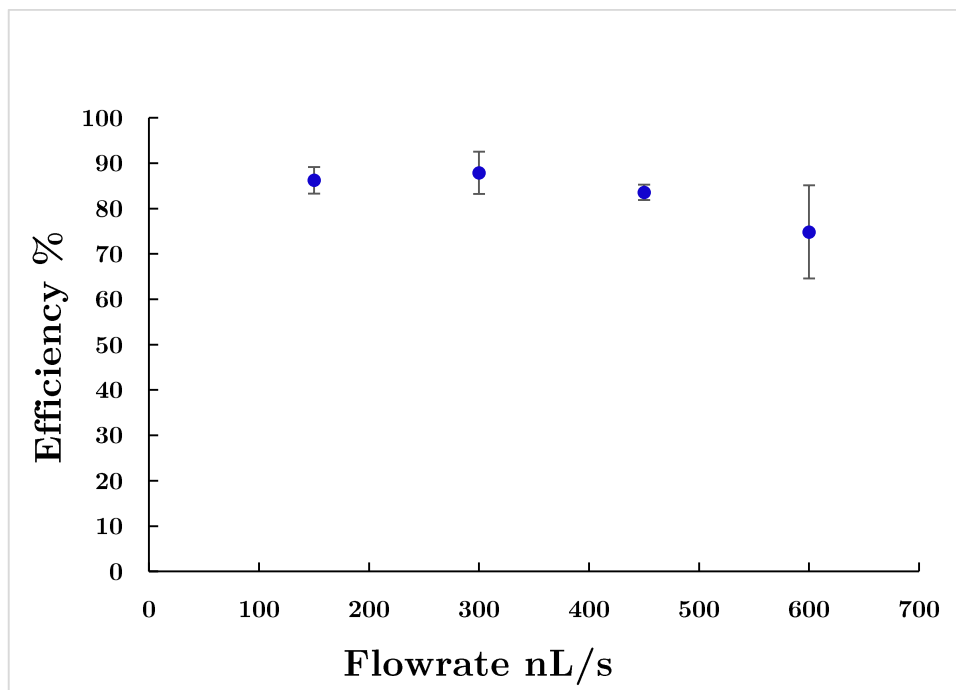


Figure 66: Efficiency as function of flowrate. N=5 in each point. Line is guide for the eye. Efficiency calculated on amplification curves of Expression level of ACTB gene in 1ng of total RNA extracted from MCF7.

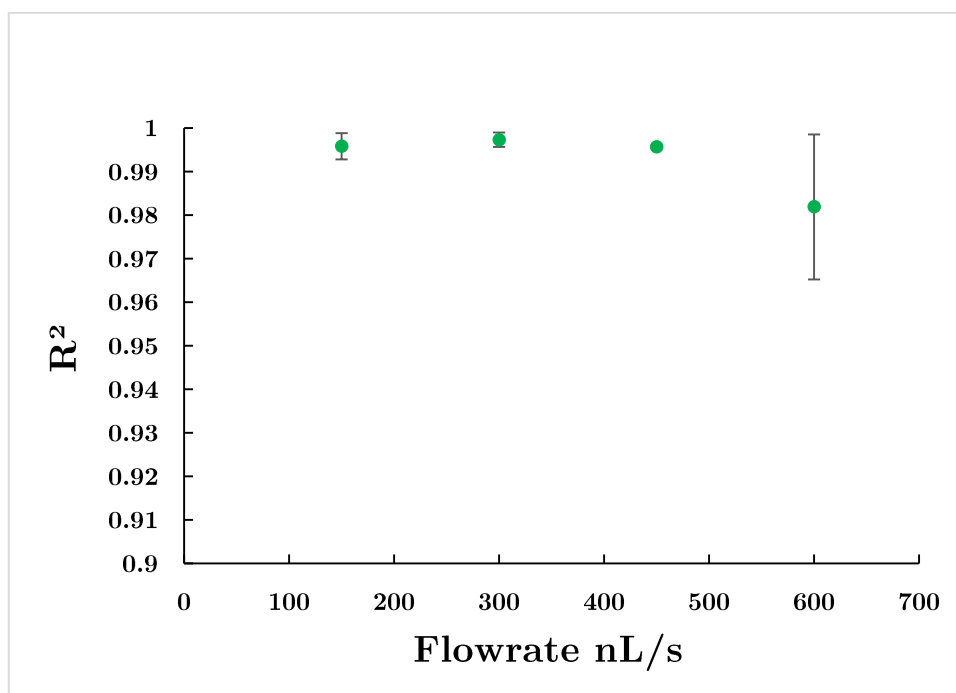
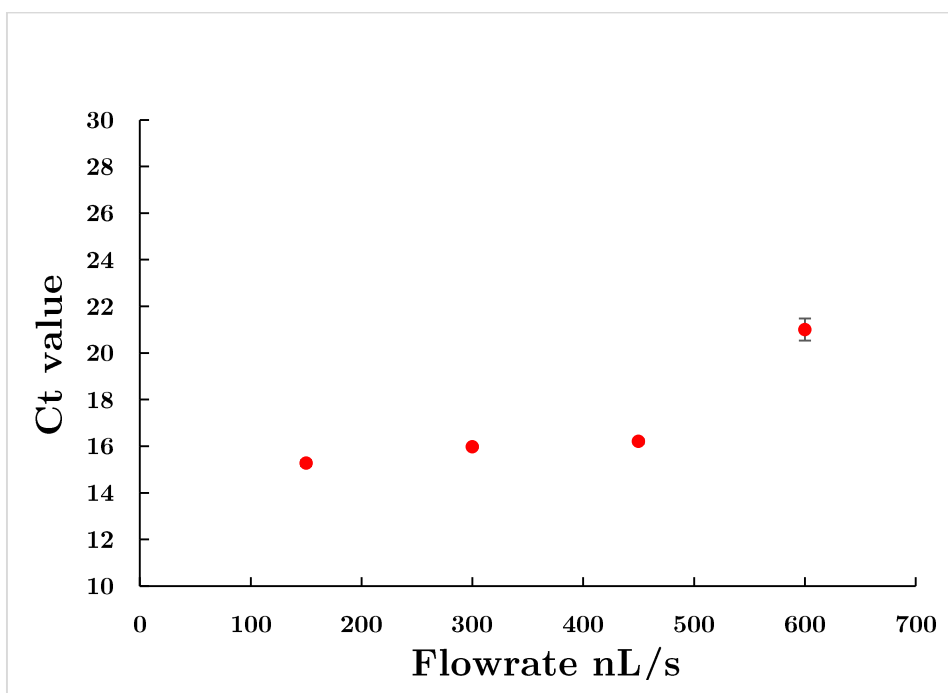


Figure 67: R<sup>2</sup> as function of flowrate. N=5 in each point except 450nL/s where N=4 (aberrant point excluded). Line is guide for the eye. R<sup>2</sup> of the corresponding efficiencies in Figure 66 calculated on amplification curves of expression level of ACTB gene in 1ng of total RNA extracted from MCF7.

### 3.3.2.5 Reverse transcriptase, RT time

As described in Material & methods, the Reverse transcriptase is performed online with the PCR but in a different heating plate set at 50°C and placed before the qPCR device. The tube containing the sample is placed inside a micro-milled piece of brass. For a fixed flowrate, the RT time is then directly proportional to the length of the milled design. In these experiments, we used a length of 1120mm, knowing that this length can be easily adapted if needed by simply milling a new brass part. To know if the RT time is limiting, we compare, for similar PCR efficiency, the Ct values corresponding to the different flowrates. If the reverse transcription does not have the time to be completed, the cDNA quantity at the beginning of the PCR is lower. Consequently, the PCR would need more cycles to reach the fluorescent threshold and thus the Ct value will be shifted up.



**Figure 68:** Ct value as function of flowrate. N=5 in each point. Expression level of ACTB gene in 1ng of total RNA extracted from MCF7. For the first 3 points, negligible variations are observed with standard deviation smaller than 0.13 (error bars confused with points representation). At 600nL/s, an increase for 5 cycles is observed with a bigger standard deviation at 0.47.

We notice on Figure 68 that no significant change in the Ct value can be observed between 150nL/s and 450nL/s. At 600nL/s we obtain an increase of almost 5 cycles. But we know from **Figure 66**, that the efficiency in this point is lower. So the Ct values are not directly comparable. We could extrapolate the initial amount of cDNA by

hypothesizing a constant efficiency over all the cycles before the end of the exponential phase. But this calculation is not necessary in our case since we cannot work at 600nL/s due to the loss in efficiency. Therefore, the RT time is not a limiting factor until at least 450nL/s and must be around 3 minutes.

---

### 3.3.2.6 Discussion & conclusion on Cycling time

We can conclude from these results that the PCR time in our device for a droplet reaction volume of 200nL, reaches a limit for flowrates between 450nL/s and 600nL/s. This corresponds to a cycle duration of ]11.78s ;15.71s]. Thereby, we proved the possibility to use the developed “Droplet qPCR” platform at a higher throughput with high efficiency and reproducibility. In comparison to recent microfluidic ultra-fast qPCR (Houssin et al. 2016), we are at the same range of processing time ~7.5 minutes for 30 cycles. We could also try to improve this limit by reducing the volume of droplets used, working on the thermal properties of the materials used or/and simply increasing the reagents concentrations as described by (Farrar and Wittwer 2015). Indeed, the latter reported, what they named “Extreme PCR”, in which a short sequence of 60-bp are amplified for 35 cycles in 14.7s thanks to reagents concentration 10- to 20-fold above typical concentrations. However, two interesting limits emerge here and worth to be explored in the future:

- The first one is for sure the **physical limitation of viscosity** that would increase with the increase in concentration and thus affect the PCR efficiency beyond a certain threshold.
- The second one is the **economical limit** and must be considered from the practical and applied point of view. Indeed, there should be an equilibrium between the reduction of cost due to processing time reduction, and on the other side the increase in cost caused by the consumption of higher quantities of reagents when increasing the concentration.

Nevertheless, compared to the approaches of Houssin or Farrar, the main advantage given by our device is the possibility to continuously flow samples with a spacing of less than 1 $\mu$ L between them. Thereby, when one droplet needs 7.5 minutes, a train of 100 droplets could be processed in less than 12 minutes and 1000 droplets in less than 54 minutes. This would, however, requires an approach for automating the injection of droplets in the device different from the one used here, i.e. preparing droplet trains. In this purpose, the system as it is, can for example be associated with a push-pull pipetting device as proposed in (Chabert et al. 2006).

### ***3.4 Conclusion and perspectives on Droplet qPCR***

As compared to a commercial system, our platform shows similar performances in terms of PCR efficiencies but with a 6-fold increase in sensitivity<sup>1</sup> (lower Ct value). This opens the door to a strong decrease in sample consumption which could have an important impact in the area of liquid biopsies and personalized medicine. Indeed, rare samples (e.g.: circulating tumor cells, or microbiopsies), imply the use of very low quantity of material. Also, the fast multiplication of targeted therapies and “signature” approaches calls for the screening of large panels of genes, which would in turn require increasingly high sample and reagents consumption. Our continuous-flow microfluidic device is well suited to allow for these progress, while keeping a low sample consumption and without exploding the cost of consumables:

- The high sensitivity of the machine allows working with very low quantities of material at high-throughput. We oriented our next application with this device on **direct single-cell RT-qPCR** to perform our assay directly on single cells encapsulated in droplet as shown in the previous chapter, without prior RNA extraction. Thereby, the developed system can be of very good interest in looking at cancer tumor heterogeneity or the heterogeneity of a cell population from specific tissue or organ in general.
- The screening of large panels of genes is possible as **multiplexing** is straightforward and already available on the discussed setup without using different channels of illumination. Since droplet samples are kept in a deterministic order, independent RNA droplets can be combined with any number of PCR master mix composed of different primers and probe triplet. With a consumption of 100 nl of sample per assay, about 200 independent target sequences can be performed with the 20µl usually consumed in tube PCR, without the complications and interferences associated with multiplex PCR in a single tube. We have already tested, successfully, this multiplexing by flowing droplets containing different mixes (for ACTB and HER2) simultaneously.

---

<sup>1</sup> It should be noted that in PCR detection, thanks to the amplification nature of the principle, which contrasts with the detection of other biomarkers such as proteins, sensitivities are generally considered regarding total mass of nucleic acid, and not concentration. We used here this convention to define sensitivity.



- 
- The quantitative experiments performed here show a 240 times reduction in volume of PCR master mix and a total suppression of solid consumables (tubes or well-plates) as they are processed in a reusable liquid support (fluorinated oil). Dealing with DNA amplification, this could raise concerns regarding sample-to-sample contamination, but through thorough tests all over the years of development of this technology, we never observed such contamination. Furthermore, the low-cost aspect of the machine itself (CMOS camera, 3D printed parts, reusable PTFE tubing) should help in a dramatic decrease of the current acquisition cost of qPCR system; between 15000€ for a basic 16 wells and 95000€ for the most sophisticated ones. Thereby, the developed system would represent a **commercial product** of promising potential in the qPCR market.

From the thesis point of view, we validated the analysis module as the Drop qPCR system can be used as shown for quantifications of nucleic acids (RNA or DNA) down to single-cell level. Apart from the adjustments still needed at preparation step, the global platform for single cell analysis is now complete with three different modules than can work either separately or by pairs or in series together.

As perspectives and first application of this platform we are planning to use it as follow:

1. We use the first module to encapsulate and prepare a heterogeneous cell population for RNA extraction by merging them with adapted reagents.
2. Thanks to the magnetic tweezers technology, we extract sequentially RNA and DNA on magnetic beads as a solid support of extraction and keep the supernatant for other analysis.
3. The extracted RNA and DNA are eluted and flown through the droplet qPCR module for the quantification of gene expression level and genomic amplification respectively, for each single cell in order to link the impact of DNA amplification to the transcriptomic level with RNA.

## Appendix: Sequences and primers

Table: Sequences of primers and probes used in RT qPCR experiments for HER2 and ACTB genes with the corresponding melting temperature, used in the Master Mix preparation reported in Table 5.

Name	Sequence	Tm
ACTB_Forward	5-GGA TGC AGA AGG AGA TCA CTG-3	55.2
ACTB_Reverse	5-CGA TCC ACA CGG AGT ACT TG -3	55.2
ACTB_Probe	5'-/56-FAM/CCC TGG CAC /ZEN/CCA GCA CAA TG/3IABkFQ/3'	61.7
HER2_Forward	5'-CTG AAC TGG TGT ATG CAG ATT GC-3'	56.3
HER2_Reverse	5'-TTC CGA GCG GCC AAG TC-3'	58.2
HER2_Probe	5'-/56-FAM/TGT GTA CGA/ZEN/GCC GCA CAT CCT CCA/3IABkFQ/3'	64.2

The targeted sequences are reported in the following, with the specified region for forward and reverse primers and the probe and their corresponding length in base pair (bp):

**ACTB:** Chromosome 7: 5,527,156-5,530,601 reverse strand. exon4 and exon5.

GGATGCAGAAGGAGATCACTG **CCCTGGCACCCAGCACAATGA**AGATCAAGATCAT  
TGCTCCTCCTGAGCG **CAAGTACTCCGTGTGGATCG**=90bp

**Sequence structure** = **Forward** 21bp + **Probe** 20bp + sequence to polymerize 29bp +  
**Reverse** 20bp

**HER2:** Chromosome 17: 39,687,914-39,730,426 forward strand. exon 24 and exon 25.

**CTGAACTGGTGTATGCAGATTGCC**CAAGGGGATGAGCTACCT**TGGAGGATGTGCGG**  
**CTCGTACACAGG****GACTTGGCCGCTCGGAA**=83bp

**Sequence structure** = **Forward** 23bp + sequence to polymerize 17bp + **Probe** 24bp +  
sequence to polymerize 2bp + **Reverse** 17bp

4. Role of tumor cells in  
Cancer Related Thrombotic  
Micro Angiopathy

This chapter reports on a clinical research study about the role of tumor cells in Cancer Related Thrombotic Microangiopathy. The study involved 4 patients diagnosed with this rare complication of cancer and necessitates the use of different techniques of cell enrichment and characterization.

The study was initiated and supervised by Pr François Clément Bidard and jointly conducted between our team and the lab of Circulating Tumoral Biomarkers leaded by Dr Charlotte Proudhon and Pr Jean-Yves Pierga. It involved in particular:

- Charles Decreane for blood (and other samples) collection and experiments on Cellsearch, Cellselector and ISET filters. Aurore Rampnou for Cellsearch experiments.

- NGS platform of Curie Institute, specifically Virginie Raynal, Patricia Legoix for library preparation and NGS processing.

- Bioinformatics platform of Curie Institute (U900) specifically Elodie Girard for data treatment of WES and RNA sequencing.

This study highly intrigued my curiosity, I took charge of it from its beginning. I was involved in the whole process from blood samples collection (behind patient door rooms) and management to the different treatments and analysis that were performed. I did the Ephesia processing and cells recovery, and learned using the CellSelector with Charles. I also organized the collection of Normal/Tumor samples and synchronized all the processes between the different platforms involved. I learned, with the help of Elodie, the different steps of bioinformatics analysis and how to interpret and discuss these types of data. Finally, I collected and analyzed all the data presented in this manuscript.

Complementary to the two previous chapters, this one shows a direct application of microfluidics in the medical field and specifically in cancer research. It also perfectly concretizes my hope of completing my training by a contact with the medical environment. As for the previous chapters, but in particular for this one, I hope that the reader will appreciate the content as much as I appreciated working and learning in this multidisciplinary environment between engineering, biology and medicine.

We will introduce this chapter by a brief introduction about circulating tumor cells and Ephesia platform, before giving a small review of the literature about cancer related thrombotic microangiopathy. We later report on the observations on our microfluidic device and describe the implementation of a more global workflow. Finally,

---

we show the first sequencing results obtained and discuss the future perspectives of this study.

## 4.1 Introduction

### 4.1.1 Circulating tumor cells

Cancer is a leading cause of death in both more and less economically developed countries; the International Agency for Research on Cancer estimates about 14 million new cancer cases and 8 million deaths in 2012 worldwide. More precisely, around 90% cancer related deaths are due to metastasis (Chaffer and Weinberg 2011). Metastasis is a multistage process where cancer cells detach from the primary tumor and enter the blood circulation by intravasation (Figure 1). Thereafter, cancer cells transit in the blood stream some of which survive (either as isolated tumor cells or larger aggregates called “microemboli”) and invade distant organs by extravasation where they further form a new tumor site. These cells might remain quiescent for various periods of time while being undetectable through in vivo imaging methods (Chaffer and Weinberg 2011). These cells are called **Circulating Tumor Cells (CTC)** and they are defined as malignant cells issued from the primary tumor and shed in the blood stream. The development of invasive metastases can take years, and CTC could provide critical information especially in the “blind” period following primary treatment.

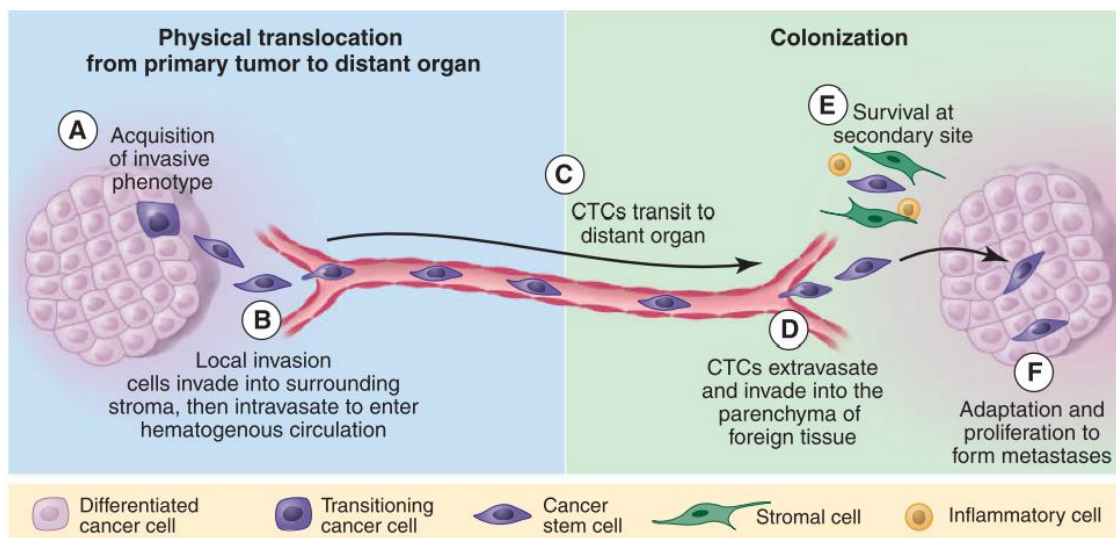


**Figure 69: Illustration of the metastatic cascade. Extracted from** (Chaffer and Weinberg 2011). CTC were first observed in 1869, in the blood of a deceased patient having 30 subcutaneous tumors (Ashworth 1869). At this time the treating clinician stated “that cells identical with those of the cancer itself being seen in the blood may tend to throw light upon the mode of origin of multiple tumors existing in the same person”. Since this first observation, dozens of years have then been necessary to develop technologies enabling CTC detection and evidencing their clinical relevance.

---

In 2004, the Cristofanilli group published a seminal study where they showed that CTC count is an independent prognostic factor of progression-free survival and overall survival for metastatic breast cancer patients (Cristofanilli et al. 2004). The cut-off to discriminate between patients with good or poor prognosis has been established at 5 CTC/7.5 mL of blood. These results have recently been confirmed on a larger panel of patients (Bidard et al. 2014). The prognostic value of CTC has also been demonstrated for early breast cancer (Bidard et al. 2018), as well as various other carcinomas (prostate, colorectal, lung).

Besides being a prognostic factor, changes in CTC count have also proven to reflect the treatment efficacy, demonstrating the dynamic character of this biomarker (Cristofanilli et al. 2004; Riethdorf et al. 2007). Many clinical trials are currently investigating the potential of CTC to guide therapeutic decision. In France, an ongoing study (Institut Curie Hospital) aims at proving that the use of CTC enumeration could be relevant in breast cancer to help the clinicians at selecting between hormonotherapy or chemotherapy and thus improving the patient's quality of life (François-clément Bidard and Pierga 2015), and the first results are really encouraging. Besides this interventional trial based on CTC count, other trials are based on CTC characterization in particular comparing CTC molecular profile to the one of the primary tumor. The objectives of these trials are to correlate the mutation profile of CTC with disease aggressiveness and treatment efficacy. Examples include the Circe TDM1 trial initiated by the Curie Institute Hospital, which evaluates the potential of targeted therapy for patients presenting a discrepancy between the HER2 negative primary tumor and the HER2 positive CTC.

There is a wide range of methods to detect CTC; they are mainly based on centrifugation and/or immunoaffinity (Riethdorf et al. 2007). Recently, microfluidics has appeared as a new paradigm for CTC detection and analysis, in particular thanks to its unique features in hydrodynamics and microfabrication. CTC presents a wide range of properties (size, cell deformability or polarizability) that can be used to sort them passively by microfluidic methods. Microfluidics also offers the possibility to apply a wide range of forces (acoustic, magnetic, electric...) for CTC detection. Besides these label-free methods, immunoextraction approaches that rely on cell surface markers such as epithelial cell adhesion molecule (EpcAM) are now considered as the dominant technique for isolating CTC. These approaches have also demonstrated their potential

at microscale. Another type of immunological immunoaffinity-based capture has been developed by (Agerbæk et al. 2018) based on VAR2CSA malaria protein and allowing an EpCAM-independent CTC collection. A more extensive review about CTCs detection methods can be found in (Alix-Panabieres and Pantel 2013; Autebert and Coudert 2012).

In parallel to CTC detection, CTC molecular characterisation is also of high interest to guide clinicians in treatment selection in particular to determine patient eligibility to targeted therapy (Toss et al. 2014). CTC can be identified through expression of surface proteins, such as EpCAM. Further, expression of specific proteins can be used as a marker to stratify certain types of cancer, such as HER2 (human epidermal growth factor receptor 2) or ER expression (estrogen receptor) in breast cancer. Protein characterization is mainly performed by immunofluorescence. More recently, CTC nucleic acid characterization has gained interest, for instance FISH (Fluorescence In Situ Hybridization) has been used to investigate gene overexpression or gene rearrangement/deletion while PCR (Polymerase Chain Reaction) and RT-PCR (Reverse transcription-Polymerase Chain reaction) have been performed to evaluate DNA mutation and gene expression of CTC. Sequencing technologies and in particular Next Generation Sequencing (NGS) have also been applied to interrogate CTC RNA and DNA for whole genome or targeted sequences analysis (Millner, Linder, and Valdes 2013).

The effervescency about circulating tumor cell and their potential clinical impact, prognosis and follow up roles for cancer patient was partially proved but still under investigation on many aspects (Cabel et al. 2017). This vision of circulating tumor cells as a potential biomarker for cancer progression raises the question of its economic impacts and sparks a high industrial interest on the topic (Leis, Lopez-mato, and Martin 2012).



## 4.1.2 Ephesia

### 4.1.2.1 Principle of the Ephesia Platform

Within our group, an immuno-detection device has been developed several years ago based on CTC EpCAM expression. It consists of four capture chambers connected in parallel, each chamber containing an array of superparamagnetic microbeads coated with anti-EpCAM antibodies. These beads are self-organized as columns thanks to an external magnetic field and positioned deterministically thanks to the magnetic anchors placed at the bottom of the chip (see **Figure 70**, and Appendix for column formation video).

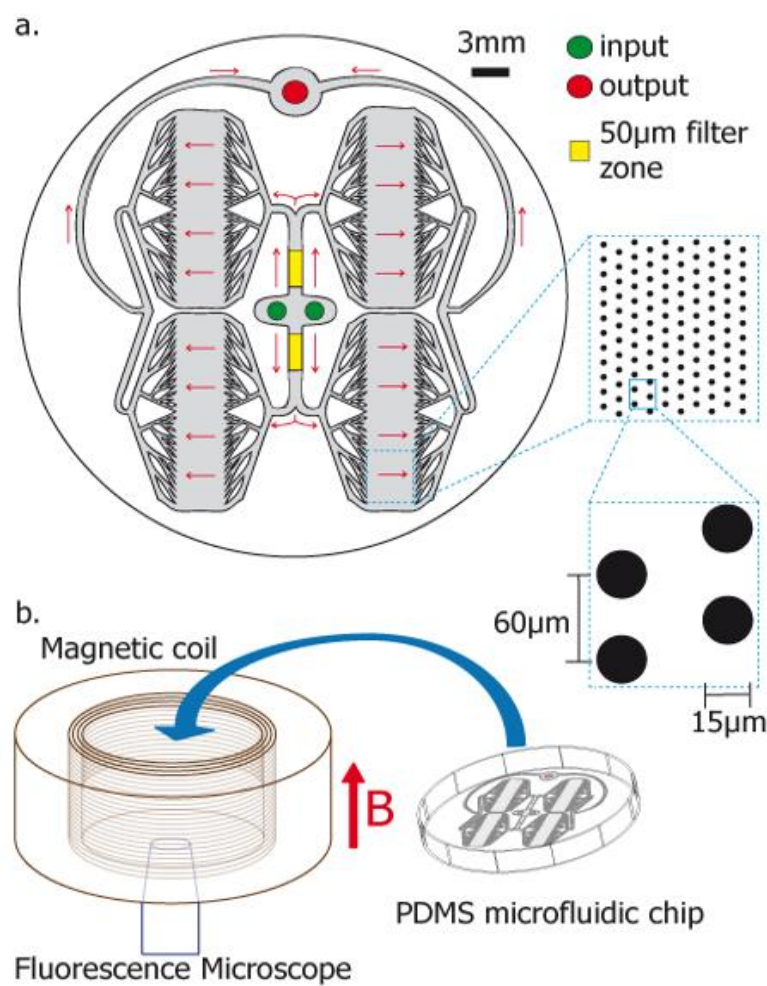


**Figure 70:** Ephesia device. a: Design of the microfluidic chambers containing magnetic array position b: positioning in the magnetic coil. The columns of beads will align with the magnetic field applied by the coil. (Autebert et al. 2015)

The beads are functionalized with an anti-EpCAM Ab that recognizes cells from epithelial origin. Thereby, when injecting a pre-sorted blood sample, the cells will come in contact with the columns of beads but only CTC that express EpCAM will be captured, all other cells can flow through the array. Later on, an immuno-staining solutions are injected inside the chip to confirm the CTC identity by staining the cell's nucleus and CD45 to discriminate, respectively, red blood cells (RBC) and white blood cells (WBC), and Cytokeratin to confirm the epithelial features of the cells. Epifluorescence imaging is performed in chip thanks to an adapted microscopy platform holding the entire system with fluidic control of the device and electric and thermal control of the surrounding coil.

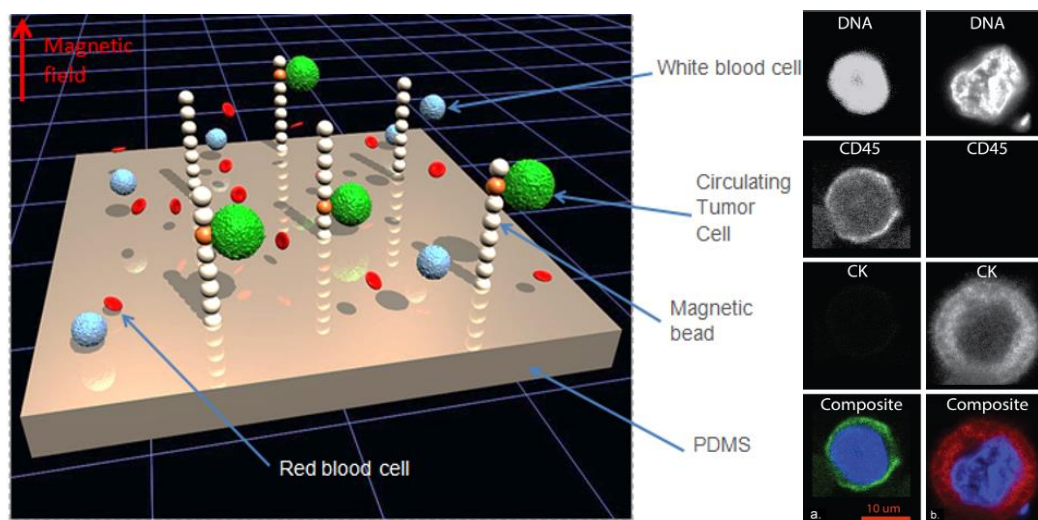


**Figure 71:** Left, 3D representation of Ephesia arrays during sample injection. Right, fluorescence images of a WBC (left column) CD45<sup>+</sup> CK<sup>-</sup> and a CTC (right column) CD45<sup>-</sup> CK<sup>+</sup> (Autebert et al. 2015). Red scale bar is 10 $\mu$ m.

#### 4.1.2.2 Ephesia from 2010 to 2018

A first Polydimethylsiloxane (PDMS) version of the device was reported by (Saliba et al. 2010), using the magnetic array in a straight channel. Further optimization was performed by (Saias et al. 2011) to maximize the device throughput without destroying the magnetic columns. This leads to the diamond shape chambers that allows homogeneous flow along these large chambers. Optimization of the CTC capture, analytical validation and testing on patient blood samples from breast and prostate patients was thus performed by (Autebert et al. 2015). In parallel, Karla Perez-Toralla developed a Cyclic Olefin Copolymer version (COC) of Ephesia to perform Fluorescence In Situ Hybridization (FISH) analysis on captured cells (Perez-Toralla et al. 2015) and Ezgi Tulukcuoglu-Guneri implemented the Proximity Ligation Assay (PLA) in Ephesia device with cell lines and processed the first tests using blood samples (Tulukcuoglu Guneri 2016) to investigate HER2/HER3 dimerization on CTC. **Figure 72** illustrates the evolution of Ephesia technology over these years, from physics (design, hydrodynamics, materials) and biology (molecular characterization) points of view.

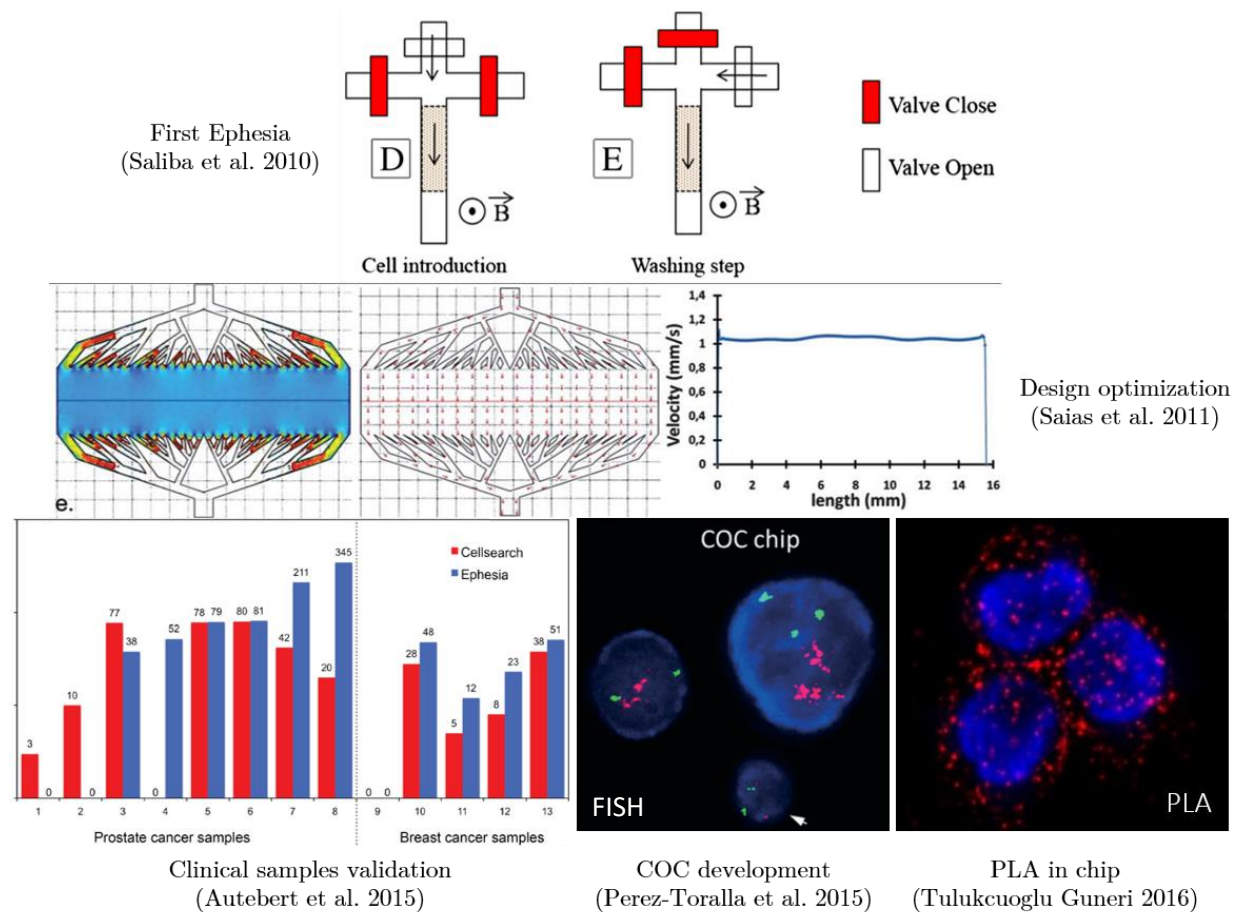


**Figure 72: Evolution of the Ephesia technology**

### 4.1.3 Cancer-related TMA

#### 4.1.3.1 Introduction: clinical context

We start this introduction by few definitions of medical terms needed for understanding the context of the study and the bibliography discussed below:

- **Anemia** is a *state* of decrease in the total amount of red blood cells (RBC) or in hemoglobin in blood or in general a lowered ability of the blood to carry oxygen.
- **Hemolysis** is the destruction of RBC and the release of their cytoplasm in the carrying fluid.
- **Hemolytic anemia** is a form of anemia due to hemolysis. This means, a decrease in the amount of RBC by their destruction.
- **MicroAngiopathic Hemolytic Anemia** or **MAHA** is a *symptom* classified in the microangiopathic subgroup of hemolytic anemia, involving disorders in small vessels that form thrombus and cause the destruction of RBC. It is identified by anemia and observation of schizocytes in blood smears (see **Figure 73**). MAHA is a symptom necessary to the diagnosis of some TMAs. For example, the diagnosis of HUS (Hemolytic Uremic Syndrome) involves MAHA, renal failure and thrombocytopenia.

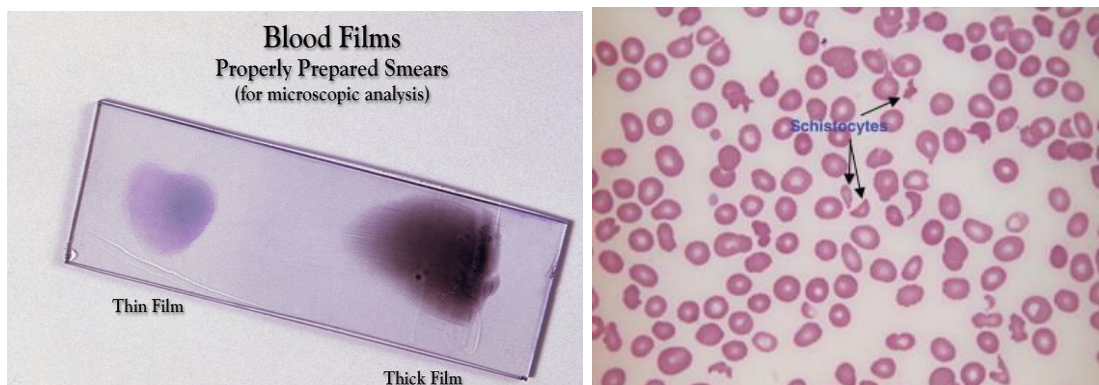


**Figure 73:** Left, Image of blood smear on a glass slide. This type of diagnosis is routinely used for the investigation of hematological disorders. Right, microscopy image of a blood smear showing schizocytes. We can notice the present of schizocytes which are fragments of RBC, compared to complete RBC (roundly shaped with a white dot in the middle due to their curvature).

- An **angiopathy** is a *pathology* i.e. disease of blood vessels. We can distinguish between macroangiopathy in arteries and veins and microangiopathy in capillaries.

- 
- **Thrombocytopenia** is the *condition* in which a patient has a low level of thrombocytes (known as platelets) in the blood. It requires emergency treatment for a platelet count below 50000/ $\mu$ L.
  - A **thrombus** is a blood clot resulting from *blood coagulation* and composed of platelets and red blood cells. Thrombus is a natural healthy response of the body to prevent bleeding but can be very harmful in the case of thrombosis, by clogging healthy vessels depriving cells and organs from oxygen.
  - **Von Willebrand factor vWF** is a large multimeric glycoprotein and produced constitutively as ultra-large vWF. It is present in blood plasma and involved in the *coagulation cascade* through platelets adhesion.
  - **ADAMTS13** is an enzyme specifically involved in the cleavage of high molecular weight **von Willebrand factor (vWF)** multimers.
  - **Disseminated intravascular coagulation (DIC or DIVC)** is a *condition* in which blood clots form throughout the body, blocking small blood vessels.
  - **Thrombotic MicroAngiopathy** or **TMA** is a *pathology* resulting in the formation of thrombus in micro-capillaries due to deterioration of the endothelial layer of the vessel. TMAs are a heterogeneous group of diseases characterized by (Oberic et al. 2009):
    1. MAHA
    2. peripheral thrombocytopenia
    3. organ failure of variable severity

TMAs can be divided in two subtypes: **thrombotic thrombocytopenic purpura (TTP)**, characterized by large bruises, fever and a variable degree of ischemic organ damage, particularly affecting the brain, heart and kidneys. And **hemolytic uremic syndrome (HUS)**, in which acute kidney failure is the major manifestation. TMAs are *very rare diseases*, the CNR-MAT (Centre de référence des microangiopathies thrombotiques coordinated by Professor Paul Coppo) in France reports 5 to 10 cases per million and per year in the country for TTP and similarly for the HUS.

TTP is usually associated with a severe ADAMTS13 deficiency leading to accumulation of unfolded vWF in microcirculation, causing intravascular vWF–platelet and platelet–platelet aggregation. As shown in **Figure 74**, the aggregates apply shear stress on RBC



and may break them, leading to hemolytic anemia (MAHA). And the recruitment of platelets implies the thrombocytopenia and leads to large bruises.

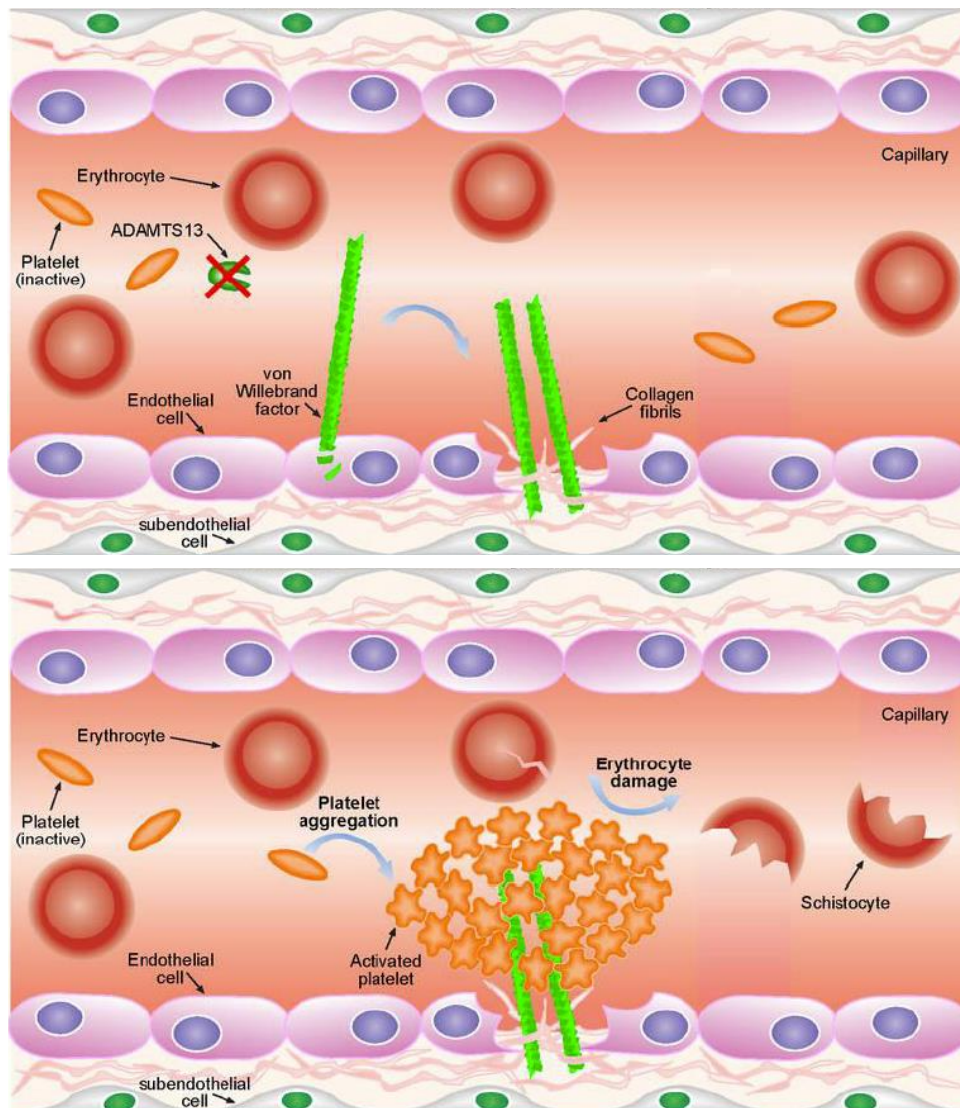


**Figure 74: Deficiency of ADAMTS13 in TTP.** The top picture shows the recruitment of large vWF because of an injury of the endothelial layer composing the capillary walls. The large vWF cannot be cleaved because of the deficiency in ADAMTS13. This implies in the second picture, the recruitment of many platelets forming a thrombus. The thrombus breaks the RBC, thus leading to hemolytic anemia. Illustrations from immunopaedia.org

Acute TTP was fatal until the introduction of plasma exchange (PE) with a healthy donor to replace the deficient ADAMTS13, which improves survival from <10% to 80–90% (Kremer Hovinga et al. 2017).

However, TMAs may also happen in a specific **context of solid tumors**, called “**cancer related TMA**” or “**cancer related MAHA**”, in which no deficiency in

---

ADAMTS13 is detected and plasma exchanges are ineffective (Babu K and Bhat 2016; Fontana et al. 2001).

We refer in the following similarly to “cancer related TMA/ CR TMA” or “cancer related MAHA/ CR MAHA” as first, the symptom and the disease are closely linked and referred in the literature with both terminologies (mainly as TMA in French medical literature and MAHA+TMA in English literature). Secondly, the MAHA is the major symptom used by clinician to diagnose CR TMA, indeed, the thrombocytopenia and organ failures are symptoms usually seen in cancer patients and may arise from many different factors, thus they are not specific.

#### 4.1.3.2 *Cancer-related thrombotic microangiopathy*

(Babu K and Bhat 2016) discriminate between 4 types of CR MAHA. We will mainly be interested in the last one but the cited literature may also refer to the other types.

The 4 types are classified by their assumed causes as follow:

1. Due to antibodies and immunotoxins
2. In the setting of bone marrow transplantation
3. As response to chemotherapy
4. A manifestation of cancer itself: as MAHA/TMA might be diagnosed correlated to cancer worsening or at cancer diagnosis from the outset, without any of the 3 previous reasons. In this case, the underlying biological mechanisms are still obscure, however, some hypothesis have been proposed in the literature as described below.

In general, very restricted literature is available on CR MAHA/CR TMA. Publications on the topic are mainly “reported cases” or reported cases joined with a review of previous work. However, two studies have been reported by (Ducos et al. 2014; Oberic et al. 2009). To our knowledge, the last review on the topic is (Takabatake and Oishi 2016). They introduce CR MAHA as a “nearly oncologic emergency” with very poor prognosis and necessitating a rapid chemotherapy intervention. We describe in the following the historical evolution of knowledge and hypothesis about potential mechanisms underlying MAHA development during cancer.

First description of CR MAHA was reported in 5 patients who developed hemolytic anemia in association with disseminated carcinoma by (Brain, Dacie, and Hourhirane 1962). They described in these patients (and twenty others who did not show evidence of carcinoma) ‘bizarre blood pictures, characterized by many contracted, distorted and fragmented red cells’ amorphous thrombi that could reduce the lumen of vessels and destruct the RBC. (Brain et al. 1970) showed observation of thrombus in arterioles of cardiac muscle (see **Figure 75**) and correlated the formation of thrombi to DIVC through thromboplastins derived from mucin-forming tumor cells. (Antman et al. 1979) reviewed several report cases and observed for four of their own patients, severe intimal proliferation of pulmonary arterioles at autopsy (see **Figure 77**). They also propose that the obstruction of the lumen is quite different from TTP and HUS cases as it may not necessarily be due to abnormal coagulation (like DIVC). 8 cases out of 55 support this hypothesis, as they showed normal coagulation parameters. Instead, Antman *et al.*



---

support that the hemolysis is caused by tumor cell emboli. Indeed, similarly to what we described for TTP in **Figure 74** with thrombus of large vWF and platelets, tumor cell emboli may mechanically block the capillaries and cause RBC breaking. This is confirmed by the fact that gastric cancers are prominent among patients with CR MAHA as some forms of gastric adenocarcinoma frequently metastasize via tumor emboli to pulmonary lymphatics and vasculature.

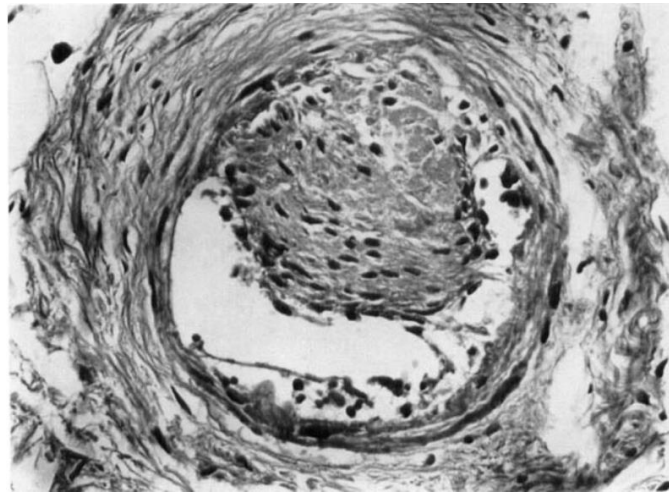


**Figure 75: Thrombus in arteriole in myocardium stained with Hematoxylin and eosin. Extracted from** (Brain et al. 1970)

(Oberic et al. 2009) describe atypical features present in 20 patients diagnosed with CR TMA, such as bone pain and wasting, erythroblastosis. Moreover, DIVC seems to be a good indication factor that might alert to look for complementary investigations to show evidence of disseminated malignancy in particular in patients with cancer antecedents.

(Ducos et al. 2014) made a cohort study of 17 CR TMA patients compared with TTP patients. They showed that acute respiratory failure, bone pain, anorexia and weight loss seems to be more frequent in CR TMA patient, whereas neurological symptoms are less frequent and platelet levels are higher than usually seen in TTP. Median ADAMTS-13 activity was about 62%.

Despite the few hypothesis and literature described above, the cancer related MAT/MAHA remains a poorly understood disease with fatal consequences and by its rarity, highly difficult to study.

#### 4.1.3.3 *First experiments and clusters images*

In February 2017, a patient treated in Curie Institute was diagnosed with MAHA related to a breast carcinoma. In order to elucidate the hypothesis of tumor emboli in capillaries, we decided to analyze a blood sample from this HER2+ breast cancer patient (referred to as patient P1) using the Ephesia device.

After cell capture, immunostainings were performed to discriminate CTCs from WBCs. We observed both single CTC (as usually) as well as clusters of CTC and WBC (see **Figure 76**).

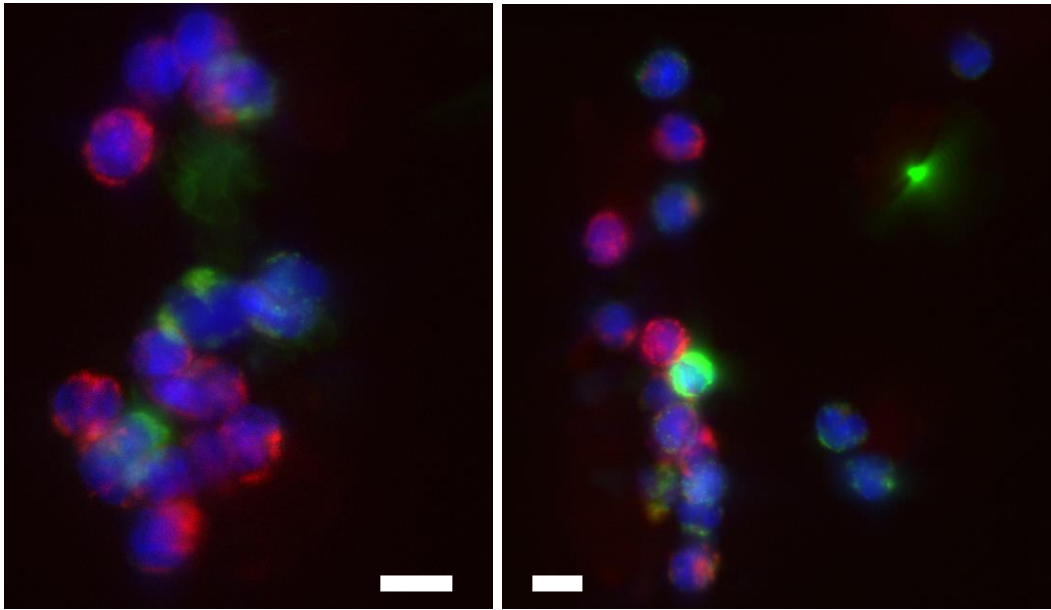


**Figure 76:** Images of CTC and WBC clusters captured in the Ephesia chip. Left, 90x magnification. Right, 60x magnification. Blue is Hoechst staining. Green is Cytokeratin staining. Red is CD45 staining. Scale bars are 15 $\mu$ m.

As far as we know, this is the first reported observation of clusters composed of WBCs and CTCs in blood of a patient diagnosed with cancer related TMA/MAHA. Furthermore, it is in accordance with the observation made by (Brain et al. 1970) in **Figure 75** and by (Antman et al. 1979) of tumor emboli in arteriole at autopsy (see **Figure 77**).

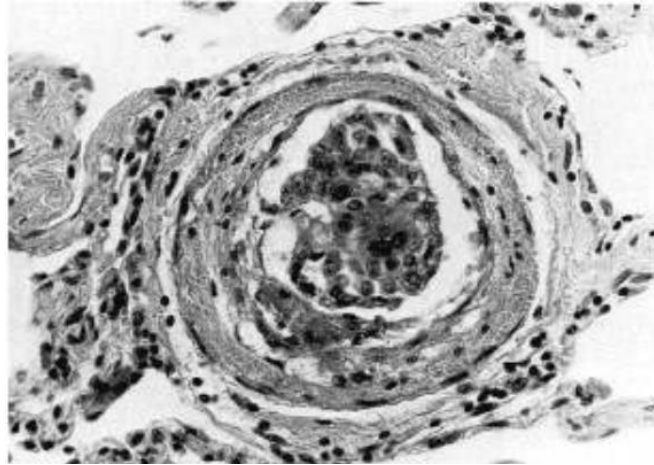


**Figure 77: Photomicrograph of a tumor emboli in pulmonary arteriole at autopsy (Staining H&E). Extracted from (Antman et al. 1979)**

On an other hand, CTC clusters have already been reported in the literature (Aceto et al. 2014; Jolly et al. 2017) for several types of cancer without a specific link to CR MAHA or CR TMA. They are assumed to be associated with cancer dissemination, as clusters of cells should better survive in circulation and proliferate more rapidly in distant organs to form metastasis. The main differences as compared to our case, consist in the fact that these patients do not necessarily present MAHA symptom and that the clusters we observed contains many of WBC.

As described in the following sections, we confirmed the presence of these clusters for several other samples from patient P1 and three other patients P2, P3 and P4, diagnosed with CR-MAHA and observed similar clusters with roughly a high variability in clusters size and composition across samples.

We thus decided to use and develop in parallel to Ephesia, other techniques and protocols to isolate and collect these clusters and to perform their molecular characterization in order to better understand the mechanisms leading to this invasive phenotype, massively pathogenic in the context of cancer related MAHA.

#### 4.1.3.4 *Patients description*

We report in the following, a brief description of the patients' diseases, treatments and clinical conditions:

- **Patient P1:**

30 years' old

12.2013: invasive breast carcinoma, no specific subtype (left side), cT2N+M0 ER+ PR+ HER2+

→ tumor sample #1

Neoadjuvant chemotherapy with anthracyclin, taxane and trastuzumab

06.2014: mastectomy and axillary clearance : absence of pathological complete response (ypT2N2)

→ tumor sample #2

adjuvant trastuzumab, radiation therapy and tamoxifen

06.2016: metastatic relapse (liver, lung, nodes, peritoneal carcinomatosis) with intracranial hemorrhage related to synchronous MAHA

5FU PERTUZUMAB TRASTUZUMAB then TAXOL PERTUZUMAB TRASTUZUMAB, 6 cycles

01.2017: maintenance with ENANTONE LETROZOLE PERTUZUMAB TRASTUZUMAB

→ 02.2017 First CTC sampling

02.2017: isolated brain tumor progression => brain radiotherapy

03.2017: disease progression and new MAHA crisis => 5FU TRASTUZUMAB => TAXOL TRASTUZUMAB

05.2017: persistence of MAHA

→ 07.2017 Last CTC sampling

FEC-TRASTUZUMAB

08.2017: death

- **Patient P2:**

65 years' old

2002: Prostate adenocarcinoma T2N0M0, Gleason 7

Endocrine therapy and radiation therapy

2010: increasing PSA levels, endocrine therapy

2016: increasing PSA levels, endocrine therapy (abiraterone)

04/2017 : MAHA and tumor progression in bone marrow

→ CTC samplings between 04.2017 and 06.2017

Chemotherapy by DOCETAXEL

10/2017: maintenance by endocrine therapy (enzalutamide)

Patient lost to follow-up

---

- **Patient P3:**

52 years' old

05/2009: invasive breast carcinoma, lobular subtype (left side), cT2N2M0 ER+ PR-HER2-

Surgery followed by adjuvant chemotherapy (anthracyclines and taxanes), radiation therapy and Tamoxifen

02/2015 : bone metastases, endocrine therapy (Fulvestrant)

11/2015 : disease progression, endocrine therapy (Letrozole)

07/2016 : disease progression (peritoneal carcinomatosis); endocrine therapy (Exemestane-Everolimus)

12/2016 : disease progression, endocrine therapy (Fulvestrant + Palbociclib)

04.2017: MAHA, disease progression. Chemotherapy (5FU)

→ CTC samplings between 04.2017 and 05.2017

05.2017: death

- **Patient P4:**

01.2018: invasive breast carcinoma, no specific subtype (left side), cT4N+M1 (liver, bone, nodes, lung), ER- PR- HER2+. MAHA present at diagnosis.

→ tumor sample #1 & 1 CTC sampling

5FU TRASTUZUMAB PERTUZUMAB followed by TAXOL TRASTUZUMAB PERTUZUMAB

Patient still alive (as of 01.2019)

## *4.2 Techniques of investigation & results*

### *4.2.1 Ephesia experiments*

#### *4.2.1.1 Controls and protocol biases*

We had to eliminate the possibility that our experimental protocol may generate the cell clusters, and thus bias our reasoning. Indeed, during the validation of Ephesia platform by Julien Autebert and in some negative controls from healthy donors, clusters of cells were observed in few samples and were linked to the activation of the coagulation cascade probably due to inappropriate use of anti-coagulation tubes (not homogenized enough after sampling). The second hypothesis, was that the RosetteSep could generate the clusters. Indeed, the principle of the RosetteSep, as described in the Appendix, is to use tetrameric antibodies targeting RBC and RBC from the two sides or RBC from one side and WBC from the other. Thus, forming a “rosette” or a cluster of WBC surrounded by RBCs (RBC to WBC ratio in blood is around 500). In this way the RBC transport the WBC to the bottom during centrifugation and the MNC layer is enriched in CTCs.

First, strong recommendations at each sampling were communicated to the nurses’ staff to carefully homogenize the tubes (EDTA or Cellsave) immediately after sampling. Secondly, to eliminate the hypothesis of rosettes can sterically block CTCs with WBC, we used in about 19 of the described experiments, Ficoll gradient only without RosetteSep.

The same clusters observations were made indifferently with both techniques (see sections of staining observations). Additionally, this hypothesis can poorly be valid as most of the RBC are removed after the density gradient sorting and no RBC was observed in the aggregates. Finally, the clusters were later also observed in CellSearch (see **Figure 82** for patient P3) and ISET experiments which use a different preparation protocol and a different CTC capture method.

---

#### 4.2.1.2 Observations & comments for the four patients

Table 6: Summary of Ephesia experiments for each patient

Patient	Total Ephesia	Staining	WES	Only capture	RNAseq bulk	RNA seq CellCelector
P1	13	8	2	5	2	3
P2	5	3	2	2	0	2
P3	4	3	2	1	0	1
P4	1	1	1	0	0	0

Table 6 resumes the experiments performed with Ephesia. The blue part indicates experiments with fixed cells from CellSave tubes or EDTA tube with fixation in chip. The cells were stained and imaged, then stored and later used for Whole Exome Sequencing. The green part indicates experiments with non-fixed cells (necessarily EDTA tubes) for whom Ephesia is used only for CTC “capture only” without fixation and staining. These cells were collected, after beads release, in lysis buffer RLT as a bulk suspension or as individual cells/clusters of cells using the CellCelector picking system.

#### 4.2.1.3 Bright field injection recording

After the third experiments performed with samples from patient P1, we also started to record bright field movies of cell injection in Ephesia device with a small Dino camera mounted on the microscope (Dino-Eye AM4023CT, Dino-lite). This allows us to carefully observe the behavior of the cells and clusters of cells during injection.

We observed thanks to these movies that some cell aggregates, as shown in the movie given in the Appendix, can travel through the array without being captured and sometimes being dismantled by the shear stress. Moreover, few other observations show that sometimes the aggregate, if big enough, can destroy the array of magnetic column, opening a preferential pathway for cells by locally reducing the hydraulic resistance. Thus, a certain number of cells are not captured in the chip because of such events.

We explain that by the fact that the column distance is optimized for individual cells and thus aggregates of this size may be prone to too high shear stress and flow at higher speed. Moreover, the cells composing the cluster are not necessarily EpCAM+, they can be WBC or EpCAM- CTCs. An alternative to capture and analyze these cells was to collect them and use the ISET filters (see dedicated section).



#### 4.2.1.4 Staining observations & discussion

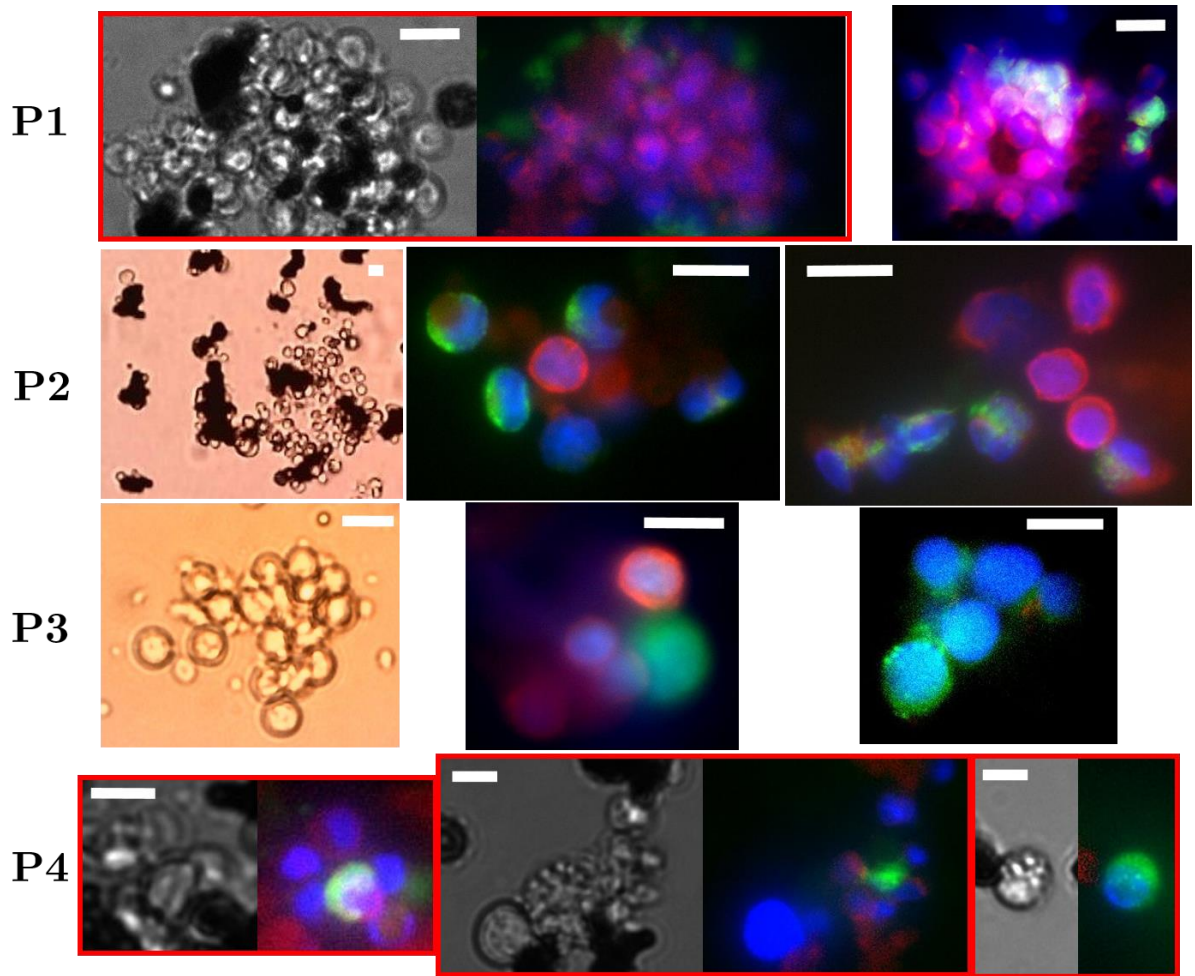


Figure 78: Images of cells/clusters of cells captured or flowing through Ephesia chip for each patient. The images coupled together with a red rectangle are, respectively from left to right, bright field and composite of three staining of the same position. The blue, green and red staining colors correspond nucleus, cytochrome and CD45 respectively. Scale bar is 15µm.

In all samples from the four patients, cells aggregates have been observed during cell injection in Ephesia device and in experiments with staining. In particular, in the staining experiments, we observed individual CTCs and also clusters of cells composed of CTCs and WBC, as shown in Figure 78. We can also notice in this figure the variability on the number of cells per cluster (sometimes referred at as “cluster size”). Indeed, as a rough estimation, this number varies from 2 to more than 25 cells. It is worth noticing that the height of the chip (50µm) limits the number of cells in the Z-direction as it might apply a mechanical stress on the cluster at the chip inlet, combined to the flow shear stress. Besides that, superposition of cells was observed inside the clusters. So when this case was observed, we took z-stack images and either take the



---

most representative stack or make an average intensity projection to obtain the final image in Figure 78.

No particular correlation between size of the aggregate or their composition (percentage of WBC vs CTCs) and patients' condition (at time of sampling) can be asserted as quantitative results on these observations could be poorly relevant. Indeed, as reported in the previous paragraph, the clusters that perturbs the homogeneity of the column array and creates preferential pathways makes the comparison even between two capture chambers of the same chip with the same sample, completely irrelevant.

#### ***4.2.1.5 Conclusion on Ephesia staining***

For all these reasons, we consider the imaging and staining experiments in Ephesia device only from a qualitative aspect and no quantitative results, for example CTCs count for comparison with CellSearch, as previously reported in (Autebert et al. 2015), are presented. Furthermore, being aware and mindful to the benefits but also to the disadvantages of Ephesia system, we looked up for many different tools and characterization possibilities available in the facilities of Curie Institute, either to complement the workflow of Ephesia after CTC capture or to have a different way of enrichment (avoiding the EpCAM+ biasing by ISET or allowing quantitative CTC enumeration by CellSearch).

### 4.2.2 Methods of investigation

We investigated several methods of enrichment and characterization of circulating tumor cells. In the following section, we describe three other techniques (CellSearch, ISET and PDX) that we tried to implement in parallel to Ephesia experiments. Moreover, we will discuss the versatility of Ephesia platform and how we did use it, complementary to CellCollector system and Next-generation sequencing, to capture and characterize CTCs from the four patients in order to investigate the underlying genetic or epigenetic mechanisms of Cancer Related TMA.

**Figure 79** shows an example of the workflows used and pictures representing some of the techniques used. Workflows vary depending on the availabilities of the systems and the number of blood tubes that could be obtained. The types of tubes for blood sampling vary also depending on the technique: CellSave tubes (**CS**) for Cellsearch and Ephesia staining experiments or **EDTA** tubes for other systems and Ephesia experiments targeting RNA sequencing.

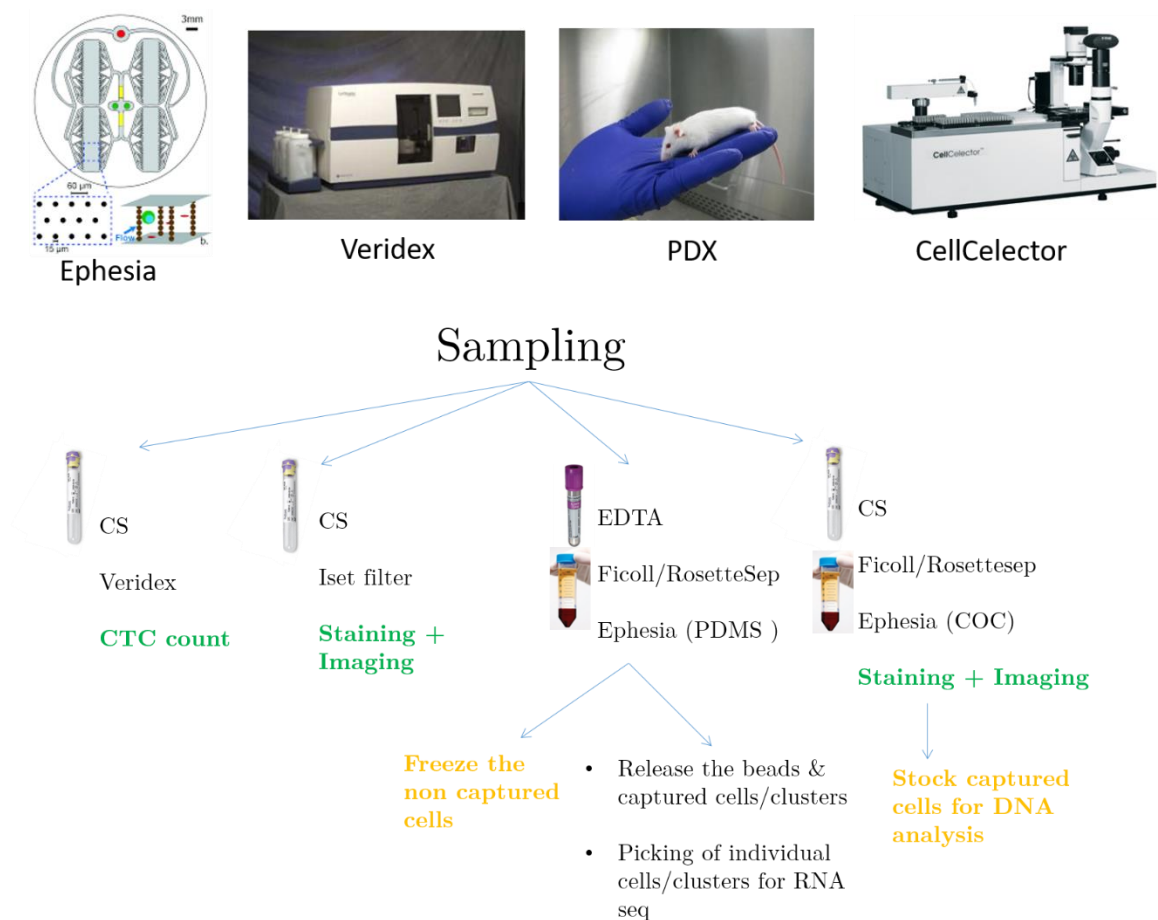


**Figure 79:** Upper pictures show few techniques for the enrichment and characterization of CTCs from CR-TMA patients. The schema below gives an example of workflow from

sampling to different characterization methods employed to observe, stain, count or recover enriched cells for next-generation sequencing.

#### 4.2.2.1 Ephesia processing

Most of the technological development of the Ephesia device microfabrication in the two materials (PDMS and COC) was achieved during the previous thesis. However, we decided to report the detailed protocols of Ephesia fabrication in the Appendix. As, first, few optimizations in the COC protocol were performed during my PhD work, second, both versions of the device have to be mastered to perfectly process precious samples in the device. Thus, the composition and fabrication of the system must be understood by the reader before going to its uses.

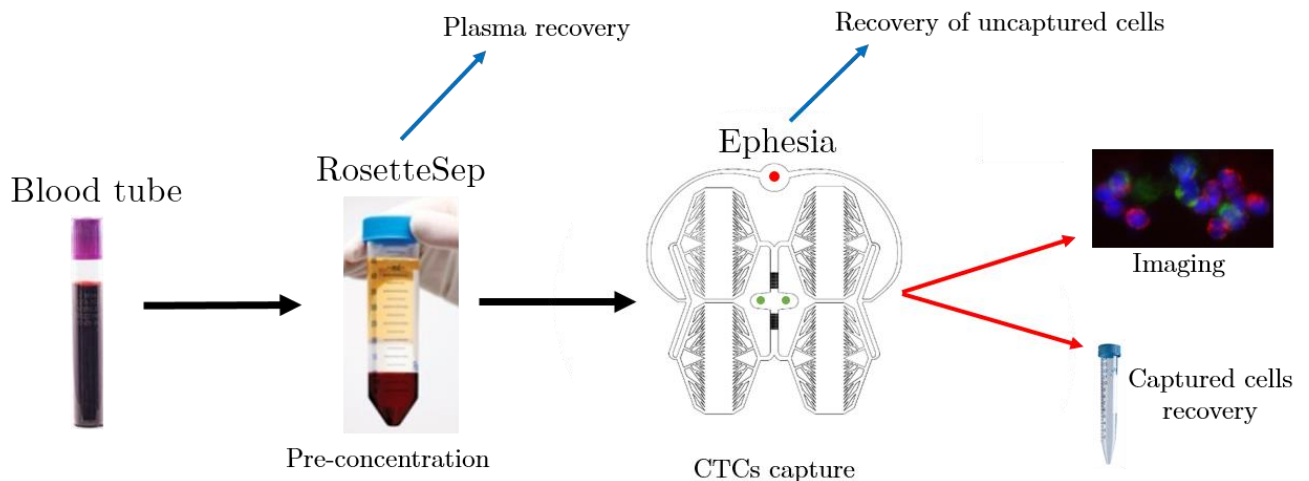


Figure 80: Ephesia experiment's workflow.

A summarized description of Ephesia experimental workflow is given in Figure 5. The process involves a pre-sorting step (by RosetteSep or Ficoll) based on immune and/or density enrichment of CTCs by removing RBC (and WBC) from the sample. Details about RosetteSep can be found in the Appendix. Then, the enriched sample resuspended in about 300 $\mu$ L is injected in Ephesia chip for CTCs capture. The captured cells can either be stained and imaged and/or recovered by releasing the magnetic columns and characterized by downstream analysis.

**Novel use of Ephesia:**

We tried to implement for the first time, the enrichment made on Ephesia in combination with CTC characterization by Next-generation sequencing. To do so, the fixed cells (stainings experiments) were used for Whole Exome Sequencing (WES). Also, specific experiments, targeting RNA sequencing, were performed in which the captured cells (without fixative) were released and picked as clusters or individual cells thanks to the CellCelector system.

Furthermore, it is possible during this process to also recover blood plasma at pre-concentration step (done for 90% of the experiments) and recover uncaptured cells (PBMC, EpCAM- CTCs and uncaptured clusters) during sample injection in Ephesia. This versatility of Ephesia platform allows also parallel molecular characterizations from the same blood sample.

#### 4.2.2.2 Veridex, CellSearch system

CELLSEARCH® technology by Menarini Silicon Biosystems is a CTC system based on EpCAM immuno-capture of CTC using superparamagnetic nanoparticles. The automate performs a centrifugation of blood stored in a CellSave tube; as in Ephesia workflow, then mix the cells with the nanoparticles of EpCAM+ enrichment in CTC. The cells are then stained with DAPI, Cytokeratin and CD45. After washing, the suspension is transferred in a “CellTrack” cartridge containing a glass slide and a magnet. Acting on the nanoparticles, the magnet will flatten the cells on the glass slide for imaging. The system automatically recognizes “events” of CTCs as DAPI+ CK+ and CD45- in a physiological range of cell size. It generates a report in which a trained used will confirm or reject the events.

Total blood stored in CellSave tubes was processed in the Cellsearch system available at the BTC lab in Curie Institute. The counts of CTC made on 11 samples from patients P1, P2 and P3 are presented in **Figure 81**.

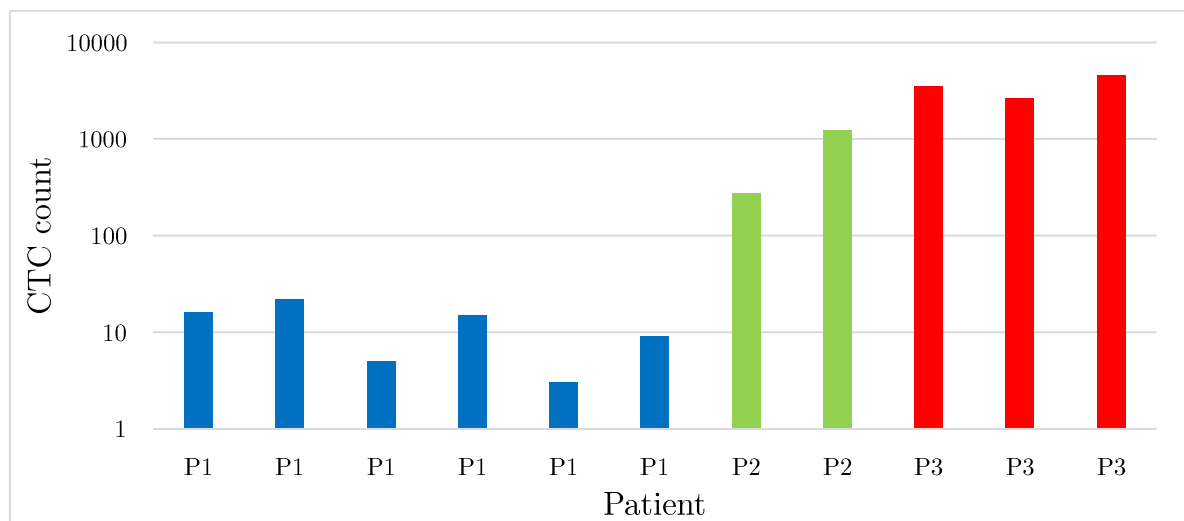


**Figure 81: CTC counts made on CellSearch system for the 3 patients P1, P2 and P3.**

We can describe and complete the data of **Figure 81** as showing that for:

- patient P1 the number of counted cells is between 3 and 22 over 6 months
- patient P2 it highly increases from 273 to 1212 in 3 days
- patient P3 it varies around ~3500 in 2 weeks

Discussion of Cellsearch results:

Individually for each patient or across the three, no specific tendency can be correlated to the patients' condition or the CR TMA. Indeed, for example, for patients P1 and P3 the last counts were performed few days before disease worsening and death, and show a high difference in number. And for patient P2, the increase between the two samples was indeed during worsening of the disease, however the patient recovered after that thanks to chemotherapy and endocrine therapy but was unfortunately lost to further follow-up.

On the other hand, the CellSearch system provides us the confirmation of the presence of cell aggregates as shown in **Figure 82**. The cells' clusters were mainly present in patient P3, only few in patient P2 and none were seen in patient P1. Nevertheless, this variability can be correlated to the number of CTC detected in each patient. Also, the CellSearch system reports only CK+ CD45- cells. So, if a cluster is composed of cells that are not necessarily CK+ or mainly of WBC (CD45+), it might not be detected as a possible "event" by the automated imaging platform of the system. Indeed, as shown in Figure 82, the few events selected containing WBC shows at maximum 2 WBC contrary to Ephesia experiments where we observed sometime more than 10 of WBC in the same cluster.

As future perspectives on the use of the CellSearch system in our project, we are planning to analyze individually the reports generated at least for patient P3. In this case, we may be able to extract quantitative information (by an automated image analysis) about the size of the clusters and their composition, even if the bias of the machine selection of events must not be neglected.

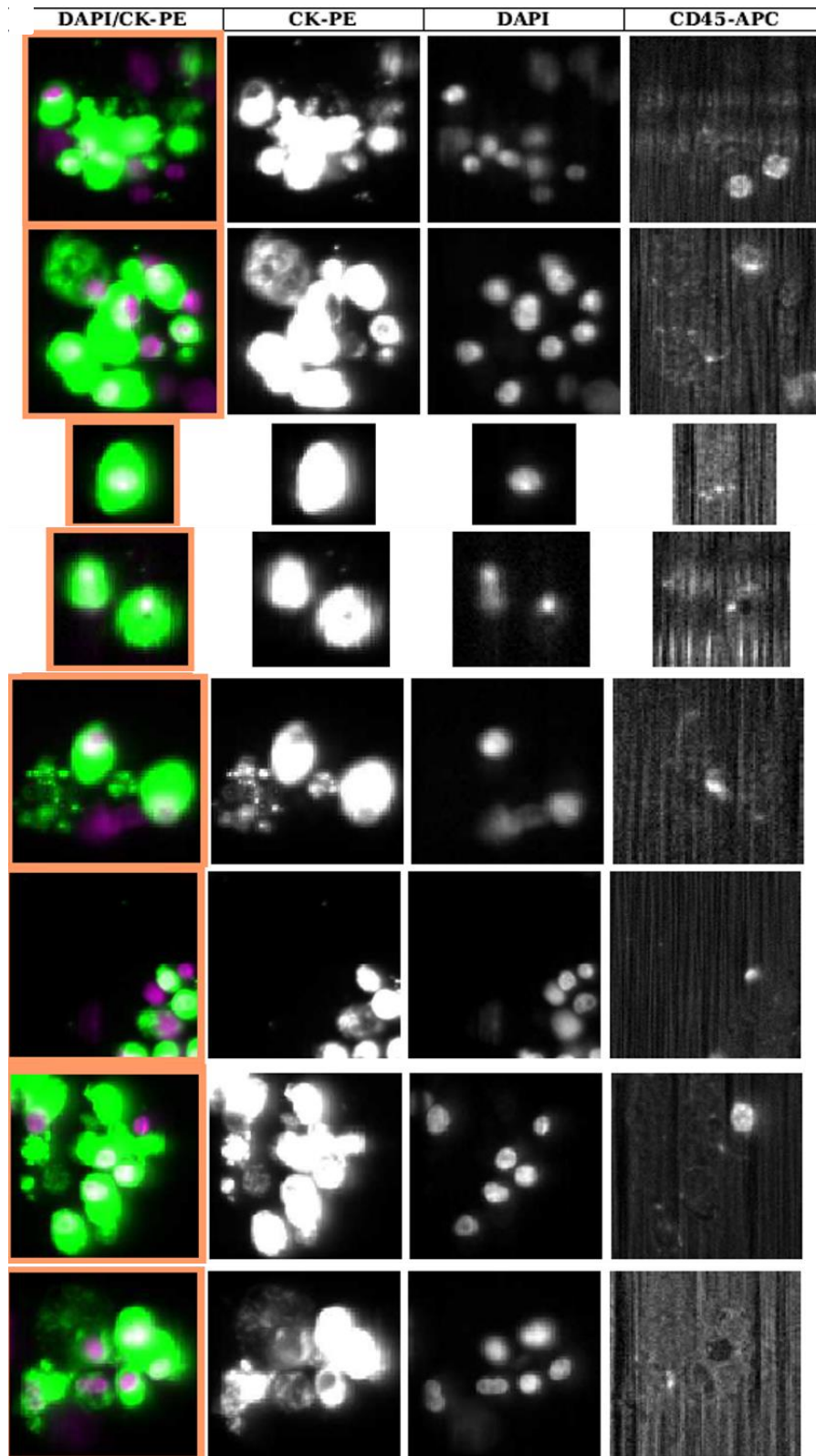
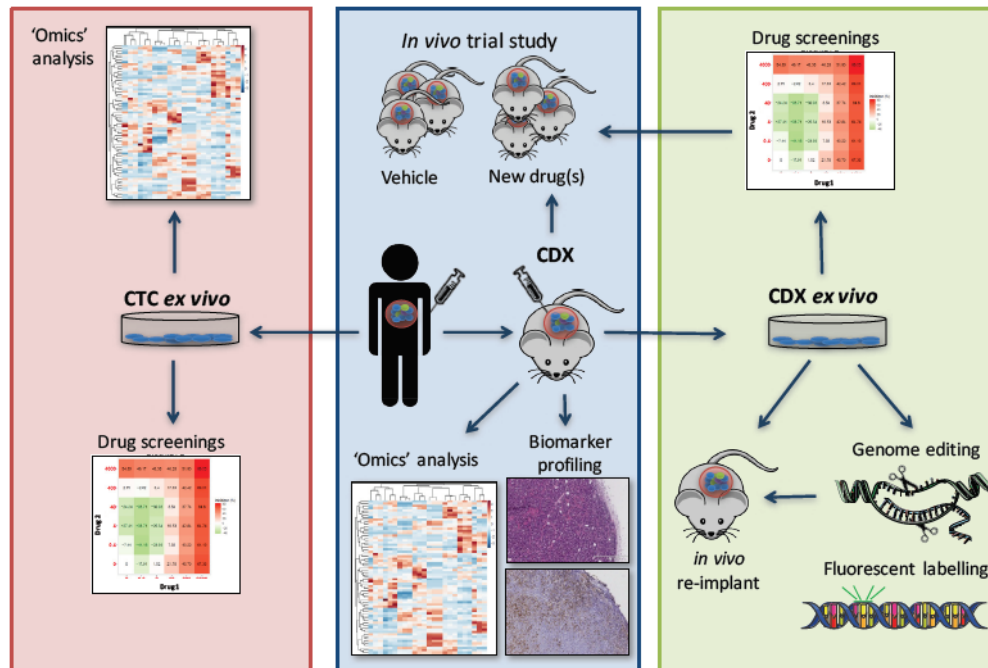


Figure 82: Screen captures of a CellSearch report for a sample from patient P3. Each row is an “event” detected by the machine, and the columns show the different stainings. We selected few events showing clusters of CTCs that sometimes include also WBCs. However, many single cells were also detected as shown in the third row. Unfortunately, scale bars could not be provided from the report.



### 4.2.2.3 Patient Derived Xenografts

We tried to develop a **Patient Derived Xenograft (PDX)** for the patients P1, P2 and P3. This technic consists on implanting patient's cancer tissue or cells in an immuno-deficient or humanized mouse to develop models of cancer that can be used for example in drug screening or biomarker profiling (see **Figure 83**, (Lallo et al. 2017)). However, the success rate of implantations has a high variability (9% to 90%) depending on the cancer type and grafting site (Jung, Seol, and Chang 2018).



**Figure 83:** Comparison between CTC culture ex vivo (with its uses, red rectangle) and CDX (with its potential uses, blue & green rectangles). Extracted from (Lallo et al. 2017)

In our case, we wanted to test the possibility of developing a mouse model of “cancer related TMA”, which would allow us to study this disease in a different manner than in the other described systems. As most of the patients showed a high level of CTC counts in the CellSearch system, we used blood as a source of tumor cells to be implanted. Starting from total blood, CTC enrichment was achieved by RosetteSep method and the cells were then injected in the mice.

The implantation was performed by Nemati Fariba from the department of translational research on immune-deficient mice. Two implantations were performed from patient P1, one from patient P2 and one from P3. Unfortunately, three out of four implantations (P1 and P3) did not show any tumor growth and the fourth one (P2), showing signs of growth, died before the intervention of the manipulator. Therefore, this technic was not successful because none of the PDX tests could be used as a cancer



---

model or for further molecular characterization of the tumor cells. We explain this by the low number of trials performed and the high variability of engraftment rate as described by (Jung, Seol, and Chang 2018).

#### 4.2.2.4 ISET filters

ISET technology is CTC sorting device based on CTC size and deformability. It uses a polycarbonate membrane containing 8 $\mu$ m-diameter pores in which the RBC and WBC can pass through; thanks to either their size or their deformability; whereas CTCs are expected to be blocked as they might be bigger and stiffer (Laget et al. 2017; Vona et al. 2000).

ISET filters available in the BTC lab, have been used in this project as a supplementary non-EpCAM biased method for CTC capture. Indeed, observations during sample injection in the Ephesia device have shown that some clusters of cells can pass through the array of beads without being captured by the EpCAM antibody coated beads. Therefore, these filters constitute a good alternative as a non-immune biased method and also a purely mechanical barrier to clusters. Furthermore, the ISET filters could allow staining and imaging of cells or their recovery for molecular characterization.

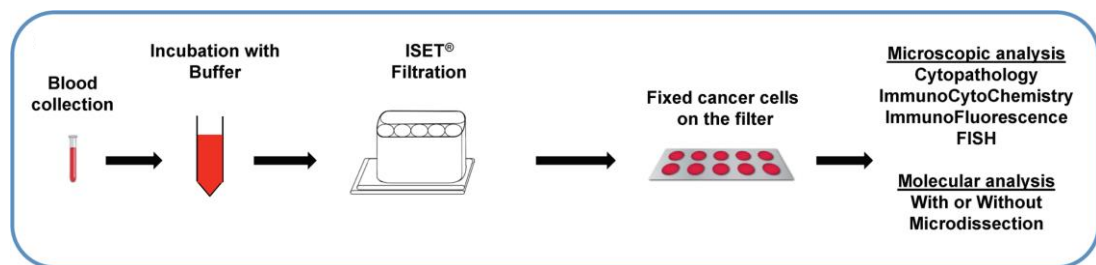


**Figure 84: ISET system workflow.** Extracted from (Laget et al. 2017)

The ISET filters were used with samples from the patients P1, P2 and P4 (3 samples from P1, 5 samples from P2 and 1 sample from P4). The bright field images of the filters confirm the presence of clusters of cells as observed previously with Ephesia. However, the staining protocol with this technique was not yet optimized at the time of sampling. So, the cells captured on the filters were fixed and stored until further analysis. And for this reason, we will not discuss more the use of this method in the following sections of this manuscript.

#### 4.2.2.5 *CellCelector*

The CellCelector is an automated system developed by ALS Automated Lab Solutions GmbH for targeted selection and isolation of single cells. The system consists in a fluorescence microscope combined with an automated XYZ pipetting robot able to aspirate/pick a single cell visualized under the microscope and release it in a microtiter plate thanks to 30µm glass tip. The device is placed under a hood allowing sterile conditions, and is controlled from outside the hood by a computer and a dedicated software.

We used this system in order to isolate single cells or the clusters of cells observed previously in order to perform RNA-sequencing and compare their phenotype to the ones of the corresponding tumors. To do so, we first enriched a blood sample thanks to Ephesia device as usual, but without the staining step in order to avoid cell fixation. The Ephesia experiment was stopped right after cell capture. The magnetic field was turned off to release the beads with captured cells on them, as described previously in this chapter and showed in the video (link in the Appendix). The cells/beads were collected in a PBS (1%BSA) solution and resuspended before plating them on the magnetized glass slide of the CellCelector. As shown in **Figure 85**, this aligns all the beads and allows good visualization of the cells before picking. A video link is also available in the Appendix, showing the cell selection and automated picking and release of a cell cluster in a dedicated micro-titer plate.

Collection of single cells and clusters made in this manner was performed as reported in **Table 6**, for 6 samples in total: from patients P1 (3 samples), P2 (1 sample) and P3 (2 samples). The cells were released in Buffer RLT<sup>2</sup> and stored at -80°C. We did not process to RNA extraction and samples preparation for RNA sequencing at this time, to focus first on whole exome sequencing and RNA sequencing of the tumors. The future treatment of these samples will be continued later in the project and is discussed in the perspectives of this chapter.

---

<sup>2</sup> Buffer RLT is a lysis buffer for lysing cells and tissues prior to RNA isolation and simultaneous RNA/DNA/Protein isolation. The exact composition of Buffer RLT is confidential. This buffer is a proprietary component of RNeasy Kits (Qiagen). Buffer RLT contains a high concentration of guanidine isothiocyanate, which supports the binding of RNA to the silica membrane.

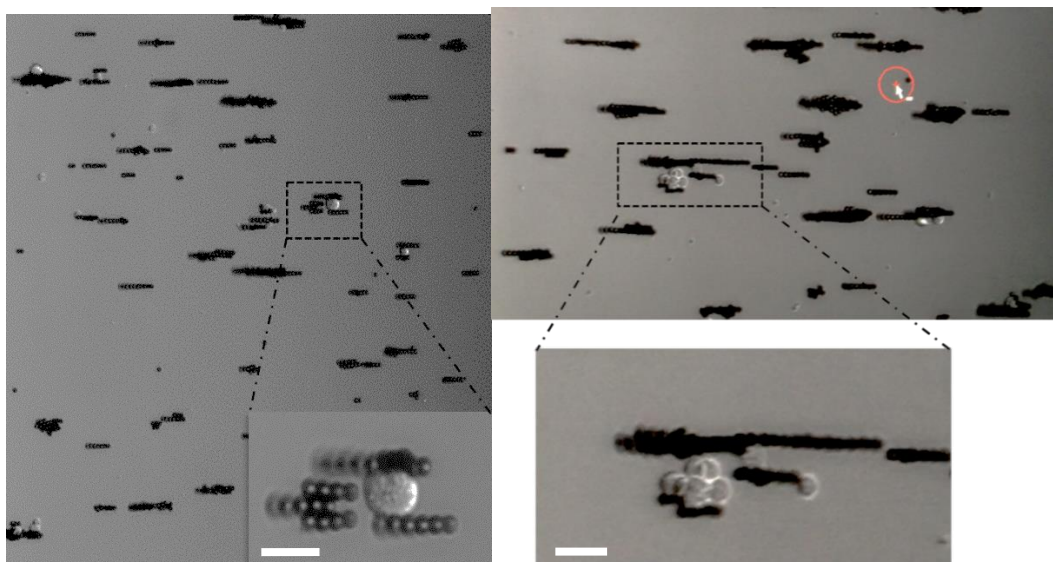


Figure 85: Images of cells and beads aligned thanks to a magnetized glass slide before picking of the cells with the CellCelector. Scale bar is 20 $\mu$ m.

#### 4.2.2.6 *Conclusion on the different methods of investigation*

To have a general view on the different techniques used, we can summarize as following:

- The four PDX implantations were not successful and can be explained given the complexity of the mechanisms involved and the success rates reported in the literature.
- Iset filters confirm the presence of clusters but are still waiting for staining to identify the composition of the aggregates.
- Cellsearch experiments report also clusters detection mainly for patient P3. The cell counts can, however, difficultly correlate with the clinical data. Further analysis of the Cellsearch reports must be perform to obtain quantitative data on clusters size and composition.
- Both Cellsearch cartridges and Iset filters can be used as DNA material resources, if needed for further analysis.
- Ephesia was used for cluster identification by staining and also as a simple enrichment tool combined for the first time with the CellCelector system. The cells recovered from staining were also used for DNA extraction that serves in Whole Exome Sequencing. This versatility of the Ephesia platform has a promising potential for CTC characterization in combination with NGS techniques.

### ***4.2.3 Whole Exome Sequencing***

#### ***4.2.3.1 Samples collection & DNA extraction***

For the four patients diagnosed with CR-MAHA in Institut Curie Hospital, we have performed a **Whole Exome Sequencing (WES)** on three types of samples for each patient. When available, these three types of samples were collected:

- 1) “Normal” healthy samples collected from a buccal swab or total blood or the peritumoral tissue. This type of sample is referred to, in the following, with the letter ‘S’ and may also refer to it in the next sections as “germline”.
- 2) “Tumor” samples extract of the tumor biopsy. This type is referred to, in the following, with the letter ‘T’ and may also referred to it in the next sections as “somatic”.
- 3) “CTC” samples are circulating tumor cells enriched thanks to Ephesia device and used for our experiments of imaging. The cells were fixed and stained then released and stored in PBS(1%BSA) at 4°C for few weeks/months before extraction.

**Our aims at this stage** are, first, to understand if there is a putative DNA mutation common to the four normal patient’s samples (S). Then, mutations of Tumor and CTC samples will be compared to the normal sample or the mutation of CTC will be compared to the ones observed in Tumor samples.

Normal and Tumor samples were given by the tumor bank as DNA extracts (Phenol–chloroform extraction). For CTC, DNA extraction was performed, using Silica membrane extraction (kit Nucleospin 8 tissues), by Anne Schnitzler from the genetic service of Pharmacogenomics unit. We then quantified all the samples using Qubit 3.0 and transferred them to NGS platform of Institut Curie for library preparation and sequencing. The sample plan for library preparation and sequencing is given in **Figure 86**.

Patient	Sample type	Quantity (ng)	Biological name	Sequencing depth	Dosage Qubit ng/ $\mu$ l
P1	Healthy (peritumoral)	374.0	P1_S	100x	37.4
	Primary Tumor	50.3	P1_T1	100x	148
	Primary Tumor	49.6	P1_T2	100x	171
	CTC	3054.9	P1_CTC1	100x	61.10
	CTC	34.8	P1_CTC2	100x	0.70
P2	Healthy (buccal swab)	62.0	P2_S	100x	6.2
	CTC	128.6	P2_CTC1	100x	2.57
	CTC	36.2	P2_CTC2	100x	0.72
P3	Healthy (total blood)	24.3	P3_S	100x	48.5
	CTC	560.5	P3_CTC1	100x	11.21
	CTC	448.9	P3_CTC2	100x	8.98
P4	Healthy (total blood)	5000.0	P4_S	100x	350
	Primary Tumor	5000.0	P4_T	100x	112
	CTC	26.5	P4_CTC	100x	0.53

**Figure 86: WES sample plan**

We can notice in **Figure 86** a huge heterogeneity in DNA samples quantity after DNA extraction (between 24ng and 5000ng). Surprisingly, there is no obvious correlation between the sample quantities and types. Indeed, we could have expected lower DNA quantities for CTC compared to healthy and tumors samples. However, for healthy and tumor samples the number of cells depend on the size of the biopsy and its nature (tissue gives higher amount than buccal swab for example) and the quantity given by the tumor bank for our project which can explain the variations observed.

In the case of CTC, an explanation could be given by the CTC counts made on the CellSearch system at the same period as Ephesia experiments. For patient P3 three count were performed (2606, 3509 and 4596 CTCs for each count) which are values notably high and correlate with the amount of DNA extracted (560ng and 448ng). Patient P2 has a CTC counts at 273 and 1212 three days apart, showing a high variability that is also observed on the DNA amount made 10 days later. Sample P1\_CTC2 is also in accordance with the CTC counts (between 3 and 16) whereas the sample P1\_CTC1 is abnormally high compared to all other results.

We will see in the next section that it sequencing quality check results were also outliers. No CTC count was performed for the sample of patient P4. Nevertheless, one should keep in mind that a nonspecific capture of WBC is always present in both devices

depending on the blood sample freshness and composition and thus may vary between experiments.

#### 4.2.3.2 Library preparation

Library preparation was first performed by the NGS platform using the Agilent SureSelect XT-HS kit on its first commercial version. Unfortunately, this preparation failed as a difference of 100bp, compared to expected value, was observed at the pre-capture step (see **Figure 87**). Previously, this kit was successfully validated by the platform on a beta version but the commercial version showed unexpected default even on other samples processed by the supplier Agilent. This problem led to loss of rare samples: P1\_T2, P1\_CTC2 and P2\_CTC2. Supplementary material was still available or could have been provided by the tumor bank for the other samples.

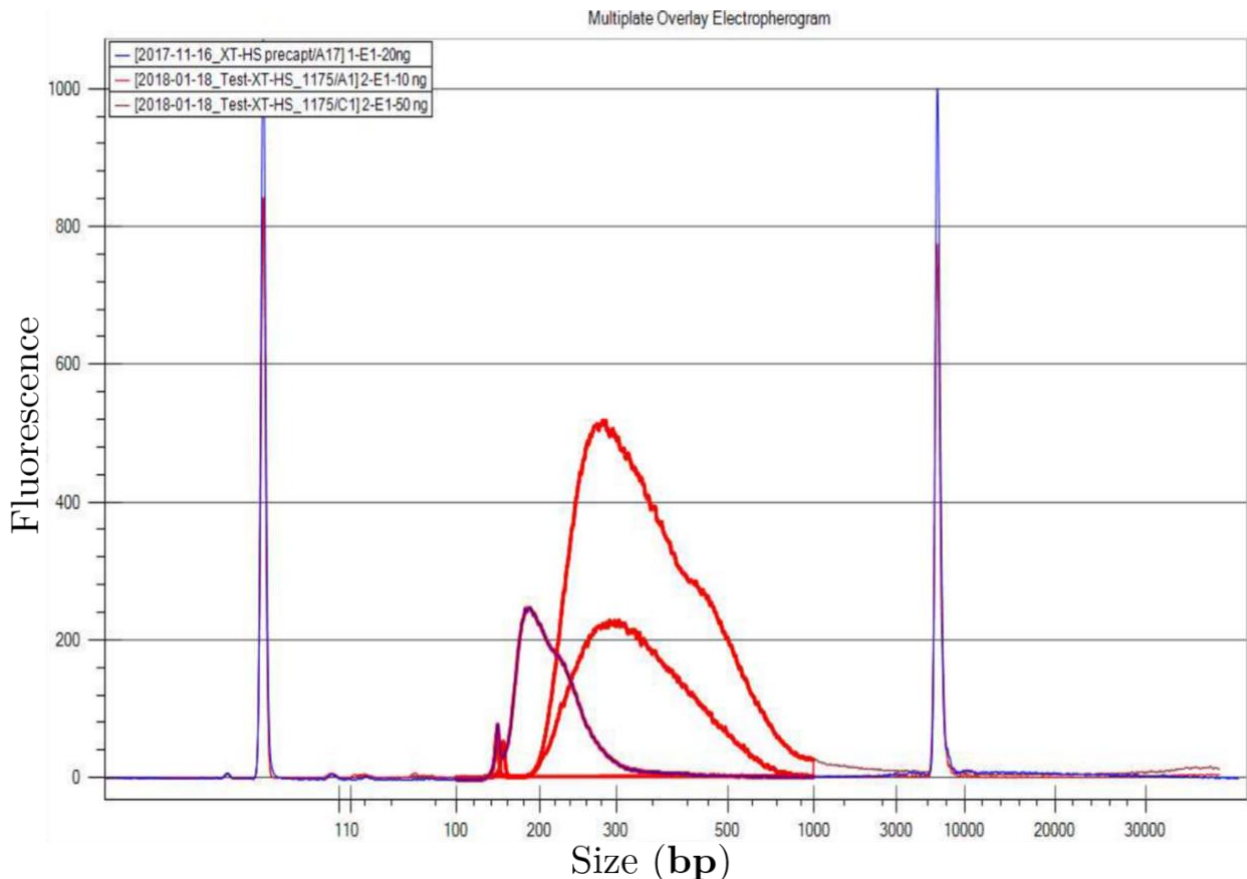


**Figure 87:** Electropherogram of the sample P2\_S prepared with the first version of the Agilent kit, curve in purple and with the second version in red. We can notice that the red curves are centered around 300bp (expected value for this kit) whereas the violet curve is at 200bp suggesting a malfunction during preparation steps.

A new batch of this kit was finally proposed by Agilent and a new library preparation showed better results allowing the sequencing of most of the samples **Figure 87**.

---

However, supplementary samples were lost at this step too: P3\_CTC2 and P4\_CTC (see column “Seq name” in Figure 14, red highlight the samples lost).

The loss of these precious samples is very unfortunate at this stage of the project as a lot work has been already achieved on their enrichment collection, extraction and preparation. Additionally, no possible replacement could have been considered as for example, the P4\_CTC was the only CTC sample for patient P4 and the patient’s condition would not allow further sampling at this time.

On the other hand, we explain these losses by first, the bad reproducibility and the problems encountered with the new Agilent kit as our samples were treated with the first commercial versions available. Secondly, the heterogeneity of the lost samples, their respective processing history and the low amount of DNA available for most of them could also explain the difference in results compared to healthy and tumor samples. Indeed, 4 out of 5 lost samples are CTCs and all samples presented less than 50ng as starting material, which is in the range of the used kit (10ng to 100ng) but seems to be a bad factor risk for library preparation in our case.

Luckily, for the patients P1, P2 and P3 a second CTC sample passes this step and could be sequenced. This allows the first demonstration of CTC captured thanks to Ephesia system, released, and analyzed by Whole Exome Sequencing after DNA extraction.



## 4.2.3.3 Sequencing and QC

Patient	Sample type	Quantity (ng)	Biological name	Seq Name	Total reads	Sample representation	Mean length	Total bases (bp)	Q20 of R1	Q20 of R2	Trimmed mean length	Trimmed reads	Discarded reads	
P1	Healthy (peritumoral)	374.0	P1_S	A920E01	206252124	13.70%	101.0 bp	20831464726	98.6%	96.90%	99.8	8.9%	0.0%	
	Primary Tumor	50.3	P1_T1	A920E02	158741596	10.60%	101.0 bp	16032901398	98.6%	97.00%	99.6	9.6%	0.0%	
	Primary Tumor	49.6	P1_T2	Lib prep failed										
	CTC	3054.9	P1_CTC1	A920E04	80086780	5.3%	101.0 bp	8088764982	98.6%	97.3%	97.7	16.9%	0.0%	
P2	CTC	34.8	P1_CTC2	Lib prep failed										
	Healthy (buccal swab)	62.0	P2_S	A920E06	187504726	12.50%	101.0 bp	18937977528	98.6%	97.70%	99.3	11.2%	0.0%	
	CTC	128.6	P2_CTC1	A920E07	167285510	11.1%	101.0 bp	16895836712	98.6%	97.4%	99.6	9.8%	0.0%	
	CTC	36.2	P2_CTC2	Lib prep failed										
P3	Healthy (total blood)	24.3	P3_S	A920E09	185550266	12.30%	101.0 bp	18740577068	98.6%	97.10%	100	7.3%	0.0%	
	CTC	560.5	P3_CTC1	A920E10	184071088	12.20%	101.0 bp	18591180090	98.6%	97.30%	99.5	10.2%	0.0%	
	CTC	448.9	P3_CTC2	Lib prep failed										
	Healthy (total blood)	5000.0	P4_S	A920E12	166192546	11%	101.0 bp	16785447348	98.6%	97.2%	99.7	9.4%	0.0%	
P4	Primary Tumor	5000.0	P4_T	A920E13	168442192	11.20%	101.0 bp	17012661594	98.6%	97.40%	99.7	9.3%	0.0%	
	CTC	26.5	P4_CTC	Lib prep failed										

Figure 88: Samples used for WES with the corresponding Raw-QC parameters (Basic Metrics)



---

Whole Exome Sequencing was performed on the 9 samples presented above, using a Pair-end reads strategy PE100 (2\*100bp reads) on Illumina Hiseq2500 system.

Some features of the quality check are given in the Figure 88 and Figure 89. To generate these data, we used Raw-QC a quality control pipeline made for controlling the quality of the sequencing data and to trim adapters.

As shown in Figure 88, the sample P1\_CTC1 has a very low representation compared to other samples: 5.3% for P1\_CTC1 versus values between 10% and 14% for the other samples, which is much closer to the expected value of 11.1% for 9 samples. Furthermore, **Figure 89** presenting the number of sequences as function of the percentage of their GC content, shows that most of the samples are aligned together (yellow) with a distribution peak around 58%. Whereas for the CTC sample P1\_CTC1 (red), there is a shift to 63% and the sum of the deviations from the normal distribution represents more than 30% of the reads of the sample. This indicates a possible contamination coming from adapter dimers or another specie during sample treatment (bacterial contamination for example). The contamination hypothesis is also in accordance with the exceptional amount of starting material discussed above. We explain the hypothetical contamination by the fact that our process of sample treatment is not 100% sterile. Indeed, even if the sample preparation and pre-concentration for Ephesia device are performed under a hood in sterile conditions, the device and the whole setup are not. This is a weakness in our protocol that might be improved in the future.

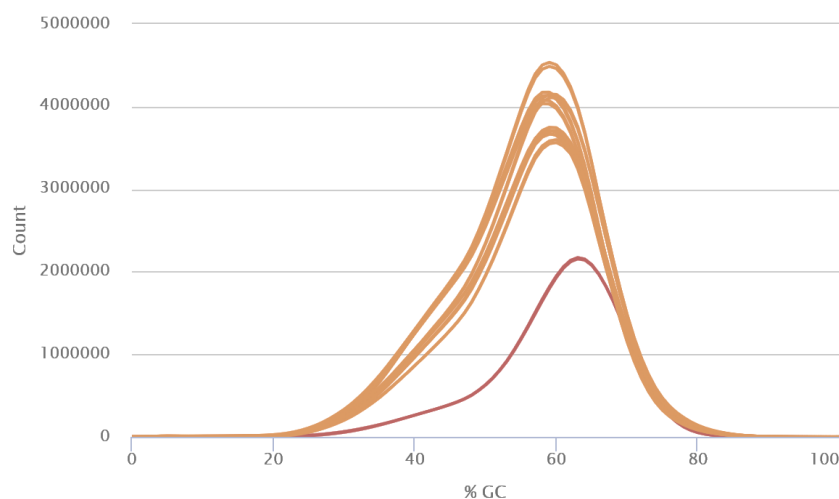


**Figure 89: Number of sequences as function of the percentage of their GC content. Each line is a sample single-read. In red, reads of the sample P1\_CTC1.**

#### 4.2.3.4 Sequencing data analysis

FastQ files were analyzed by Elodie Girard from the bioinformatics unit U900 of Institut Curie. She proceeds as described in the following sections.

##### A. Mapping

###### A.1 Mapping & unique hits

Each sample was mapped to the hg19 reference genome using the software Burrows-Wheeler Aligner (BWA). Only alignments falling inside the targeted regions (from “SureSelect Clinical Research Exome Regions.bed”) were kept and quantified with the BEDTools suite (v2.21.0). Then, only reads that mapped only once; unique position, noted as “unique hit” in **Figure 90**; were kept.

**Figure 90** shows the percentage of unmapped, unique and multi-hits reads. We can notice from this figure that, except the sample P1\_CTC1, all samples have <1% of unmapped reads and <10% of multi-hits which are good statistics for WES and insure the quality of our data. The sample P1\_CTC1, once again, shows signs of possible contamination or error during library preparation and confirm our previous observations.

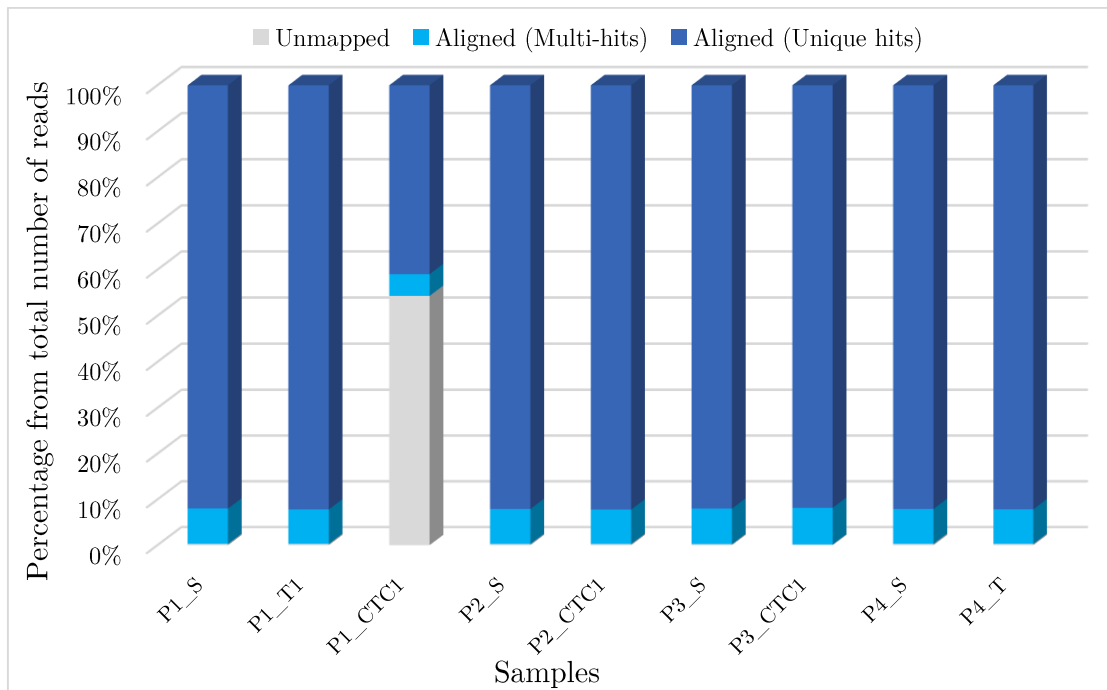


**Figure 90:** For each sample, the percentage of unmapped reads and within the mapped, the percentage of unique reads and multi-hits reads.

## A.2 Duplicates

PCR duplicates may arise from the library preparation step. After ligation of the adapters to both ends of the fragments, a PCR amplification is performed to increase the signal arising from each fragments during sequencing. At this step, depending on the initial amount of material and the number of PCR cycles, a statistical error can happen when two copies of the same template molecule get onto different primer lawns in a Flowcell and thus, introduce noises in the variant detection (propagation of false positives) during data analysis.

Even if there is still a debate on the necessity of the PCR duplicate removal (Ebbert et al. 2016), we made the choice to discard them in order to remove any bias, in particular, due to our samples with very low amount of initial material.

Therefore, PCR duplicates were quantified and discarded using Picard Tools (v.2.6.0). Figure 91 shows the number of duplicate per sample. These values (most samples <30%) are in accordance with quality standard WES data. Color code of the figure highlights the fact that no specific correlation between the percentage of duplicate and the type of sample can be made.

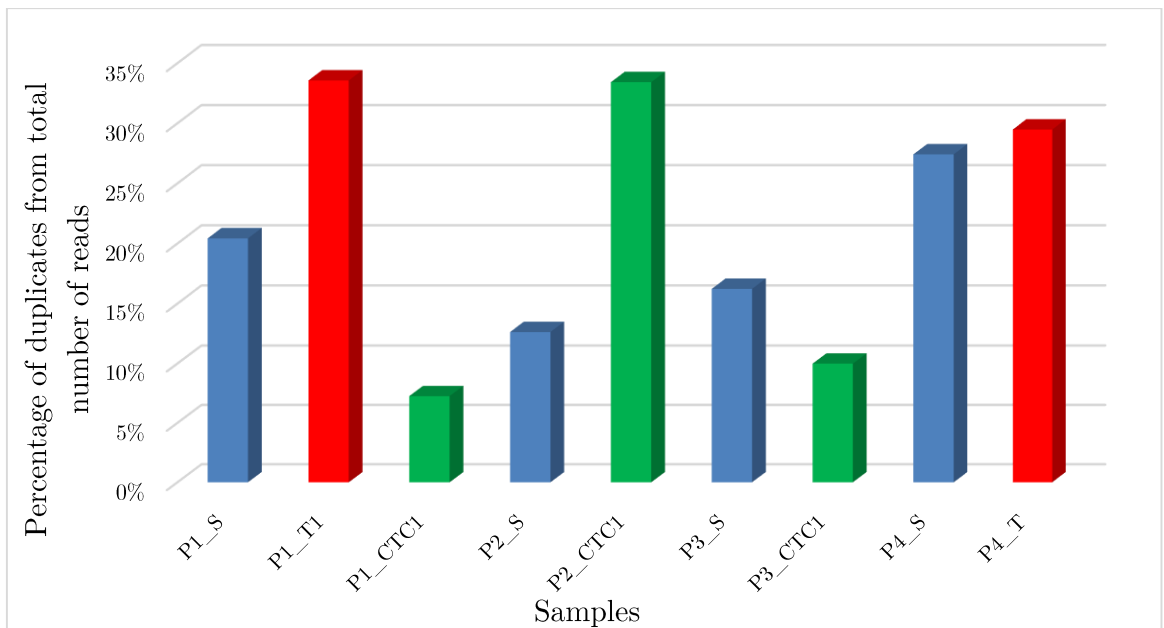


**Figure 91:** For each sample, the percentage of duplicates compared to the total number of reads. Blue, red and green distinguish respectively between Normal, Tumor and CTC.

### A.3 Mapping quality & coverage analysis

A mapping quality (MAPQ) is associated to each alignment and characterizes its confidence in the position. Reads mapping on repeated elements or low-mappability regions will tend to have low or null mapping qualities. These repeated or low mappability regions have an impact on the coverage distribution (low and high coverage regions) as the mapping is highly uncertain. In order to keep only alignments of confidence, all alignments with a mapping quality (MAPQ) below 20 were discarded from further analysis using SAMtools (v.0.1.19).

The resulting alignment files were then used to perform coverage analysis and qualify the target enrichment. The average depth of coverages for the normal, primary tumor and CTC samples are respectively 171X[137-191X], 124X[115X-133X] and 113X[28X-188X], complete profiles are given in **Figure 92**.

Except P1\_CTC, the two other samples CTC samples have a high average coverage (123X and 188X), even equal or higher than tumors. This is the final **validation** of our whole experimental workflow regarding the possibility of **using CTCs captured through Ephesia system for Next Generation sequencing**. Observations made on P1\_CTC1 at each step will help us improving our workflow for further analysis.

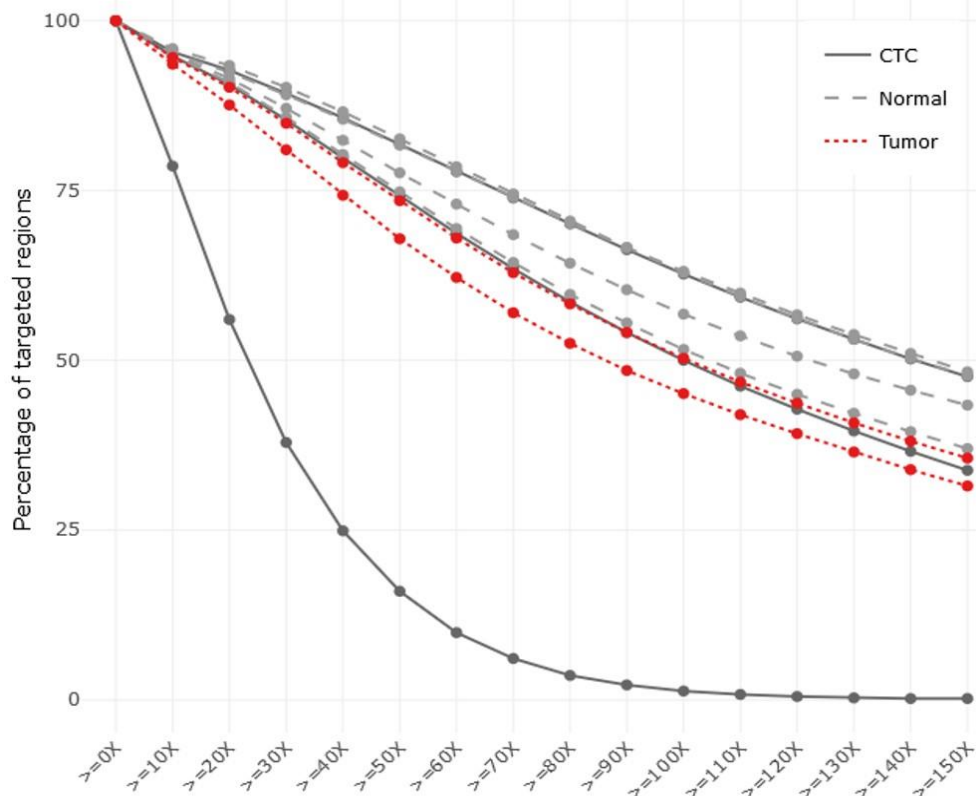


**Figure 92:** Percentage of targeted regions as function of coverage

## B. Variant Calling:

In order to detect small variations such as **single nucleotides variations (SNVs)** or **insertions/deletions (indels)**, a variant calling using Mutect2 (v.4.0.2.1) was performed using the following parameters: a minimum mapping quality of 20 and a base quality of 13 to respectively keep an alignment/a base, a minimum variant quality phred score of 30 to report a variant. Then, a germline variant calling was also performed using HaplotypeCaller (GATK v.4.0.2.1) in order to identify putative sample swap (variant clustering) and putative germline variant of interest. Indeed, germline predisposition to MAHA is linked to homozygous or compound heterozygous mutations in the ADAMTS13 gene.

### B.1 Variants Clustering:

Prior to any filtering analysis, a hierarchical clustering was performed using the variants state in all types of samples (independently of the allelic ratio) with the Jaccard distance and the Ward linkage function. The clustering Figure 93 shows that all samples from the same patient (pairs of: tumor/germline, CTC/germline, or triplet of CTC/Tumor/Normal) cluster well together and confirm that no mismatching occurred during samples preparation. However, no specific link between samples type (germline, tumor and CTC) or cancer type (prostate vs breasts) can be extrapolated.

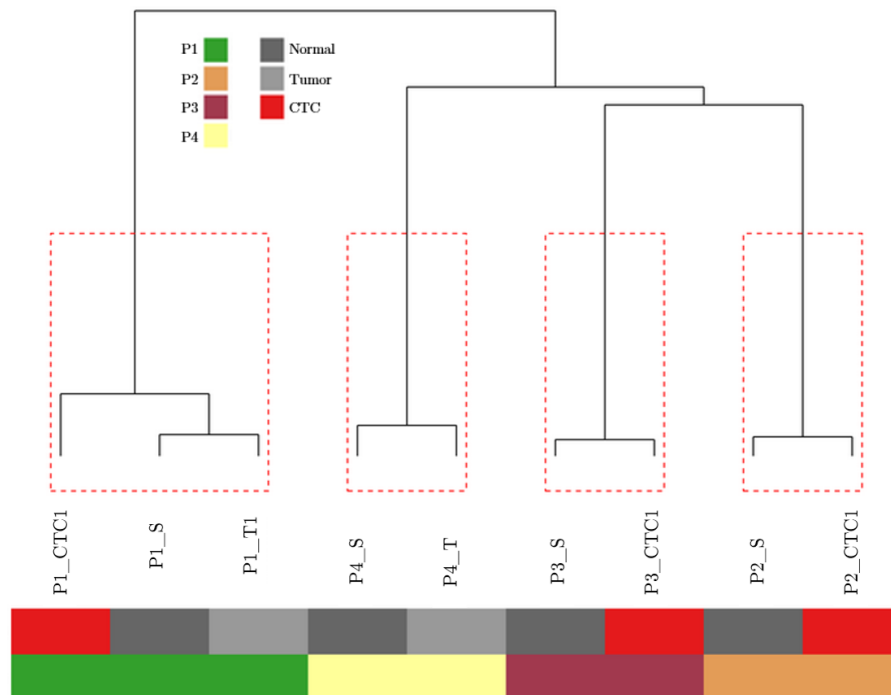


Figure 93: Clustering hierarchy of the samples based on the variants state.

## B.2 Variants annotation

Germline variants:

Prior to any filtering, a first round of variant detection was performed and gives around 150000 SNV events. Seven types of filters were then applied to these events and are described in the coming section. Furthermore, we used the ClinVar database (Landrum et al. 2014) to help find putative germline pathogenic variants in specific diseases.

Four common variants to all samples and noted as “pathogenic” in ClinVar can be found: rs1154510, rs1799983, rs804280, rs6471482. Three of them are exonic and the last one is a intronic (splicing). They are linked to diseases such as: coronary artery spasm and ischemic stroke and ischemic heart disease. Deeper analysis of these variants will be performed in the continuing of the project.

Within this variant call, a specific restriction to ADAMTS13 variants (gene linked to TMAs) is shown in Figure 94. We can notice that only two intronic SNV are common to the 9 samples. However, rs2301612 is present in all samples, except the ones of patient P2. This variant is predicted as pathogenic in Upshaw-Schulman syndrome, the hereditary TTP (see Figure 94, line of recurrence 7).

pos in chr9	ref alt	Func	ExonicFunc.refGene	P1_S	P1_T1	P1_CTC1	P2_S	P2_CTC1	P3_S	P3_CTC1	P4_S	P4_T	rec	CLINSIG	CLNDBN
136287582	C T	exonic	nonsynonymous_SNV	NA	NA	NA	39.77%_171X	44.44%_126X	46.51%_172X	53.01%_166X	53.97%_126X	34.71%_121X	6	Benign Likely benign	Upshaw-Schulman_syndrome
136290672	G A	exonic	synonymous_SNV	NA	NA	NA	NA	NA	47.26%_438X	51.61%_403X	49.28%_347X	40.74%_270X	4	Benign Likely benign	Upshaw-Schulman_syndrome
136291063	C T	exonic	synonymous_SNV	NA	NA	NA	100%_276X	100%_120X	99.12%_226X	100%_224X	100%_166X	100%_137X	6	NA	NA
136291361	C T	exonic	synonymous_SNV	NA	NA	NA	NA	NA	49.5%_503X	45.24%_588X	46.07%_382X	46.63%_356X	4	Benign Likely benign	Upshaw-Schulman_syndrome
136291469	T G	intronic	NA	NA	NA	NA	NA	NA	48.63%_364X	46.05%_304X	47.64%_254X	40.16%_244X	4	Benign Likely benign	Upshaw-Schulman_syndrome
136295232	C T	intronic	NA	NA	NA	NA	NA	NA	39.68%_310X	48.38%_308X	46.28%_242X	46.88%_224X	4	Benign Likely benign	Upshaw-Schulman_syndrome
136295290	A C	intronic	NA	100%_292X	99.56%_227X	100%_47X	99.42%_343X	100%_207X	100%_288X	100%_304X	100%_246X	100%_207X	9	NA	NA
136297880	G A	intronic	NA	NA	NA	NA	NA	NA	49.21%_378X	49.47%_475X	45.69%_313X	39.84%_256X	4	NA	NA
136298729	G C	intronic	NA	NA	NA	NA	100%_367X	100%_208X	49.39%_413X	47.79%_429X	52.7%_241X	58.72%_235X	6	NA	NA
136301982	C G	exonic	nonsynonymous_SNV	100%_170X	100%_155X	100%_21X	NA	NA	45.1%_153X	47.16%_176X	41.67%_120X	43.38%_136X	7	Pathogenic Benign Benign	Upshaw-Schulman_syndrome
136304497	A G	exonic	synonymous_SNV	NA	NA	NA	100%_233X	100%_91X	56.05%_157X	46.15%_156X	41.96%_143X	55.86%_111X	6	NA	NA
136305530	C G	exonic	nonsynonymous_SNV	NA	NA	NA	NA	NA	46.19%_591X	45.94%_603X	43.06%_425X	40.12%_334X	4	Benign Likely benign	Upshaw-Schulman_syndrome
136305738	C G	intronic	NA	NA	NA	NA	NA	NA	51.92%_52X	64.86%_37X	NA	NA	2	NA	NA
136308542	C T	exonic	synonymous_SNV	NA	NA	NA	100%_145X	100%_107X	47.5%_160X	44.62%_130X	51.45%_138X	53.85%_117X	6	NA	NA
136310108	G A	exonic	nonsynonymous_SNV	NA	NA	NA	NA	NA	NA	NA	52.65%_321X	62.36%_263X	2	NA	NA
136310908	C T	exonic	nonsynonymous_SNV	NA	NA	NA	NA	NA	50.61%_247X	45.45%_209X	NA	NA	2	Benign Likely benign	Upshaw-Schulman_syndrome
136311017	G A	intronic	NA	100%_215X	100%_140X	100%_36X	43.63%_204X	48%_150X	100%_203X	100%_192X	100%_150X	100%_143X	9	NA	NA
136319489	T C	intronic	NA	NA	NA	NA	NA	NA	NA	NA	44.72%_161X	38.89%_162X	2	Benign	not_specified
136319496	G A	intronic	NA	NA	NA	NA	NA	NA	NA	NA	44.44%_162X	38.24%_170X	2	Benign	not_specified
136319600	G A	exonic	synonymous_SNV	NA	NA	NA	NA	NA	NA	NA	46.86%_207X	44.21%_233X	2	Benign Likely benign	Upshaw-Schulman_syndrome
136324239	C A	exonic	synonymous_SNV	100%_409X	100%_231X	100%_50X	NA	NA	46.23%_398X	51.24%_402X	NA	NA	5	Benign Benign	Upshaw-Schulman_syndrome

Figure 94: Recurrent SNP in ADAMTS13 gene with their function (exonic or intronic), their percentage over the sample and the corresponding coverage, the recurrence over all samples and indication of their clinical significance based on ClinVar (Landrum et al. 2014).

Filtering:

Variants were then annotated using Annovar (July 2017 version) and the following annotations: refGene (October 2015 version), dbsnp150 and 1000G (08/2015 version, all), Exome Sequencing Project (ESP6500, all), ExAc project, Cosmic (v81), ICGC (v21), clinvar (September 2017 version), prediction algorithm such as SIFT, PolyPhen2, LRT, MutationTaster, PhyloP and CADD (version dbnsfp33a).

Several metrics were then used to tag variants (following Mutect2 recommendation using FilterMutectCalls). Among these parameters, the “normal-artifact-lod” can be increased to allow a higher number of reads supporting the variant in the normal sample. In our case, with a high contamination of the CTC in the normal samples, especially in total blood, this parameter was relaxed from 0 to 2.5.

#### ***4.2.3.5 First results & perspectives***

At this stage of the project, the reader should keep in mind that no relevant comparison between CTC and tumor samples can be made. Indeed, for three patients, either the tumor was not available from the beginning of the protocol or the CTC sample was discarded during sample preparation and for P1 the CTC sample shows bad coverage results. Therefore, no Tumor vs. CTC comparison can be done as targeted initially in the project.

However, after applying the filters described above, we wanted to reduce our field of view on the data to commonly altered genes between the Tumor & CTCs samples in order to possibly highlight a specific mutation common to the two sample types compared to normal samples. **Figure 95** shows the 20 genes remaining after this selection with for each gene, the number of variants on each sample and the associated key words from Pathcards a database of human biological pathways.

On a first view of this panel, no particular gene draws our attention by being directly linked to the pathophysiology of the TMAs, as ADAMTS13 previously. Mutations in AHNAK and TP53 are, for example, well known to be cancer drivers in many types of cancers and may not be relevant in the present case. Nevertheless, CSPG4 gene may be a good candidate, as it shows two types of variants on each of the samples P1\_T1 and P2\_CTC1 and it is highlighted in Pathcards as involved in cell adhesion pathways. However, to complete this aspect of the project, a deeper analysis of all pathways that may be activated by the variants of these genes and their possible combinations will be explored in the future.



Gene	P1_T1	P1_CTC1	P2_CTC1	P3_CTC1	P4_T	SuperPathway ( <a href="http://pathcards.genecards.org">http://pathcards.genecards.org</a> )
AHNAK	1		1			
AHNAK2			1		1	
ANKRD11			1		1	
ARHGAP23	1			1		p75 NTR receptor-mediated signalling ; Signaling by Rho GTPase
CSPG4	2		2			Cell adhesion_Cell-matrix glycoconjugates ; Wnt / Hedgehog / Notch
FLG	1		5		1	Keratinization
FOXF2	1		1			
KBTBD6	1		1			Class I MHC mediated antigen processing and presentation
LILRA3	1		2		1	Class I MHC mediated antigen processing and presentation
MYLK	1		1			NgR-p75(NTR)-Mediated Signaling ; Integrin Pathway ; ERK signaling
OR10G9	1		1			Olfactory Signaling Pathway
PKD1	1		1			Simplified Interaction Map Between LOXL4 and Oxidative Stress Pathway
PKP2	1		1			Keratinization
POU5F1	1		1			Human Early Embryo Development ; Transcriptional regulation of pluripotent stem cells ; Wnt / Hedgehog / Notch
PRODH			1		1	Arginine and proline metabolism
RHPN2			1		1	RHO GTPases Activate Rhotekin and Rho GTPases
TP53	1				1	TP53 Network
TTC30B		1			1	Intraflagellar transport
VWF			1		1	GP1b-IX-V activation signalling ; Oncogenic MAPK signaling ; PI3K-Akt signaling pathway
ZNF717	1			1		

Figure 95: Commonly altered genes between Tumor and CTC samples of all patients

#### 4.2.4 RNA sequencing

As a second step of molecular characterization, we decided to perform RNA sequencing on tumor cells of these patients in order to detect phenotypic changes that would be linked or could explain the pathophysiology of the TMAs and the CTC/WBC clusters that we observed previously.

##### 4.2.4.1 Sample type & extraction

Thus, a first batch of tumor samples was sequenced. Only three available tumor samples were collected for this run: Two primary tumor sampling for patient P1 (P1\_T1, P1\_T2) and one for patient P4 (P4\_T). P1\_T2 biopsy was performed 6 months after P1\_T1 and just before a TMA relapse. As previously for WES, samples were provided by the CRB as RNA extracts and were transferred to the NGS platform for library preparation.

Sample name	Sample type	RIN	260/230 Ratio	RNA quantity (ng)	Volume (µl)
P1_T1	Primary Tumor	8.4	2.16	1000	50
P1_T2	Primary Tumor	8.9	1.76	1000	50
P4_T	Primary Tumor	6.9	2.18	1000	50

Figure 96: RNA samples with the corresponding characteristics

##### 4.2.4.2 Library preparation, sequencing, QC results & mapping

**Library preparation** was performed using the kit TruSeq Stranded mRNA by Illumina on the total RNA DNase treated, provided by the CRB. **RNA Sequencing** was run using a Pair-End reads strategy PE100 (2\*100bp reads) on Illumina Novaseq system with S1 Flowcell type.

**Figure 97** shows results of **quality check data** using the same software MultiQC as for WES. All other parameters of the quality check were excellent. For example, in **Figure 98** we can see that almost all sample reads follows a normal distribution with a peak centered around 51%. Thereby, and since no experimentally new type of sample was explored for this run as previously with CTCs in WES, we will not discuss further the QC results.

Sample Name	Total reads	Sample representation	Mean length (bp)	Total bases (bp)	Q20 of R1	Q20 of R2	Trimmed mean length (bp)	Trimmed reads	Discarded reads
P1_T1	1.35E+08	32.80%	101	13584662206	99.30%	98.60%	100.3	7.00%	0.00%
P1_T2	1.55E+08	37.80%	101	15689433324	99.30%	98.60%	100.3	6.90%	0.00%
P4_T	1.21E+08	29.40%	101	12185767766	99.30%	98.70%	100.5	5.90%	0.00%

Figure 97: Quality Check data of RNA sequencing for the 3 tumor samples

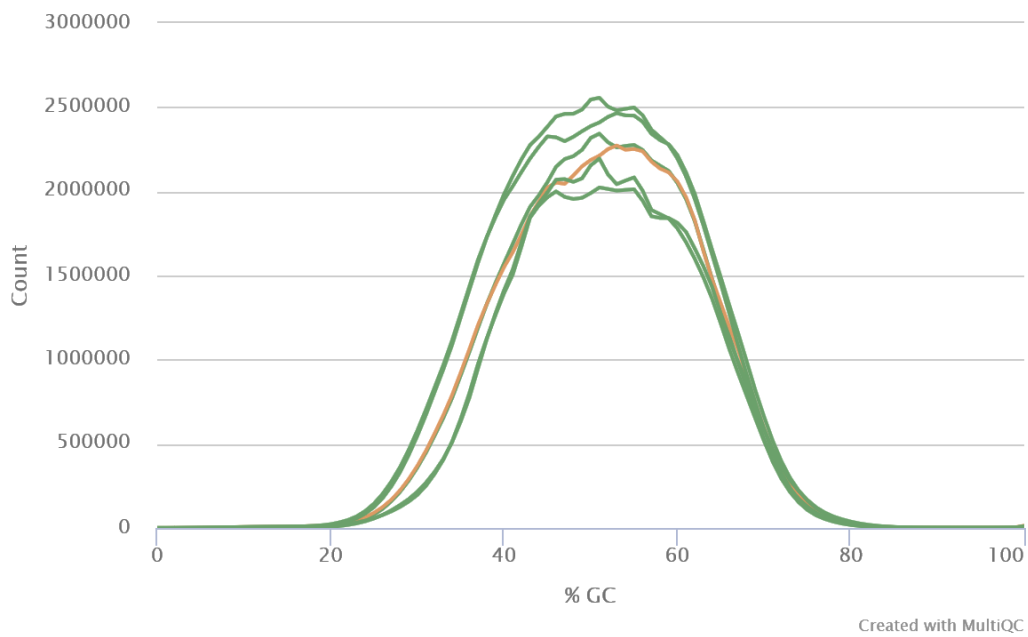
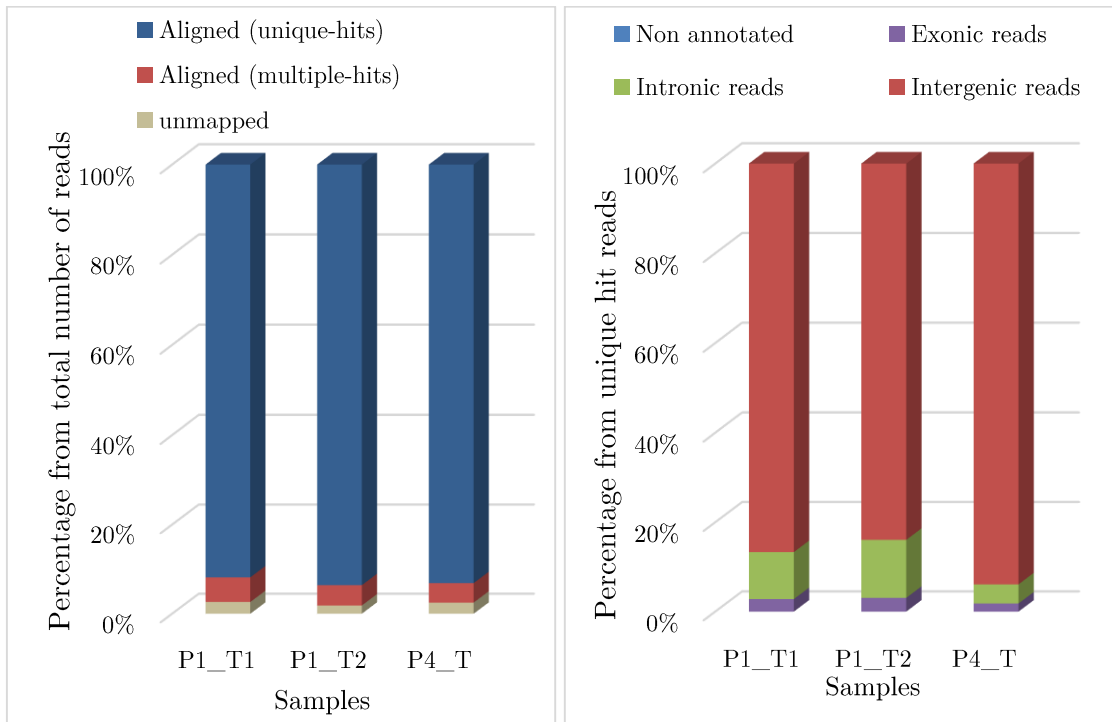


Figure 98: Number of sequences as function of the percentage of their GC content. Each line is a sample single-read. Orange highlight one read of the sample P1\_T1 slightly tilted to the right but not significantly different from the others.

A first **mapping** made by the NGS platform was performed on hg19 reference genome. Left graph in **Figure 99** shows the results of this mapping. For the three samples, more than 97% of the reads were mapped and more than 91% with a unique hit. Right graph in Figure 25 gives the distribution of unique hits into: exonic, intronic and intergenic. Indeed, even if we target only mRNA during library preparation it is possible to get intronic regions from precursor RNA for example. However, in this case the “contamination” does not exceed 13% in each sample and most of the uniquely mapped reads (86% to 93%) are exonic.



**Figure 99:** Left, percentage of unmapped reads, aligned with unique and multiple hits. Right, the percentage of intronic, intergenic and exonic reads within the unique hits.

---

#### 4.2.4.3 *Bioinformatics data analysis*

FastQ files were then analyzed by Elodie Girard and produced the results described below.

##### Comparison to TCGA

Using TCGA biolinks and `cgdsr` R packages, raw counts processed with HTSeq on hg38 reference genome and clinical information were obtained for the TCGA-BRCA project. Out of the 1223 patients, 113 were HER2+ and selected for future analysis (P4 and P1 are patients diagnosed HER2+ breast cancers).

In order to minimize the biases (different sequencing, different number of samples...), our samples were mapped again to the hg38 reference genome using STAR (v2.5.3, stranded) and the GTF Gencode gene information provided by the TCGA pipeline. Reads falling into the different genes were then counted using HTSeq (v2.7.13). One should have in mind here that the mapping results presented in the previous section on hg19 should not differ so much from hg38. Also, the correlation between RNA seq and WES that was also mapped on hg19 can only be improved by the results presented in the following. Indeed, hg38 is a corrected and improved version of hg19.

##### Normalization

Raw counts were filtered per group in order to discard genes poorly covered in each group: genes with the sum of each reads count per group below 10 were discarded. 55% of the genes were filtered out. Filtered raw counts were normalized using DESeq2 R package and the estimated size factors.

##### Principal Component Analysis

Normalized counts were then transformed by a Variance-Stabilizing Transformation in order to use them for preliminary exploratory analysis by Principal Component Analysis PCA (FactoMineR R package).

PCA is a mathematical method for dimension reduction. It is often used in gene expression analysis to highlight the most important set of genes varying within a population (different types of cells or different patients for example) and thus, creating population clustering when representing the variables in the two orthogonal dimension of maximum variance called the principal components or transcriptional component (Todorov, Fournier, and Gerber 2018).

Figure 26 shows results of PCA applied to our three samples and the 113 samples of TCGA. We can notice in **Figure 100** that both tumors from the same patient (on the top right corner) stand out from the other patient tumor (on the left). And that all the MAHA samples (red dots) can be easily distinguished from TCGA HER2+ patients (blue triangles). However, this might not be meaningful due to all biases: different library preparation, different sequencing...etc; and also due to the weak scores of the principal components (4.9% and 4.3%).

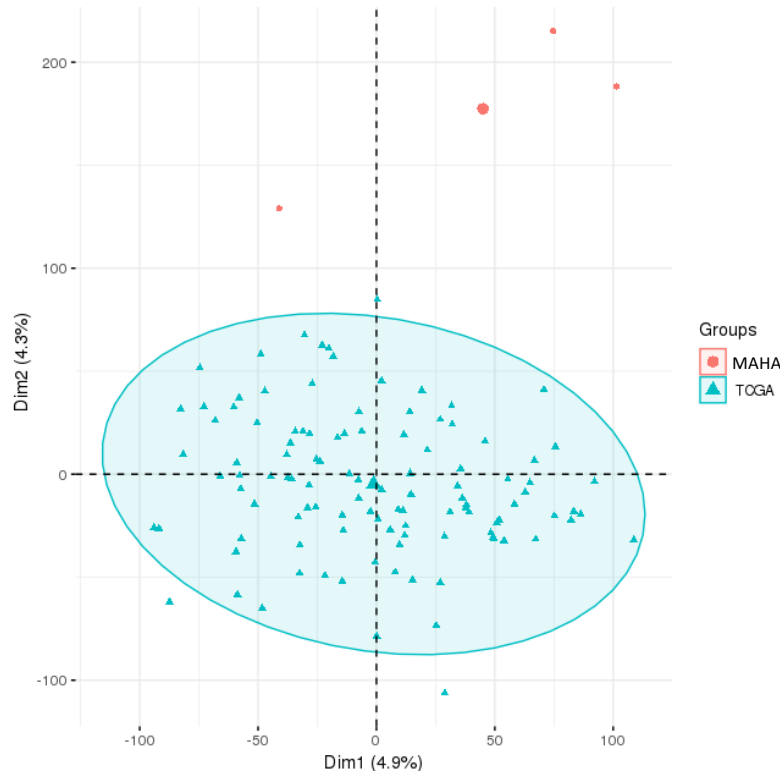


**Figure 100: Principal Component Analysis of the tumor samples of patient with MAHA and the 113 TCGA samples**

Up/Down regulated genes using differential analysis:

Differential analysis of the 3 MAHA samples compared to the 113 TCGA samples was performed using DESeq2. Due to the variability of patient numbers per group, this analysis might not be perfectly robust.

A log<sub>2</sub> fold change of 2 and an adjusted p-value of 5% were used to assess up (397 genes)/down (258 genes) regulated protein coding genes. From another side, for each gene, 5% and 95% quantiles of the TCGA normalized counts distribution were produced and the normalized count of each MAHA patient was compared to these values in order to keep a list of **outlier genes per patient**. In total, there were 473 upregulated protein coding genes and 253 downregulated in all MAHA samples.

The intersection of these two analyses gives 86 genes downregulated and 182 upregulated. Out of these genes, 9 presented mutations in WES sequencing of MAHA patients presented previously. And intersecting this group of genes with GO terms (from Gene Ontology database) associated with: membrane, cell-cell adhesion, coagulation... etc. that can be linked to the MAHA pathophysiological signs gave us the list of genes showed in the heat map **Figure 101**.

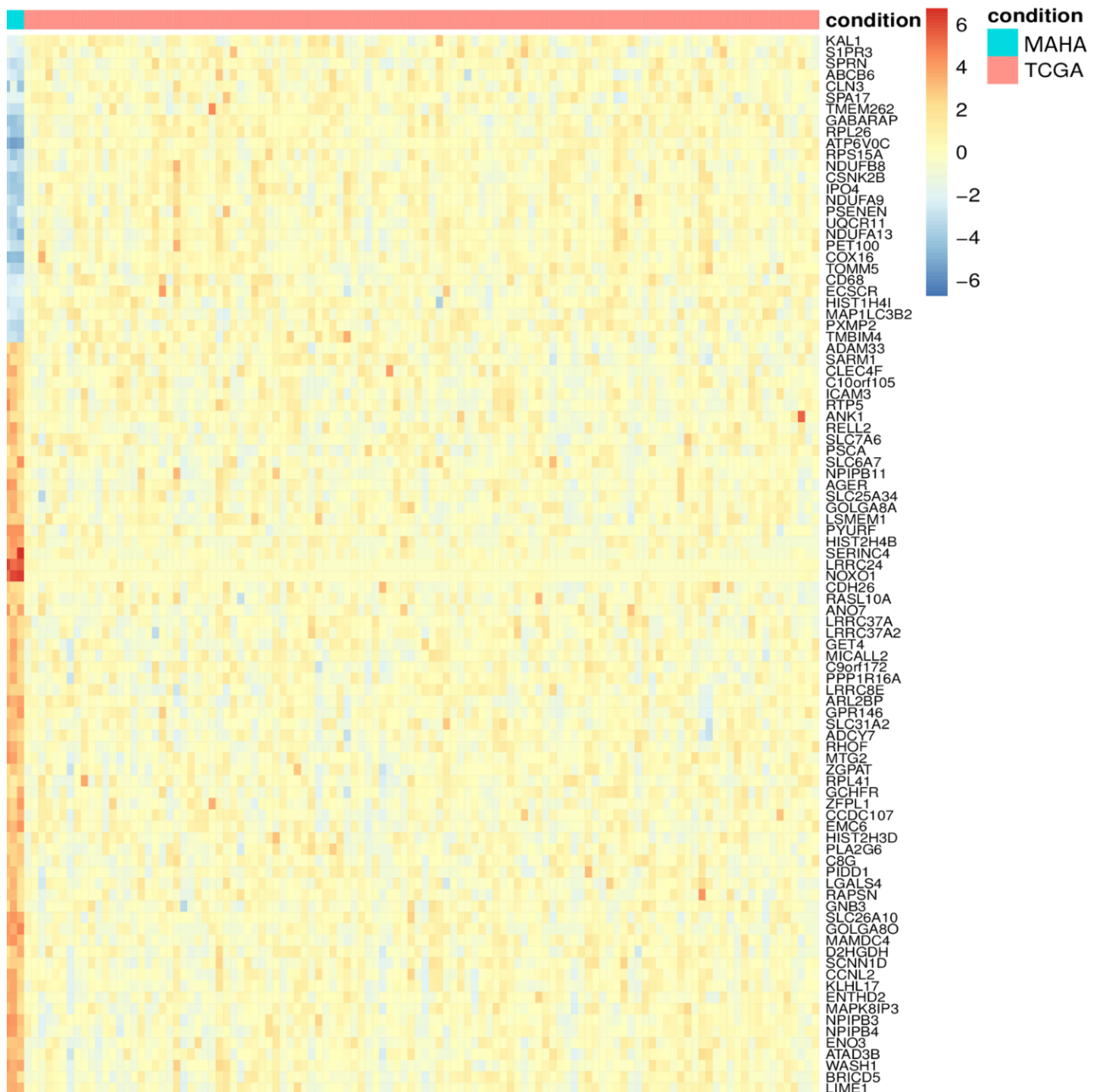


**Figure 101:** Heat map of upregulated and downregulated genes with GO terms that can be associated the pathophysiological signs of MAHA.

#### *4.2.4.4 Next steps & perspectives*

A deeper review of the literature concerning the genes found in **Figure 101**, is needed to complete this analysis and also to combine it with the analysis of the WES for the 9 genes in common (mutated in WES and up/down regulated in RNA Seq).

On the other hand, the next experimental step of this part of the project is to start samples preparation and RNA Seq of the **single cells** (CTC and WBC) collected thanks to Ephesia and sorted by the CellCelector picking technique. To do so, we are planning to use the protocol of (Picelli et al. 2014) that is currently used by our colleague Raquel Perez Palacios from the unit of Genetic & developmental biology of Curie Institute. I had already followed her several times during her sample preparation. The protocol is long (2 days) and very rigorous, so I will first train myself on single cells from cell lines until the step of “quality check of the final cDNA library” before performing on the patient samples. Indeed, as we saw previously with the WES, the material extraction and library preparation steps can be critical for sequencing.

The results that we will obtain from clusters/single cells RNA Seq, will be analyzed and compared to the ones described in this chapter: WES on Normal, Tumor and CTC and RNA Seq of the two primary tumors.



---

### *4.3 Conclusion CR TMA & perspectives*

We presented in this chapter, an exploratory clinical research study about a rare complication of cancer called “Cancer Related Thrombotic Microangiopathy”. The study involved 4 patients diagnosed with different types of cancer supplemented by this complication. We faced several challenges dealing with such rare samples and trying to implement new analysis workflow with diversifying the methods of CTCs capture and complementing our Ephesia platform with downstream characterization. We can summarize the present achievements of this study as follow:

- From the technological point of view: We took up the challenge of analyzing very rare samples of patients diagnosed with CR TMA by different leading-edge technologies that can be complementary to each other. Notably, we demonstrated for the first time the coupling of CTC enrichment by Ephesia system, with a molecular characterization using whole exome sequencing by a NGS technology.
- From the research study point of view: Thanks to the diversity of the techniques involved, we report for the first time, the presence of cell aggregates composed of CTCs and WBCs in different samplings of the blood of 4 patients diagnosed with CR TMA. These observations are in accordance with (Antman et al. 1979; Brain et al. 1970) and confirm their findings in capillaries at autopsy.

Furthermore, we wanted to understand the mechanisms by which these clusters are formed and their role in the Cancer Related TMAs. To do so, we analyzed by WES healthy, tumor and CTC samples; and by RNA Seq tumor samples of these patients. A deep analysis is still needed to conclude on the sequencing results. Moreover, the next step of the project will be to use the single CTCs and clusters collected, thanks to Ephesia and the CellCelector, for RNA Seq to explore their phenotypic changes. In parallel, staining experiments on Iset filters and deeper analysis of the Cellsearch results would bring complementary quantitative data to our results using a wide diversity of technological resources.

## *Appendix*

### *Ephesia video links*

We give in the links below, different videos related to Ephesia and discussed during the chapter of this manuscript:

- columns formation

[https://xfer.curie.fr/get/nil/8MZKq3yR6qZ/Ephesia\\_Columns%20formation.wmv](https://xfer.curie.fr/get/nil/8MZKq3yR6qZ/Ephesia_Columns%20formation.wmv)

- columns release after cell capture

[http://xfer.curie.fr/get/RK7bABiYAHd/Ephesia\\_Beads%20release%20for%20cell%20recovery\\_I.Hajji.wmv](http://xfer.curie.fr/get/RK7bABiYAHd/Ephesia_Beads%20release%20for%20cell%20recovery_I.Hajji.wmv)

- Cell aggregates flowing through the column array of Ephesia

[https://xfer.curie.fr/get/NxicILi8eAE/P1%20sample\\_clusters%20passing%20through%20the%20column%20array%20of%20Ephesia.wmv](https://xfer.curie.fr/get/NxicILi8eAE/P1%20sample_clusters%20passing%20through%20the%20column%20array%20of%20Ephesia.wmv)

- CellCelector post Ephesia capture

[https://xfer.curie.fr/get/P9TPnCkIMUH/CellCelector\\_post%20Ephesia%20capture.mp4](https://xfer.curie.fr/get/P9TPnCkIMUH/CellCelector_post%20Ephesia%20capture.mp4)

---

## *Ephesia protocols of chip fabrication processing*

We summarize in the following sections the protocols of fabrication of Ephesia chips in PDMS and COC versions, and describe the corresponding setup and steps for sample processing.

### ***PDMS chip protocol***

#### **Top part:**

##### **Silicon wafer mold:**

1. Create the design of the chip using a layout editor (e.g. CleWin)
2. Print your design on a Chromium or a plastic layer to obtain a mask (Selba company, Switzerland)
3. Use a classical photolithography with SU-8 2050 and a 2-inch Silicon wafer to obtain a 50 $\mu$ m height mold with the desired design. (exact protocol described in Processing guidelines by MicroChem)

##### **PDMS Molding:**

4. Place the master mold prepared into Petri dish
5. Pour PDMS base resin (SYLGARD<sup>®</sup> 184) and its curing agent in a 10:1 ratio (wt/wt) in a disposable plastic cup, and manually mix the contents using an ice cream stick. To remove air bubbles and facilitate the mixing of the two components, degas the mixture in a vacuum jar until all bubbles disappear, but for no less than 20 min in any case.
6. Pour the mixed PDMS over the master mold to a height of 5 mm. Degas in a vacuum jar until the air bubbles disappear.
7. Cure the PDMS by placing the coated mold on the oven at 70 °C for 2 h.
8. Once the PDMS is cured, remove the mold from the hot plate and allow it to cool down. Cut along the border of the mask plate with a razor blade, and slowly peel off the cured PDMS.
9. Punch inlet and outlets with the 1mm puncher (Dutscher)

##### **Bottom part:**

10. Use the same protocol as top mold with SU8-5 for 5  $\mu$ m height (see Processing guidelines by MicroChem)
11. Spincoat a drop of PDMS on the silicon wafer (1000rpm for 30s)
12. Place in the 70°C oven for 15min to cure the PDMS

##### **Return the PDMS bottom on glass slide:**

13. Put the bottom PDMS before removing it from the wafer + glass slide (5cm diameter 1mm thick, or thinner if needed for imaging) in the plasma machine (Pico PCCE, diener)
14. Run the plasma program as following (5 min vacuum, 3min O<sub>2</sub> injection, 30s Plasma, 45s air injection)

15. Remove the glass slide and the wafer from the machine
16. Pour isopropanol on the PDMS and cut with a lancet the PDMS
17. Insert slightly isopropanol between the PDMS and the wafer to remove it easily
18. Pour isopropanol on the glass slide
19. Using a flat tweezer, return the PDMS on the glass slide
20. Dry slightly the glass slide with an air gun, starting from the center of the glass slide and drawing a spiral shape move to the edges

#### **Beads anchors on the bottom:**

More details can be found in (Delapierre et al. 2017)

21. Wash 150  $\mu$ L of Dynabeads™ M-270 Carboxylic Acid with milliQ water (twice)
22. Resuspend in a (500 $\mu$ L water+ 1:1 solution of SDS and Tween
23. Using the motorized translation stage (PI M-410DG from Physik Instrumente (PI) GmbH). Initialize the device by startup Axis -> Reference move
24. Place the chip patterned bottom part on the stage
25. Align the structures in the PDMS with the axis
26. Turn on the vacuum pump to fix the position of the bottom part
27. Clip rectangular glass slide on top of the stage and place it the closest to the PDMS at 5 mm in X direction from the structures
28. Place it at 1 mm in Z direction from the PDMS (using a micromanipulator)
29. Put a 150 $\mu$ L drop between the chip bottom part and the glass slide
30. Move the holder at 0.025 mm/s until the end of the two lines of patterned arrays (for 35 mm, it takes around 24 min)
31. Remove the drop and clean the chip from beads dust with Isopropanol

#### **Bonding of PDMS chip:**

32. Put the top part after punching the channels and bottom part after magnetic anchor placement, designs facing up, in the Plasma machine (Pico PCCE, diener) same program as before
33. At the end of the program, remove the two parts from the machine
34. Return the top part on the bottom part and press slightly around the chambers

#### **Tubing connection:**

35. Cut 10 cm of strong PTFE tubing (I.D.  $\times$  O.D. 0.56mm  $\times$  1.07mm Bohlender™) for each inlet and outlet
36. Cut 10 cm of the soft flexible Silicone tubing I.D. 1.07mm (Fisherbrand Translucent Platinum-Cured Silicone Tubing by Fischer scientific) for each inlet and outlet
37. Connect each soft tubing piece with a strong tubing one

- 
38. Connect the other side of the PTFE tubes with the PDMS chip. No glue is needed with PDMS. The thickness and elasticity of the PDMS are sufficient to hold the tubing.

The chip is ready to be connected with the other parts of the setup.

### *COC chip protocol*

#### **Top part:**

#### **Hot embossing:**

39. Cut the 5 mm thick COC TOPAS 8007 to obtain a circular piece of 5cm
40. Turn on the heat press (SCAMEX 3T)
41. Set the bottom plate temperature at 50°C, top plate temperature at 25°C and the pressure at 5 bar
42. Place the round COC piece on top of the Nickel master
43. Place a 5 mm thick flat PDMS on top of the COC to insure homogeneous contact with the upper plate
44. Place the 3 pieces in the PRESS
45. Close the press and set temperature at 125°C
46. Wait 30 min and decrease the temperature to 50°C
47. Open the press and remove the 3 pieces
48. Remove the PDMS and place the COC and the Nickel master under cold water for a minute, they will detach from each other

#### **Holes drilling:**

49. Fix the 1.1 mm drill in a drilling machine
50. Adjust the wheel at its lowest speed
51. Place the COC chip under the machine designs facing up and align the drill with the inlet
52. Adjust the high of the drill at 5 mm from the COC and to be able to go 7 mm through the COC
53. Put a drop of water (to cool down the COC during the drilling and collect the COC dust)
54. Turn on the machine and go in contact with COC through the water drop
55. Drill at very low speed (should take 40 s to go through the 5 mm COC)
56. Clean the chip and check that the hole is at the good diameter using a 1.07 mm tubing
57. Remove the edges of the holes made by drilling using a scalpel to insure that the tube will easily go through even after the collage.

#### **Rolling embossing:**

58. Pour 5 mm of PDMS SYLGARD® 184 at 1:10 ratio on top of the SU8 bottom part
59. Vacuum pump for 15min
60. 2 hours in 70°C oven
61. Remove the PDMS and cut the edges to obtain a uniform flat peace of PDMS with holes
62. Pour NOA80 on the PDMS and Spincoat NOA on a piece of copper (See Figure 102 and (Perez-toralla 2013))

- 
63. Put the copper piece on the PDMS (contact made between the NOA faces in each)
  64. Cure under UV light for 10
  65. Set the laminator (RLM 419) at 140°C, pressure 0.5 and speed 0.2m/min
  66. Prepare an Aluminum plate of 20cmx20cmx2mm with two polyimide (PI) sheets taped with Polyimide adhesive tape on its surface one on top of the other. The COC sheet and the copper/NOA mold will be inserted between them in three steps.
  67. Clean the plate, PI sheets, the 245  $\mu\text{m}$  COC sheet and the mold from dust by ethanol and air gun drying
  68. Heat the plate by inserting it twice in the laminator
  69. Place the 245  $\mu\text{m}$  sheet of COC 8007 between the PI sheets and insert the plate in the laminator, keeping the upper PI sheet in contact with the wheel to avoid bubbles trapping.
  70. Cool down the plate for 1min, open and take the structured COC sheet

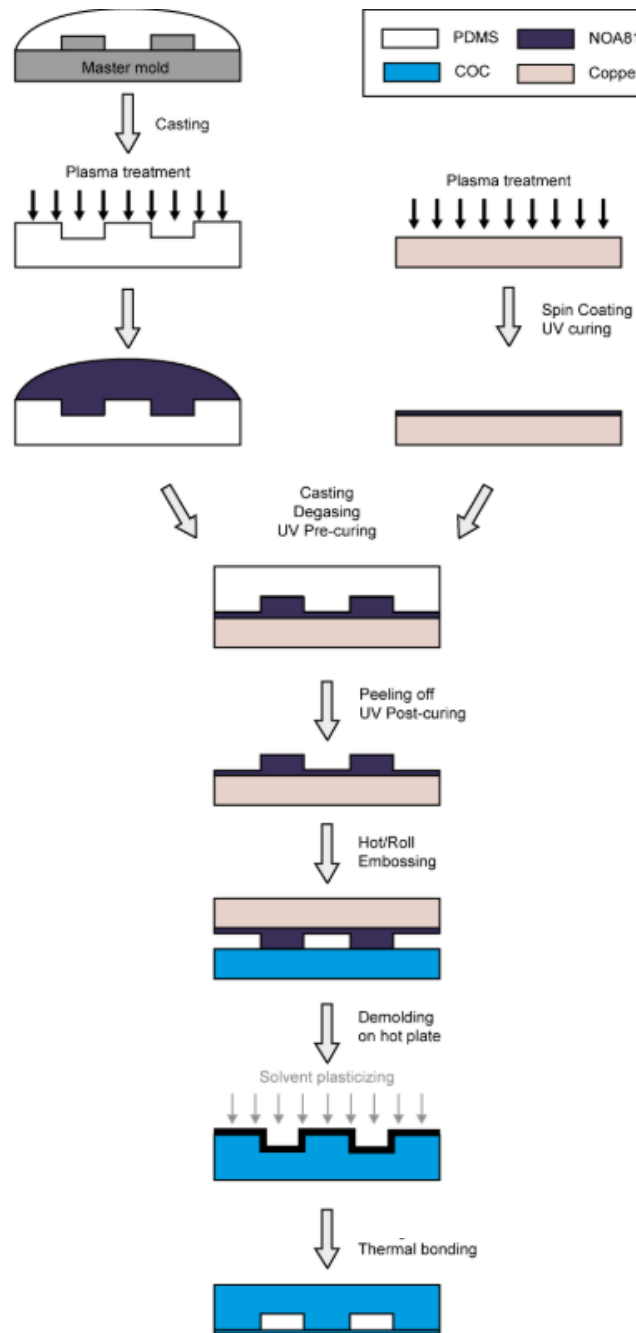


Figure 102: Protocol for the fabrication of NOA mold and its COC replicate. (Perez-toralla 2013)



---

### **Bonding COC chip:**

71. Set the bottom plate temperature at 70°C, top plate temperature at 25°C and the pressure at 5 bar
72. Prepare 15% solution of isopropanol in Hexadecane (H0255, Sigma-Aldrich)
73. Clean the upper and the bottom (except the anchors) parts with ethanol and dry with an air gun
74. Take a bottom part of a 15 cm Petri dish, place a Kimtech paper inside the dish and make it as flat as possible
75. Pour 1 mL drop of the isopropanol/Hexadecane solution on the Kimtech paper and spread it homogeneously. Put the upper part in contact with the paper press with your thumb on the upper part to insure complete wetting of the COC
76. Remove the upper part from the Kimtech paper
77. Align the chambers of the upper part with the lines of the bottom part and put them quickly in contact before the solution dries
78. Place a 5 mm PDMS flat; from which you already removed the lines of the anchors and the inlets/outlets; on top of the 245 µm COC sheet. This will insure homogeneous contact with the upper plate and the holes in the PDMS will avoid the collapsing.
79. Place an aluminum plate on top of the PDMS
80. Put the structure under the press and close it. (20 min)
81. Remove the structure from the press. Remove the aluminum and the PDMS.
82. Check if the collage is homogeneous under light with a black background.

### **Tubing connection:**

83. Cut 10 cm of strong PTFE tubing (I.D. × O.D. 0.56mm × 1.07mm Bohlender™) for each inlet and outlet
84. Cut 10 cm of the soft flexible Silicone tubing I.D. 1.07mm (Fisherbrand Translucent Platinum-Cured Silicone Tubing by Fischer scientific) for each inlet and outlet
85. Connect each soft tubing piece with a strong tubing one
86. Connect the other side of the PTFE tube with the inlet/outlet of the COC chip
87. Use a small 10 µL tip to spread the Epoxy glue (Sader) in the tubes at the entrance of the chip channels (pay attention to not dirty places others than the inlets with the glue, this could compromise the imaging if on top of the chambers)

The chip is ready to be connected with the other parts of the setup.

## *Experiments processing*

### Experimental setup

We present here the setup of the experiment and the preparation of the chip for sample injection: chip coating (for PDMS and COC) and columns building

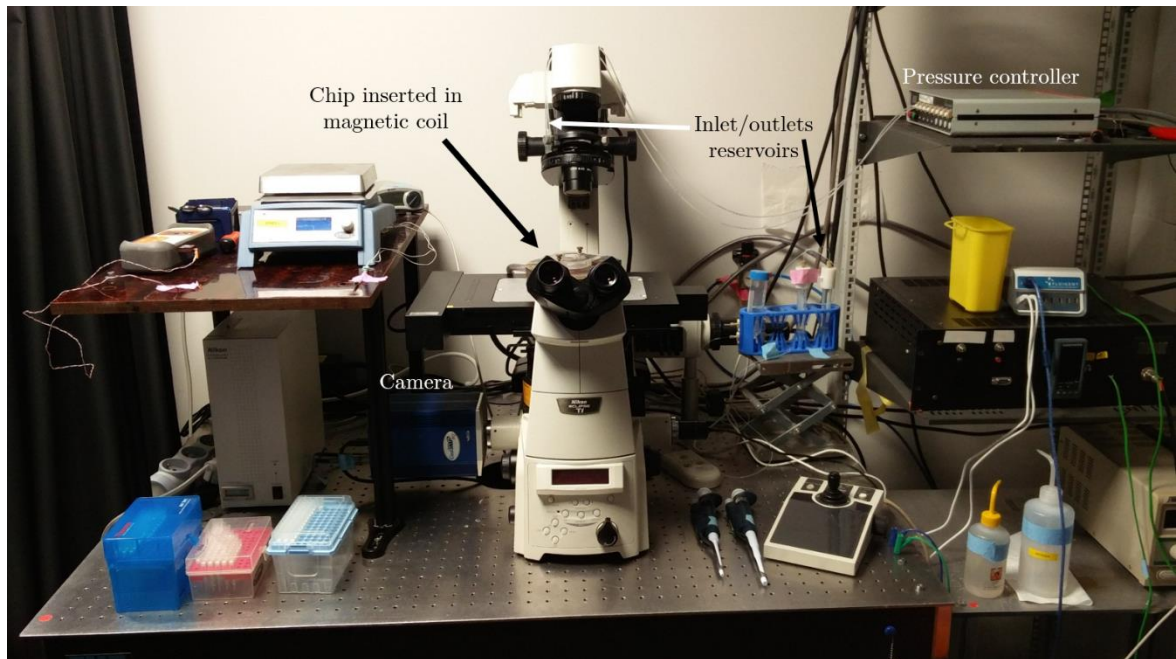


Figure 103: Ephesia setup with its different components

#### Fluidic & electric connections:

88. As shown **Figure 70**, the chip is inserted inside the magnetic coil
89. The coil is placed in a customized aluminum plate, to fit with an Eclipse Ti-E Nikon microscope mounted with a CoolSnap HQ2 Monochrome camera from Photometrics
90. Connect the inlets soft tubes to 1 mL pipette tips without filters and the outlets to 15mL Falcon reservoirs
91. Place small valves on the soft tubing to control the flow
92. Connect the 1 mL tips to the MFCS (Fluigent)
93. Turn on the coil power supply (keep it at 0V 0A) and the cooling system

#### PDMS coating & bubbles removal:

94. Put the chip under plasma machine (Pico PCCE, diener)
95. Inject at 300 mbar, 400 $\mu$ L of PDMA-AGE to fill the chambers and coat the PDMS
96. Remove the bubbles by directly pushing on the PDMS with a pipette tip and applying pressure
97. Close all the outlets and keep the inlet at 40 mbar for 1h and remove the remaining bubbles
98. Rinse with MilliQ water

---

99. Inject PBS (1%BSA)

**COC coating & bubbles removal:**

100. Inject Ethanol with Purge Mode
101. Remove the bubbles by applying very high pressure (or directly pushing on the COC, to avoid)
102. Rinse with MilliQ water
103. Inject 400 $\mu$ L of Pluronic F127(REF???) to fill the chambers and the tubing
104. Close all the outlets and keep the inlet at 40 mbar for 1h to coat the COC and remove the remaining bubbles
105. Rinse with MilliQ water
106. Inject PBS (1%BSA)

**Beads injection:**

107. Rinse EpCam beads (epithelial enrich Dynabeads, 16102 Thermo-Fischer) twice
108. Resuspend in 120  $\mu$ L of PBS (1%BSA)
109. Connect the magnetic coil to the power supply and turn it on (but keep at 0A 0V for the moment)
110. Inject in the beads suspension by the second inlet
111. Wait for the beads to completely fill all the chambers
112. Turn on the magnetic field (13V 3.5A) and observe the column formation (see video link “Ephesia\_Columns formation” at the beginning of this appendix)
113. Never push at more than 40 mbar ( $\sim$ 40  $\mu$ L/min) after this step
114. Close the outlet
115. Back flow the beads to the second inlet by injecting PBS (1%BSA) from the 1<sup>st</sup> inlet
116. Close the second inlet
117. Rinse the excess of beads in the chambers
118. Lower the level of PBS (1%BSA) in the inlet tip at minimum before reaching the tube
119. Place the vibrator (4mm vibration motor-11mm type, by Precision Microdrives) in contact with the inlet

The Chip is now ready to receive the cell sample

***Sample pre-treatment***

120. **Cell lines** are directly injected into Ephesia after trypsin treatment and resuspension in 300 to 400  $\mu\text{L}$ .
121. **Blood samples** are treated by a combination of immune and density method called RosetteSep by Stemcell Technologies (see Figure 104). Enriched cells are resuspended in 300 to 400  $\mu\text{L}$ .

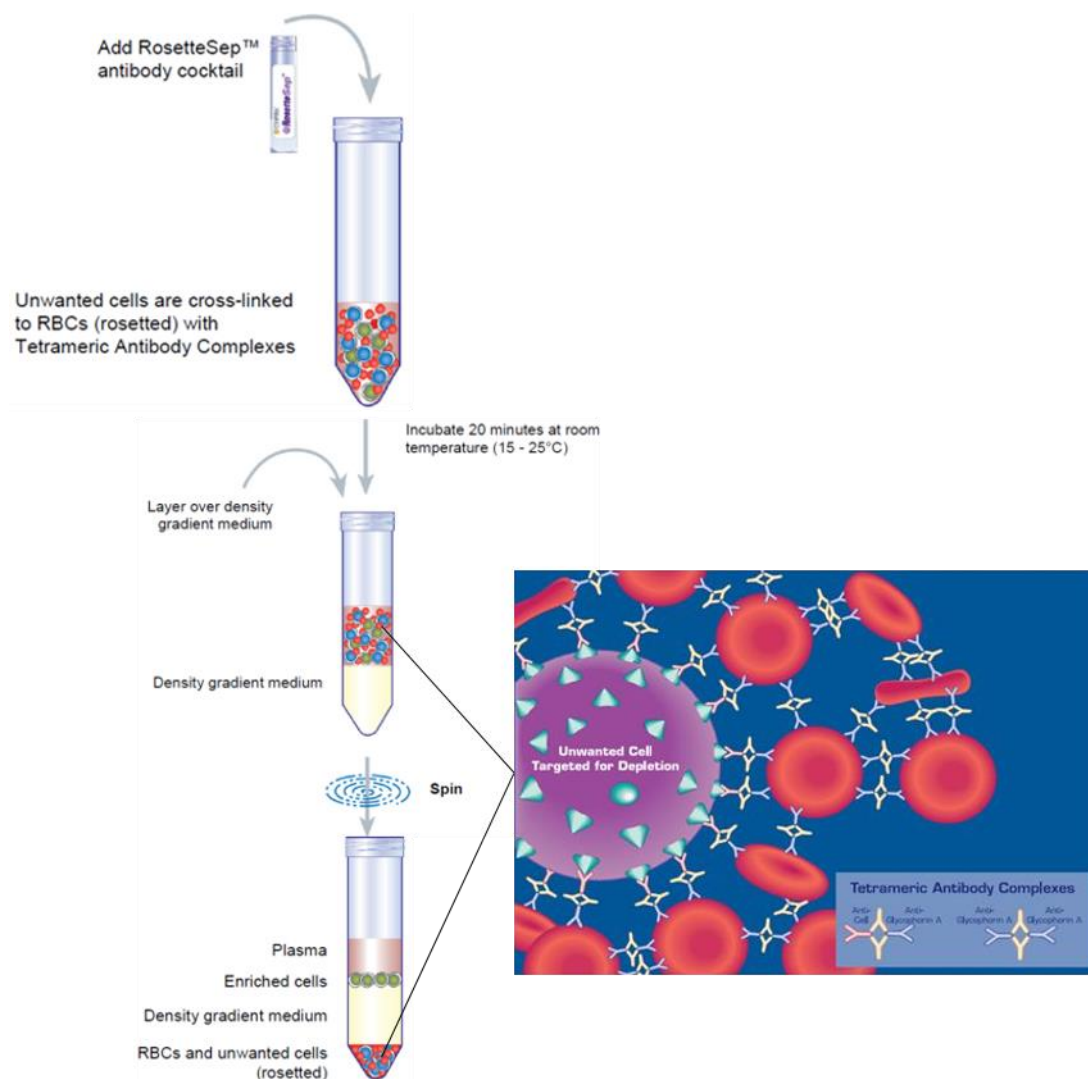


Figure 104: CTC enrichment by RosetteSep protocol. The first type of tetrameric antibody is against Glycophorin A from two sides, thus joining red blood cells (RBC) together. The second type is against Glycophorin A on one side and unwanted cells from the other side. Depending on the unwanted cells this second antibody can be varied. Here white blood cells (WBC) are targeted by antibody against CD45. Therefore, rosette of WBC and RBC are formed and thanks to the Ficoll Density gradient centrifugation, the rosettes are pushed to the bottom of the tube allowing the recovery of the CTCs in the cell ring below plasma

---

Sample injection:

122. The sample is putted in the inlet tip and injected in the chip using the vibrator on the tubes to avoid cell adhesion on the wall or at junctions.
123. The chip is rinsed twice with 100 $\mu$ L of PBS (1%BSA) to insure passage of all the cells in the magnetic columns array.

Depending on the experiment, several type of assays can be performed on the cells captured by the beads “in chip” keeping the magnetic field ON or performed “out-of-chip” by turning OFF the magnetic field, thus releasing the columns and cells attached (see video link in the Appendix).

The different protocols will be described in the corresponding section later in this chapter. We give in the following paragraphs the common protocol used in all the experiments for cell staining.

***Cell fixation & staining***

References for the products used here are below. In the following steps, rinsing of the chip is performed with 200 $\mu$ L of PBS(BSA1%).

Cell Fixation:

124. Prepare a solution of Formaldehyde at 4% in PBS(BSA1%).
125. Inject 200 $\mu$ L in chip, wait 30 min and rinse.

Nucleus staining:

126. Dilute 1 $\mu$ L of Hoescht in 1mL of PBS(BSA1%).
127. Inject 200 $\mu$ L in chip and wait 10min. Rinse.

Cytokeratin staining:

128. Mix 5 $\mu$ L of Ck with 15 $\mu$ L of AF488. Wait for 6min.
129. Prepare Solution A= (Ck + AF488) + 15 $\mu$ L blocking reagent. Wait for 6min.
130. Meanwhile, prepare Solution B = 131.5  $\mu$ L PBS(BSA1%) + 18.5  $\mu$ L Triton
131. Mix (Solution A + Solution B)
132. Inject in chip, wait 30min and rinse.

CD45 staining:

133. Mix 8 $\mu$ L of CD45 with 192 $\mu$ L of PBS(BSA1%)
134. Inject in chip, wait 30min and rinse.

**Staining references:**

**Triton: Triton X-100 (1%)**

<https://www.thermofisher.com/order/catalog/product/HFH10>

**Nucleus:**

Thermofischer : Hoescht33342

<https://www.thermofisher.com/order/catalog/product/H3570>

**Cytokeratin:**

*Anticorps:* Dako, mouse anti-human cytokeratin clone AE1/AE3

[https://www.agilent.com/store/en\\_US/Prod-M351529-2/M351529-](https://www.agilent.com/store/en_US/Prod-M351529-2/M351529-2?navAction=push&catId=SubCat3ECS_86427&pCatName=Primary%20Antibodies)

[2?navAction=push&catId=SubCat3ECS\\_86427&pCatName=Primary%20Antibodies](https://www.agilent.com/store/en_US/Prod-M351529-2/M351529-2?navAction=push&catId=SubCat3ECS_86427&pCatName=Primary%20Antibodies)  
&navCount=0

*Fluorophore:* <https://www.thermofisher.com/order/catalog/product/Z25002>

**CD45:**

Thermo Scientific CD45 antibody, Alexa Fluor 647 conjugate (MEM-28)

<http://www.thermofisher.com/1/1/35022-100-tests-cd45-antibody-alexa-fluor-647-monoclonal-mem-28.html>

## 5. General conclusion

During this thesis, we worked on the development of a microfluidic platform for single cell isolation and characterization in water-in-oil droplets and used Ephesia platform, jointly with other devices, to isolate and characterize circulating tumor cells in a clinical study about cancer related thrombotic microangiopathy.

The developed droplet platform consists in an encapsulation device, an on-demand merging chip and a drop qPCR system. In the encapsulation and sorting system we investigated surfactant effects on droplet generation beyond CMC in the studied geometry. We used this mechanism to encapsulate and sort cells in fluorinated oil instead of mineral oil used previously. Then, we constructed a chip dedicated to merging droplets containing cells (4pL) from the first device with droplets containing reagents (50nL) by a purely passive method. The 'on-demand' option is still the bottleneck to validate this device and use the prepared droplets in the drop qPCR system.

The drop qPCR system described in the following chapter, is validated starting with droplets containing total RNA to quantify the expression level of HER2 gene in cell lines. The throughput of the system was then increased to test its limits in term of PCR cycling time and was validated for performing 30 cycles in less than 8 minutes. This device is complementary with the presented droplet platform but can also be considered as an individual block. Indeed, its performances in time and cost reduction by a factor higher than 200 represent a tremendous attraction for industrial development.

The last chapter describe a clinical research study initiated during the course of this PhD and conducted jointly with the BTC lab and clinicians from Curie Institute Hospital. We report for the first time, in the blood of four CR TMA patients, the presence of cell aggregates composed of WBCs and CTCs. Moreover, we implemented during this study, a novel workflow for samples treatment combing Ephesia and other platform of CTC enrichment. We also showed for the first time the possibility of using cells captured with Ephesia chip for Next-generation sequencing. The results of the whole exome sequencing and RNA sequencing may allow us, shortly, to understand the mechanisms involving circulating cancer cell aggregates in the CR TMA.

On the fight against cancer, we hope that the work presented in this thesis brings to the scientific community a useful set of tools. And that finally, some of these tools, jointly with other works, can compete cancer in time as they are based on the same weapon that the disease uses to proliferate, namely diversity.







## Résumé en langue française :

Cette thèse traite du développement et de l'utilisation d'outils microfluidiques pour l'encapsulation et l'analyse de cellules uniques dans le cadre d'applications en biologie et en cancérologie. Deux approches de recherche y ont été adoptées. La première est une approche technologique qui met à profit les avantages de la microfluidique pour :

- La manipulation de volumes allant de quelques picolitres à plusieurs centaines de nanolitres afin d'isoler, manipuler et trier des cellules biologiques par des effets purement hydrodynamiques à haut débit (dizaines de kilohertz).
- La rapidité des échanges thermiques et l'augmentation du rapport signal sur bruit à échelle micrométrique afin d'optimiser le temps des réactions en chaîne par polymérase (PCR) ainsi que les sensibilités des systèmes de PCR quantitatives.

La seconde approche part d'interrogations médicales et biologiques, et utilise des outils microfluidiques en compléments d'autres techniques classiques et/ou innovantes afin de répondre à ces questions. Nous présentons ainsi dans le cadre d'une étude de recherche clinique sur les microangiopathies thrombotiques liées au cancer (CR TMA), l'utilisation d'une seconde plateforme microfluidique 'Ephesia' permettant la capture de cellules tumorales circulantes, afin d'étudier leur rôle dans les microangiopathies thrombotiques liées au cancer par séquençage nouvelle-génération.

La première partie de ce manuscrit, composée des chapitres 2 et 3, relate la mise en place et le développement d'une plateforme de microfluidique en gouttes pour l'analyse en cellule unique. Cette plateforme est constituée de plusieurs modules permettant : l'encapsulation et le tri de cellule unique dans des gouttes aqueuses, l'injection et le mélange des cellules avec des réactifs et enfin l'analyse de leur contenu par un système de PCR quantitative en gouttes (voir Figure 105).

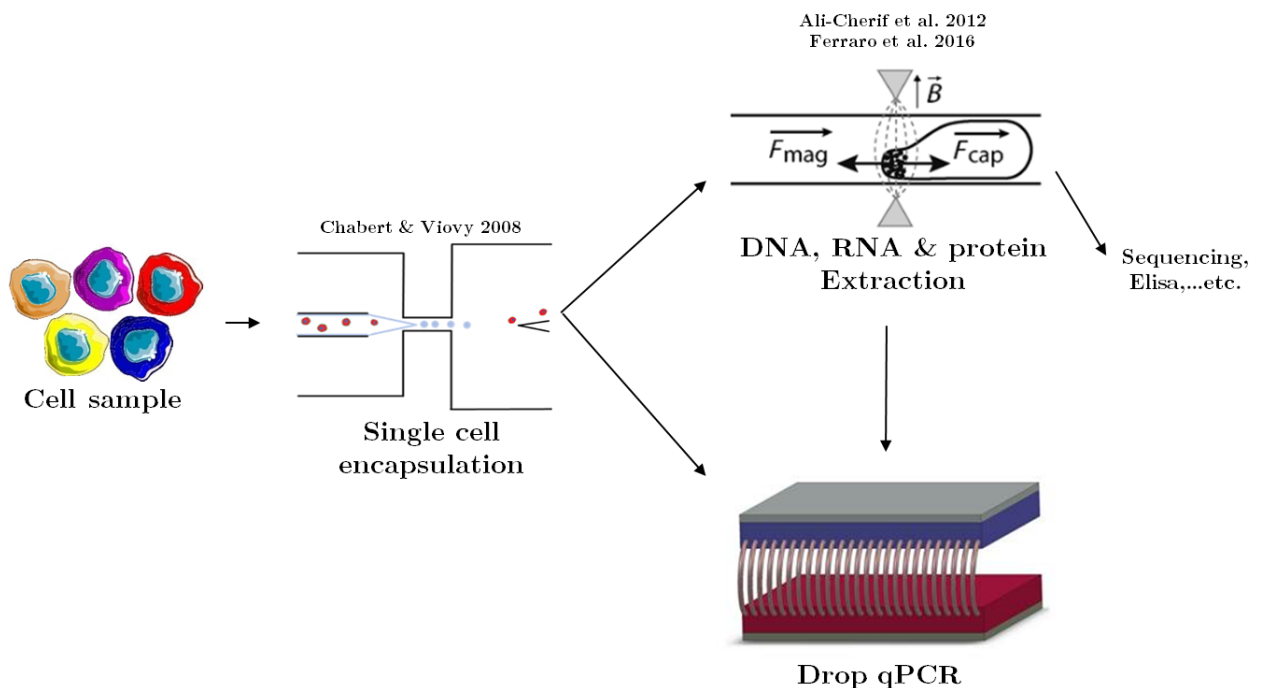


Figure 105: Plateforme d'analyse de cellules uniques. Cette plateforme est composée de trois modules de microfluidique en goutte. Le premier permet l'encapsulation individuelle de cellules dans des gouttes picolitriques et le tri de ces gouttes ne contenant pas de cellules. Le second module est une pince magnétique permettant l'extraction de molécules d'intérêt (contenu cellulaire) d'une goutte et leur relargage dans une seconde. Le dernier module est un système de PCR quantitative en gouttes. Ces modules ont été développés et fonctionnent de façon indépendante les uns des autres. Ils peuvent cependant fonctionner en série l'un après l'autre ou par paire selon les applications.

---

Le second chapitre commence par décrire le système d'encapsulation et de tri de cellule développé précédemment au sein de notre équipe (Chabert 2007 ; Chabert and Viovy 2008). Nous expliquons par la suite la nécessité de convertir ce système d'un fonctionnement en huile minérale vers un fonctionnement en huile fluorée pour des raisons de biocompatibilité, d'augmentation des débits ainsi que pour sa compatibilité avec les autres modules de notre plateforme. Nous observons tout d'abord par l'expérimentation que la formation des gouttes est affectée par la concentration de tensioactif au-delà de la concentration micellaire critique (CMC) dans l'huile minérale. Nous comparons ainsi cet effet entre les deux types d'huiles en utilisant les tensioactifs suivants : Span20 et Span80 dans l'huile minérale légère puis 1H,1H,2H,2H-perfluoro-1-decanol et Krytox 157FSH dans l'huile fluorée FC40. Nos comparaisons se basent sur la mesure du diamètre des gouttes ainsi que sur l'observation de leurs régimes de génération (dripping, jetting...) et de la forme de l'interface huile/eau juste avant sa rupture pour la formation des gouttes. Ce travail nous a permis de mieux comprendre les effets de tension de surface dynamique dans notre système. Par la suite, il nous a été utile dans le choix d'une gamme de diamètre de gouttes générées en huile fluorée adaptée aux cellules choisies. Et pour laquelle nous avons vérifié avec succès la possibilité d'encapsuler et de trier les cellules comme présenté sur la Figure 106.

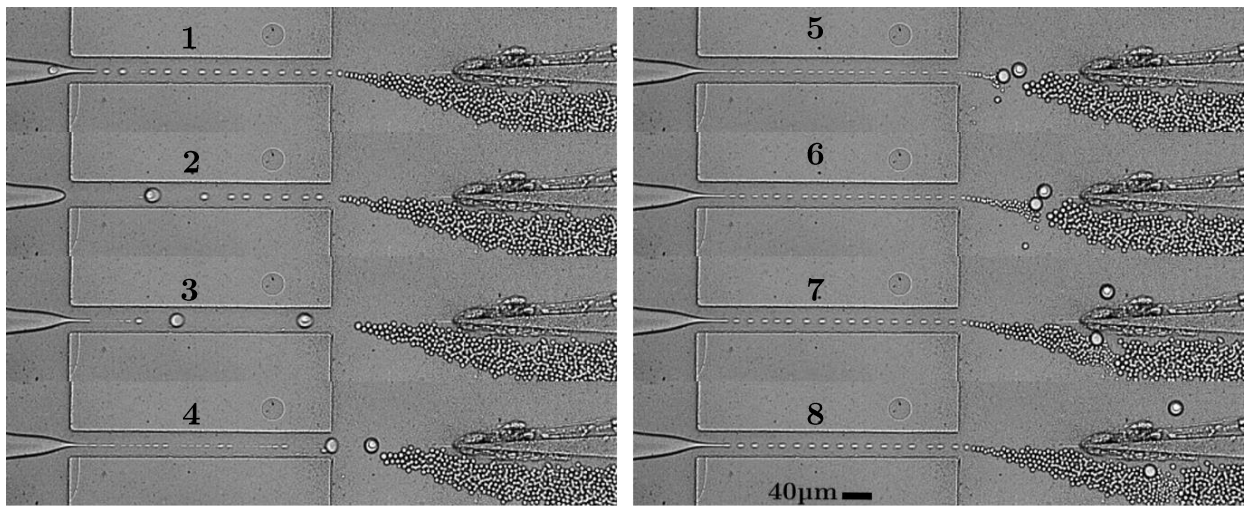


Figure 106: Système d'encapsulation et de tri de cellules uniques en gouttes. La figure comporte une série d'images montrant l'encapsulation et le tri d'une cellule unique de la lignée de cancer du sein SKBR3, avec de l'huile fluorée (FC40) comme phase externe.

---

La deuxième partie du second chapitre décrit le développement de différentes puces microfluidiques permettant la récupération des cellules encapsulées précédemment, leur stockage et leur injection sur demande dans le but de les mélanger avec des gouttes contenant des réactifs. Nous avons validé toutes ces étapes, hormis l'approche « on-demand » que nous sommes actuellement en train d'optimiser.

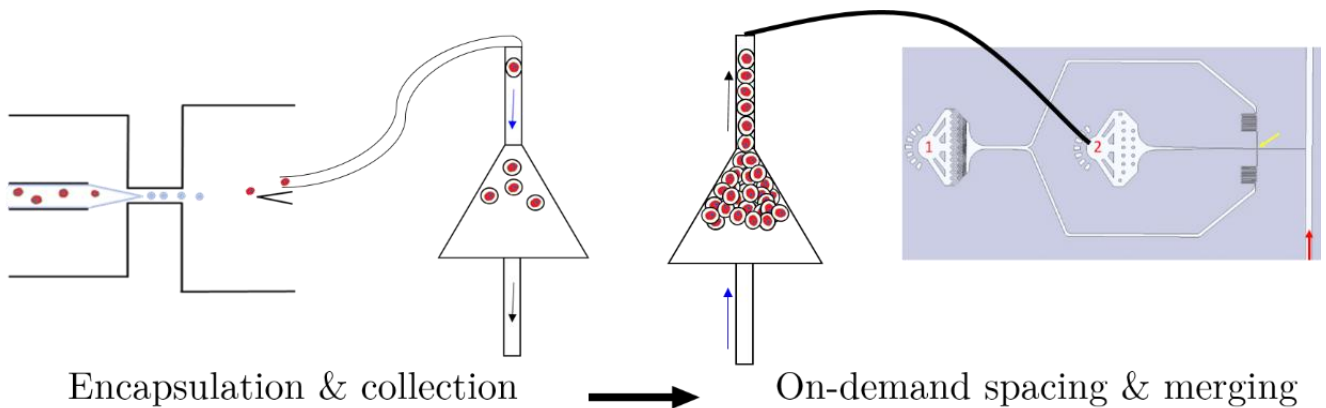


Figure 107: Schéma de principe pour la collection et le mélange « sur-demande » des gouttes contenant des cellules avec des gouttes de réactifs. Dans un premier temps, les gouttes (de quelques picolitres) sont récupérées du système d'encapsulation et de tri, et concentrées par une méthode passive utilisant la différence de densité entre l'huile et l'eau. Une seconde phase est ensuite amorcée pour l'injection de ces gouttes dans un dispositif permettant leur mélange avec des gouttes de 50nL contenant des réactifs (de PCR par exemple) également par une méthode passive de changement de tensioactif.

Le chapitre 3 décrit un système de qPCR en goutte. Nous y décrivons la composition du système, sa fabrication et sa validation par RT qPCR sur de l'ARN total extrait de lignées cellulaires humaines. Comme décrit sur la Figure 108, le système est composé de 3 parties : un dispositif de pompes à seringues et de tubes en PTFE permettant la génération et le mélange de paires de gouttes (échantillon et mix de RT PCR). La goutte résultante traverse ensuite une plaque chauffante maintenue à 50°C pour la rétro-transcription avant d'arriver dans le dispositif de qPCR (Figure 108). Afin de valider le système, nous avons évalué le niveau d'expression du gène HER2 relativement au gène ACTB dans deux lignées cellulaires : SKBR3 (HER+) et MCF7 (HER2-). Pour cela, j'ai cultivé ces cellules, extrait et quantifié leur ARN total puis préparé une série de 7 dilutions de 1ng, jusqu'à 15pg (correspondant à une cellule unique). J'ai effectué les RT PCR et généré les courbes standards permettant d'extraire l'efficacité des PCR ainsi que les niveaux d'expression. De plus, j'ai effectué les mêmes réactions dans une machine commerciale afin de comparer les deux systèmes. Nos résultats montrent que notre système en goutte est aussi fiable que le système commercial en tube avec une division des coûts par un facteur supérieur à 200, une plus grande sensibilité (et ce jusqu'au niveau de cellule unique) permettant une très faible consommation d'échantillon (32 à 64 fois moins qu'en tube à Ct égal).

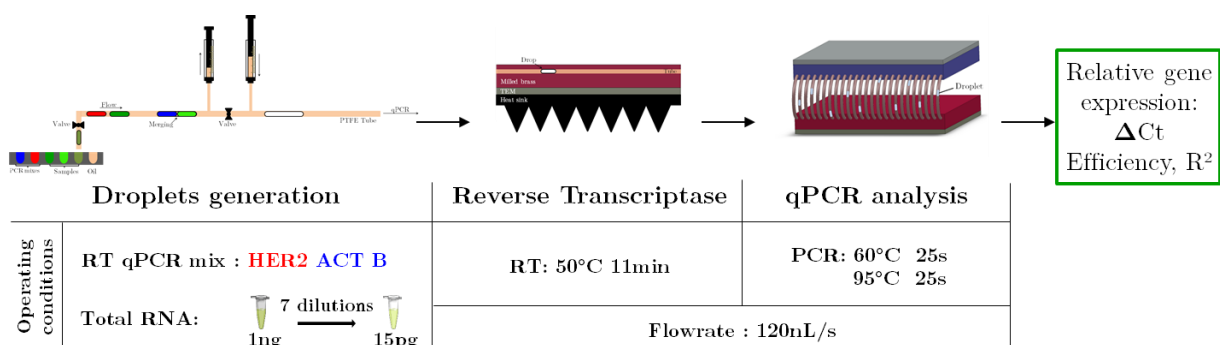


Figure 108: Workflow de RT qPCR en goutte.



Dans un second temps, nous avons exploré la rapidité à laquelle l'essai de RT qPCR pouvait être réalisé dans notre système. Pour ce faire, nous avons fixé une lignée et une concentration d'ARN total (1ng par goutte) et un seul gène et réalisé des RT qPCR en 5 répliques pour 4 débits différents (Figure 109). Nous avons ensuite comparé les valeurs de Ct, d'efficacité et de  $R^2$  pour chaque débit. Ceci nous a permis de valider notre outil pour un fonctionnement 8 fois plus rapide qu'initialement, avec la possibilité de faire 30 cycles de PCR en moins de 8min et ainsi de potentiellement passer 1000 échantillons en 54 minutes.

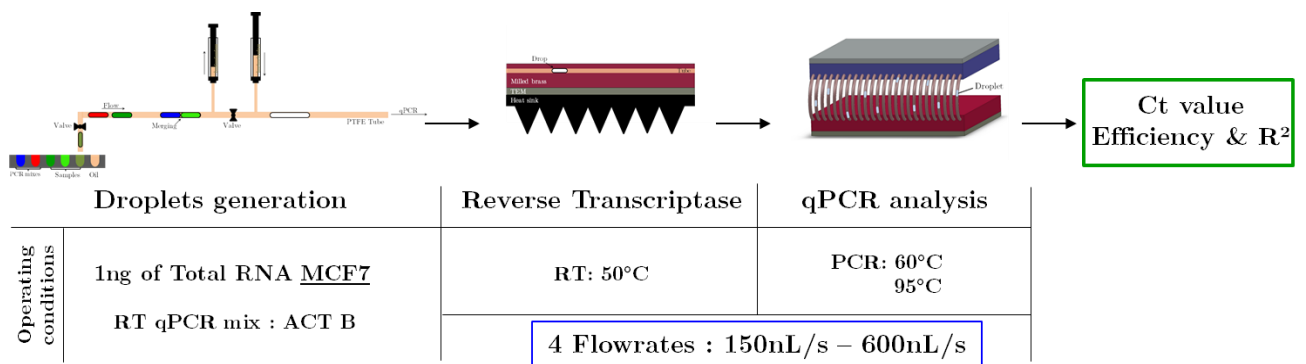
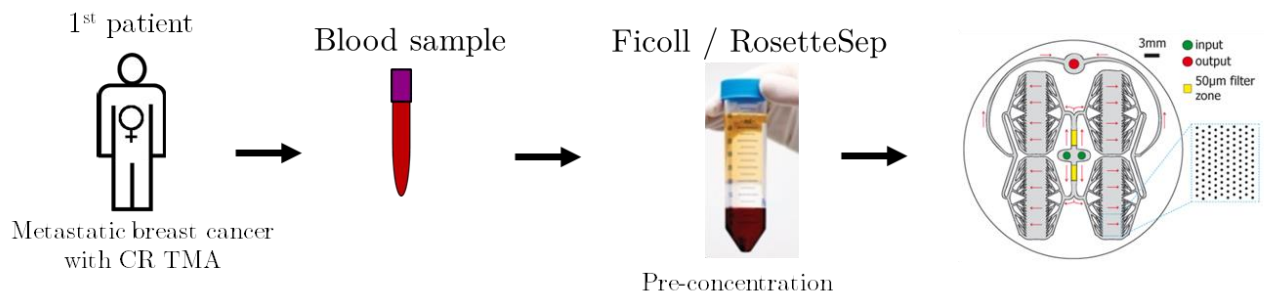


Figure 109: Workflow pour les tests de rapidité de RT qPCR.

---

Le chapitre 4 est consacré à une étude clinique sur la microangiopathie thrombotique paranéoplasique. Nous y avons utilisé des échantillons sanguins prélevés sur quatre patients atteints de cette maladie et suivi le workflow présenté dans la Figure 110 pour la capture de cellules tumorales circulantes dans la puce microfluidique Ephesia. Ceci nous a permis de montrer un premier résultat original sur cette maladie rare qui consiste en l'observation d'agrégats de cellules tumorales et de globules blancs dans le sang de ces patients (voir Figure 111). Ce résultat est de plus en accord avec les précédentes observations dans des artères pulmonaires ou cardiaques, faites il y a une quarantaine d'années et décrit dans la littérature, lors d'autopsies de patients atteints de cette maladie.



**Figure 110: Workflow Ephesia pour la capture de cellule tumorale circulantes**

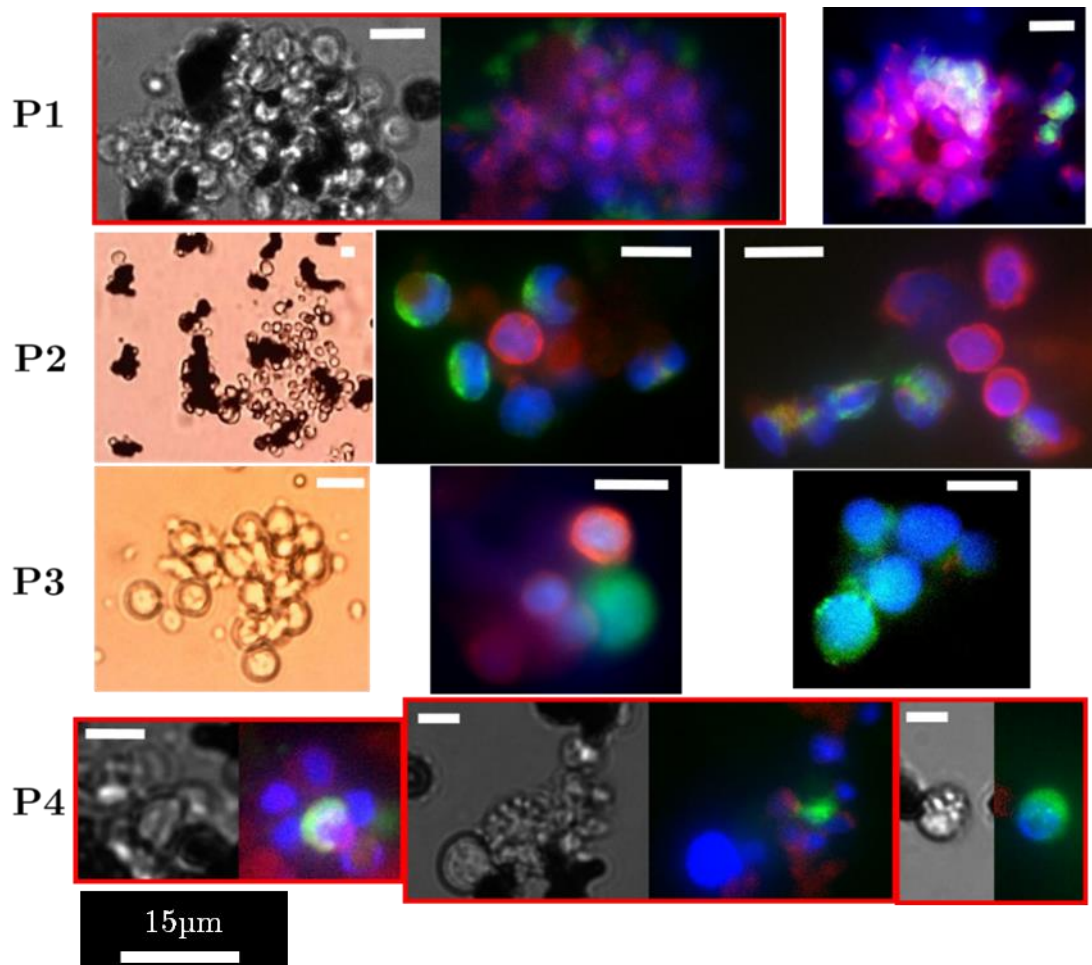
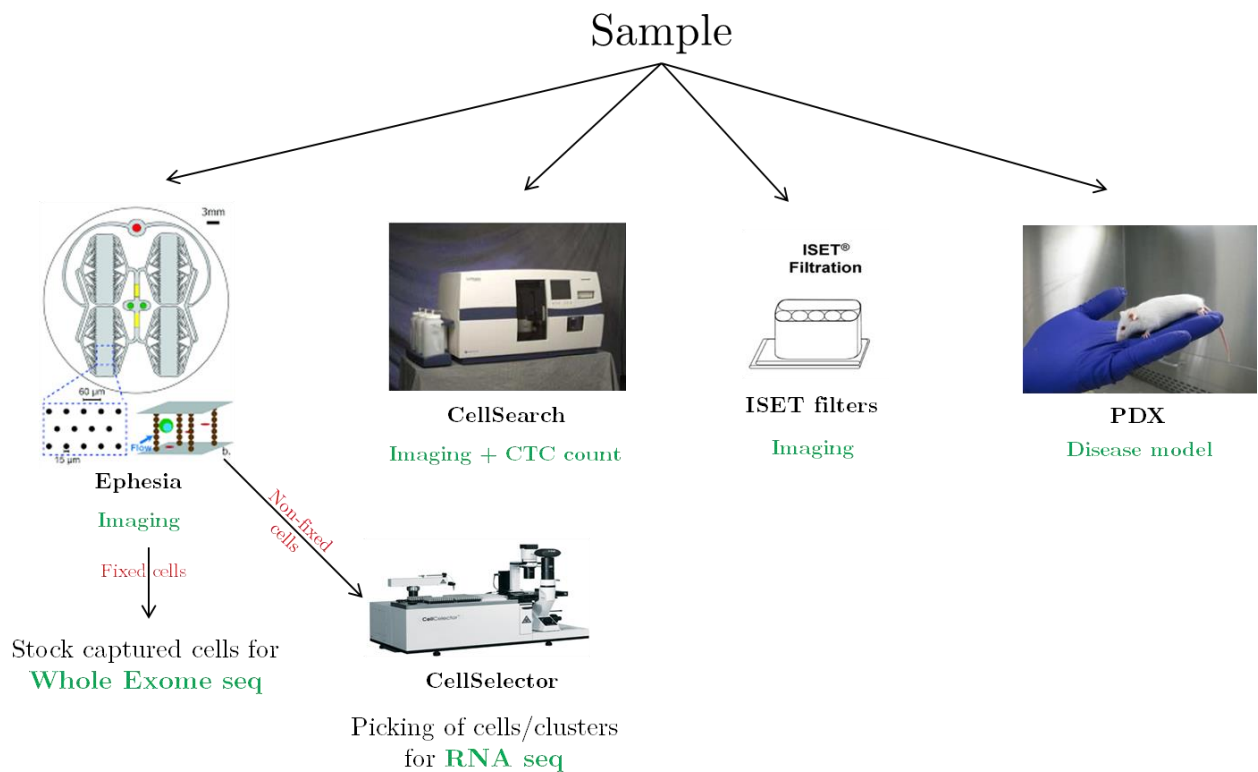


Figure 111: Images d'agrégats de cellules capturées dans la puce microfluidique Ephesia sur des prélèvements sanguins de 4 patients atteints de CRTMA, en champ clair et en marquages immunologiques (par paire correspondantes lorsque encadrées en rouge). Les couleurs rouges, vert et bleu correspondent respectivement au marqueur de globules blancs CD45, au marqueur des CTCs Cytokeratin et au marqueur du noyau cellulaire Hoechst33342.

Par la suite, nous avons voulu analyser le contenu de ces agrégats de cellules. Pour cela, nous avons réalisé avec succès et pour la première fois du Whole Exome Sequencing sur des cellules capturées en Ephesia et comparé leurs résultats avec du tissu sain et du tissu tumoral lorsqu'il était disponible. Nous avons également commencé à mettre en place la récupération de cellules individuelles capturées sur Ephesia en utilisant le CellCelector afin de réaliser du RNA seq sur ces cellules (Figure 112). Ces résultats technologiques sont très prometteurs car ils peuvent être exploités dans tout autre contexte d'étude sur des populations rares de cellules.

Et ceci, grâce à la complémentarité de notre système de capture microfluidique Ephesia avec les autres outils utilisés dans cette étude, tel que le CellCelector et le séquençage nouvelle-génération, et permettant ainsi la capture, la manipulation et le typage de ces cellules.



**Figure 112: Workflow de l'étude Clinique avec l'implémentation de Whole Exome Sequencing et de la récupération de cellules individuelles grâce au CellCelector pour du séquençage d'ARN.**

# Bibliography

- Abate, A. R. et al. 2010. "High-Throughput Injection with Microfluidics Using Picoinjectors." *Proceedings of the National Academy of Sciences* 107(45): 19163–66. <http://www.pnas.org/cgi/doi/10.1073/pnas.1006888107>.
- Agerbæk, Mette et al. 2018. "The VAR2CSA Malaria Protein Efficiently Retrieves Circulating Tumor Cells in an EpCAM-Independent Manner." *Nature Communications* 9(1). <http://dx.doi.org/10.1038/s41467-018-05793-2>.
- Ahrberg, Christian D., Andreas Manz, and Bong Geun Chung. 2016. "Polymerase Chain Reaction in Microfluidic Devices." *Lab on a Chip* 16(20): 3866–84. <http://dx.doi.org/10.1039/C6LC00984K>.
- Ali-Cherif, Anaïs et al. 2012. "Programmable Magnetic Tweezers and Droplet Microfluidic Device for High-Throughput Nanoliter Multi-Step Assays." *Angewandte Chemie - International Edition* 51(43): 10765–69.
- Alix-Panabieres, C., and K. Pantel. 2013. "Circulating Tumor Cells: Liquid Biopsy of Cancer." *Clinical Chemistry* 59(1): 110–18. <http://www.clinchem.org/cgi/doi/10.1373/clinchem.2012.194258>.
- Anna, Shelley L., and Hans C. Mayer. 2006. "Microscale Tipstreaming in a Microfluidic Flow Focusing Device." *Physics of Fluids* 18(12).
- Antman, KH et al. 1979. "Microangiopathic Hemolytic Anemia and Cancer: A Review." *Medicine (Baltimore)* 58: 377–84.
- Ashworth, Thomas Ramsden. 1869. "A Case of Cancer in Which Cells Similar to Those in the Tumours Were Seen in the Blood after Death." *Australian Medical Journal* XIV.
- Autebert, Julien et al. 2015. "High Purity Microfluidic Sorting and Analysis of Circulating Tumor Cells: Towards Routine Mutation Detection." *Lab Chip* 15(9): 2090–2101. <http://xlink.rsc.org/?DOI=C5LC00104H>.
- Autebert, Julien, and Benoit Coudert. 2012. "Microfluidic: An Innovative Tool for Efficient Cell Sorting."
- Babu K, Govind, and Gita R. Bhat. 2016. "Cancer-Associated Thrombotic Microangiopathy." *Ecancermedicalscience* 10: 1–11.
- Baret, Jean Christophe et al. 2009. "Fluorescence-Activated Droplet Sorting (FADS): Efficient Microfluidic Cell Sorting Based on Enzymatic Activity." *Lab on a Chip* 9(13): 1850–58.
- Baroud, Charles N., Francois Gallaire, and Rémi Dangla. 2010. "Dynamics of Microfluidic Droplets." *Lab on a Chip* 10(16): 2032. <http://pubs.rsc.org/en/content/articlehtml/2010/lc/c001191f> (July 1, 2015).
- Bidard, François-clement et al. 2018. "Circulating Tumor Cells in Breast Cancer Patients Treated by Neoadjuvant Chemotherapy: A Meta-Analysis." *Journal of the National Cancer Institute* 110(6): 560–67.
- Bidard, François-clément et al. 2014. "Clinical Validity of Circulating Tumour Cells in Patients with Metastatic Breast Cancer: A Pooled Analysis of Individual." 15(April).
- Bidard, François-clément, and Jean-yves Pierga. 2015. "Clinical Utility of Circulating Tumor Cells in Metastatic Breast Cancer." *Journal of Clinical Oncology*.
- Bontoux, N. et al. 2008. "Integrating Whole Transcriptome Assays on a Lab-on-a-Chip for Single Cell Gene Profiling." *Lab on a Chip* 8(3): 443–50.

- Brain, M. C. et al. 1970. "Microangiopathic Haemolytic Anaemia and Mucin-forming Adenocarcinoma." *British Journal of Haematology* 18(2): 183–94.
- Brain, M. C., J. V. Dacie, and D. O. Hourhirane. 1962. "Microangiopathic Haemolytic Anaemia: The Possible Role of Vascular Lesions in Pathogenesis." *British journal of haematology* 8: 358–74.
- Brosseau, Quentin, Jérémy Vrignon, and Jean-Christophe Baret. 2014. "Microfluidic Dynamic Interfacial Tensiometry (MDIT)." *Soft matter* 10: 3066–76. <http://www.ncbi.nlm.nih.gov/pubmed/24695668>.
- Bustin, Stephen A. 2009. "The MIQE Guidelines: Minimum Information for Publication of Quantitative Real-Time PCR Experiments." *Applied and Environmental Microbiology* 65(8): 3605–13.
- Di Carlo, Dino, Daniel Irimia, Ronald G Tompkins, and Mehmet Toner. 2007. "Continuous Inertial Focusing, Ordering, and Separation of Particles in Microchannels." *Proceedings of the National Academy of Sciences of the United States of America* 104(48): 18892–97. <http://www.pubmedcentral.nih.gov/articlerender.fcgi?artid=2141878&tool=pmcentrez&rendertype=abstract>.
- Chabert, Max et al. 2006. "Automated Microdroplet Platform for Sample Manipulation and Polymerase Chain Reaction." *Analytical Chemistry* 78(22): 7722–28.
- . 2007. "Micro Uidique de Gouttes Pour Les Analyses Biologiques."
- Chabert, Max, Kevin D. Dorfman, and Jean-Louis Viovy. 2005. "Droplet Fusion by Alternating Current (AC) Field Electrocoalescence in Microchannels." *Electrophoresis* 26(19): 3706–15. <http://doi.wiley.com/10.1002/elps.200500109>.
- Chabert, Max, and Jean-Louis Viovy. 2008. "Microfluidic High-Throughput Encapsulation and Hydrodynamic Self-Sorting of Single Cells." *Proceedings of the National Academy of Sciences of the United States of America* 105(9): 3191–96. <http://www.ncbi.nlm.nih.gov/pubmed/18316742>.
- Chaffer, Christine, and Robert Weinberg. 2011. "A Perspective on Cancer." *Science* 331(6024): 1559–65. <http://science.sciencemag.org.ezproxy.is.ed.ac.uk/content/331/6024/1559.full.pdf+html>.
- Chan, P. C.H., and L. G. Leal. 1979. "The Motion of a Deformable Drop in a Second-Order Fluid." *Journal of Fluid Mechanics* 92(1): 131–70.
- Chung, Meng Ting, Daniel Núñez, Dawen Cai, and Katsuo Kurabayashi. 2017. "Deterministic Droplet-Based Co-Encapsulation and Pairing of Microparticles: Via Active Sorting and Downstream Merging." *Lab on a Chip* 17(21): 3664–71.
- Collins, David J. et al. 2015. "The Poisson Distribution and beyond: Methods for Microfluidic Droplet Production and Single Cell Encapsulation." *Lab on a Chip* 15(17): 3439–59.
- Cristofanilli, Massimo et al. 2004. "Circulating Tumor Cells, Disease Progression, and Survival in Metastatic Breast Cancer." *The New England journal of medicine*: 781–91.
- Curcio, Mario, and Johan Roeraade. 2003. "Continuous Segmented-Flow Polymerase Chain Reaction for High-Throughput Miniaturized DNA Amplification." *Analytical Chemistry* 75(1): 1–7.
- Dagogo-Jack, Ibiayi, and Alice T. Shaw. 2018. "Tumour Heterogeneity and Resistance to Cancer Therapies." *Nature Reviews Clinical Oncology* 15(2): 81–94.
- Daniel, J. H. et al. 1998. "Silicon Microchambers for DNA Amplification." *Sensors and*



- Actuators, A: Physical* 71(1–2): 81–88.
- Delapierre, François Damien et al. 2017. “High Throughput Micropatterning of Interspersed Cell Arrays Using Capillary Assembly.” *Biofabrication* 9(1).
- Diguet, Antoine et al. 2011. “Photoreversible Fragmentation of a Liquid Interface for Micro-Droplet Generation by Light Actuation.” *Lab on a Chip* 11(16): 2666–69.
- Dorfman, Kevin D. et al. 2005. “Contamination-Free Continuous Flow Microfluidic Polymerase Chain Reaction for Quantitative and Clinical Applications.” *Analytical Chemistry* 77(11): 3700–3704.
- Ducos, Guillaume et al. 2014. “Metastatic Cancer-Related Thrombotic Microangiopathies: A Cohort Study.” *Future Oncology* 10(10): 1727–34.
- Ebbert, Mark T.W. et al. 2016. “Evaluating the Necessity of PCR Duplicate Removal from Next-Generation Sequencing Data and a Comparison of Approaches.” *BMC Bioinformatics* 17(Suppl 7). <http://dx.doi.org/10.1186/s12859-016-1097-3>.
- Edd, Jon F. et al. 2008. “Controlled Encapsulation of Single-Cells into Monodisperse Picolitre Drops.” *Lab on a Chip* 8(8): 1262–64.
- Eyer, Klaus et al. 2017. “Single-Cell Deep Phenotyping of IgG-Secreting Cells for High-Resolution Immune Monitoring.” *Nature Biotechnology* 35(10): 977–82. <http://dx.doi.org/10.1038/nbt.3964>.
- Farrar, Jared S., and Carl T. Wittwer. 2015. “Extreme PCR: Efficient and Specific DNA Amplification in 15-60 Seconds.” *Clinical Chemistry* 61(1): 145–53.
- Ferraro, Davide et al. 2016a. “Microfluidic Platform Combining Droplets and Magnetic Tweezers: Application to HER2 Expression in Cancer Diagnosis.” *Scientific reports* 6(April): 25540. <http://www.ncbi.nlm.nih.gov/pubmed/27157697>.
- . 2016b. “Microfluidic Platform Combining Droplets and Magnetic Tweezers: Application to HER2 Expression in Cancer Diagnosis.” *Scientific Reports* 6(1): 25540.
- . 2018. “Controlling the Distance of Highly Confined Droplets in a Capillary by Interfacial Tension for Merging On-Demand.” *Lab on a Chip*. <http://pubs.rsc.org/en/Content/ArticleLanding/2018/LC/C8LC01182F>.
- Fleige, Simone, and Michael W. Pfaffl. 2006. “RNA Integrity and the Effect on the Real-Time QRT-PCR Performance.” *Molecular Aspects of Medicine* 27(2–3): 126–39.
- Fontana, S. et al. 2001. “Microangiopathic Haemolytic Anaemia in Metastasizing Malignant Tumours Is Not Associated with a Severe Deficiency of the von Willebrand Factor-Cleaving Protease.” *British Journal of Haematology* 113(1): 100–102.
- Gruner, Philipp et al. 2015. “Stabilisers for Water-in-Fluorinated-Oil Dispersions: Key Properties for Microfluidic Applications.” *Current Opinion in Colloid and Interface Science* 20(3): 183–91.
- Gu, Hao, Michel H.G. Duits, and Frieder Mugele. 2011. “Droplets Formation and Merging in Two-Phase Flow Microfluidics.” *International journal of molecular sciences* 12(4): 2572–97.
- Gu, Hao, Florent Malloggi, Siva A. Vanapalli, and Frieder Mugele. 2008. “Electrowetting-Enhanced Microfluidic Device for Drop Generation.” *Applied Physics Letters* 93(18): 2012–15.
- Hasin, Yehudit, Marcus Seldin, and Aldons Lusic. 2017. “Multi-Omics Approaches to Disease.” *Genome Biology* 18(1): 1–15.

- Hayes, Christopher J., and Tara M. Dalton. 2015. "Microfluidic Droplet-Based PCR Instrumentation for High-Throughput Gene Expression Profiling and Biomarker Discovery." *Biomolecular Detection and Quantification* 4: 22–32. <http://dx.doi.org/10.1016/j.bdq.2015.04.003>.
- Higuchi, Russell., Carita. Fockeler, Gavin. Dollinger, and Robert. Watson. 1993. "Kinetic PCR Analysis: Real-Time Monitoring of DNA Amplification Reactions." *Nature Biotechnology* 11: 159–1564. <http://www.nature.com/nbt/journal/v11/n12/abs/nbt1293-1559.html>.
- Holland, Pamela M., Richard D. Abramson, Robert. Watson, and David H. Gelfand. 1991. "Detection of Specific Polymerase Chain Reaction Product by Utilizing the 5' to 3' Exonuclease Activity of *Thermus Aquaticus* DNA Polymerase." *PNAS* 88(August): 7276–80. <http://www.pnas.org/content/88/16/7276.long>.
- Houssin, Timothée et al. 2016. "Ultrafast, Sensitive and Large-Volume on-Chip Real-Time PCR for the Molecular Diagnosis of Bacterial and Viral Infections." *Lab on a Chip* 16(8): 1401–11. <http://dx.doi.org/10.1039/C5LC01459J>.
- Jung, Jaeyun, Hyang Sook Seol, and Suhwan Chang. 2018. "The Generation and Application of Patient-Derived Xenograft Model for Cancer Research." *Cancer Research and Treatment* 50(1): 1–10.
- Kamalakshakurup, Gopakumar, and Abraham P. Lee. 2017. "High-Efficiency Single Cell Encapsulation and Size Selective Capture of Cells in Picoliter Droplets Based on Hydrodynamic Micro-Vortices." *Lab on a Chip* 17(24): 4324–33.
- Kopp, Martin U., Andrew J. De Mello, and Andreas Manz. 1998. "Chemical Amplification: Continuous-Flow PCR on a Chip." *Science* 280(5366): 1046–48.
- Köster, Sarah et al. 2008. "Drop-Based Microfluidic Devices for Encapsulation of Single Cells." *Lab on a Chip* 8(7): 1110–15.
- Kovalchuk, Nina M. et al. 2018. "Effect of Surfactant on Emulsification in Microchannels." *Chemical Engineering Science* 176: 139–52. <https://doi.org/10.1016/j.ces.2017.10.026>.
- Laget, Sophie et al. 2017. 12 PLoS ONE *Technical Insights into Highly Sensitive Isolation and Molecular Characterization of Fixed and Live Circulating Tumor Cells for Early Detection of Tumor Invasion*.
- Lallo, Alice et al. 2017. "Circulating Tumor Cells and CDX Models as a Tool for Preclinical Drug Development." *Translational Lung Cancer Research* 6(4): 397–408. <http://tlcr.amegroups.com/article/view/14974/12187>.
- Landrum, Melissa J. et al. 2014. "ClinVar: Public Archive of Relationships among Sequence Variation and Human Phenotype." *Nucleic Acids Research* 42(D1): 980–85.
- Lawson, Devon A. et al. 2018. "Tumour Heterogeneity and Metastasis at Single-Cell Resolution." *Nature Cell Biology* 20(12): 1349–60. <http://www.nature.com/articles/s41556-018-0236-7>.
- Leis, Olatz, Paz Lopez-mato, and Angel G Martin. 2012. "Circulating Tumor Stem Cells as Biomarkers for Cancer Progression." *Recent Patents on Biomarkers*: 36–53.
- Marcus, Joshua S., W. French Anderson, and Stephen R. Quake. 2006. "Parallel Picoliter RT-PCR Assays Using Microfluidics." *Analytical Chemistry* 78(3): 956–58.
- Mary, Pascaline et al. 2011. "Analysis of Gene Expression at the Single-Cell Level Using Microdroplet-Based Microfluidic Technology." *Biomicrofluidics* 5(2): 1–10.
- Mazutis, Linas et al. 2013. "Single-Cell Analysis and Sorting Using Droplet-Based



- Microfluidics.” *Nature Protocols* 8(5): 870–91.
- Millner, Lori M, Mark W Linder, and Roland Jr. Valdes. 2013. “HHS Public Access.” *Ann Clin Lab Sci.* 43(3): 295–304.
- Mullis, Karis et al. 1986. “Specific Enzymatic Amplification of DNA In Vitro: The Polymerase Chain Reaction.” *Cold Spring Harb Symp Quant Biol.* 7(1): 29–105.
- Nakano, Hideo et al. 1994. “High Speed Polymerase Chain Reaction in Constant Flow.” *Bioscience, Biotechnology and Biochemistry* 58(2): 349–52.
- Navarro, E., G. Serrano-Heras, M. J. Castaño, and J. Solera. 2015. “Real-Time PCR Detection Chemistry.” *Clinica Chimica Acta* 439: 231–50. <http://dx.doi.org/10.1016/j.cca.2014.10.017>.
- Niu, Xize, Fabrice Gielen, Joshua B. Edel, and Andrew J. DeMello. 2011. “A Microdroplet Dilutor for High-Throughput Screening.” *Nature Chemistry* 3(6): 437–42. <http://dx.doi.org/10.1038/nchem.1046>.
- Nunes, J. K., S. S.H. Tsai, J. Wan, and H. A. Stone. 2013. “Dripping and Jetting in Microfluidic Multiphase Flows Applied to Particle and Fibre Synthesis.” *Journal of Physics D: Applied Physics* 46(11).
- Oberic, L. et al. 2009. “Cancer Awareness in Atypical Thrombotic Microangiopathies.” *The Oncologist* 14(8): 769–79. <http://theoncologist.alphamedpress.org/cgi/doi/10.1634/theoncologist.2009-0067>.
- Opawale, Fo, and Dj Burgess. 1998. “Influence of Interfacial Properties of Lipophilic Surfactants on Water-in-Oil Emulsion Stability.” *Journal of colloid and interface science* 197(1): 142–50. <http://www.ncbi.nlm.nih.gov/pubmed/9466854>.
- Perez-toralla, Karla. 2013. “MICROFLUIDIC SYSTEMS FOR IN SITU MOLECULAR CHARACTERIZATION OF CIRCULATING TUMOR.”
- Perez-Toralla, Karla et al. 2015. “FISH in Chips: Turning Microfluidic Fluorescence in Situ Hybridization into a Quantitative and Clinically Reliable Molecular Diagnosis Tool.” *Lab Chip* 15(3): 811–22. <http://xlink.rsc.org/?DOI=C4LC01059K>.
- Picelli, Simone et al. 2014. “Full-Length RNA-Seq from Single Cells Using Smart-Seq2.” *Nature protocols* 9(1): 171–81.
- Riaud, Antoine et al. 2014. “Lattice-Boltzmann Method for the Simulation of Multiphase Mass Transfer and Reaction of Dilute Species.” *Physical Review E - Statistical, Nonlinear, and Soft Matter Physics* 89(5): 1–14.
- . 2018. “Numerical Study of Surfactant Dynamics during Emulsification in a T-Junction Microchannel.” *Langmuir* 34(17): 4980–90.
- Riethdorf, Sabine et al. 2007. “Detection of Circulating Tumor Cells in Peripheral Blood of Patients with Metastatic Breast Cancer: A Validation Study of the CellSearch System.” *Journal of Clinical Oncology* 25(1): 13(3): 920–29.
- Roach, L. Spencer, Helen Song, and Rustem F. Ismagilov. 2005. “Controlling Nonspecific Protein Adsorption in a Plug-Based Microfluidic System by Controlling Interfacial Chemistry Using Fluorous-Phase Surfactants.” *Analytical Chemistry* 77(3): 785–96.
- Rutledge, R. G., and C. Côté. 2003. “Mathematics of Quantitative Kinetic PCR and the Application of Standard Curves.” *Nucleic Acids Research* 31(16): 93e–93. <https://academic.oup.com/nar/article-lookup/doi/10.1093/nar/gng093>.
- Saias, Laure, Julien Autebert, Laurent Malaquin, and Jean Louis Viovy. 2011. “Design,

- Modeling and Characterization of Microfluidic Architectures for High Flow Rate, Small Footprint Microfluidic Systems.” *Lab on a Chip* 11(5): 822–32.
- Saliba, A.-E. et al. 2010. “Microfluidic Sorting and Multimodal Typing of Cancer Cells in Self-Assembled Magnetic Arrays.” *Proceedings of the National Academy of Sciences* 107(33): 14524–29. <http://www.pnas.org/cgi/doi/10.1073/pnas.1001515107>.
- Sciambi, Adam, and Adam R Abate. 2015. “Accurate Microfluidic Sorting of Droplets at 30 KHz.” *Lab Chip* 15(1): 47–51. <http://pubs.rsc.org/globalproxy.cvt.dk/en/content/articlehtml/2015/lc/c4lc01194e%5Cn> <http://xlink.rsc.org/?DOI=C4LC01194E>.
- Svec, David et al. 2015. “How Good Is a PCR Efficiency Estimate: Recommendations for Precise and Robust QPCR Efficiency Assessments.” *Biomolecular Detection and Quantification* 3: 9–16. <http://dx.doi.org/10.1016/j.bdq.2015.01.005>.
- Takabatake, Daisuke, and Kazuyuki Oishi. 2016. “Microangiopathic Hemolytic Anemia Associated with Metastatic Breast Cancer: Case Report and Literature Review.” *SpringerPlus* 5(1).
- Todorov, Hristo, David Fournier, and Susanne Gerber. 2018. “Principal Components Analysis: Theory and Application to Gene Expression Data Analysis.” *Genomics and Computational Biology* 4(2): 100041. <https://genomicscomputbiol.org/ojs3/GCB/article/view/41>.
- Toss, Angela, Zhaomei Mu, Sandra Fernandez, and Massimo Cristofanilli. 2014. “CTC Enumeration and Characterization: Moving toward Personalized Medicine.” 2(11).
- Tulukcuoglu Guneri, Ezgi. 2016. “Development of Microfluidic Device for High Content Analysis of Circulating Tumor Cells.”
- VanInsberghe, Michael et al. 2018. “Highly Multiplexed Single-Cell Quantitative PCR.” *PLoS ONE* 13(1): 1–18.
- Vermeulen, Joëlle et al. 2011. “Measurable Impact of RNA Quality on Gene Expression Results from Quantitative PCR.” *Nucleic Acids Research* 39(9).
- Vona, G. et al. 2000. “Isolation by Size of Epithelial Tumor Cells: A New Method for the Immunomorphological and Molecular Characterization of Circulating Tumor Cells.” *American Journal of Pathology* 156(1): 57–63.
- Wang, K., Y. C. Lu, J. H. Xu, and G. S. Luo. 2009. “Determination of Dynamic Interfacial Tension and Its Effect on Droplet Formation in the T-Shaped Microdispersion Process.” *Langmuir* 25(4): 2153–58.
- Wang, Kai, Liming Zhang, Wanlu Zhang, and Guangsheng Luo. 2016. “Mass-Transfer-Controlled Dynamic Interfacial Tension in Microfluidic Emulsification Processes.” *Langmuir* 32(13): 3174–85.
- White, A. K. et al. 2011. “High-Throughput Microfluidic Single-Cell RT-QPCR.” *Proceedings of the National Academy of Sciences* 108(34): 13999–4. <http://www.pnas.org/cgi/doi/10.1073/pnas.1019446108>.
- Wu, Liang et al. 2013. “Encapsulation of Single Cells on a Microfluidic Device Integrating Droplet Generation with Fluorescence-Activated Droplet Sorting.” *Biomedical Microdevices* 15(3): 553–60.
- Xu, Jh H et al. 2012. “The Dynamic Effects of Surfactants on Droplet Formation in Coaxial Microfluidic Devices.” *Langmuir* 28(25): 9250–58.

<http://pubs.acs.org/doi/abs/10.1021/la301363d>.

Zhou, Hongbo, and Shuhuai Yao. 2014. "A Facile On-Demand Droplet Microfluidic System for Lab-on-a-Chip Applications." *Microfluidics and Nanofluidics* 16(4): 667–75.

Zhu, Pingan, and Liqiu Wang. 2017a. "Passive and Active Droplet Generation with Microfluidics: A Review." *Lab on a Chip* 17(1): 34–75. <http://dx.doi.org/10.1039/C6LC01018K>.

———. 2017b. "Passive and Active Droplet Generation with Microfluidics: A Review." *Lab on a Chip* 17(online): 34–75. <http://pubs.rsc.org/en/Content/ArticleLanding/2016/LC/C6LC01018K%5Cnhttp://dx.doi.org/10.1039/C6LC01018K>.

Zhu, Ying et al. 2015. "Printing 2-Dimensional Droplet Array for Single-Cell Reverse Transcription Quantitative PCR Assay with a Microfluidic Robot." *Scientific Reports* 5: 1–7.





## RÉSUMÉ

---

Cette thèse traite du développement et de l'utilisation d'outils microfluidiques pour l'encapsulation et l'analyse de cellules uniques dans le cadre d'applications en biologie et en cancérologie. Nous y relatons la mise en place et le développement d'une plateforme de microfluidique en gouttes composée de plusieurs modules permettant : l'encapsulation et le tri de cellule unique dans des gouttes aqueuses, l'injection et le mélange des cellules avec des réactifs et enfin l'analyse de leur contenu par un système de PCR quantitative en gouttes. Nous présentons ensuite dans le cadre d'une étude de recherche clinique, l'utilisation d'une seconde plateforme microfluidique 'Ephesia' permettant la capture de cellules tumorales circulantes, afin d'étudier leur rôle dans les microangiopathies thrombotiques liées au cancer par séquençage nouvelle-génération.

## MOTS CLÉS

---

Microfluidique ; Cellules tumorales circulantes ; Microfluidique de gouttes.

## ABSTRACT

---

This thesis reports on the development and use of microfluidic tools for the encapsulation and analysis of single cells with applications in biology and cancerology. We describe the development and characterization of a droplet microfluidic platform composed of several modules allowing: the encapsulation and sorting of single cells in aqueous droplets in oil, the injection and merging of the cells with reagents and finally, the analysis of their content by a droplet quantitative PCR device. Thereafter, we present in the context of a clinical research study, the use of a second microfluidic platform 'Ephesia' allowing the capture of circulating tumor cells, to study their role in cancer related thrombotic microangiopathies by next generation sequencing.

## KEYWORDS

---

Microfluidics ; Circulating tumor cells ; Droplet microfluidics.